Alternative chemical methods for the catalytic processes within hydrogen fuelled proton exchange membrane fuel cells

by

James Matthew Courtney

A thesis submitted to the University of Birmingham for the degree

DOCTOR OF PHILOSOPHY

The Centre for Hydrogen and Fuel Cell Research

School of Chemical Engineering

College of Engineering & Physical Sciences

The University of Birmingham

June 2016

UNIVERSITY OF BIRMINGHAM

University of Birmingham Research Archive

e-theses repository

Abstract

This thesis explores three routes to alleviating the economic barriers to proton exchange membrane fuel cells through reducing, recycling and removing platinum group metals (PGMs).

The reduction of PGM content is explored using electrochemistry to assess the novel materials produced when combining fullerene based compounds with electron beam lithography. This technique yields the potential to precisely control the distance between platinum (or other metal) atoms embedded within carbon materials. It is shown that the material alters the onset potential of proton reduction compared to glassy carbon and the methodology for study is developed.

The recycling of PGMs is demonstrated by testing the electrochemical behaviour and particle structure of deposited palladium within biomass produced through biohydrometallurgy. Electron microscopy and electrochemistry is used to investigate the biohydrometallurgy process and how the substrate, leachate and reducing agent effect both the particles produced and the electrochemistry observed. Concluding that the un-processed materials may function as future electrocatalysts without further processing steps.

The removal of PGM content is investigated, through the electrochemical characterisation of the adsorbed layers and solutions of phosphomolybdic acid, singularly substituted vanadophosphomolybdic acid and doubly substituted vanadophosphomolybdic acid. Describing the complicated multi-electron, multi-step redox chemistry of the potential mediator species, with specific focus on electrode material and the effect of pH.

Glossary of terms

AFC	Alkaline Fuel Celll
APU	Auxillary Power Unit
BPP	Bi-Polar Plate
BPPG	Basal plane pyrolytic graphite
CCM	catalyst coated membrane
CDT	Centre for Doctoral Training
CL	Catalyst Layer
CNT	Carbon nano-tube
DMFC	Direct Methanol Fuel Cell
DoE	Department of Energy
DTC	Doctoral Training Centre
E(0)	Standard Equilibrium Potential
ECSA	Electrochemical surface area
ECSA	Electrochemical Surface Area
EIS	Electrochemical Impedance Spectroscopy
EPPG	Edge plane pyrolytic graphite
F	Faradays Constant
FFP	Flow Field Plate
ful-bipy	fulleropyrrolidine bipyridine
ful-bipy-pt	fulleropyrrolidine bipyridine platinum chloride
G	Gibbs free energy
GC	Glassy Carbon
GDE	Gas diffusion electrode
H	Enthalpy
HOPG	Highly ordered pyrolytic graphite
HOR	Hydrogen Oxidation Reaction
HPA	Heteropolyacid
HV1PMA	singularly substituted hydrogen vanadophosphomolybdic acid
HV2PMA	doubly substituted hydrogen vanadophosphomolybdic acid
IAHE	International Association for Hydrogen Energy
IMechE	Institution of Mechanical Engineers
kJ	Kilojoule
kW	kilowatt
MCFC	Molten Carbonate Fuel Cell
MEA	Membrane Electrode Assembly
MGE	Monitoring Gasket Electrode
NASA	National Aerospace and Space Administration
NaV1PMA	singularly substituted sodium vanadophosphomolybdic acid

NaV2PMA	doubly substituted sodium vanadophosphomolybdic acid
OFN	oxygen free nitrogen
OPEC	Organisation of Petroleum Exporting Countries
ORR	Oxygen Reduction Reaction
PAFC	Phosphoric Acid Fuel Cell
PEM	Proton Exchange Membrane
PEMFC	Proton Exchange Membrane Fuel Cell
PFCE	Plastic formed carbon electrode
PGM	Platinum Group Metals
PMA	Phosphomolybdic acid
POM	Polyoxometalate
ppi	pores per inch
R	Universal gas constant
RVC	reticulated vitreous carbon
S	Entropy
SOFC	Solid Oxide Fuel Cell
STP	Standard Temperature and Pressure
T	temperature
XAS	x-ray adsorption spectroscopy
XRD	x-ray diffraction spectroscopy

Dedication

There is not a page long enough to list all of those who have helped, guided and dragged the author through the production of this thesis.

The author would however like to thank his family for the immense support he has always received, the opportunity and privilege that they have given him to produce the work described within this document and for putting up with his exasperating ideas.

The friends who have lifted the author up and carried him to finish line shall forever be remembered for the sacrifices they have made and the shoulders they have provided to enable him to produce this piece of work. Mention must be given to Mr Tim Davies, Mr David Twyman, Miss Micaela Winter, Dr Angela Murray and Dr Katie Howe without whom the author would have given up a long time ago.

The support and guidance provided by supervisors and mentors over this period is immeasurable and the author would like to specifically thank Dr Neil Rees, Dr Richard Greenwood, Dr Trevor Davies, Professor Greg Wildgoose, Professor Frank Marken, Professor Lynne Macaskie, Dr K Deplanche and Dr Andy Creeth. Special thanks must also be given to the Mr John Hooper, Mrs Lyn Draper and Mrs Christine Dickinson as well as Bob and Bill.

The support provided by ACAL Energy Ltd, The University of Birmingham and the Doctoral Training centre for hydrogen and fuel cells was truly appreciated.

Acknowledgements

Contents

List of Figures

Summary

The introduction (Ch.1) describes global energy demand, the need for a sustainable energy system and how the hydrogen economy, including proton exchange membrane fuel cells (PEMFCs), can enable such a system. The chemistry of PEMFCs is explored with a description of basic electrochemistry and the current barriers to market given. The need to reduce, recycle and/or remove platinum from PEMFCs; and how this can be achieved with spatially resolved platinum group metal (PGM) nanoparticles, bio-hydrometallurgy and alternative fuel cell mechanisms, provides the focus for the thesis.

Chapter 2 focuses on the areas of reducing and recycling PGMs. Reduction is investigated via spatially resolved platinum particles using novel complexes and lithography techniques. Recycling of PGMs, and the electrochemistry created, through bio-hydrometallurgy is explored. Alternative fuel cell mechanisms are explored in chapter 3 with surface-adsorbed phosphomolybdic acid, followed by studies into surface-adsorbed singularly substituted vanado-phosphomolybdic acid.

Chapter 4 explores the effect of electrode surface and pH on the electrochemistry observed. With Chapter 5 observing the change from surface bound to solution phase behaviour. Further substitution of vanadium into the species is investigated in chapter 6, with the surface and solution phase electrochemistry of doubly substituted vanado-phosphomolybdic acid.

Chapter 7 details supporting experimental work, such as development of electrode design. A short concluding chapter in presented in chapter 8, followed by the appendix.

1. Introduction

This thesis disseminates the findings and insights reached whilst researching the chemistry and methods that can be used to overcome the economic barriers to the implementation of hydrogen fuelled proton exchange membrane fuel cells (PEMFCs), which are currently too expensive for serious commercial consideration.[1] Exploring the main themes of reducing, recycling and removing the platinum group metal catalysts currently in use.

The following introduction frames the work within the field of energy-focused research, whilst providing context for the research conducted and developing the reasoning for experimental work.

1.1 The 'Energy Crisis'

The term 'energy crisis' is common in mainstream conversation,[2–4] and refers to the anticipated gap between supply and demand within the energy system. This gap arises due to the decommissioning of power generators, increases in the price of natural gas, and the onset of 'peak oil', being paired to the, increasing demand for energy. The Institute of Mechanical Engineers have even suggested a 40-55% energy gap in 2025 in a worst case scenario.[5]

Anxiety surrounding non-sustainable energy generation has been common for over a century and 'peak oil' (defined as - "the point in time when world oil production reaches its highest rate, after which it goes into permanent decline."[6]) has been a large concern due to its national strategic

importance. The Day's report (1909) is just one example of the initial attempts to quantify resources.[7]

These predictions have always been contentious with some like Adelmann et al. arguing it is more a case of "depletion vs. knowledge".[8] However, incorporating economic elements, producing 'Hubbart's curves', enabled success in predicting real world events.[9] Such as the prediction of the peak in U.S. oil production in 1971[10] and the resulting energy crisis.[11] As with many predictions, the context and implications of the energy crisis is lost to the debate around the exact point of peak oil. One study instead plotted the accumulative probability, showing a 90% probability of reaching peak oil by 2018.[12] The issue of finite energy reserves and specifically the permanent decline of fossil fuel energy per capita is even more stark when taken alongside the increasing demand for these resources (Figure 1.1).
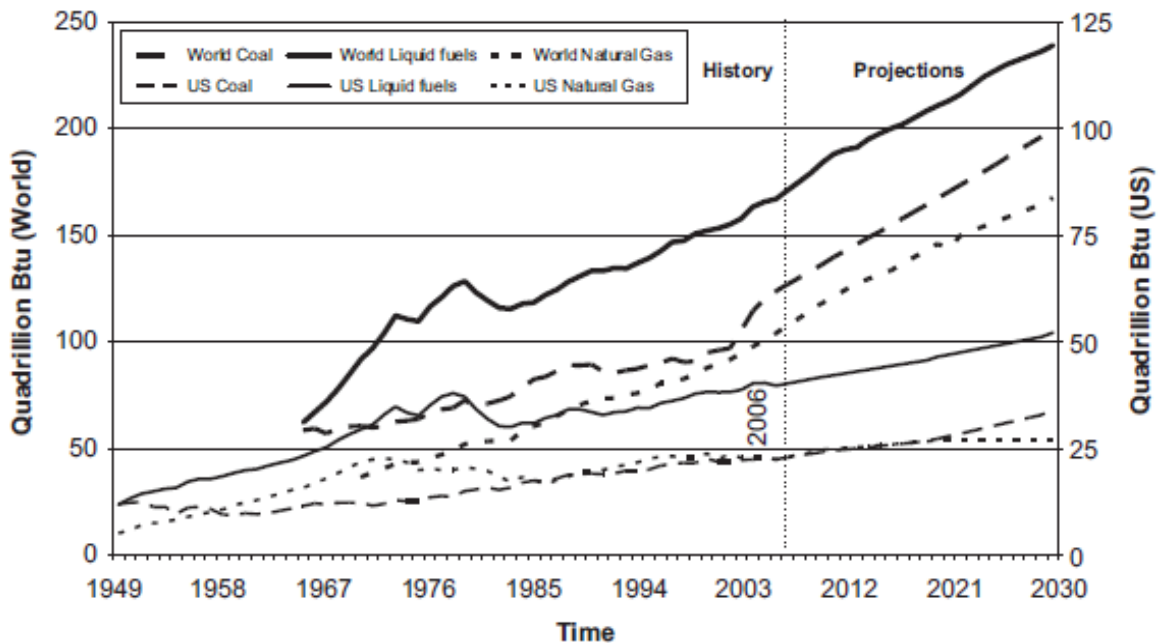
Figure 1.1 - Resource consumption for energy. Data collected from EIA and BP by Shafiee et al.[13] Figure reused with permission from Elsevier (licence 4084920320188).

These points lead to the need for a sustainable energy system, and an alternative energy supply, from a purely economic standpoint, without including the complex arguments regarding the environmental crisis. However, the Stern review concisely summarises,

"Climate change will affect the basic elements of life for people around the world.''[14]

1.2 The hydrogen economy

There have been many ideas proposed for a coherent, economically viable and environmentally friendly energy system. There is a large range of technological, socio-economic and socio-technical methodologies being developed and for a future energy crisis is to be avoided a myriad of these techniques must be implemented without reliance on a single 'silver bullet'.[15–19]

The now popularized view of the hydrogen economy was proposed as a response to the dramatic increase in gasoline prices in the 1970's[20–23] and was strengthened by the 1973 OPEC oil embargo.[24] Which led to a drive to find alternative sources of energy, with the founding of the IAHE (International association for Hydrogen Energy, 1974) and the DoE (Department of Energy, 1977).

The hydrogen economy is based around hydrogen as an energy vector (or carrier).[25] As such the hydrogen economy is split into distinct stages; initial energy generation, the subsequent conversion to hydrogen, the storage and transportation of hydrogen to the user, and the conversion of hydrogen into energy.

1.2.1 Fuel cells

The fuel cell was conceptualized by Christian Friedrich Schoebein (1839) and demonstrated practically in the 'gas battery' by Sir William Grove (1845).[24,26,27] They remained a scientific curiosity until the early 20th century when the Royal Navy saw the advantages of non-toxic exhausts within submarines. A 5kW unit was developed by Sir Francis Bacon and showed the first significant power generation by a fuel cell unit in 1959.[28] Only three months later Harry Karl Ihrig, of the Allis-Chalmers company, used the 'Bacon cell' to power a tractor, Figure 1.2.[24]

Figure 1.2 – The first fuel cell vehicle the Allis-Chalmers Fuel cell Tractor, 1959. Reused under the fair use policy from the National Museum of American History website[29]

The technology failed to reach the public due to high costs and only saw practical application within the NASA space program. The oil crisis (1970s) led to new developments and production of

prototype fuel cell passenger vehicles. However, constraints on the energy market eased and interest waned until the 1990s. Recently, interest has again increased as climate change and the energy crisis took on a cultural and political significance, producing a revival in non-CO_2 producing energy generation.

This has seen large scale commercial testing and sales of PEMFCs. These include the use of Ballard fuel cells in buses;[30] the use of DMFCs (Direct Methanol Fuel Cells) as APUs (Auxiliary Power Units), like those offered by SFC Energy;[31] the use of PEMFCs within fork lift trucks;[32] and now commercially available fuel cell and fuel cell hybrid cars such as the Toyota HCV, Figure 1.3.

Figure 1.3 – Colleagues and myself test driving the Toyota FCHV in 2011.

Fuel cells represent a highly efficient method for the conversion of hydrogen (as well as other fuels) into energy. Primarily, as electricity but also as heat through CHP (combined heat and power)

units.[33] There are defined types of fuel cell (Figure 1.4), nominally divided into groupings by the methods used to separate the anode and cathode of the cells and the temperatures these become functional.[34] The transport sector is responsible for 30% of the total energy used in the U.K.[35] and in this sector PEMFCs are highlighted to be successful.

	Electrolyte	Operating Temperature (°C)	Fuel	Application
Direct Methanol fuel Cell	Polymer electrolyte membrane	60-130	Methanol	Small device, Auxiliary power
Proton Exchange Membrane Fuel Cell	Polymer electrolyte membrane	40-90	Hydrogen	Transportation, Military, Potable power
Alkaline Fuel Cell	Potassium hydroxide/ Alkaine membrane	40-200	Hydrogen	Military, Space program, transportation, Auxiliary power
Phosphoric acid Fuel Cell	Phosphoric acid	200	Hydrogen	Auxiliary power, Distributed power
Molten Crbonate fuel cell	Molten Carbonate	650+	Methane, Hydrogen, Carbon Monoxide	Distributed power, Large-scale generation
Solid Oxide Fuel Cell	Solid Oxide	500-1000	Methane, Hydrogen, Carbon Monoxide	Auxiliary power, Distributed power, Large scale generation

Figure 1.4 – Simple table showing the different types of fuel cell.[34,36]

6

1.2.2 Issues restricting the market exploitation of P.E.M fuel cells

There are three primary barriers restricting the market penetration of P.E.M. fuel cells: the cost of primary PGM resources, the lack of infrastructure and public perception. The main obstacle is the high cost of fuel cell technology.

Consumers are willing to pay for 'prestige' goods, but current fuel cell technology is simply too expensive.[37–40] Alongside, it is worth noting that without significant work to overcome issues with infrastructure and public perception the technology will not successfully penetrate the market.[41–43] When considering the development of a hydrogen infrastructure a 'chicken and egg' scenario appears. However, if rolled out successfully a hydrogen infrastructure is capable of producing a return in investment, as demonstrated by work published in the paper "Development of a hydrogen fuelling infrastructure in the Northeast USA''.[44]

Fuel cells and hydrogen technology suffer from poor public perception, particularly regarding safety. Although hydrogen cannot be described as an inherently safe product, when compared with incumbent technology the risk is comparable.[45,46] It is the responsibility of those in the field to educate the consumer and reduce this constraint on demand.

The high cost of hydrogen fuel cell technology is the primary barrier to market.[47] Currently the cost is too high to justify a wide market launch when compared to current and alternative energy technologies, even when considering environmental benefits.[48,49] The exact cost of hydrogen fuel cell power is also complicated due to its fluctuation dependent on geographic considerations.[50]

Despite the daunting challenge there are several areas where cost reduction can be achieved. Figure 1.5 shows a cost breakdown per kW of a PEMFC. It shows that other system components can be targeted for reducing cost. The primary example of this would be the flow-field plates or B.P.P.'s (bi-polar plates) which need to be reduced in both weight and cost for automotive applications.[51]
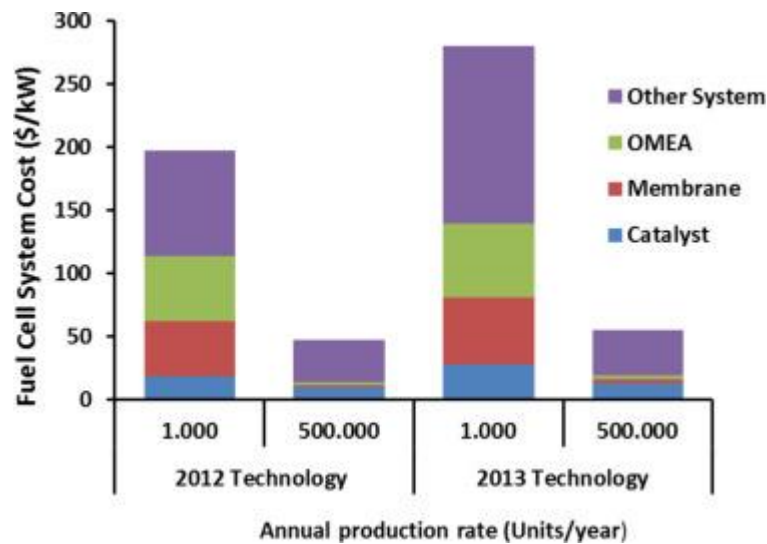
Figure 1.5 - Low and high volume cost per component per kW for a PEMFC[52] Reused with permission from Elsevier. (licence 4084941240578)

The membrane electrode assembly (MEA) is often targeted as the area most likely to enable cost reduction. With focus primarily residing on reducing the mass of precious metal catalyst required to give a certain power per surface area (or per volume). The DoE produces targets that researchers aspire to achieve. Figure 1.6 shows the DOE targets from 2008, highlighting that in 2015 the target was a cost of \$30/kW.[53]
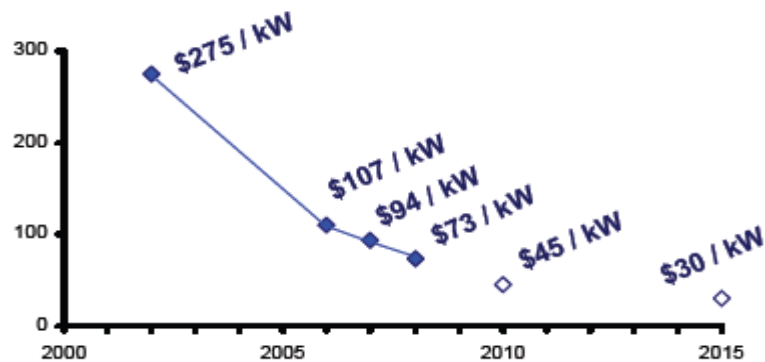
Figure 1.6 - DoE fuel cell price/kW targets from 2008.[53] **Reused under the 'fair use' policy from the U.S. Department of Energy website**

If these predictions and aims are compared to the same figure from the 2014 report, Figure 1.7.[54] the problem with over optimism and futurology becomes clear.
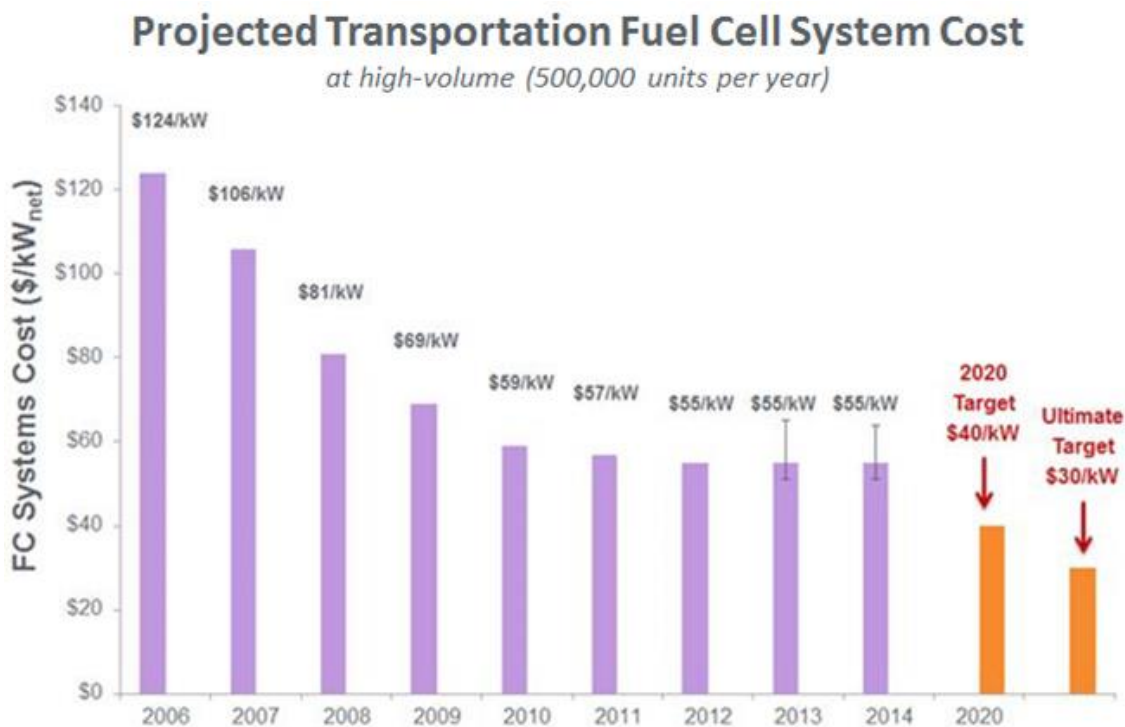
Figure 1.7 - Cost per kW for a PEMFC system achieved and further targets taken from the 2014 DOE annual report.[54] **Reused under the 'fair use' policy from the U.S. Department of Energy website**

The principle reason for the high price is the scarcity of the resources behind the precious metal catalyst, with up to 95% of reserves in South Africa.[55] The price of platinum has risen dramatically in recent history with the price also dependant on market speculation.[56,57] Often, energy security is cited as a reason for a hydrogen economy; however, this geological restriction and price volatility negates such arguments, whilst still relying on platinum.

1.3 Proton exchange membrane fuel cells

Within hydrogen fuelled proton exchange membrane fuel cells, hydrogen is oxidised at the anode and paired to the reduction of oxygen at the cathode. This is achieved by establishing two exclusive pathways, for protons (through the proton exchange membrane) and electrons (through an external circuit) between the reaction sites at the anode and cathode. The reactions take place within a cathodic and anodic catalyst layer, where platinum group metal (PGM) nanoparticles, anchored on carbon microparticles, provide the surface for reaction, as shown in Figure 1.8. Electrons are conducted through the network of carbon particles and protons migrate along Nafion[(r)] chains.
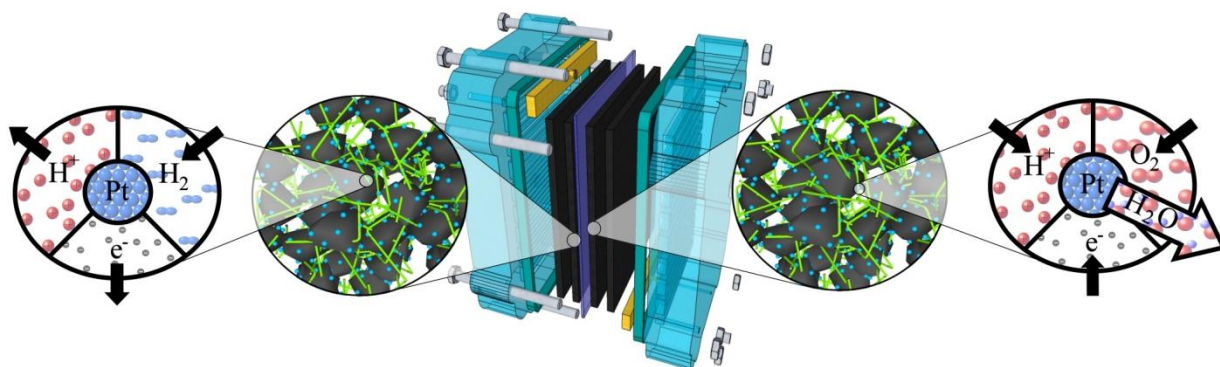
Figure 1.8 - PEMFC diagram showing catalyst layers and the HOR and ORR.

Many PEM fuel cells are 'air breathing' using atmospheric oxygen to fuel the cathodic oxygen reduction reaction (ORR), the cell in Figure 1.9 is an example. Hydrogen is supplied from a stored supply and when supplied oxygen is used, as the examples in the space program[58], flow-field plates (FFP) need to be designed to not interfere with the collection of current but also distribute the gases.
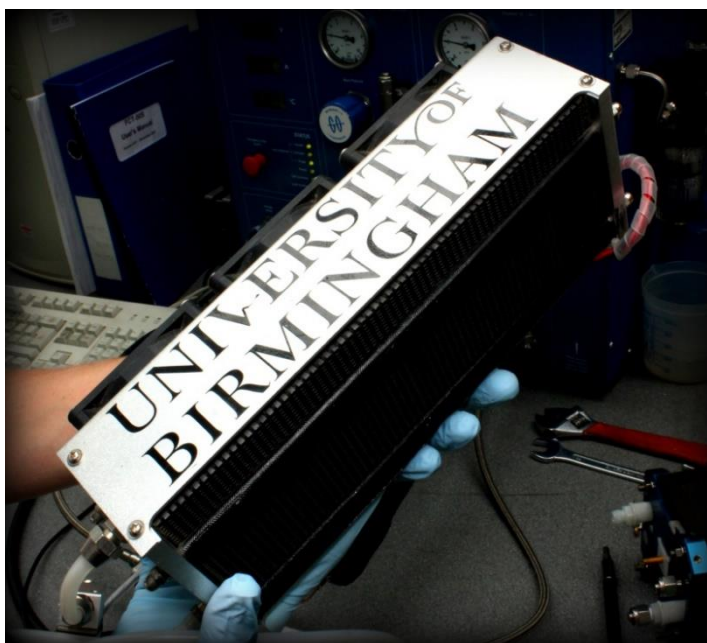
Figure 1.9 - 1kW PEM fuel cell stack.

The first cells to be constructed in this manner were pioneered by General Electric in the 1960's.[59] These solid polymer designs were enabled by development of the proton conducting membrane Nafion® by Dupont.[60] Many new proton exchange membrane materials have been investigated but Nafion® remains the commercial lead.[61,62] However, ever since the first hydrogen conversion devices were conceived there has always been a reliance on precious metal catalysts due to the electrochemical properties of the reactions.

1.4 Electrochemistry

This section aims to introduce the concepts within modern electrochemistry and provide an insight for the reader into the techniques used (described in detail in the experimental sections of each chapter). The theory within this section is adapted from numerous textbooks and lectures.[63–72]

1.4.1 Thermodynamic Electrochemistry
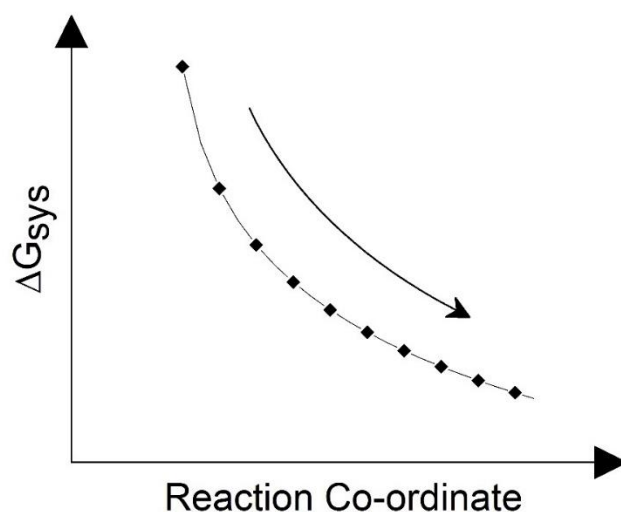
Figure 1.10 - Illustration of the movement to a thermodynamic equilibrium at the energy minimum for the system

When at equilibrium, the change in Gibbs energy of a system is zero and can be expressed as shown in Equation 1.1.

Equation 1.1

$$\Delta G_{sys} = -RTlnK$$

where, R is the ideal gas constant (8.313 J K^{-1} mol^{-1}), T is the absolute temperature (in Kelvin) and K is the equilibrium constant. In general, K for a generic reaction can be described as per Equation 1.2 & Equation 1.3.

Equation 1.2

$$wA + xB \rightleftharpoons yC + zD$$
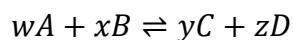
Equation 1.3

$$K = \frac{[C]^y[D]^z}{[A]^w[B]^x}$$

The simplest possible electrochemical experiment, is to consider a wire placed into a solution of metal ions. The example in Figure 1.11 uses Fe^{2+} and Fe^{3+} (Equation 1.4) in solution with a platinum wire inserted into the solution.
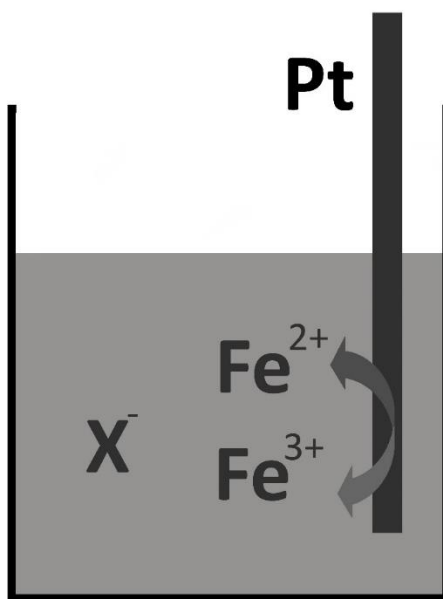
Figure 1.11 - A diagram showing a platinum wire inserted into a beaker containing Fe^{2+} and Fe^{3+} ion species with a counter anion, X^-

Equation 1.4

$$Fe^{3+}_{(aq)} + e^-_{metal} \rightleftharpoons Fe^{2+}_{(aq)}$$
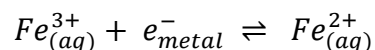
When the wire encounters the solution, charge can pass back and forth through the wire to the species in solution to reach a thermodynamic equilibrium, Figure 1.10 and Figure 1.11. This movement to a thermodynamic equilibrium can be viewed as balancing the Fermi level occupied in the metal, to the HOMO (highest occupied molecular orbital) and LUMO (lowest unoccupied molecular orbital) of the two charged metal species (Figure 1.12). It should also be noted that although the same molecular orbital is being vacated and filled on the two metal ion species, there

is a slight difference in energy of the orbital between the two states due to the change in solvation field of the charged species.
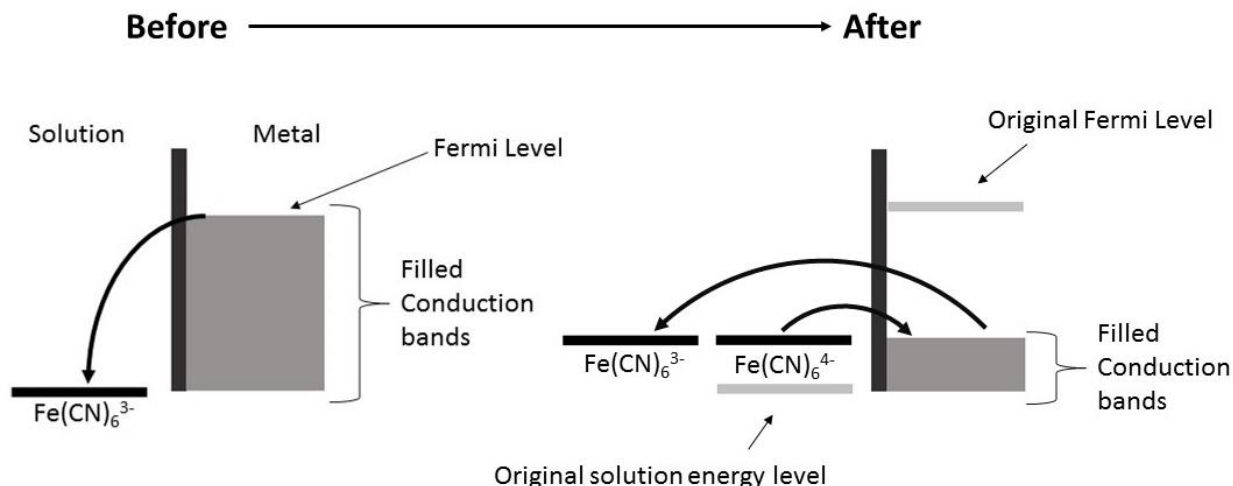
Figure 1.12 - Diagram showing the change in occupied energy levels in the solution and metal before and after the metal rod is inserted into the solution containing ferricyanide.

This movement to a thermodynamic equilibrium creates a charge difference between the surface of the electrode and solution, establishing a potential at the interface of the solution and the electrode as charge is exchanged across that interface. That potential and charge is dependent on temperature and the individual equilibrium constant for the given scenario.

Taking the reaction in Equation 1.5 a specific equilibrium constant can be described Equation 1.6.

Equation 1.5

$$Fe(CN)_{6(aq)}^{3-} + e_{metal}^{-} \rightleftharpoons Fe(CN)_{6(aq)}^{4-}$$
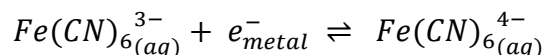
As the electrons reside in the solid phase, the concentration is taken as unity, meaning the equilibrium constant can be simplified.

Equation 1.6

$$K = \frac{\left[Fe(CN)_{6(aq)}^{4-} \right]}{\left[Fe(CN)_{6(aq)}^{3-} \right]}$$

1.4.2 Two electrode systems

The simplest case where measurement is possible is that of the two-electrode system, where the potential (or polarity) between two electrodes can simple be measured with use of a digital volt meter (DVM).
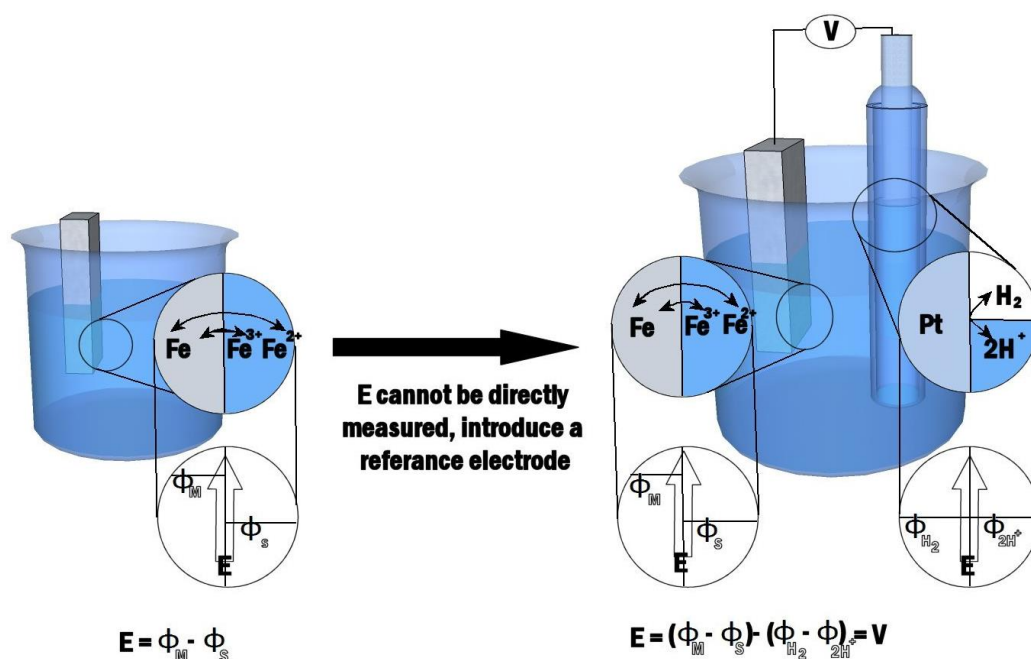
Figure 1.13 - Diagram demonstrating the effect of introducing a second electrode into a solution to allow measurement

The use of two electrodes allows for a measurement to be taken, provided that, an equilibrium is established at both electrodes (if this is not the case, the measurement will show a drifting voltage and the measurement will be dynamic). Figure 1.13 shows a schematic of the Standard Hydrogen Electrode (SHE) to which all other potentials are ultimately referenced to (under the International Union of Pure and Applied Chemistry (IUPAC) standards). To establish a correct SHE, the acid

concentration must be 1.18 M (unit activity) and the pressure of the H_2 gas equal to 1 atm. The potential could then be converted to the Gibbs Energy of the system using Equation 1.7.

Equation 1.7

$$\Delta G^{\ominus} = -nFE^{\ominus}$$

where n is the number of electrons, F is the Faraday constant (96487 Coulombs) and E is the equilibrium potential. Through combining this equation with the previous equation for Gibbs free energy a form of the Nernst equation can be obtained (Equation 1.8, using the previous example of the ferri/ferrocyanide example).

Equation 1.8

$$E = E^o - \frac{RT}{nF} ln \frac{\left[Fe(CN)_{6(aq)}^{4-}\right]}{\left[Fe(CN)_{6(aq)}^{3-}\right]}$$

where E^0 is the standard equilibrium potential for the ferri/ferrocyanide couple.

1.4.3 The Thermodynamic relationship of equilibrium potential and pH

The Nernst potential and the thermodynamic understanding of equilibrium potential described above relies on a system which does not significantly change bulk concentration, or in practicality pass large net currents. A description of kinetic parameters follows this section. However, it is important to first consider the effect of changing the bulk concentrations with respect to establishing equilibrium potentials. The most common of these is the effect of changing the pH of the solution, which can have a large effect on the observed thermodynamic equilibrium potential. If a generic electron transfer (half reaction) is taken to be (Equation 1.9),

Equation 1.9

$$A + e^- \rightleftharpoons B$$
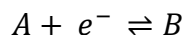
the reality, generally, will be that the uptake of a negative charge by A to produce B will be accompanied by the uptake of a balancing charge, in this case a proton, so that the reaction becomes (Equation 1.10),

Equation 1.10

$$A + xH^+ + ye^- \rightleftharpoons B$$
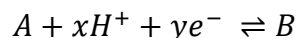
Forming the relevant Nernst equation as described above (Equation 1.8) it can be shown as (Equation 1.11),

Equation 1.11

$$E_{eff} = E^0_{f_{A/B}} - \frac{RT}{yF} ln \frac{[B]}{[A][H^+]^x}$$

This can be rearranged, so that (Equation 1.12),

Equation 1.12

$$E_{eff} = E^0_{f_{A/B}} - \frac{RT}{yF} ln \frac{1}{[H^+]^x} - \frac{RT}{yF} ln \frac{B}{[A]}$$

Leading to (Equation 1.13),

Equation 1.13

$$E_{eff} = E^0_{f_{A/B}} - 2.303 \frac{xRT}{yF} pH - \frac{RT}{yF} ln \frac{B}{[A]}$$

This shows the direct correlation between pH and the observed equilibrium potential. If (as will be seen in analysis in chapters 4-8) a plot is taken of observed equilibrium (or $E_{1/2}$) is plotted against pH the slope of that graph will depend on x/y. If x=y, then the gradient will equal 59 mV.

1.4.4 Dynamic Electrochemistry

Most electrochemical measurements depend on a movement of electrons and the monitoring of current. Taking the two electrode system above, if either of the electrodes sees a passing of current the equilibrium is shifted and no longer represents the thermodynamic equilibrium resulting in an

incorrect measurement. It is possible to perform experiments using two electrodes whilst passing current. However, careful consideration must be taken as any potential observed (or applied) represents a polarisation between the electrodes without knowing which electrode is primarily being polarised. Using a three electrode (Figure 1.14) system allows for the isolation of the reference electrode from passing current, as such the reference value can be maintained at a stable equilibrium.
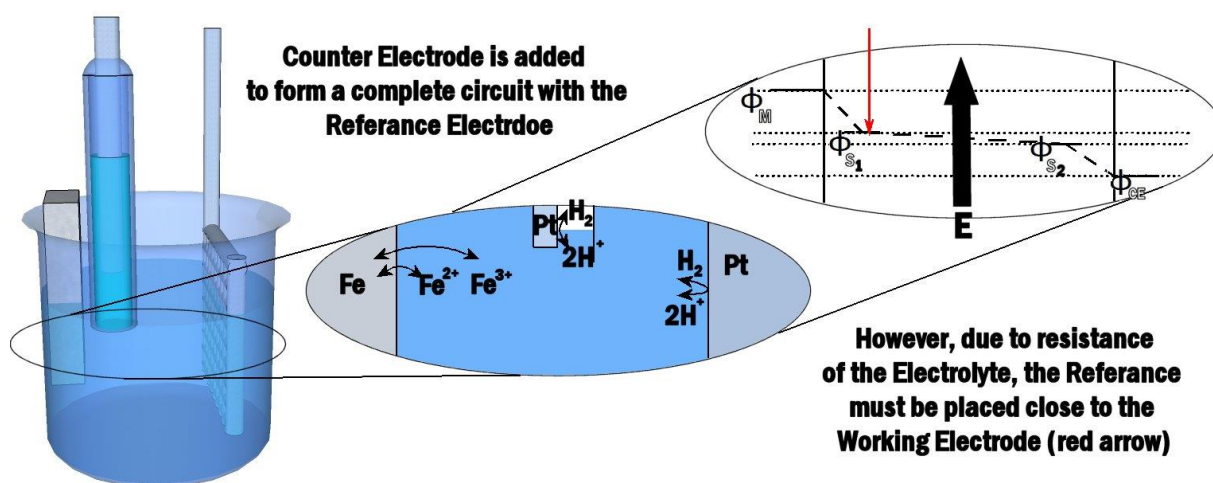
Figure 1.14 - Three electrode system

The notation for the electrodes are, the reference electrode (RE), the working electrode (WE) and the counter electrode (CE). In Figure 1.14 the RE is shown as an SHE. The CE is used to pass current with the RE isolated from this part of the system with a high/infinite impedance. A voltage is applied between the CE and WE to achieve a desired polarisation between the RE and WE. The WE is where the reaction being studied is taking place and again several considerations need to be made to ensure this is the case. The largest consideration must be that the reaction at the counter electrode, passing a balancing charge transfer, must be significantly labile and uninhibited as to not

affect the passing of current at the WE. This leads to the CE commonly being a large surface area Pt mesh.

The method of applying a polarisation to the working electrode plays an important role in determining the information gathered from the system. First, consideration must be given to the effect on the system of moving the potential at the interface away from its equilibrium potential.

The electrode/solution interface where electron transfer takes place has been modelled in a variety of ways. Many models have been developed to consider the decay of potential into the solution and these are shown in section 1.4.7. A simplistic model is shown in Figure 1.15, depicting the same electron transfer highlighted in previous sections.
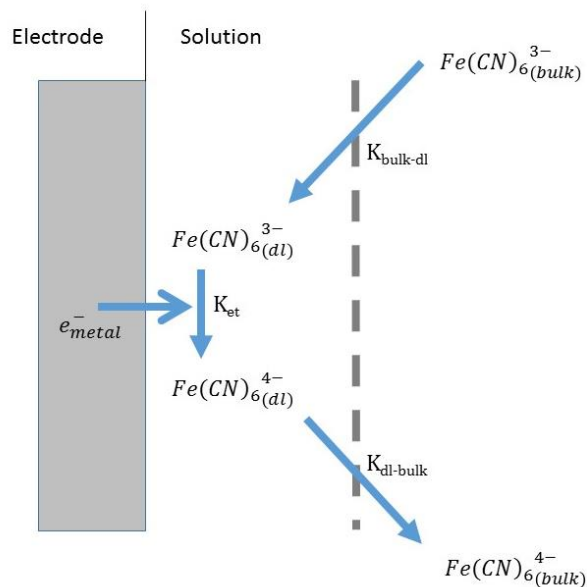
Figure 1.15 - Simplistic diagram of electron transfer at an electrode/solution interface

In this given example, the reactant must move to the vicinity of the electrode surface before undergoing reduction. The magnitude of the current passed due to this reduction is proportional to the flux, j (Equation 1.14 (mol cm^{-2} s^{-1})) of reactant undergoing reduction at the surface.

Equation 1.14

$$I = nFAj$$

where, I represents the current, n is the number of electrons involved in the reaction (in the reduction shown in Figure 1.15, $n=1$) and F is the faraday constant. The rate equations governing the rate at interfacial regions can generally be defined in a similar manner to those of homogenous reactions so that (Equation 1.15),

Equation 1.15

$$Rate = k_n[reactant]^n_{sur}$$

where, k_n is an nth order rate constant. It is important to note that the concentration is that at the surface rather than the bulk solution (denoted $[]_{dl}$ in Figure 1.15). In reality Figure 1.15 is too simplistic to describe the system fully. Additionally, the heterogeneous rate constant, as denoted in Equation 1.15, is extremely sensitive to the electrode potential as will be explored in the following sections (1.4.6).

1.4.5 Mass transport

As can be seen in Figure 1.15 the movement of a reactant species towards the surface of the electrode has a large effect on the surface concentration of the species and as such any observed current. If a reaction proceeds via a fast charge-transfer process (Figure 1.15, k_{et}) and is fully reversible (often termed Nernstian) then the rate of reaction will be completely dependent on the

rate at which a reactant species is brought to the surface (Figure 1.15, $k_{bulk-dl}$). There are three principle mechanisms for the arrival of a reactant species to the surface. Those of,

- Migration – the movement of charged species across an electric potential gradient

- Diffusion – the movement of a reactant species due to a chemical potential gradient, such as a concentration difference

- Convection –either natural convection, the natural movement of molecules due to density gradients, or forced convection where movement is induced mechanically such as through stirring.

A full mathematical description of these processes is very complex in 3 dimensions, however they can be treated in one dimension relatively easily. As will become clear in section 1.4.8, due to the effects of surface area on mass transport these assumptions prove valuable experimentally. The description is given by the Nernst-Planck equation (Equation 1.16),

Equation 1.16

$$j_r(x) = D_r \frac{\delta C_r(x)}{\delta x} - \frac{z_r F}{RT} D_r C_r \frac{\delta \phi(x)}{\delta x} + C_r v(x)$$

Where, $j_r(x)$ is the flux of species r, at a distance of x from the surface, D_r is the diffusion coefficient of species r, C_r is the concentration of r, z_r is the charge of the species, ϕ is the potential and υ is a velocity of a given volume moving across the axis. Care is given to designing experiments which can reduce the corresponding parts of the equation to negligible quantities so that the equation can be solved for a given example. For example, when large concentrations of supporting electrolyte are used the effect of migration across a potential gradient for a given reactant species (r) can be ignored. Additionally, in the case of hydrodynamic experiments such as the rotating disc electrode (RDE) such large velocity elements are used that they become the dominant factors.

1.4.6 Kinetics (Butler-Volmer)

Mass transport although a large factor in the current observed is secondary to the kinetics exhibited by a set reaction. Taking the same reaction as previously (Equation 1.5), it can be expressed (Equation 1.17),

Equation 1.17

$$Fe(CN)_{6(aq)}^{3-} + e_{metal}^{-} \underset{k_o}{\overset{k_r}{\rightleftharpoons}} Fe(CN)_{6(aq)}^{4-}$$
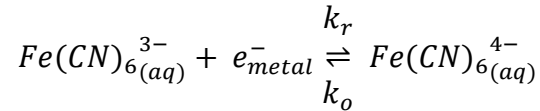
Where k_r and k_o are the reductive and oxidative rate constants. It thereby follows that (Equation 1.18),

Equation 1.18

$$Rate = k_r \left[Fe(CN)_{6(aq)}^{3-} \right]_{sur} - k_o \left[Fe(CN)_{6(aq)}^{4-} \right]_{sur}$$

As was briefly mentioned earlier k_r and k_o are dependent on potential. Both the reactant and product of the reduction are charged species and as such will be affected by the potential of the solution or the electrode. As such, the Gibbs energy reaction profile changes as the potential of either the solution or the electrode is changed. This either favours the products or the reactants at a given potential difference between the solution and electrode, and creates a dynamic change with respect to the rate constants, k_r and k_c.

Two Arrhenius equations can be used to relate the rate constants to the Gibbs energy of activation. These both include a pre-exponential factor relating to the collision frequency of reactants with the electrode (Equation 1.19Equation 1.20).

Equation 1.19

$$k_r = A_r exp \left[\frac{-\Delta G_r^t}{RT} \right]$$

Equation 1.20

$$k_o = A_o exp \left[\frac{-\Delta G_o^t}{RT} \right]$$

These Arrhenius equations can be taken with the conversion of the Gibbs energy of the transition states and the conditions at equilibrium to give equations directly relating to overpotential (η, that is the difference between observed potential, E, and the formal potential, E_f). These equations also include the transfer coefficients α (Equation 1.21) and β (Equation 1.22).

Equation 1.21

$$k_{red} = k^0 \, exp \left[\frac{-\alpha n \eta}{RT} \right]$$

Equation 1.22

$$k_{ox} = k^0 \, exp \left[\frac{\beta n \eta}{RT} \right]$$

For a simple 1 electron transfer (fully reversible) the transfer coefficients α and β follow the relationship (Equation 1.23),

Equation 1.23

$$\alpha = 1 - \beta$$

The magnitude of α relates to the position of the transition state between the reactants and products along the reaction co-ordinate; if alpha is close to 1 then the transition state is similar to the products, whereas if it is close to zero than the transition state is close to the reactants. In most cases, and as a first approximations, these terms α and β are approximate to 0.5.

These equations are a form of the general Butler-Volmer equation (Equation 1.24) which describes the current produced due to overpotentials away from the equilibrium potential.

Equation 1.24

$$j = j_0 \left[exp \left[\frac{\beta n \eta}{RT} \right] - exp \left[\frac{-\alpha n \eta}{RT} \right] \right]$$

It must be noted that the Butler-Volmer equation is only valid when the current is not influenced by the mass transfer phenomena previously mentioned (section 1.4.5.). The limiting cases of the equation provide useful analysis tools.

Specifically, in high anodic and cathodic overpotentials the equation can be reduced to the contribution of only either anodic or cathodic elements. As such, the equation can be transformed into the anodic (Equation 1.25) and cathodic (Equation 1.26) Tafel Equations.

Anodic,

Equation 1.25

$$\log(i) = \log(i_o) + \frac{\beta nF}{RT}\eta$$

Cathodic,

Equation 1.26

$$\log(i) = \log(i_o) - \frac{\alpha nF}{RT}\eta$$

Where i_o is the exchange current density, the rate of reduction and oxidation at equilibrium.

1.4.7 Interfaces within Electrochemistry

The effective control of current by the kinetics of the reaction and the mass transport of reactants is largely determined by the state of the interface between electrode and solution. An important consideration is that the reactant species is usually the minor component within the overall system. The major constituent is the solvent, in most cases this is water (**Error! Reference source not found.**Figure 1.16) which possesses a dipole and will react to any potential applied or local charged species, creating either a solvent sphere around charged species or the electrode.
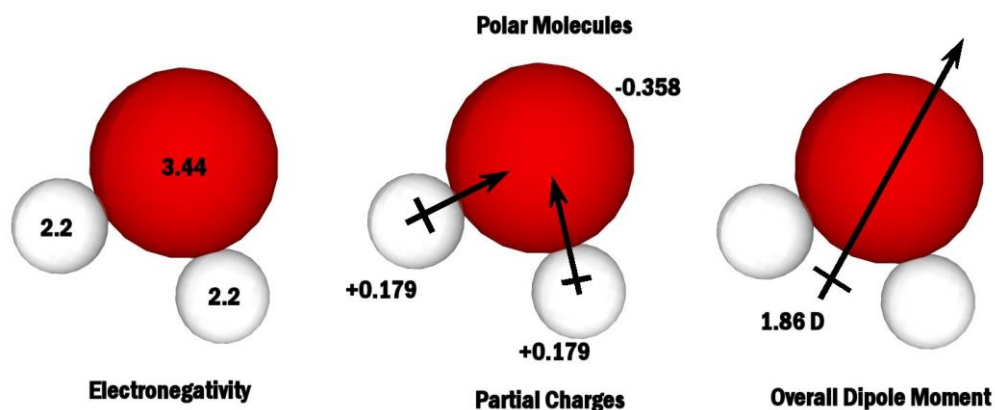
Figure 1.16 - Water molecule

In addition to the solvent, the system will also commonly contain an electrolyte, to increase conductivity of the solution, minimise Ohmic drop between the working and reference electrode, suppress effects of migration and decrease the size of the double layer. The electrolyte is in much greater concentration than the analyte, meaning that the behaviour of the electrolyte species chosen can have a large impact on the electrochemistry observed. As such, the solvent and electrolyte play a large role in determining the nature of the interface between electrode and solution.

The nature of charged species, or those with dipoles, to orientate themselves with electric fields or around charged species leads to several key characteristics of interfaces. Figure 1.17 shows the concept of the 'Helmholtz' model and introduces the concept of the Helmholtz plane or electrical double layer.
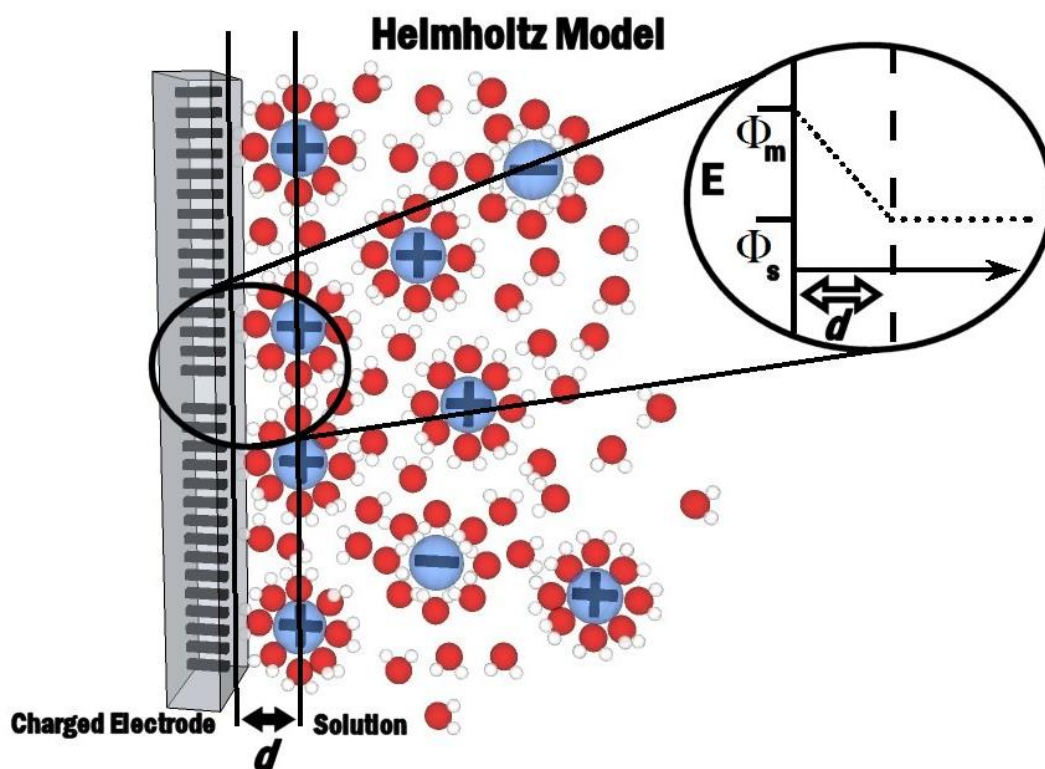
Figure 1.17 - Helmholtz model describing capacitive double layer - Diagram adapted from lectures presented by Dr S. L. Horswell, University of Birmingham

If the surface of the electrode has a potential difference to that of the solution it possesses a charge. This is balanced by an equal and opposite charge in the system, if the system is at equilibrium. This effect can be modelled as a capacitor; with oriented charged species and oriented solvent molecules acting as one capacitor plate and the electrode the other. In Figure 1.17 the distance d is the distance between the electrode surface and the centre of the charge balancing species in solution. This distance is directly proportional to the capacitance of the system and represents the distance between capacitive plates when modelled as a capacitor. The 'Helmholtz' model is very simplistic and only applies to very simple models at equilibrium, not accounting for surface roughness nor for diffusion when the system is moved from equilibrium.
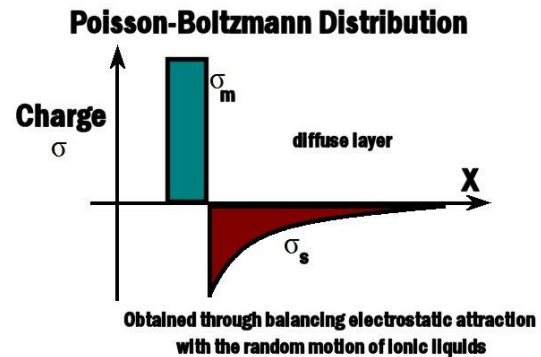
Figure 1.18 - Gouy-Chapman Model of Capacitive Double layer, Diagram adapted from lecture notes presented by Dr S.L. Horswell, University of Birmingham

To account for the oversimplification numerous models have been developed. Figure 1.18 shows a diagram of the Gouy-Chapman model which describes a fall of charge extending into the solution away from the electrode surface. When the Gouy-Chapman model and the Helmholtz model are combined, a model is generated describing two capacitors in series; to incorporate an inner layer close to the electrode surface and a second diffuse region into the solution. This model is commonly known as the Stern model and is shown in Figure 1.19.
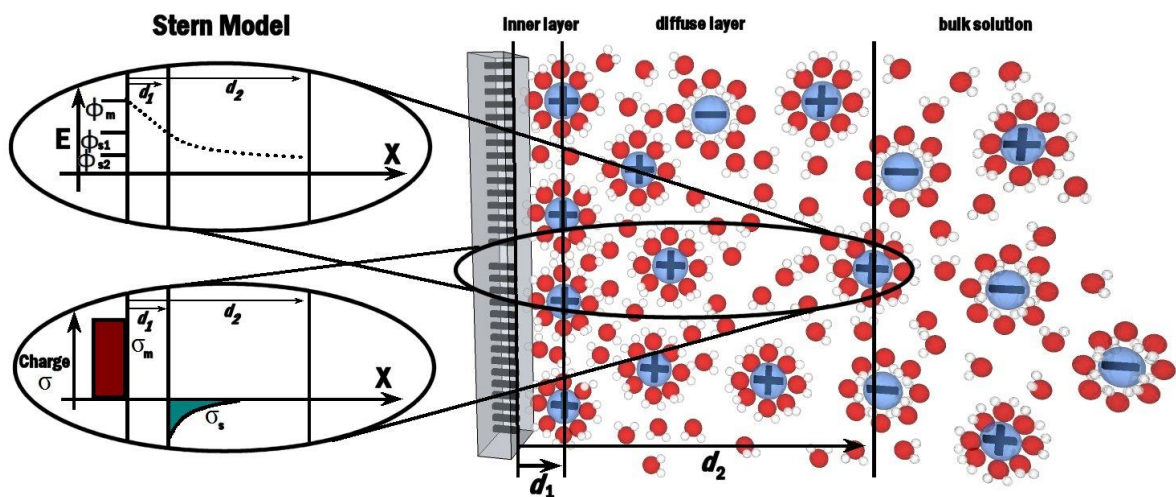
Figure 1.19 - Stern Model of Capacitive double layer, Diagram adapted from lecture notes presented by Dr S.L. Horswell, University of Birmingham

27

These models do not account for any interaction with the actual surface of the electrode across the interface. Molecules will break through their solvation sphere and directly interact and bond with the surface. The Grahame model (Figure 1.20) takes this into account separating the inner layer of the Stern model into an inner and outer Helmholtz plane.
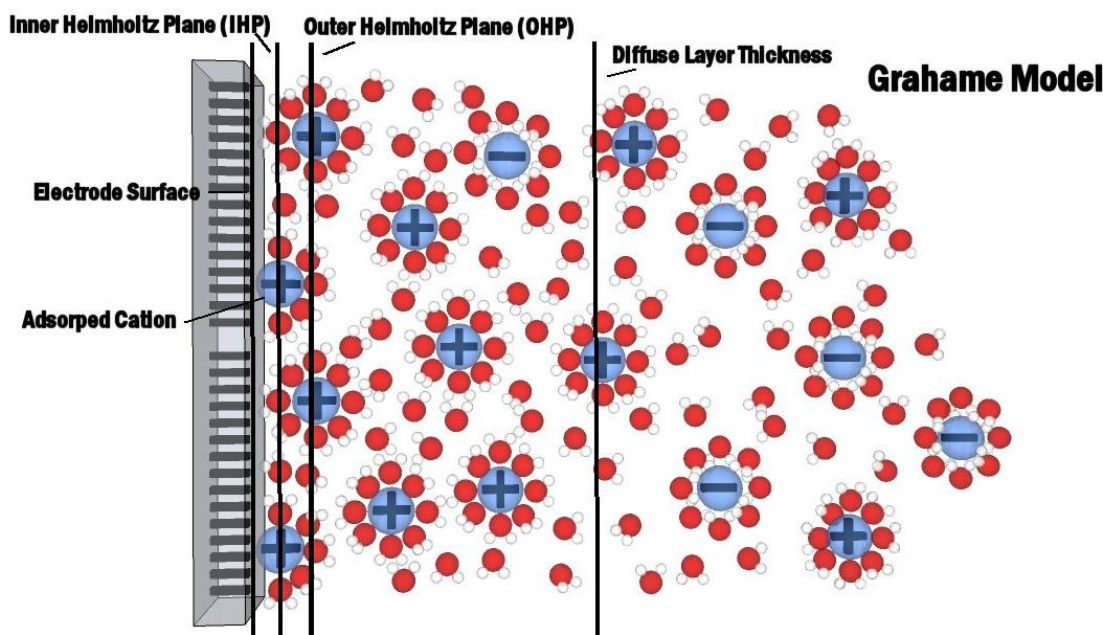
Figure 1.20 - Grahame Model of capacitive double layer, Diagram adapted from lecture notes presented by Dr S.L. Horswell, University of Birmingham

1.4.8 Measurement in electrochemical systems

As previously discussed measurement in electrochemistry commonly makes use of the three electrode cell. Techniques using two and four electrodes are also used but are much less prevalent. Control of either the potential (potentiometry) or the current passing (galvanometry) at the WE is used to investigate the phenomena observed. Perturbations away from equilibrium (for a system) cause a current to flow in response and the nature and magnitude of this response details that systems behaviour. To control the potential a potentiostat (or galvanostat if controlling current) is used like that shown in Figure 1.21.
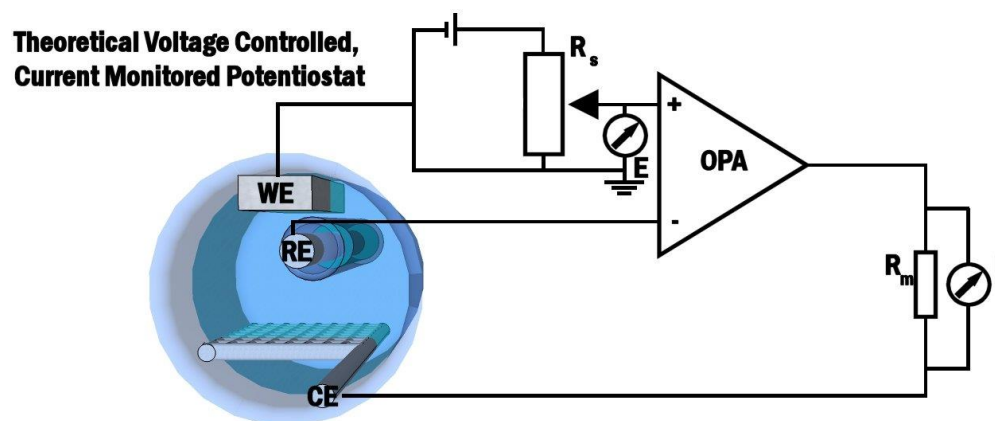
Figure 1.21 - Basic Voltage controlled, Current monitored potentiostat diagram with the connections shown to a three electrode cell.

Figure 1.21 shows the basic practical potentiostat which allows for the control of potential applied through a variable resistor included within the circuitry connecting the WE, RE and OPA. The current is monitored by measuring across a resistor connected between the OPA and the CE.

Linear Sweep Voltammetry

The simplest form of voltage signal applied to a system is linear sweep voltammetry. The potentiostat applies an increasing voltage between the WE and CE. The increase is linear with time, with the scan rate, recorded in $V.s^{-1}$. As potential scanned it causes a response in current described by the Butler-Volmer equation and the Tafel equations. However, as the potential is moved further away the concentration at the surface and in the bulk solution differ, as such mass transport dominates the current produced.
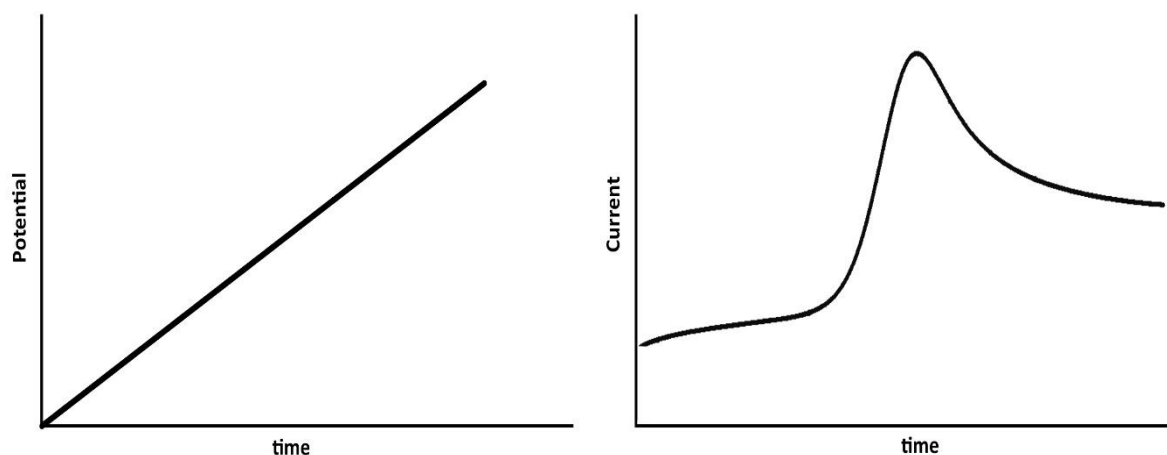
Figure 1.22 - Potential with time and a typical current response for linear sweep voltammetry

Figure 1.22 shows a typical positive sweep linear scan voltammogram, showing the potential profile with time and the current observed with time. This is shown to be a positive current as an anodic reaction is taking place, the initial increase in current can be calculated by the anodic Tafel equation. This reaches a maximum where the concentration at the electrode surface has shifted from that of the bulk and mass transport dominates the current observed creating the archetypical voltammogram 'wave' shape.

Cyclic Voltammetry

Cyclic voltammetry uses the same underlying principle as linear sweep voltammetry using a constantly increasing or decreasing voltage applied to the WE at a set scan rate. However, the voltage is cycled, from a chosen point to a set value before returning in a cyclic nature. A typical voltage-time profile is shown in Figure 1.23.
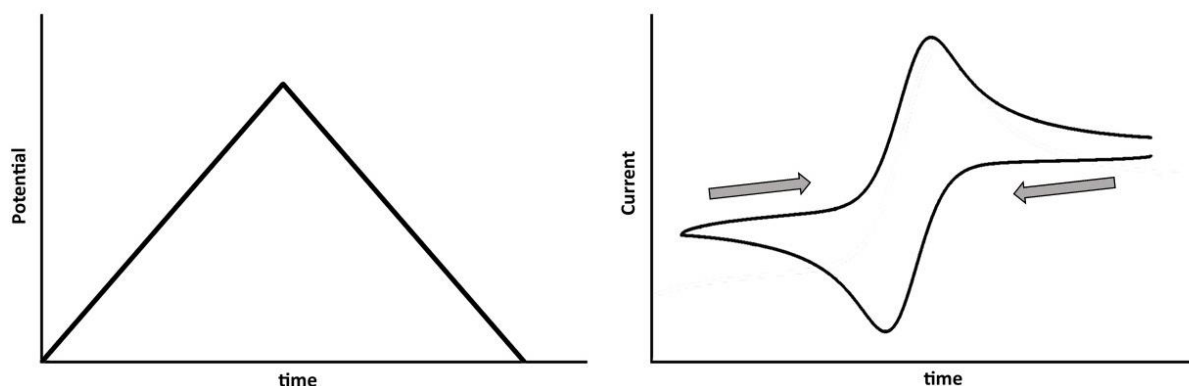
Figure 1.23 typical voltage-time profile and current time profile for a cyclic voltammogram

Figure 1.23 shows a simplistic profile and the typical current response of a reversible system. As with the linear sweep voltammetry the typical 'wave' shape is observed but as the potential is cycled it is observed in both the forward and reverse sweeps as the anodic and cathodic waves (the oxidative and reductive reactions).

Wave-shape and characteristics

Due to the cyclic nature of the excitation both the cathodic and anodic responses are seen during the scan and because the scan covers a large potential window, areas of high and low over-potential are exerted on the redox couple investigated. This produces an anodic and cathodic curve, often referred to as a wave. The point of peak current (both anodic and cathodic) represents the point where the concentration within the double layer has been exhausted and the current is totally mass-transport limited moving further in excitation from the redox couple's equilibrium potential. The value of peak current (for a fully reversible redox process) is given by the Randles-Sevcik equation (Equation 1.27).

31

$$i_p \; = \; 268,600 \; n^{3/2} A D^{1/2} C v^{1/2}$$

where, i_p = peak current, 268,600 is a constant applicable at room temperature (25 ^{0}C), n = number of electrons transferred, D is the diffusion coefficient, C is the concentration and v = the scan rate.

This equation has the potential to allow the determination of diffusion coefficients for a given redox species if a series of scans is completed across a few decades of scan rate values.

Surface bound electrochemistry

Redox active adsorbed layers behave differently to a standard solution phase redox couple. The adsorbed species can act as a capacitor but is an additional layer between the substrate and the solution. This can be imagined to be a region of a differing concentration to the bulk solution. These can be described by certain isotherms and a discussion of these is taken further in chapter 3.

The difference in concentration profile produces a markedly different wave shape as to that observed for solution based redox couples. As the concentration at the surface cannot be replenished a symmetrical peak is formed, eventually returning to zero current as the reactant concentration is fully depleted. If the system is fully reversible and follows a traditional Langmuir isotherm of adsorption the peak occurs at the equilibrium potential.

Perhaps the most crucial difference experimentally between the solution phase cyclic voltammetry and surface adsorbed species cyclic voltammetry is the change in the relationship of peak current. As there is a finite amount of material the response is no-longer diffusion controlled, this allows

for the calculation of the number of species attached (if the number of electrons is known) through charge transferred and a different equation for peak height, Equation 1.28.

Equation 1.28

$$i_p = \frac{n^2 F^2}{4RT} v A \Gamma$$

where, Γ is surface coverage.

Electrochemical Impedance Spectroscopy

Traditional voltammetry yields potential dependent information, whilst EIS can use a type of voltammetric measurement to yield frequency dependant information. It yields benefits of being relatively nonintrusive to the system and yielding time dependent information quickly. Simply, EIS measures the change of a frequency signal between the input and output. In the case of a voltammetric technique an alternating current (AC) signal of changing frequency is applied on top of a predetermined direct current (DC) signal.
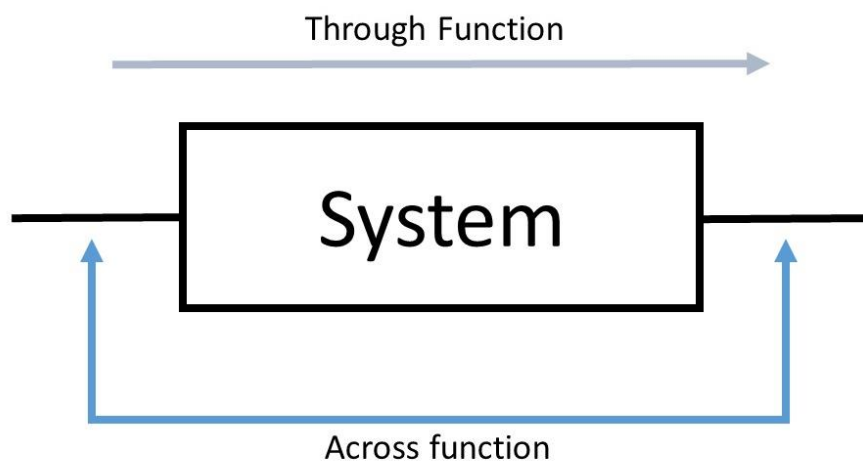
Figure 1.24 - a simple linear circuit element diagram explanation

Figure 1.24 shows a simple linear circuit element, the system could be a resistor, with the through function being current and the across function being voltage, defined by Ohm's law (Equation 1.29).

$$V = R \times I$$

This can be related to the impedance of the circuit element through the definition shown in Equation 1.30.

$$Impedance = \frac{across\ function}{through\ function} \quad or \quad Z = \frac{V}{I}$$

The difference in input and output signal can be quantified and yield information. Input and output functions can be described to be related through a transfer function. As such, the above example, could be ascribed to have a current transfer function and a voltage transfer function.

Any system has an equivalent circuit that can be used to describe (and model) the effect that the system has on an input signal. Another basic circuit element is the capacitor with the relationship Equation 1.31,

$$I = C \times \frac{dV}{dt}$$

It is important to note that the relationship includes a time factor, unlike that of a resistor. The input signal used is commonly of a linearly increasing frequency. This dependency on a time constant for a specific element of capacitance means that if these two elements are combined in a system, information about the individual elements can be isolated. The difference in input and output signals, yields this information. Figure 1.25 shows an example of a single frequency signal

that can be applied, with an example of an output signal. It shows the difference in angular moment of a single point of that signal. The two components which are measurable are the magnitude and the phase of the input and output signal.
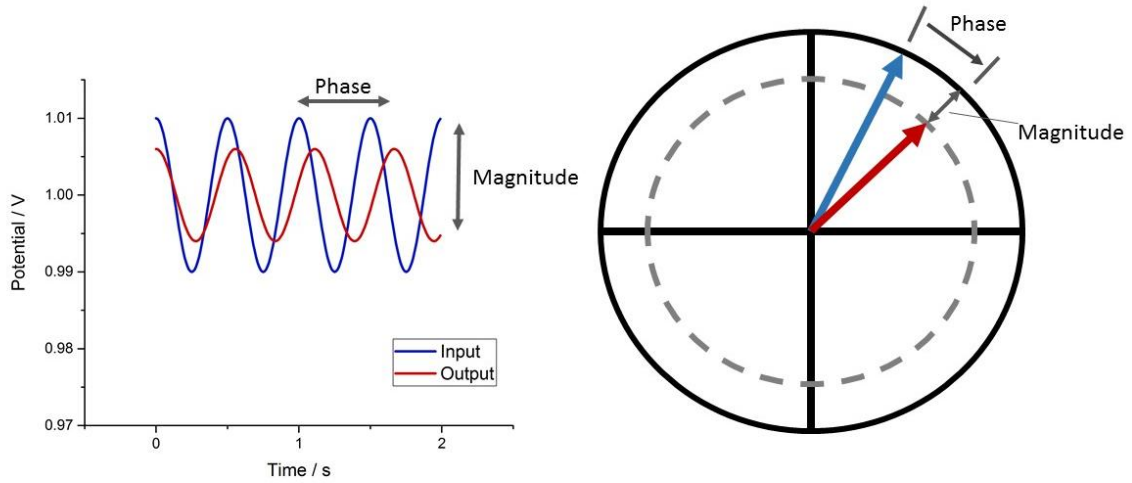
Figure 1.25 – Left, example of a single frequency input and 'typical' output signal at 0.5 Hz with a single sine amplitude of 0.01 V on-top of a DC 1 V signal. Right, a view down the X-axis (time) of a single point if the input and output signal

Obtaining the information and representing it, is achieved with the use of complex exponentials, a full description of this mathematical treatment is beyond the scope of this introduction. However, this treatment allows for the information of phase and magnitude to be separated and for the data to be represented to yield information. If the impedance (Z) has magnitude ($|Z|$) and phase (θ) then it can be expressed as Equation 1.32, Equation 1.33 & Equation 1.34.

Equation 1.32

$$Z = |Z| e^{j\theta}$$

Equation 1.33

$$Z = |Z| \cos(x) + |Z| j\sin(x)$$

Equation 1.34

$$Z = Real(Z) + Imaginary(Z)$$

Figure 1.26 demonstrates how this mathematical treatment generates each point that is plotted on a Nyquist plot.
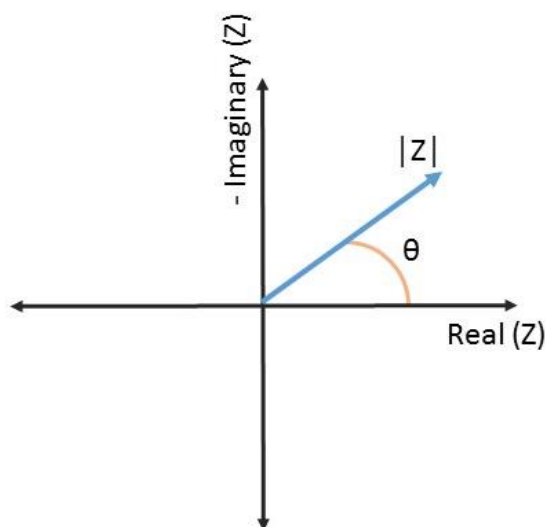
Figure 1.26 - Explanation of treating EIS data mathematically to produce data for a Nyquist plot

This technique can be used to gain valuable information about a system if the correct equivalent circuits are used. Taking a simple resistor, its effect on input signal and the effect of increasing frequency can be imagined, as shown in Figure 1.27.
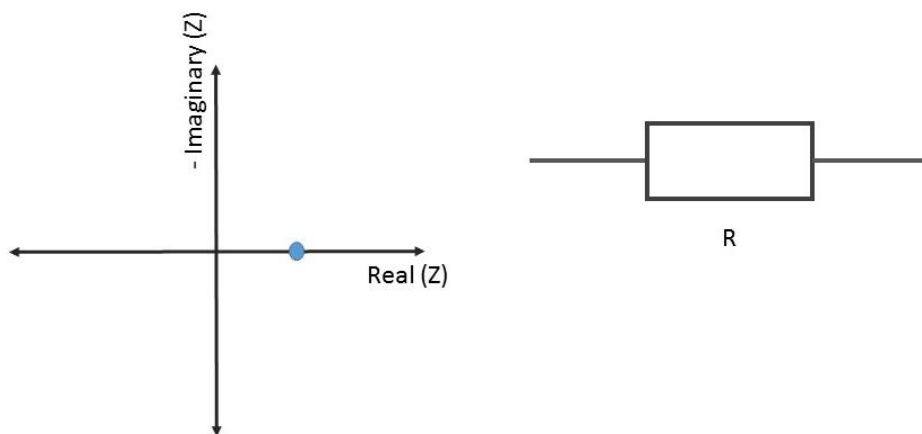
Figure 1.27 - Example of a resistor equivalent circuit and the complex plane representation

A resistor creates no phase change between voltage and current, both components are in phase and there is no imaginary component in the complex plane. However, if instead a capacitor is taken as the equivalent circuit it produces a different transformation as shown in Figure 1.28.
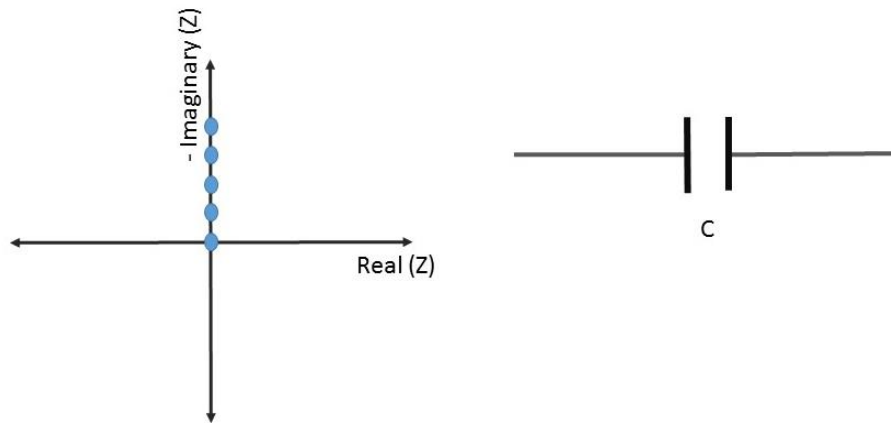
Figure 1.28 - Example of the complex plane exhibited by a capacitor circuit element

If both elements are included in series, they produce both effects, shown in Figure 1.29.
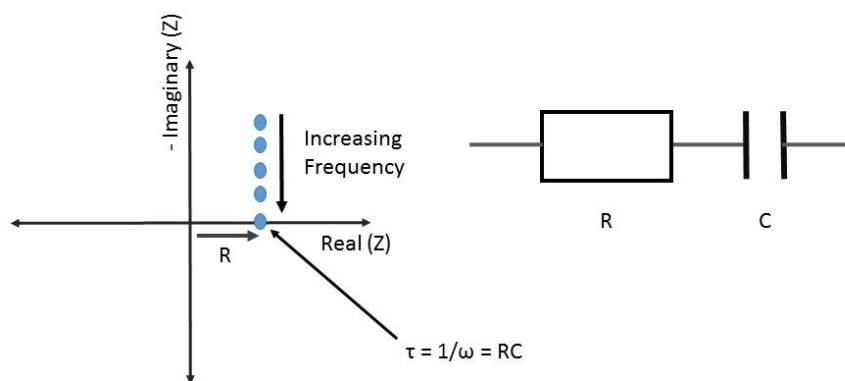
Figure 1.29 - diagram showing the complex plane exhibited by a R and C in series equivalent circuit

Figure 1.29 helps show the important difference between a resistor and a capacitor within the complex plane representation. At high frequency, the resistor dominates and at low frequency, the capacitor dominates the effect on the input signal. There is a point of transition that can yield valuable information on the system, highlighted in the figure.

If the elements are placed in series the effect is harder to imagine and Kirchoff's law (parallel addition) is used to build a system model. The effect on the complex plane can be seen in Figure 1.30. The combination leads to a more complicated complex plane with information harder to attain. However, the transition point, relating to the time constant yields information.
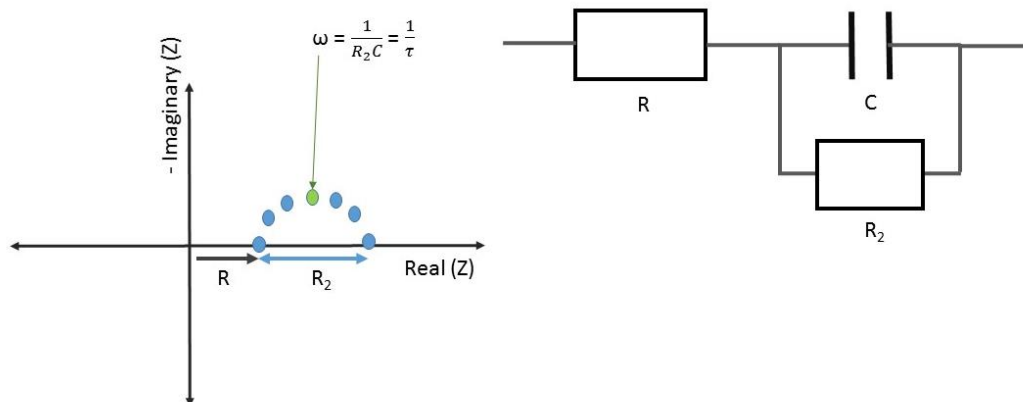
Figure 1.30 - the complex plane exhibited by a series and parallel circuit of resistors and capacitors

The complex plane is an excellent way to show the effect of circuit on a signal however data compression can occur in these plots. Depending on the complexity of the circuit, Bode plots may be yield more valuable information (see bottom left of Figure 1.31).

An additional element is needed to describe traditional electrochemical systems. Resistors and capacitors can be used to model an electrochemical system close to the equilibrium potential,

within the limits of kinetically controlled current (and current holding true to the Butler-Volmer Equation) but with the addition of mass transport effects, another element is needed to describe diffusion to the electrode. This element is called the Warburg impedance and factors diffusion into the part of the model system describing charge transfer. Together with resistors describing the uncompensated resistance (sometimes referred to as the system resistance, or commonly solution resistance) and charge transfer resistance; and a capacitor to describe the double layer charging effect. A Warburg element helps complete the Randles equivalent circuit describing charge transfer, this is shown in Figure 1.31.
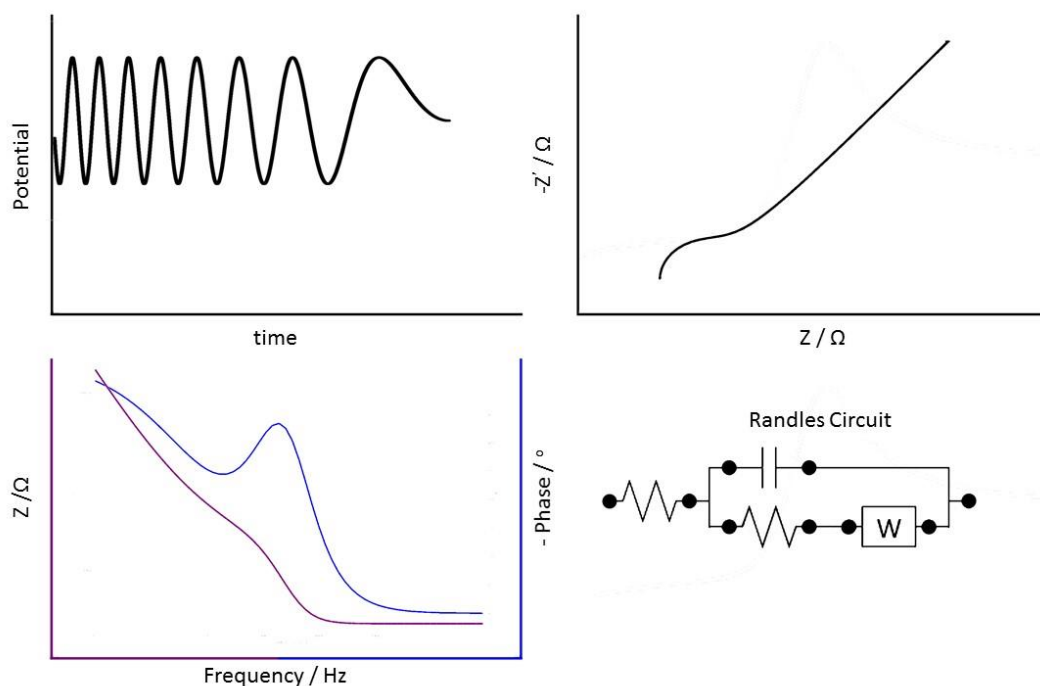
Figure 1.31 - Top left, input signal, top right - Nyquist plot, bottom left the bode plot and bottom right the equivalent circuit (the Randles circuit)

1.4.9 Electrodes

The material that the working electrode is constructed from has a dramatic effect on the interface, the way a redox couple can interact and on the adsorption properties of a given substance. As such the material chosen for the working electrode can affect the electrochemistry observed and the performance of any device.

The aim of analytical electrochemistry is to establish a known system so precise characteristics of that system can be identified. This leads to the need for materials with very well defined and documented behaviour and physical properties.[73] Commonly metals such as gold and platinum are used due to the extensive research conducted into the materials, their noble nature and understood catalytic properties. However, carbon materials now dominate analytical electrochemistry due to their large solvent window, lower catalytic activity, lower price and ease of use.

Carbon Electrodes

Carbon can be used to form many different conductive materials from boron-doped diamond (BDD) to graphene. The ability of carbon to interact with a large variety of elements leads to a large range of surface modifications.[74] Each material has distinct characteristics affecting any interaction and adsorption profile of redox active layers. The most prevalent material in use within analytical electrochemistry is glassy carbon (GC).

Glassy Carbon

Glassy carbon is formed by heating a polymeric resin (the first being a phenolic resin[75]) under a controlled atmosphere across its glass transition temperature. This leads to a graphitic structure

based on large, loosely tetrahedral, interconnected and inter-woven ribbons with a basic sp^2 (or fullerene) like bonding structure. This is achieved through the elimination of water and hydrogen from the starting material, initially forming the ribbons and subsequently creating crosslinks.[75] The surface of the material is affected by the preparation technique used to prepare the electrode for experimentation.[76] If the surface is left for too long before use in experiments, the surface can become 'dull' due to oxidation of the surface. Different methodologies for creating GC products exist, exhibiting different electrical properties, for example heating above 1500 °C decreases the hardness of the material but increases crystallinity due to the 'straightening' of the ribbons.[75] Additionally, the functional groups at the surface of the carbon structure greatly affect the type of interaction occurring and subsequently the electron-transfer process.[76]

Traditional graphite, even basic pencil 'lead' has been used as electrochemical working electrodes. Basic graphite can be a cost effective alternative to some exotic carbons and as discussed below is commonly used within fuel cells as a bi-polar plate material. The structure of bonded sheets of sp^2 hybridised carbon leads to a highly conductive soft material. However, its soft nature and unordered natural state can produce difficult to interpret data.

Highly Ordered Pyrolytic Graphite (HOPG)

HOPG can be used as a more precise, but more expensive, option to natural graphite. With a very well ordered structure, it can either be obtained through chemical vapour deposition or the heat treatment of carbon material to graphitise the material producing a high degree of crystallisation.

Highly ordered pyrolytic graphite

Basal Plane
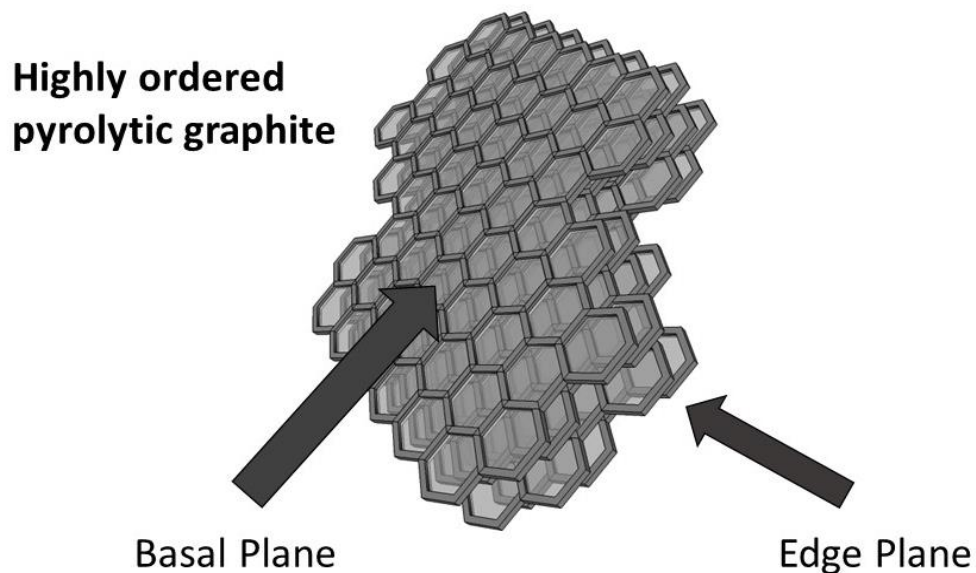
Edge Plane

Figure 1.32 – Diagram of the structure of HOPG, highlighting the edge and basal planes, the use of which subsequently produces the EPPG and BPPG elecrtodes surfaces.

EPPG and BPPG

The orientation of the crystal graphite can produce edge plane pyrolytic graphite (EPPG) and basal plane pyrolytic graphite (BPPG) (Figure 1.32). These two orientations of the graphite crystal can result in drastically different electrochemistry, with some redox couple showing reversibility at EPPG whereas irreversible behaviour at BPPG.

EPPG electrodes are obtained by orienting the crystal with the sheet planes perpendicular to the electrode surface, therefore upon polishing exposes a high degree of edge surface sites and a higher electron conductivity. Whereas, BPPG is obtained with the sheets orientated flat to the surface,

depending on the preparation method the degree of edge-site character of the BPPG can differ due to the fracturing of surface sheets leading to steps on the surface exposing edge sites.

Plastic Formed Carbon Electrode

An additional material is the relatively new plastic-formed carbon (PFCE): A material formed by mixing graphite with binders and heating to a relatively low temperature when compared to that of glassy carbon. The resulting material exhibits electrochemical properties similar to that of HOPG but is much cheaper. Additionally, the ability to form the material has led to its suggested use as a material for electrodes within fuel cells, batteries and solar cells.

Modification of Electrode Surfaces

Surfaces of electrodes have been modified to make use of the different chemical and electrochemical properties of the modifying element or molecule. Many different methodologies exist for creating a modification, from simple dipping techniques through to complicated plasma vapour deposition. Modifications with heteropolyacids are discussed later within this introduction (section 1.10). In sensors, the selectivity of either a film or specific molecules are used to produce electronic signals from a very specific target chemical or physical condition.

In other areas, the unique catalytic or redox properties of a chemical are used to produce a specific type of reaction or to produce catalysis. Within Fuel cells typically carbon is used as the 'bulk' electrode material with a modification of both Nafion™ and Pt nano-particles to enhance proton transport and to catalyse the HOR and ORR.

Fuel Cell and Application based Electrodes

Fuel cells and application based electrodes are not just concerned with the catalytic activity of an electrode surface but at what economic cost that activity is achieved. The most commonly associated Hydrogen fuelled proton exchange membrane fuel cell electrode surface can be ascribed in at least two parts. The MEA and the bipolar plate, both can be described as electrodes (or in the case of the MEA an assembly of electrodes).

The MEA, in generals aim to create the highest current density ($mA.cm^{-2}$) by maximising the exposure and activity of a Platinum surface. The Bi-polar plates have a lot in common with other electrodes structures in Batteries (both conventional and flow) and even electroplating. They can be constructed in a variety of materials, evolving from pressed metal sheets, expanded metal (and carbon) foams, Computer Numerical Control (CNC) milled graphite, through to conductive polymers and composites.

1.5 The chemistry and catalysis of current PEMFCs

The established techniques to extract energy from fuels uses combustion to release the stored chemical energy. However, completing this process electrochemically is more efficient by at least 20-30%.[77] It is difficult to isolate an exact working efficiency for a PEMFC due to the different efficiency calculations that are used, whether its well-to-wheel, combined heat and power, or pure coulombic efficiency, but typically values between 40-60% are quoted for the operating efficiency of a PEMFC stack.[78–80]

The reasons for this increase in efficiency are attributed to the reduction in wasteful energy conversions occurring. The overall reaction involved is the conversion of hydrogen and oxygen to water (Equation 1.35).

Equation 1.35

$$2H_2 + O_2 \xrightarrow[Cat]{} 2H_2O \qquad\qquad E^0 = 1.23\ V$$

This reaction has a large thermodynamic driving force of around -237 kJ.mol^{-1} (maximum electrical work) and combined with the density of hydrogen (0.09 g.L^{-1} at STP) is the reason hydrogen is such a desirable fuel when combined with its relative abundance. Without separation into two half reactions this principle reaction would proceed via combustion and the energy could not be extracted directly as electricity. However, as Grove showed the reaction can be split into two half reactions, Equation 1.36 and Equation 1.37.

Equation 1.36

$$2H_2 \rightleftharpoons 4H^+ + 4e^- \qquad\qquad E^0 = 0.00\ V$$

Equation 1.37

$$O_2 + 4H^+ + 4e^- \rightleftharpoons 2H_2O \qquad\qquad E^0 = 1.23\ V$$
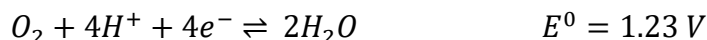
If the concentrations of reactants are maintained at the electrodes and a suitable catalyst is used a stable voltage can be maintained. However, losses within the cell lead to a depressed operating voltage and, due to kinetic limitations and design issues, lower current densities than one might expect. Some of these losses are due to electrical resistance or ionic resistance through the membrane, often referred to as ohmic losses.[81,82] Additionally, a mixed-potential loss can be incurred if side reactions occur, such as hydrogen peroxide formation at the cathode, which can additionally corrode the carbon support.[83,84] It must also be noted the effect that poisoning can have on the cell performance, with CO poisoning of the anode catalyst a big research priority, due to the need for expensive, high purity fuel streams.[85–87]

Losses can be described mathematically and a complete description can be found in the textbook "Fuel Cell Systems Explained'', authored by Larminie, J. and Dicks, A.[88]. Activation loses can be described by using a form (Equation 1.38) of the previously described Tafel equations (Equation 1.25Equation 1.26).

Equation 1.38

$$V = A \ln\left(\frac{i}{i_o}\right)$$

In Equation 1.38, the constant A reflects the rate of reaction, i is the observed current and i_o is the exchange current density. A was described as Equation 1.39 in 1976 by Mcdougall[89] for a hydrogen fuelled fuel cell. With exchange current density being a measure of the activity of the catalytic surface, nominally being the current value at which voltage losses are observed.

Equation 1.39

$$A = \frac{RT}{2\alpha F}$$

Activation losses occur at the cathode and anode, leading to Equation 1.40.

Equation 1.40

$$V_{activation\ loss} = A_c \ln\left(\frac{i}{i_{0,c}}\right) + A_a \ln\left(\frac{i}{i_{0,a}}\right)$$

However, the losses are different between electrodes, with much lower losses at the anode due to faster HOR kinetics and small mass transport losses. This leads to huge difference in the catalyst loadings between the anode and cathode. The DOE currently states the state of the art total catalyst loading is 0.15 mgPGM.cm^{-2} with a mass activity 0.47-0.67 A.mgPGM^{-1}@900mV.[90,91] Loadings as low as 0.01-0.03 mgPt.cm^{-2} have been reported[92–94] although commonly these do not meet the DOE degradation targets or are tested at unrealistic load conditions. Commonly the anode is attributed to around 20% of the PGM content of the PEMFC unit.[94–98]

This means that the activation losses can in general be described with one term, reflecting the losses at the cathode. An initially depressed voltage, from the Nernstian 1.23V, can be caused by fuel crossover and internal currents, due to hydrogen crossing the membrane and the migration of electrons across the polymer producing an 'internal current density'.[88] Often termed a mixed potential this leads to a highly volatile OCP and an initial drop in voltage. This can be modelled by incorporating the internal current density (i_n) into Equation 1.38 and using the predicted equilibrium potential (E) leading to Equation 1.41.

Equation 1.41

$$V = E - A \ln\left(\frac{i + i_n}{i_0}\right)$$

The description of Ohmic losses can be achieved simply through the uses of Ohm's law (Equation 1.29). However, the losses of due to mass-transport of reactants and products is more complicated and a complete description is given by Larminie, J et al.[88] A change in reactant pressure on the voltage of the cell can be described by Equation 1.42.

Equation 1.42

$$\Delta V = \frac{RT}{nF} \ln\left(\frac{P_2}{P_1}\right)$$

This can be converted into current values and due to the dominance of the cathode, isolated to the mass transport of oxygen so that the effective voltage loss can be described,* (Equation 1.43).

Equation 1.43

$$V = -\frac{RT}{4F} \ln\left(\frac{i}{i_l}\right)$$

---

*These descriptions are not a practical simulation but merely a guide to the losses within a PEMFC.

The term i_l denotes the limiting current at which mass transport becomes a dominant factor in the voltage/current relationship. The relationships defined by Equation 1.35Equation 1.43 can be combined to reach an overall description for the current/voltage relationship often observed for a PEMFC and the characteristic 'I/V curve' or 'Power Curves' that can be obtained experimentally. This results in Equation 1.44 and the plot in Figure 1.33.

Equation 1.44

$$V = E - (i + i_n)r - Aln\left(\frac{i + i_n}{i_0}\right) + \frac{RT}{4F}ln\left(1 - \frac{i + i_n}{i_l}\right)$$
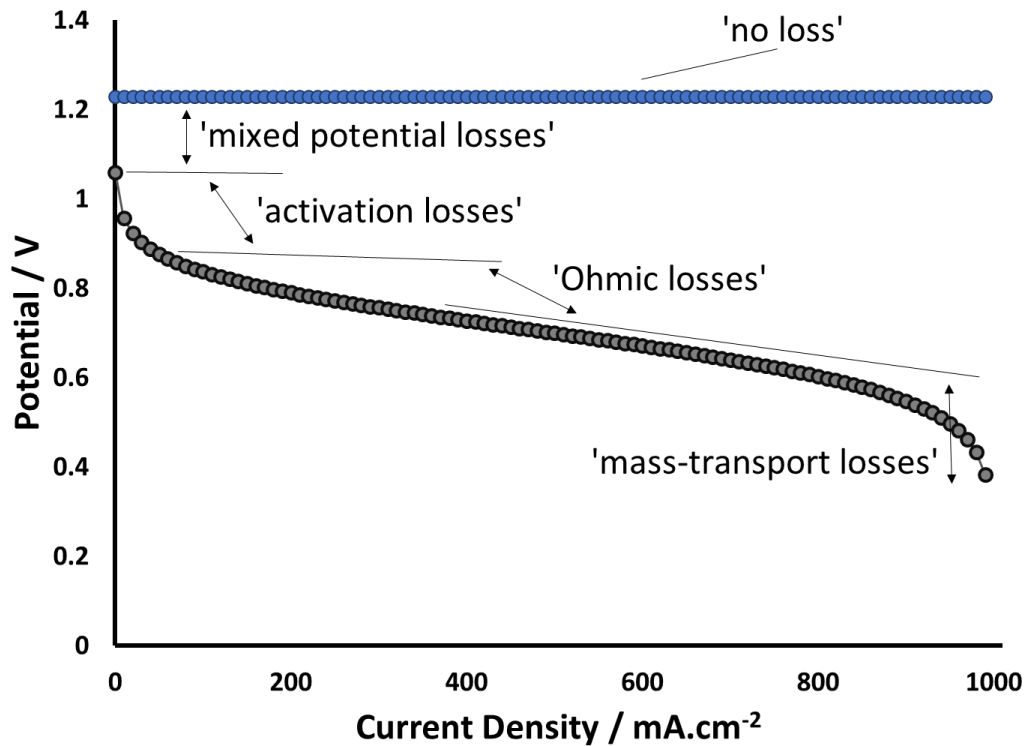
Figure 1.33 – Plot using the equations described (Equation 1.35 to Equation 1.44) to model a description of the different losses within a hydrogen fuelled PEMFC. For values used within equations please see Table 0-1 in appendix section 10.1.5.

The focus for reducing these loses has been catalyst development. When referring to the anode catalysts, many studies focus on the poisoning effect of CO within the fuel stream as this is seen

as the predominant area for improvement with regard to these catalysts. The mechanism is assumed to proceed through an interaction with an adsorbed Pt-H (or PGM-H) species predominated with adsorption to the Pt(111) crystal face.[99–104]

With reference to the ORR reaction, there is still much debate about the reaction pathway and mechanism, with a host mechanisms suggested depending on temperature, pressure, potential and pH.[30,105–109] Some argue, that at low temperatures (below the desorption temperature of water) the reaction proceeds autocatalytically through water reacting with unreacted O adatoms to adsorbed OH groups, whereas, at high temperature the reaction proceeds through H adatoms interacting with O adatoms through standard kinetic steps.[110] Others have studied the reaction with in-situ XRD and XAS and suggested the reaction proceeds predominantly through a Pt-O intermediate with both α and β Pt-O_2 species detected.[111]

1.6. Alleviating reliance on primary platinum sources

This thesis concentrates on three routes to alleviate the reliance on primary platinum sources. The first route explored is that of reduction: continuing to source platinum from primary ores but to reduce the mass of platinum used to generate the same current (or power) densities within a PEMFC. There have been many studies in this direction and section 1.7 explores these in detail. Experimentally the use of lithographic techniques to precisely place platinum atoms on surfaces to create atomically designed surfaces is demonstrated in section 2.1.

The second is recycling: to increase the ability to recycle platinum and other PGMs from sources which are currently uneconomical. Section 1.8 discusses the current techniques and the possibility of recovering PGMs through biohydrometallurgy and experimentally the electrochemistry exhibited by palladium biomass material produced through biohydrometallurgy is investigated in section 2.2.

The third method is to replace platinum and PGMs within the PEMFC. There have been many attempts to develop alternative catalysts and section 1.9 focuses on this area. Introducing the possibility of changing the chemical architecture of the PEMFC to accommodate a different catalytic route to the ORR through a technique brought to the market by ACAL Energy Ltd. Much like the chemistry of the ORR, the chemistry of this system is currently not fully understood and trying to understand this chemistry and its subsequent electrochemical behaviour forms the core of this thesis. Chapters 3 to 7, cover the experiments conducted towards developing an understanding of the complex electrochemistry involved.

1.7 Reducing platinum content within PEMFC units

Some researchers have focused on maintaining an active platinum surface whilst reducing the mass of platinum within the PEMFC, developing particulate catalysts that generate the highest electrochemical surface area per gram of platinum. The first steps towards this was the use of platinum black,[112] followed by the use of carbon supports for particulate platinum.[94,109] These development steps have established the current leading commercial catalysts; produced by

supporting nano-particulate platinum on macro-particulate carbons which are then manufactured into a catalyst layer (CL) containing an interlaced web of Nafion® within the CL.

These techniques produced gains in current (or power) densities within a PEMFC (for a given mass of platinum). However, they can also lead to degradation, with carbon corrosion or agglomeration of platinum nanoparticles, leading to reduced performance over time. This has led research into carbon support materials[113] and stabilising platinum nanoparticles on the surface[114,115], or indeed manufacture methods which all effect performance.[114,116,117] Currently the best performing, high surface area platinum structure is a relatively new concept of designed platinum structures developed by 3M supported by the DoE[54]; they have produced a novel open cage platinum structure, generating huge surface areas per gram of platinum whilst exhibiting relatively low long-term degradation.

The ability to construct platinum structures and place platinum directly in positions available for electrocatalytic behaviour is intriguing and is investigated in chapter 2.1. Electron beam lithography has shown the ability to manufacture very precise placement of atoms, however fundamentally it is a technique that is time consuming and expensive.[118–121] Chemical scaffolding is a technique that has been used to produce manufactured shapes and designed spatially resolved placement of chemicals.[122–127] Combining the two techniques may potentially alleviate the expense and time needed for electron beam lithography whilst improving the spatial resolution of chemical scaffolds.

The combination of these techniques to produce electrochemically active platinum surfaces is demonstrated in chapter 2.1.

1.8 Recycling platinum resources

The aim of reducing demand on primary PGM reserves can be achieved by recycling established PGM materials. Traditional methods such as hydrometallurgy[128,129] and pyrometallurgy[130–133] are costly (financially and environmentally) pushing low-grade sources (both from waste and primary sources) to become economically unviable. The incorporation of biocatalysts in bio-hydrometallurgy[134–141] can reduce the energetic, financial and environmental cost.

Within the process, enzymes within the bacteria and the nature of microbes to act as 'hoovers', are used to produce deposits of metals on (or within) the microbe structures.[142–145] Hydrogenase can be used to couple the oxidation of hydrogen (or another 'fuel') to the reduction of a metal in a raised oxidation state. [146–150]

Previous studies have explored the possibility of using the nanoparticles formed within PEMFCs. However, it is an area needing further investigation.[151–153] Experimental errors were possible due to the fabrication method and the particles were not used directly but pretreated.[154,155] The effect of microbial strain, reducing agent and metal species on the growth of PGM particles and their subsequent potential electrochemistry is not fully understood. As such, experimental investigations into the use of different microbial strains, reducing agent and synthetic leachates are shown in section 2.2.

1.9 Replacing platinum

The most desirable route to alleviating the reliance of fuel cell technology on primary platinum reserves is to remove PGMs from the PEMFC altogether through the introduction of alternative catalysts. The most common approach is to replace the platinum surfaces with a like-for-like catalyst which can simply be substituted into current PEMFC architectures. Many researchers point to the 'volcano plots' developed on the Sabatier principle to find the surface that is just right for the ORR reaction. When considering the ORR the most common plot shows the exchange current density (or activity) with the oxygen binding energy,[156] as shown in Figure 1.34.
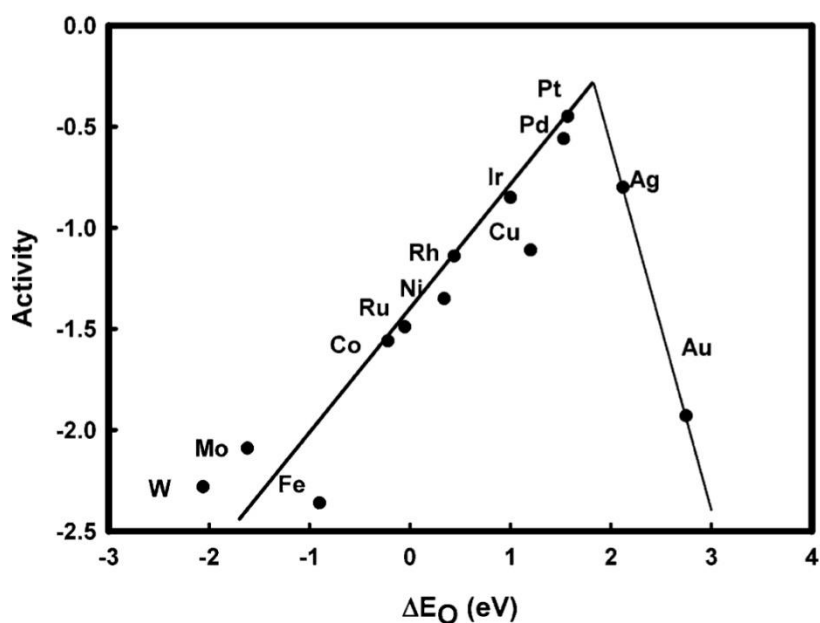
Figure 1.34 - Volcano plot of ORR activity versus oxygen binding energy for different metals[157] reprinted with permission from reference 157. Copyright 2004 American Chemical Society.

As can be seen in the graph, platinum occupies the optimum position amongst metals. However, others have also plotted alloys (binary and ternary) which show that Pt_3Co and Pt_3Ni both occupy

higher positions than pure platinum meaning that not only are there possible candidates that could replace platinum but also outperform platinum.[158,159]

Many methods of creating these alloyed materials have been trialled, including promising core-shell compounds. However, almost all examples suffer from fast degradation as a result of leaching or reconfiguration of the active surface.[160–167] Different approaches have been taken to produce complexes capable of performing the ORR, some use biomimetic compounds which try to produce active centres similar to enzymes or that of haemoglobin.[168–171] However these also suffer large degradation issues and from relatively low kinetics producing slow reaction rates.

The issue with these examples is that they are trying to copy an existing mechanism. A different approach is establishing a different catalytic architecture allowing for the use of non-PGM catalysts. One of the main reasons for the slow reactions rates demonstrated by the majority of alternative catalysts is due to the underlying mass transport issues within PEMFCs.[172–175] The heterogeneous catalysis forces a slow rate of material transfer to and from the reaction sites. A different fuel cell architecture has been demonstrated by ACAL Energy Ltd, similar to that of flow batteries, and allows for alternative homogeneous catalysts to be introduced.

1.9.1 ACAL Energy Ltd. and liquid catholyte proton exchange fuel cells

ACAL Energy Ltd. has developed a novel method for reducing the kinetic limitation of the ORR, implementing an electron mediator into the reaction schematic of the fuel cell. This is achieved by using a liquid catholyte that circulates between the cathode of the fuel cell and a 'lung' where it is

regenerated. However, separate issues arise due to the complicated design. The liquid catholyte section of the fuel cell is trademarked as Flowcath[(tm)].
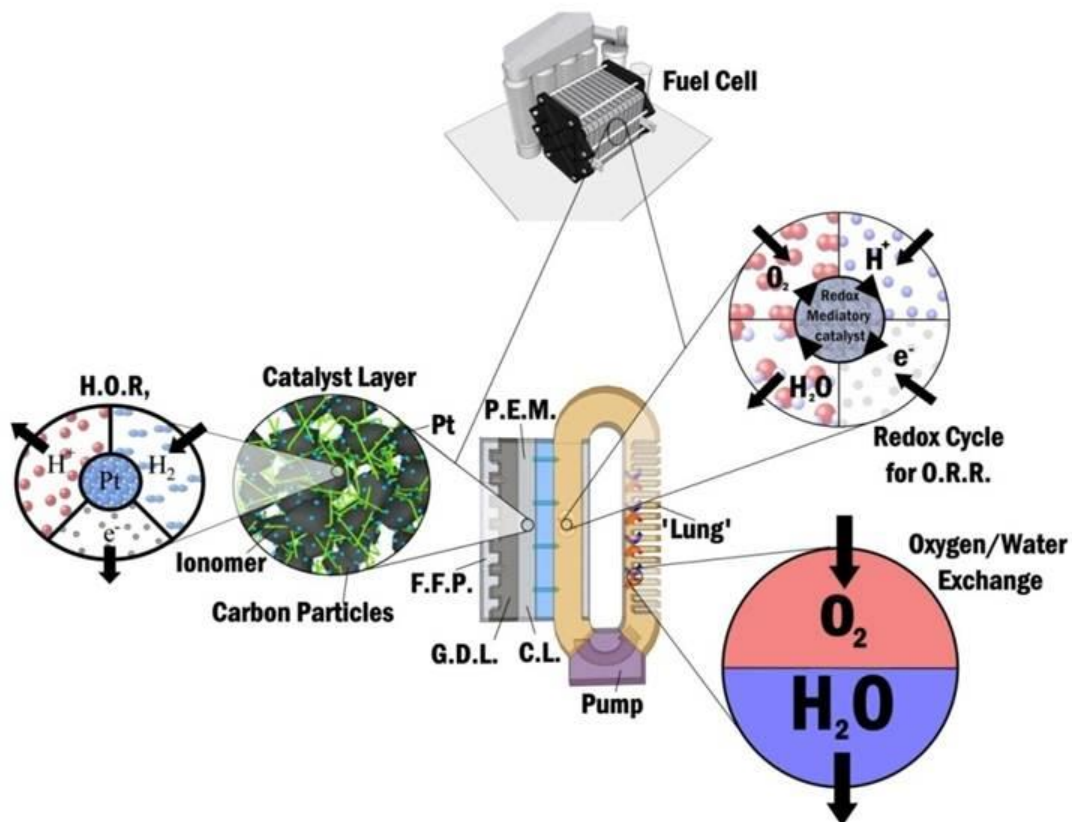
Figure 1.35 Single Cell liquid catholyte PEM fuel cell

Figure 1.35 shows a schematic of a single cell used within a liquid catholyte fuel cell unit. As can be seen the anode side of the cell is representative of a conventional PEM fuel cell, however the cathode is a unique geometry. The cathode geometry presents a unique electrochemical challenge to maximise the interaction of the electrode surface with the catholyte solution whilst producing the lowest pressure drop possible. To achieve this highly porous electrode materials are inset within a cathode plate, as shown in Figure 1.36.
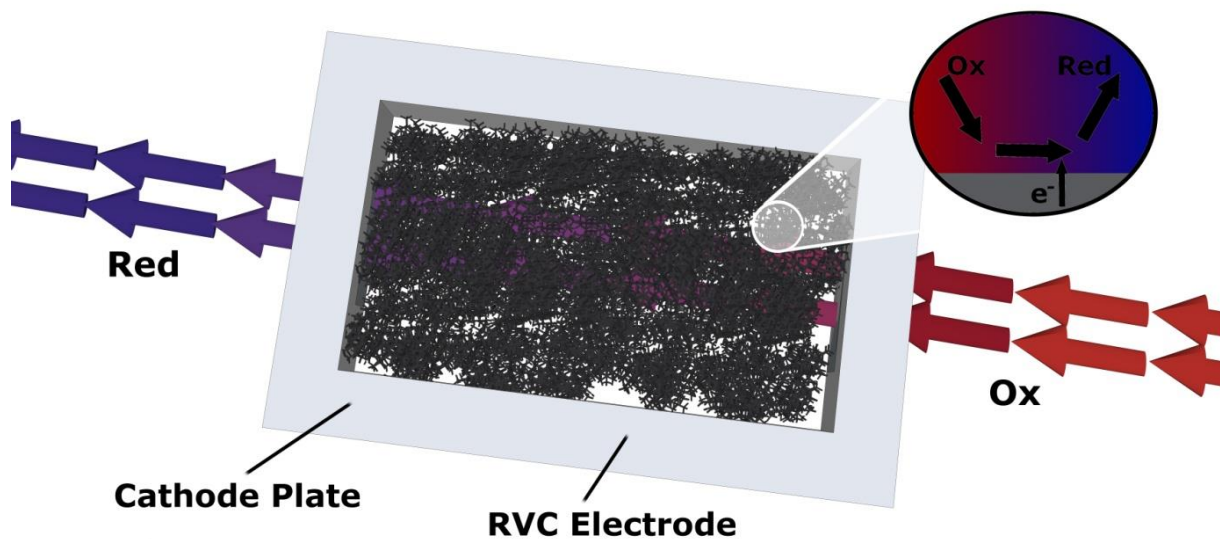
Figure 1.36 - Cathode section of liquid catholyte PEM Fuel cell single cell

There are many materials that could perform as the porous electrode within the cathode. Commonly carbon based materials provide a wide range of porosities and structures whilst retaining relatively high conductivities. However, a method for analysing these materials must be devised. To devise such a method one must look at the processes occurring within the system. The primary concern within the electrochemical engineering challenge is the reduction of the electron mediator.

Anode

The anode used within a liquid catholyte proton exchange membrane fuel cell is similar in design to that of a regular fuel cell. The flow-field plate design, GDL, catalyst layer and the membrane are the same as within normal PEMFCs. However due to unique characteristics of design with a liquid catholyte cell some subtle changes are made.

One of the most complicated areas of traditional PEMFC design is the humidification of the hydrogen fuel supply,[62,176–178] in order to ensure the membrane does not dry out and reduce functionality. However, in a liquid catholyte design the humidification of the membrane is maintained by the cathode. This means humidification of the oxidant fuel is not needed. It also adds the benefit that the cells can be run 'dead ended' in that a continuous flow of hydrogen is not needed to clear excess fluid built up by the humidity of inlet gases condensing within the flow field design. Instead a simple purge valve can be used to periodically flush the system. There is however a question of whether, with the humidification of the membrane provided by the catholyte, crossover of the mediator compound can occur reducing the efficiency of the anode.

Cathode

The cathode design within liquid catholyte fuel cells is unique. Oxidised mediator is pumped into the cell, where it is reduced at the electrode surface before exiting the cell and being pumped back to the oxidiser unit. The details of the interactions occurring are the principle focus of this thesis. As such sections 1.9.2 and chapter 3 provide a deeper analysis of the cathode design and the reaction schematics occurring.

Oxidiser

The oxidiser aims to minimise parasitic energy losses while maximising re-oxidation of the mediator. If incomplete oxidation occurs it reduces the operating voltage of the cell, in accordance with the Nernst equation. As such the largest interaction with oxygen is required within the unit; it is also essential to remove the water produced so the concentration of mediator compound is not diluted, reducing the voltage produced.

1.9.2 Catholyte

The catholyte and the reaction occurring within the cathode are the focus of this thesis and the work conducted. The use of mediator compounds to shuttle electrons and shift redox pathways has long been used in nature. In this system, a polyoxometalate compound is used as the electron shuttle. However, the form and nature of the reduction at the electrode surface is not fully understood. Consequently, the subsequent reactions that occur are not fully understood. As such identifying the reactions and compounds allowing the advantages of this type of fuel cells to develop is essential.

1.10 Polyoxometalates

Polyoxometalates are a huge class of compounds, the scope of which is too large to fully describe here. The first mention of them as a class of species was reportedly in 1826[179] and ever since they have been researched and used commercially in a huge range of applications. Generally defined as early transition metal oxygen anion clusters[180] they can first be defined into two groups, those containing only metal oxide clusters, the isopolyoxometalates, and those containing one or more p, d or f block atoms, the heteropolyoxometalates (the type under discussion in this thesis).[181] Such is the volume of material on polyoxometalates many large reviews have been conducted, with many also struggling to suitably define subclasses of compounds. Relatively early reviews such as those by Griffth,[182] Papaconstantinou,[183] and Zubieta[184] along with the longstanding contributions of Pope[181,185,186] and Hill[180,181,187] led to a revival of polyoxometalate chemistry in the late 1990's.[188–191] This has recently resurfaced due to their application in energy devices[192–198] and specifically as

additives to fuel cells with a recent review by Kourasi[199] highlighting this application. In general the compounds are defined either by their overall structure or the metal oxides that they consist of.

1.10.1 Structures of Polyoxometalates

The full range of structures exhibited by polyoxometalates is almost infinite and even when limited to heteropolyoxometalates seems limitless. However, the structures of interest within this thesis and for this application are the relatively simply self-assembled heteropolyacid structures. In particular, the Keggin structured heteropolyacids. The most common of these are phosphotungstic and phosphomolybdic acid, which are of particular interest due to their ability to have their electrochemistry tailored by the insertion of different metals into their structure.

Generally, these structures form complex anions with simple supporting cations. The anions in the examples of Keggin structured compounds follow the general formula, $[PX_{12-a}Y_aO_{40}^{(3+a)-}][(3+a)Z]$ where X is a transition metal (normally W, Mo or V), Y is an early d-block transition metal and Z is the supporting cation.[200] The structure is shown in Figure 1.37, which is a graphical representation based on crystallographic data provided by ACAL Energy Ltd.
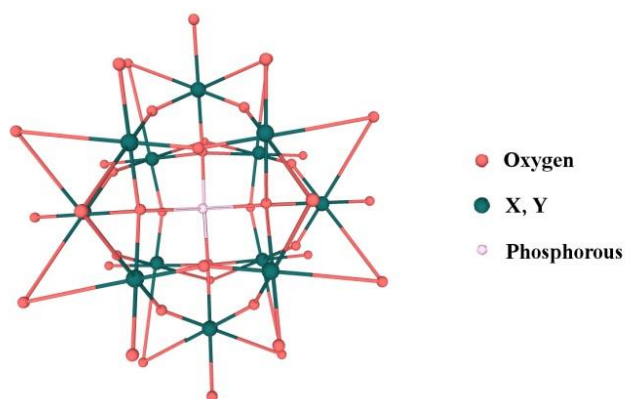
Figure 1.37 - Graphical representation of the Keggin structured heteropolyanion

59

It is the ability to tailor the chemistry of the compounds combined with their ability to possess multiple oxidation states that appeals to energy science.[187,201] The particular interaction that has been highlighted between molybdenum containing and vanadium containing compounds, often cited as being biomimetic, draws attention to tailoring the chemistry of phosphomolybdic acid derivatives with vanadium inclusion.[202–205]

1.10.2 Phosphomolybdic acid

Phosphomolybdic acid has proved a chemical useful in many applications, especially in the detection of phosphates but additionally in staining and imaging techniques.[206–212] More recently it is its ability to function as a multiple oxidation state catalyst that has seen it receive research attention,[190,213,214] including its functionality towards the methanol oxidation and the oxygen reduction reaction within fuel cells.[215,216]

Interestingly the species is known to form complex layers on the surface of electrodes as well as exhibit solution phase electrochemistry.[217,218] Research has been directed at using phosphomolybdic acid to activate electrode surfaces for electro catalytic reactions.[219–221] Due to the large volume of work on phosphomolybdic acid, both in solution and whilst adsorbed to a surface, it formed the base-line for experimentation in chapter 3 before incorporating vanadium into the structure in later chapters. In addition, the electrochemical behaviour at different electrodes and its relationship to pH have not been fully investigated previously, therefore these parameters are explored experimentally in chapter 4.

1.10.3 Vanadium substituted phosphomolybdic acid

The inclusion of vanadium into the heteropolyanion has been shown to affect the chemistry and electrochemistry of the compound when compared to the parent species.[190,222,223] Significantly, it changes the manner of the electron transfer within the species. Shifting the onset of reduction in a positive direction when compared to the parent phosphomolybdic acid but also altering the magnitude of electron transfer.[224–227]

It has also been shown that pH affects the overall process.[228] However, the exact effect of vanadium substitution within the phosphomolybdic species have not been fully investigated. Especially with respect to the effect on the adsorbed layer electrochemistry of the electrode material or the effect that pH has on the electron transfer in aqueous solutions. Further, the interaction with the solution phase between the adsorbed species is not fully understood.

It is with this in mind, together with the knowledge of the species' application towards the ORR, that experimental work focusses on the electrochemical behaviour of singularly substituted vanadophosphomolybdic acid. It initially investigates the adsorbed layer (chapter 3 and chapter 4) and the solution phase (chapter 5) before exploring further into the effect of doubly substituting vanadium into the phosphomolybdic acid structure (chapter 6).

1.11 Conclusion

The introduction shown that within each of the areas of reducing, recycling and removing PGM catalysts, efforts are being made to develop PEMFCs into an economically attractive alternative

within the current energy landscape. The use of specifically constructed platinum structures has been explored and the use of lithography to create unique structured surfaces has been highlighted as a method of reducing the mass of platinum for a given activity to the ORR. Biohydrometallurgy has been introduced as a novel way to increase the efficiency of recycling PGMs and thereby shift the dependence on primary ores. The ultimate approach, that of removing PGM materials from the PEMFC unit, has been explored with the introduction to ACAL Energy Ltd.'s FlowCath® technology.

In each of these areas, it was shown that electrochemical engineering and electrochemistry play a key role in developing and understanding these novel approaches. Consequently, basic electrochemical theory and experimental techniques have been discussed. Additionally, the introduction highlighted how the particular case of the materials used within the FlowCath® cell need further understanding to enable the production of improved devices. It has been shown that this can be achieved through the study of phosphomolybdic acid derivatives with inclusion of vanadium within their structure.

However, it has also been discussed that due to the multiple multi-electron transfers observed with the electrochemical investigation of phosphomolybdic acid that quantitative analysis has proven difficult. Additionally, the formation of adsorbed layers on electrodes, and the interaction between the adsorbed layer, the electrode and the bulk solution has emerged as a key area to focus research.

The following chapters detail the experimental work conducted into the areas introduced. After the introduction, chapter 2 starts by exploring the reduction of PGM content through lithography before

discussing the potential of biohydrometallurgy to produce functional PEMFC materials. The third chapter explores the formation of phosphomolybdic acid (PMA) and singularly substituted vanadophosphomolybdic (V1PMA) acid adsorbed layers, highlighting the initial difficulties in obtaining quantitative results. The fourth chapter further develops an understanding of these layers, through investigations into the effect of parameters such as electrode material and pH. The fifth introduces the solution based electrochemistry of PMA and V1PMA species, developing an understanding of the interaction between the adsorbed layers and the bulk solution. The sixth chapter explores the effect of increasing the substitution of vanadium into the PMA structure by examining the adsorbed layer and solution electrochemistry of doubly substituted vanadophosphomolybdic acid species (V2PMA). The final experimental chapter, chapter 7, shows the additional work conducted into the FlowCath® system and the unique experimental developments made to within this project to enable those investigations. The thesis is then concluded in chapter 8, which provides a summation of the thesis and its findings. The appendix provides details of additional work conducted, supporting information as well as side-project work.

2. Reducing and recycling

The previous chapter highlighted the concepts surrounding reducing, recycling and removing PGM content from fuel cells. This chapter aims to discuss methods and experimental work into reducing and recycling the PGM content.

2.1 Reducing platinum content through spatially resolved particle placement

This section of chapter two discusses the experimental work conducted into possible methods for reducing the platinum content within the PEMFC.

2.1.1 Introduction

There is an extensive array of methods used to research and produce more effective PGM catalysts. These catalysts can largely be divided into three categories: those that maximise the stable surface area of platinum group metals; those that mimic the active surface of bulk platinum; and those that can be described as biomimetic. The method discussed herein tries to generate the largest stable surface area of platinum for the smallest mass unit of platinum.

The full mechanism of the ORR is still relatively unknown, with multiple pathways put forward for the reaction to proceed through. Many quote the Wroblowa[229] or a modified Wroblowa mechanism[230] as the base mechanistic pathway for the ORR. This is further confused by the multiple adsorption species and the multiple crystal facets of a platinum surface. Arguments exist

over the dominant crystal plane for these reactions, as it is dependent on the electrolyte used for experimentation due to the poisoning caused by sulphur oxide and chloride ions.[231–235]

These poisons preferentially bind to different crystal faces leading to confusion over the dominant plane. Interestingly the particle size effect is connected to the dominance of a crystal edge leading to non-linear increases in activity per gram as the nanoparticles reduce in size below 2-3nm.[236] This is due to the transition from dominant crystal planes to edge sites as the particles reduce in size.[237]

This must be considered when designing a platinum surface structure, as in this project. Instead of trying to maximise a certain crystal surface for a given mass of platinum, an attempt is made to spatially deposit platinum atoms within a carbon surface with the use of designed complexes controlling the spatial dispersion of platinum atoms. The aim of this project was to determine whether these structures create electrochemical behaviour similar to a platinum surface.

Platinum can form many different complexes with a multitude of ligands due to its multiple oxidation states. In this project, it is the ability to convert the ligand material into a carbon structure during e-beam lithography and the placement of the then reduced platinum atom within this structure that is of interest.

The complexes used in this project contain a fullerene structure linked with a pyrrolidine to a platinum metal centre with a co-ordinating bipyridine ligand, 1 and 2, Figure 2.1. The complexes were synthesised by Dr Tom Chamberlain (University of Nottingham) before being used to modify electrode surfaces. It is an interesting balance between the chemistry of the complex and the

material processing that leads to the designed surface structures potentially forming a catalytic platinum surface.[238–241]
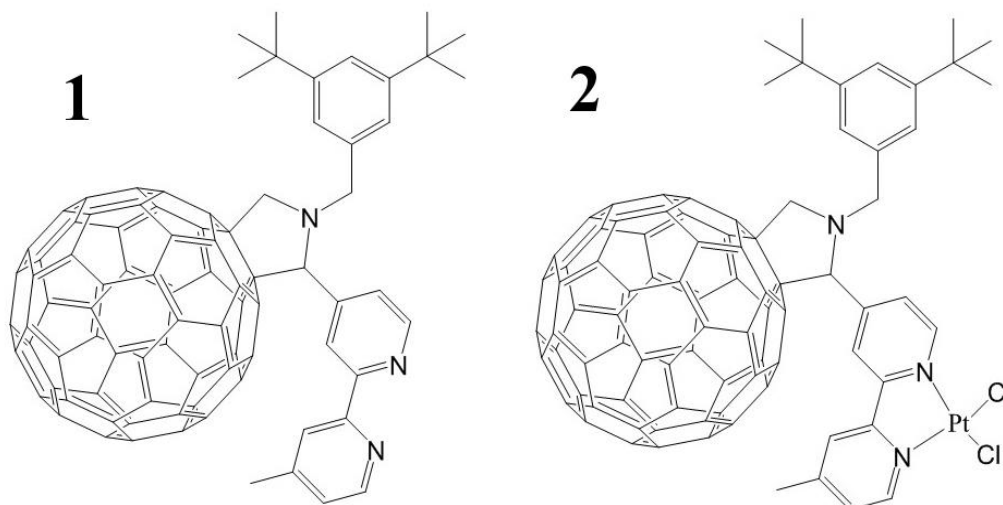
Figure 2.1, 1 - 4-methyl,4'-(2-(N(3,5-di-tert-butylphenlymethyl))fulleropyrrolidineo)-bipyridine, 2 - 4-methyl,4'-(2-(N-(3,5-di-tert-butylphenylmethyl))fulleropyrrolidineo)-bipyridine platinum chloride

The organic element of the compound can be broken down to form an amorphous carbon material similar to glassy carbon when exposing it to an ion beam.[238,239,242,243] This leaves the now reduced platinum atoms embedded within a glassy carbon like, electron conductive material. The distance between the platinum species, or indeed other metals such as ruthenium, can be controlled through the spacing groups in the original compound.

An additional element is the ability to use the electron beam lithography technique to produce specific shapes and sizes of the new material on the surface, with the excess removed.[238] This could add a further element to reducing the platinum content as structured surfaces have been demonstrated in this way.[244–247]

Aims and objectives

Following discussions with Dr Alex Robinson (University of Birmingham) it was decided to investigate the material generated from exposing platinum fullerene compounds (Figure 2.1, 1 and 2) to an ion beam, for potential electrochemical applications and possible use within fuel cells due to the potential reduction in platinum content and the incorporation of additional metals which could lead towards CO tolerance.

The aim was to develop methods to test the material and then perform initial investigations into its electrochemical behaviour.

2.1.2. Experimental

Synthesis

The compounds were synthesised by collaborators at the University of Nottingham and were supplied by Dr Alex Robinson, and only the structures were given as additional information.

Electrode construction

Working electrodes were fabricated from 5mm diameter glassy carbon (GC) rods (Sigradur, Germany) and cut to size (l to 4 mm) with a diamond saw. Before further modification, the surfaces were polished sequentially with 45, 15, 9, 6, µm diamond pastes on polishing pads (Buehler, Germany), followed by 1, 0.3 and 0.05 µm alumina slurries (Buehler, Germany) on polishing pads. The polished GC electrodes were thoroughly rinsed and sonicated in ultrapure water and then dried in a stream of nitrogen before further use. Blank samples were not further modified. Untreated

samples of the C60 derivatives were drop-cast onto the electrode surface in 10 µL aliquots and air-dried. Treated samples were drop-cast in the same manner before further treatment with the electron beam (e-beam). The surfaces were then adhered to brass rods using copper tape and areas not to be analyzed were masked with epoxy resin (Evo-Stik, Bostik) and cured for 24 hours.

In addition to epoxy covered electrode construction a novel electrode design was developed to allow for quick coating. This was achieved through spin coating or drop casting of compound material, giving the ability to mount, remove and remount the electrode repeatedly to subject the electrode to multiple procedures and analytical tests. This development led to several electrode designs which are explored in more detail in the chapter 7 of this thesis.

The electrode design in this example was produced by taking a glassy carbon stub which was created as above and inserting it within a cap of PEEK. The cap of PEEK was produced by taking a 6 mm (diameter) PEEK rod (directplastics.co.uk) and cutting a 5 mm length. A 2.75 mm hole was drilled or lathed at the centre. The cap was placed within an oven at 150^{0}C (the procedure can also be replicated with a Teflon cap but at a temperature of 80^{0}C). This was then allowed to cool forming a seal around the glassy carbon stub with a diameter of 3 mm, before polishing to a desired height (as low as 1 mm for some modification machinery) and a mirror finish as above. This process formed the electrode tip and in subsequent experiments it demonstrated flexibility in modifying the tip not just with spin coating and e-beam treatment but also with plasma vapour deposition.

The shaft of the electrode was created by taking a 6 cm length of the 6 mm PEEK rod and drilling a 2.5 mm bore hole down the centre of the rod. Down this central bore a 2.75 mm copper rod was

inserted under force (either with a pneumatic press or hammer) with a 2 cm length left at one end and the other sanded down to flat surface. Silver impregnated epoxy resin (RS components) was used to form a connection between the tip and the shaft, with an insulating ring of standard epoxy used to stop exposure of the silver to the electrolyte solution. A schematic of this design can be seen in chapter 7.

Ion beam treatment

The treatment of the compounds with an e-beam inside a SEM results in a change in the compound with the C_{60} decomposing and the formation of glassy carbon impregnated with single platinum and ruthenium atoms. Then through using lithography techniques, specific surface structures can be achieved. The e-beam treatment was conducted by members of Dr Alex Robinson's research group. For the purpose of this study, only square surface (0.1×0.1 cm) structures were produced. To investigate surface area effect multiple squares on the same electrode were created.

Modified surface electrochemistry

Cyclic voltammetry was used to investigate the redox properties displayed by adsorbed layers of various C_{60} derivatives. Proton reduction was used as a test reaction. A standard three electrode electrochemical cell set-up was used throughout, connected to a IVIUMstat potentiostat (Alvatek Ltd, UK) controlled by an external desktop PC using IviumSoft (Alvatek Ltd, UK) software.

The counter electrode was a bright platinum gauze of large surface area. Two reference electrodes were used in experimentation, a saturated calomel electrode (ALS, Japan) and a saturated Ag/AgCl electrode (CH instruments, England). The electrolytes were aqueous solutions of 0.095M sodium

perchlorate (Sigma Aldrich) and 5.0 mM Perchloric acid (Sigma Aldrich) in ultrapure water of resistivity not less than 18.2 MΩ.cm (Milli-Q, Millipore).

Microscopy

To investigate whether the electrodes had been correctly prepared and to assess the surface area of the compound after treatment, light microscopy was used to produce images of the surfaces of the samples both before and after the electrochemical experiments. These were than assessed using image processing software (GIMP).

2.1.3 Results and discussion

The aim of the experimental work was to determine whether electrodes modified with the C_{60}-bipy compounds and their lithographed counterparts produced any electrochemical properties and whether these were similar to those of platinum surfaces.

To compare with the later modified electrodes, first solution phase experiments were conducted into the C_{60}-bipy compounds in both acetonitrile and chloroform. The experimental detail for these experiments can be found in appendix 10.2.1. These experiments were found to be the highly sensitive to trace water and oxygen. However, it was observed that the compounds exhibited multiple redox waves as has previously been observed for fullerene compounds.[248–250] Despite this observation, the difficulty in obtaining presentable results led to the move to examining modified electrode surfaces, in aqueous solutions as this was where the aims of the project lay.

Samples and preparation

The need to produce electrodes that could be treated with ion beam lithography led to significant development of experimental methods. The need to process the surfaces without altering the samples led to the need to use a small (by volume) electrode tip that could still be used for hydrodynamic study on a rotating disc electrode (RDE). The development of these electrodes led to a large volume of work and is covered in chapter 7 (7.2).

The physical nature of the electrode surfaces formed a key role in the project. The different techniques that the compounds underwent to produce electrode surfaces meant there was a chance that any differences seen were a result of physical layer morphologies rather than a true chemical trait.

The different treatments, especially the lithography left differing surface areas of actual material modification on the surface of the glassy carbon, requiring inspection and measurement via optical microscopy. The e-beam lithography is currently a time-consuming procedure and means only relatively small areas can be created. When the lithographed area is removed, it leaves a significant difference in modified area between the samples. A drop cast electrode without lithography treatment is shown in Figure 2.2.
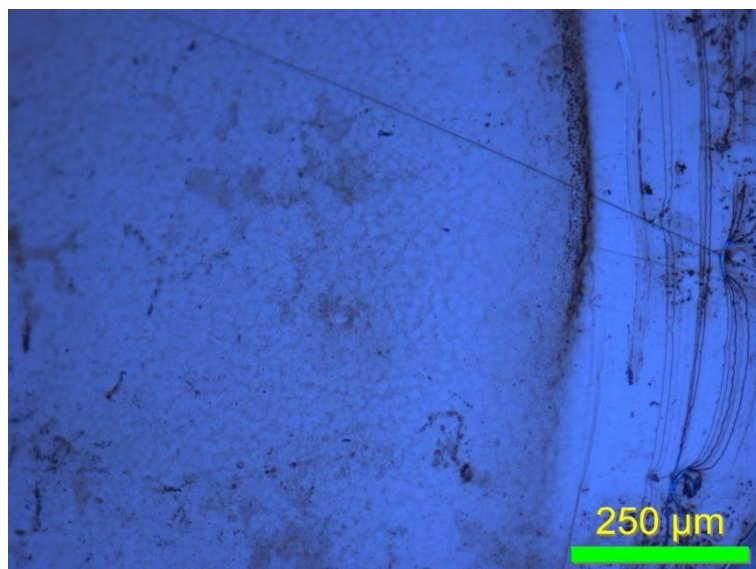
Figure 2.2 -Image at 10× magnification of a drop cast fulleropyrrolidine-bipyridine platinum chloride modified electrode (3mm GC) surface

It can be seen in the figure that the drop cast technique produces a relatively smooth and uniform layer right up to the edge of the glassy carbon surface (far right of image). This is not the case when looking at the lithographed electrode surfaces which have had the non-treated segments removed.

Figure 2.3 shows an example image of a spin-coated and then lithographed electrode modification. It clearly shows the reduced area of the modification. Through these images the surface area of modification was calculated for each electrode allowing for a true comparison of the electrochemical response.
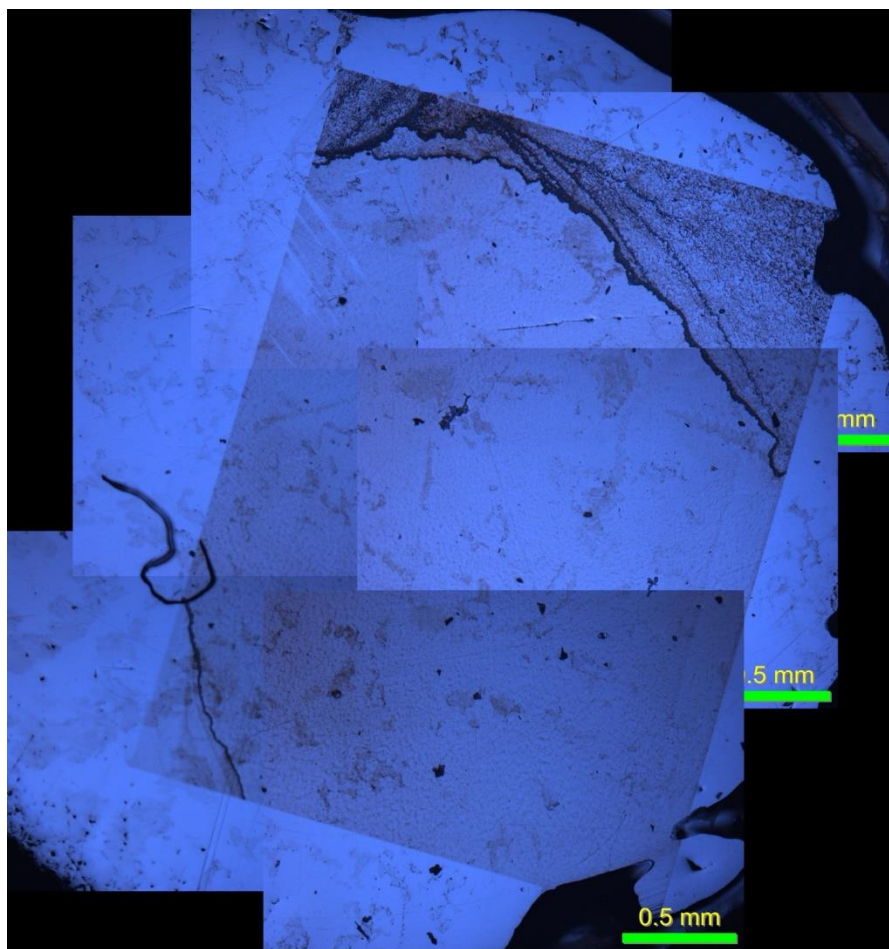
Figure 2.3 – The image is a compilation of microscope images showing a fulleropyrrolidine-bipyridine platinum chloride lithographed electrode surface. The Image shows the rectangular feature across the 3mm GC electrodes surface where the e-beam treatment has occurred.

Figure 2.3 also shows the delamination effect caused by the removal of non-treated sections, which can be an issue with surface modifications produced through lithography techniques.[251–253] Figure 2.4 highlights one of these delaminated areas (A) compared to the regular surface (B). Electrodes with de-lamination had to be discarded as the delamination would lead to reduced conductivity and large uncertainties in any data obtained.
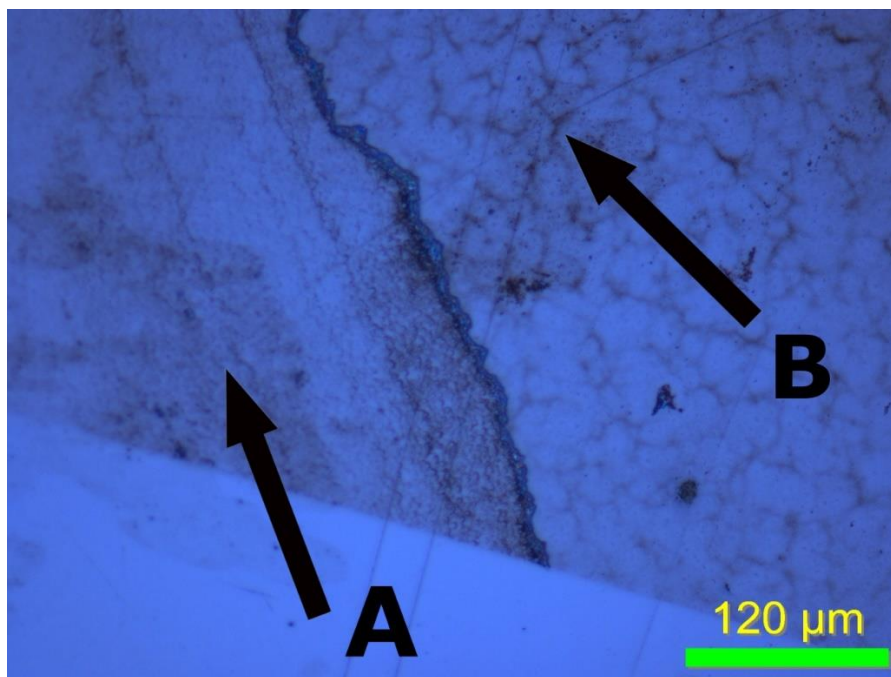
Figure 2.4 – Microscope image at 20× magnification of fulleropyrrolidine-bipyridine platinum chloride spin coated and lithographed electrode, highlighting where the treated area has delaminated area (A) and is unaffected surface (B)

Once the electrodes had been inspected with microscopy, deemed undamaged and the surface areas calculated they were then subjected to electrochemical testing.

Proton reduction as a test case

Cyclic voltammetry was used to investigate the modified electrodes response in 5 mM of perchloric acid, 0.095 M sodium perchlorate solution. The set-up was chosen as it allows specifically for the reduction of protons to be used as a test reaction. The large difference in onset potential between glassy carbon and platinum surfaces for the reaction allows for an assessment of any modification towards the behaviour of a platinum surface. Additionally, the reaction in perchloric acid is often used as a test of electrochemical surface area (ECSA) for fuel cell catalysts.

The original C$_{60}$-bipy complex modified electrodes were difficult to fully characterise due to the fragility of the modified layer. Additionally, the layers required repeated cycles to 'clean' the electrochemical response, shown in Figure 2.5.
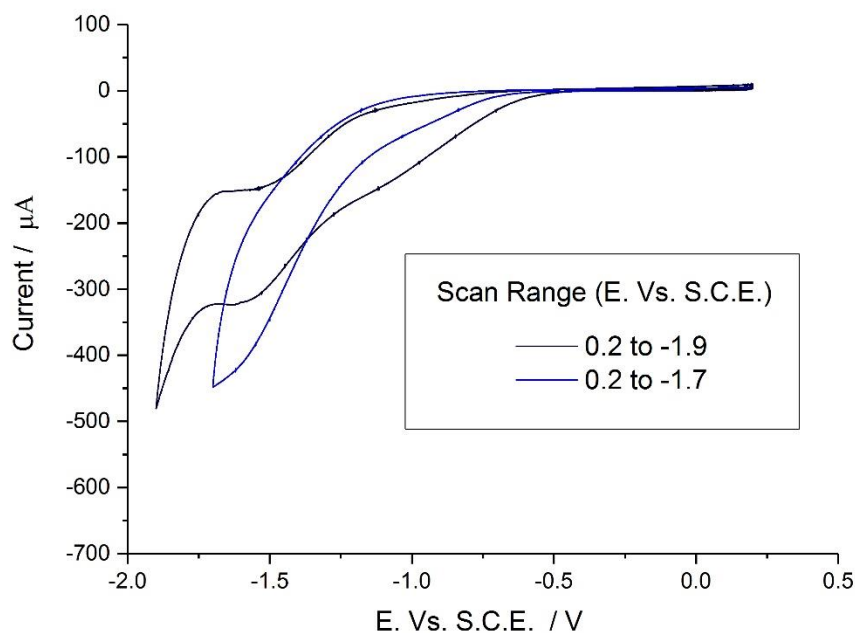
Figure 2.5 - Cyclic voltammograms at a scan rate of 100 mV.s^{-1} of a fulleropyrolidine bipyridine complex modified 3mm GC electrode in an aqueous solution of 5 mM perchloric acid and 95 mM sodium perchlorate.

It was necessary to repeatedly scan the electrode surface so that the excitation potential ventured just into the solvent breakdown region. When this was completed, a small wave could be seen pre-solvent breakdown. However, this activity was short lived with repeated scanning as shown in Figure 2.6.
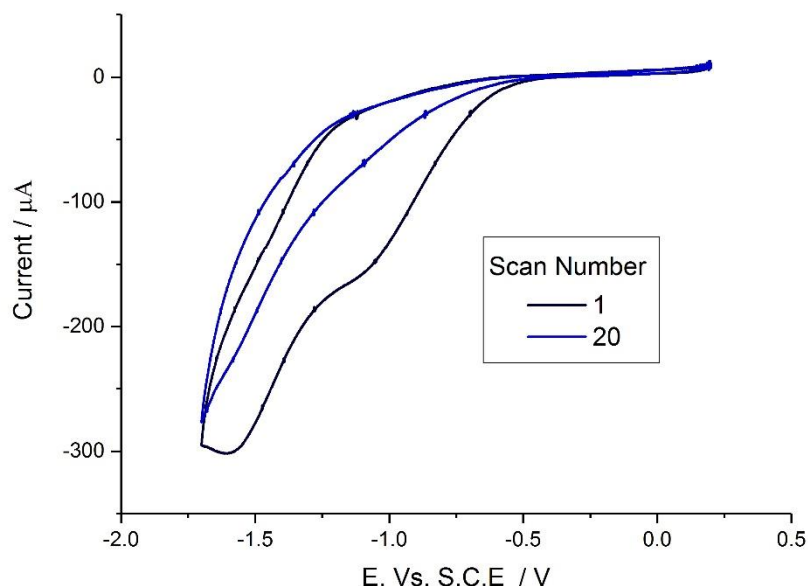
Figure 2.6 – The 1st and 20th scan when repeatedly recording cyclic voltammetry at 100 mV.s^{-1} of a fulleropyrolidine bipyridine complex modified 3mm GC electrode in an aqueous solution of 5 mM perchloric acid and 95 mM sodium perchlorate

The original signal quickly disappeared on repeated scanning and led to an inability to fully characterise the compound. This fast degradation was also observed for electrodes modified with the lithographed sample of the non-platinum containing compound shown in Figure 2.7.

Figure 2.7 also shows that the initial wave that grows on 'cleaning' is not present in the lithographed electrode sample for the non-platinum containing compound. This is due to the lithography treatment which has been proposed to produce a glassy carbon like substance as the original full-bipy complex is broken down by the electron beam treatment. This results in the disappearance of the redox signal but as can be seen an increased current response due to the increase in surface area effect created by the modification.
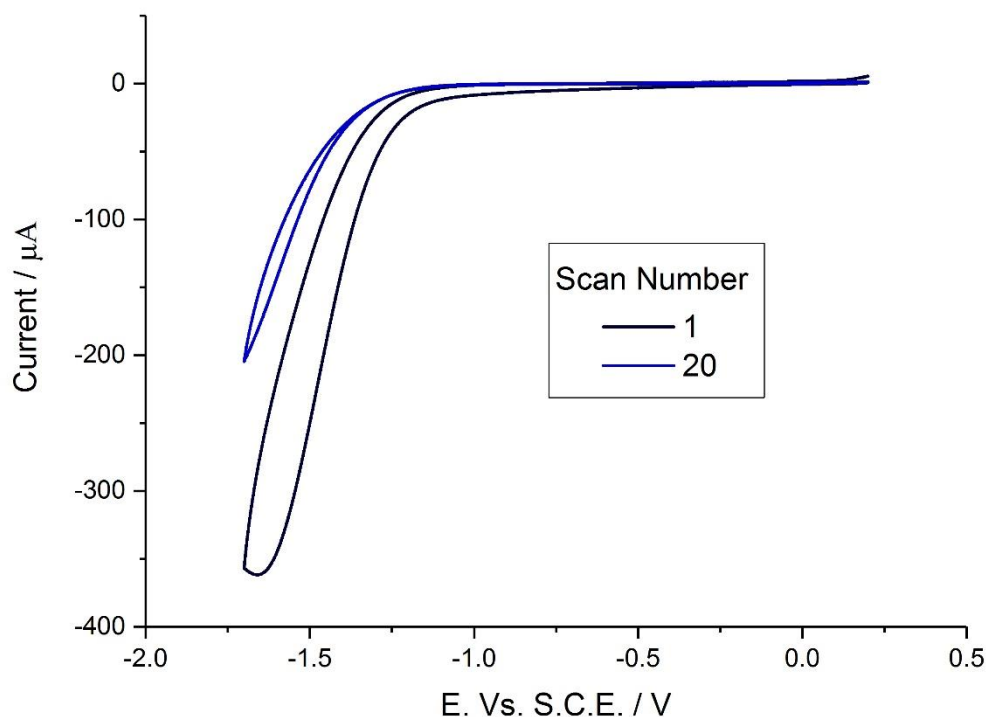
Figure 2.7 - The 1ˢᵗ and 20ᵗʰ scan when repeatedly recording cyclic voltammetry at 100 mV.s⁻¹ of a fulleropyrolidine bipyridine complex modified 3mm GC electrode which has then been subjected to e-beam treatment in an aqueous solution of 5 mM perchloric acid and 95 mM sodium perchlorate

After assessing the non-platinum compound the fulleropyrrolidine bipyridine platinum chloride was tested. The drop cast sample was tested without e-beam treatment and it was observed to be more fragile than the equivalent non-platinum containing electrode although it produced a small forward wave that disappeared after initial scans. However, after lithography treatment the electrodes exhibited markedly different character, although still required initial 'cleaning', as shown in Figure 2.8
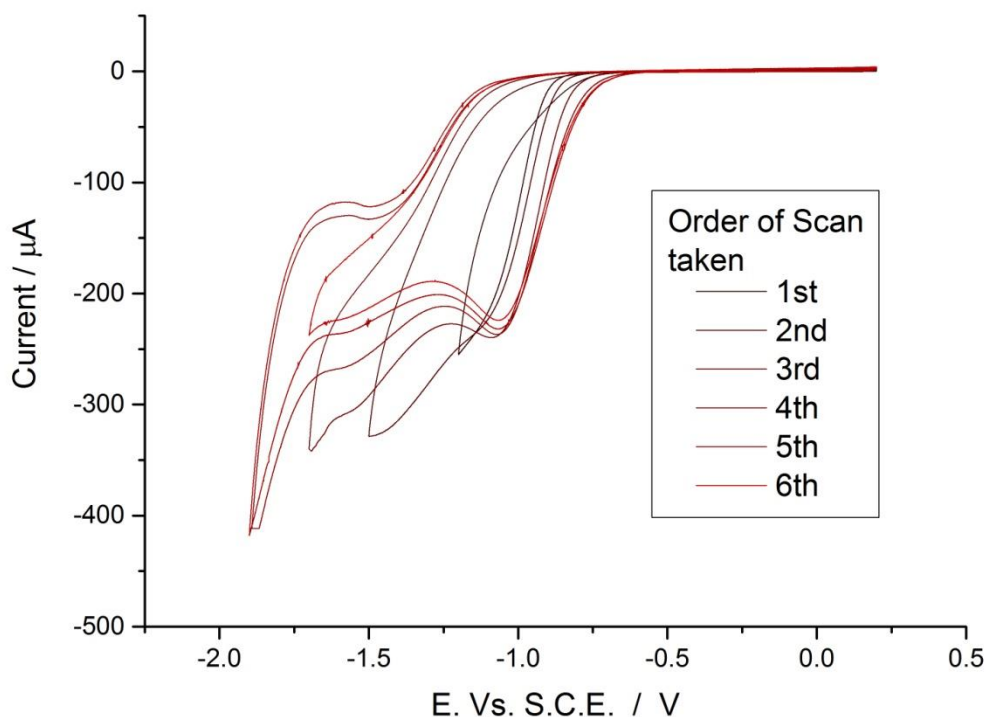
Figure 2.8 - Cyclic voltammetry at 100mV/s⁻¹ with an expanding potential window for a fulleropyrrolidine bipyrridine platinum chloride modified 3mm GC electrode with additional e-beam lithography treatment in an aqueous solution of 5 mM perchloric acid and 95 mM sodium perchlorate

Figure 2.8 shows the results of expanding the potential window used for the cyclic voltammetry. It shows the emergence of what is thought to be the peak relating to proton reduction as cycles are repeated. Subsequently this peak was investigated using multiple scan rates across the range showing the peak, 0.2 to -1.7V. This was to ascertain the type of reaction taking place and whether repeated scanning across this window would 'clean' the surface further or cause a loss of activity.
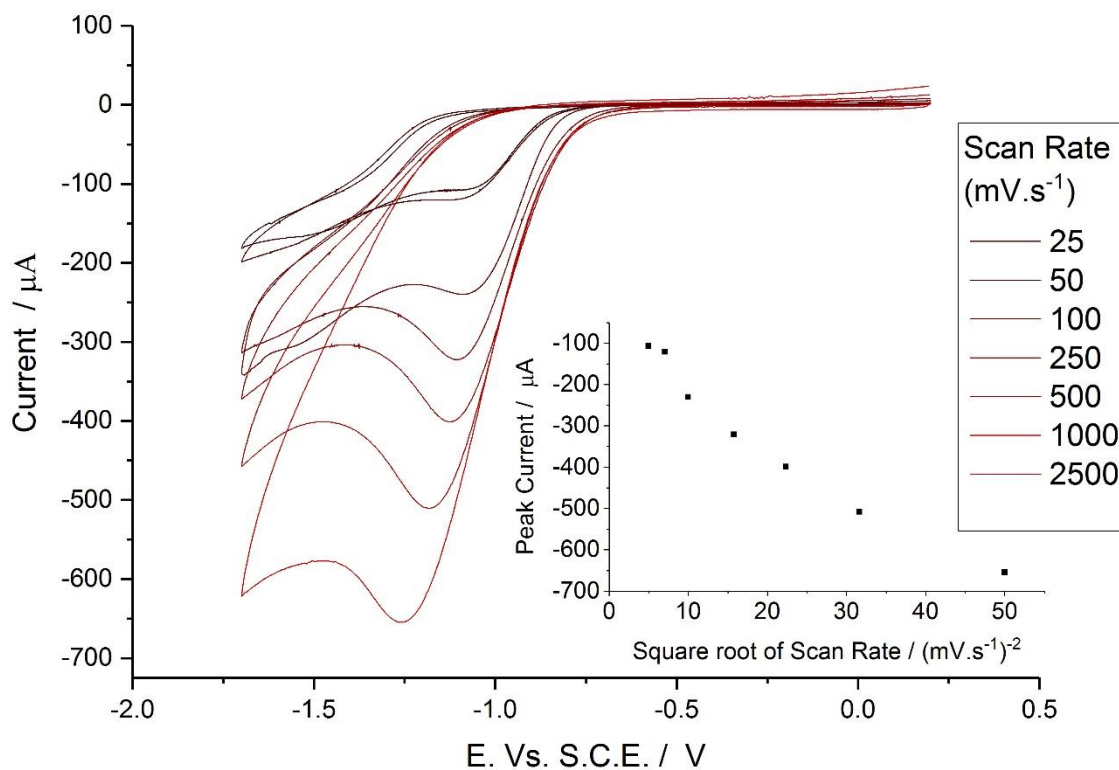
Figure 2.9 - Scan rate analysis of a fulleropyrrolidine bipyrridine platinum chloride modified 3mm GC electrode with additional e-beam lithography treatment in an aqueous solution of 5 mM perchloric acid and 95 mM sodium perchlorate

Figure 2.9 shows the results of the variable scan rate (VSR) study, with the inset showing the relationship between the square root of scan rate and the peak current, identifying a linear relationship in accordance with a Randles-Sevcik relationship. The electrode was then repeatedly scanned between 0.2 and -1.7V at a scan rate of 100mVs^{-1}. Figure 2.10 shows the degradation of the peak current at the modified electrode surface.
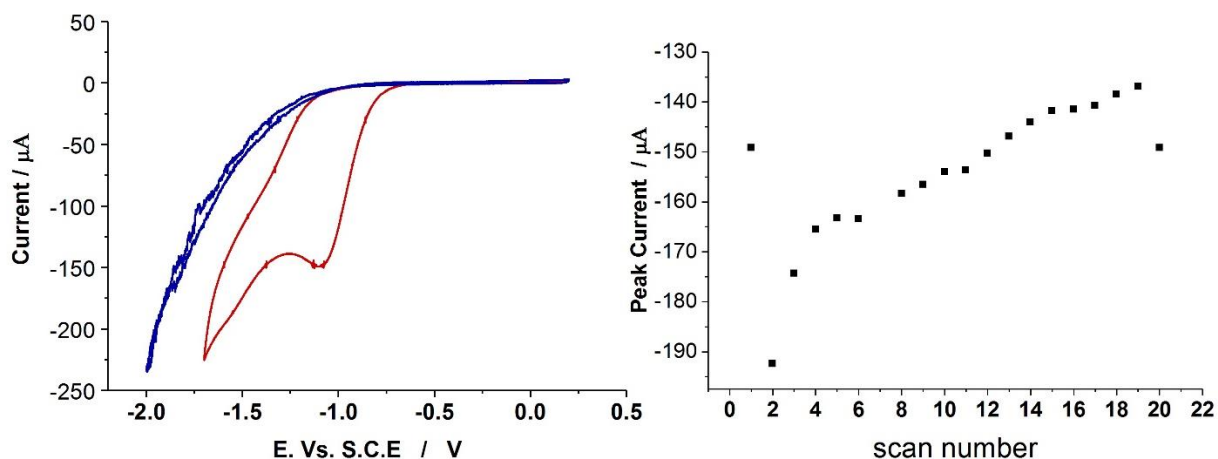
Figure 2.10 – Left, cyclic voltammetry of a fulleropyrrolidine bipyrridine platinum chloride modified 3mm GC electrode with additional e-beam lithography treatment (shown in red) and a blank 3mm GC electrode (shown in blue) in an aqueous solution of 5 mM perchloric acid and 95 mM sodium perchlorate. Right, The peak current values for the reduction seen during repeated cyclic voltammetry of a fulleropyrrolidine bipyrridine platinum chloride modified 3mm GC electrode with additional e-beam lithography treatment in an aqueous solution of 5 mM perchloric acid and 95 mM sodium perchlorate.

This reduction in peak current is a sign that either material is releasing form the surface of the electrode or that the surface is reducing in activity. It is proposed that the reduction is a result of material being disturbed by the formation of microscopic bubbles of hydrogen forming on the surface at the extreme limits of the scan range approaching solvent breakdown.

Taking this data and adjusting it for the surface area, with the measurements obtained from the microscope investigations, enables a direct comparison between the modified electrodes, a blank GC sample and a bulk platinum electrode, as shown in Figure 2.11.
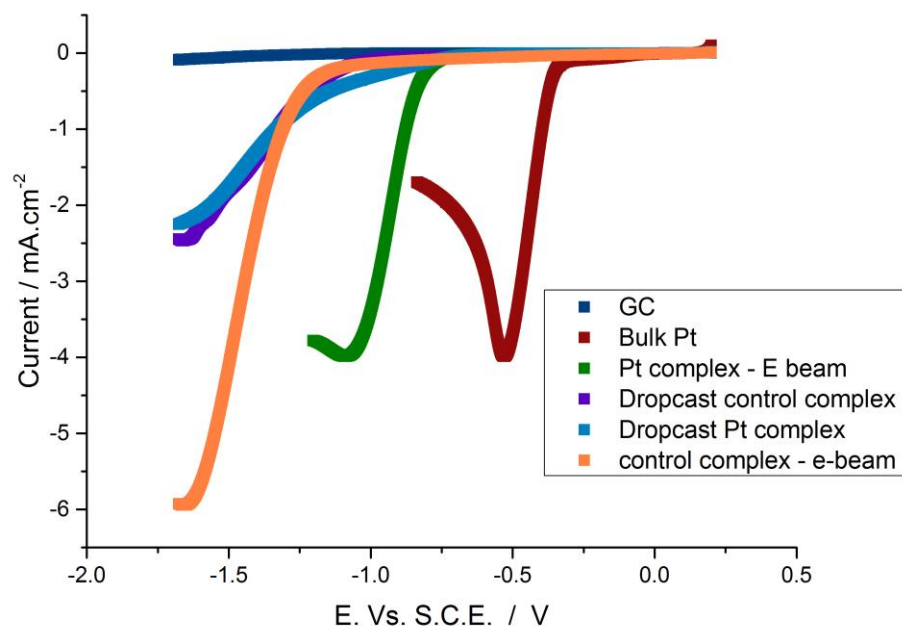
Figure 2.11 - Linear scan voltammetry showing proton reduction across the modified, blank and bulk Pt electrodes at 100mV.s^{-1} in an aqueous solution of 5 mM perchloric acid and 95 mM sodium perchlorate

The figure shows that although the lithography treated fulleropyrrolidine bipyridine platinum chloride (ful-bipy-pt) complex is a significant improvement towards normal platinum behaviour it doesn't match the response of bulk platinum. Table 2-1 shows the collected onset values (obtained from plotting pseudo tafel plots).

electrode base	modification	proton reduction onset value (E. Vs. S.C.e
GC	none	-1.11
GC	E-beamed control complex	-1.13
GC	dropcast control complex	-0.994
GC	E-beamed Pt complex	-0.8
GC	dropcast Pt complex	-0.748
Pt	Bulk Pt	-0.38

Table 2-1 Onset potentials for proton reduction across the modified electrodes. Potentials recorded in an aqueous solution of 5 mM perchloric acid and 95 mM sodium perchlorate, with 3mm electrodes of stated modificiation.

The table highlights the similarity of onset between the ful-bipy-Pt complex with and without lithography treatment. It shows that the Pt complex does exhibit some extra redox characteristic over the non-Pt complex and GC but that due to the modification technique it cannot be observed. Interestingly, the current peak values for the bulk platinum and for the lithographed ful-bipy-Pt electrodes give a diffusion coefficient of 7.7×10^{-5} cm^2.s^{-1} and 7.5×10^{-5} cm^2.s^{-1} respectively. These values are close to literature values for the diffusion coefficients of protons an example being 9.31×10^{-5} cm^2.s^{-1} by Cussler.[254] This would be suggestive that although the modification on the surface has a lower onset value for proton reduction, the surface is acting as a bulk surface rather than a reduced surface area. This may be caused by a random and unconnected succession of individual Pt atoms.

2.1.4 Conclusions on the potential for reducing platinum content through spatially resolved platinum placement

The work into the ful-bipy complexes has shown that by incorporating platinum into the complex the onset potential for the reduction of protons can be shifted positive on modified electrodes. The work has shown that that further modifying the electrode through lithography maintains this positive shift in onset potential but also creates an electrode surface that is more durable and tends towards a stable surface.

It has also been shown that this modification acts as a bulk surface, but that the electrode potential is still much more negative than for bulk platinum. However, it is important to remember that these layers are only 14% Pt by mass or 0.8 % by number of atoms (based on work awaiting publication from Dr Alex Robinson).

Following this initial screening study, the work is to be reported in a paper which is currently in draft and the electrode surfaces produced via this method were deemed appropriate for further study. The work has been continued by a colleague. This project therefore continued with its primary aim of developing novel chemical routes for the removal of platinum from hydrogen fuelled proton exchange membrane fuel cells.

2.2 Recycling platinum through biohydrometallurgy

The previous section discussed the possibility of reducing the PGM content within PEMFCs and the use of designed surfaces to achieve this goal. This section discusses recycling PGM resources, through the incorporation of biohydrometallurgy, and investigations into the materials produced as potential electrocatalysts.

2.2.1 Introduction

The first example of biohydrometallurgy is debated, some cite the discovery of iron-oxidising acidophilic archea in 1965,[255] however, some cite the Kennecott Copper Corporation demonstrations of bioleaching in the 1950s.[256] Many argue that biohydrometallurgy is environmentally advantageous and could lead to low-grade ores becoming economical.[257] Thereby reducing demand for primary ores, energy and waste disposal sites.[258] However, the price competitiveness compared to pyrometallurgy is often debated due to the power requirement and reactor design.[259]

Metals are involved in many of the natural processes within the natural environment and those of microbes in particular. Their role as indirect and direct electron donors and acceptors for energy conservation within microbial metabolism leads to the possibility of exploiting them in many processes.[260]

Two methods of utilisation would be those of biosorption[261] and biomineralisation[146] at the surface of and within microbes. One of the main issues when dealing with PGM sources is the low-abundance. Microbes have been shown to be able to overcome this through binding the metals to the surface of both active and dead biomass, producing a biomass with a much higher metal concentration than the solution.[262] Many strains of bacteria have been shown to exhibit this ability,[263,264] *Desulfovibrio vilgaris, Desulfovibiro fructosivorans* and *Desulfovibrio desulfuricans,* for example.[265] *Desulfovibrio desulfuricans* in particular was shown in 1998 to reduce Pd(NH$_3$)$_4$Cl to form 50 nm particles of Pd^0 on its surface.[266]

Additionally, in 2003 it was shown that by using a electrobioreactor, Pd, Pt and Rh could be recovered from automotive catalyst waste.[267] Subsequently it was shown that by bubbling hydrogen through the solution, acting as a reducing agent the same process occurred with waste circuit board leachates without the need for an applied potential.[268] With Lengke *et al.*[269] showing the formation of Pt nanoparticles.

The mechanisms involved are still not fully understood, but it has been reported that the reduction of Pt^{IV} to Pt^0 proceeds through two different hydrogenase enzymes. It is thought that the octahedral Pt^{IV} is too sterically hindered for direct bonding to the enzyme or to pass through the cell membrane. It is at first reduced to Pt^{II} at a cytoplasmic oxygen-sensitive hydrogenase and then secondly a periplasmic hydrogenase to Pt^0. This allows the formation the deposits within the periplasmic space of the bacteria.[270] With a similar two or three hydrogenase enzyme model proposed for palladium deposit formation.[147]

PGM bio-catalysts

The use of this biomass material has been tested in several scenarios[263], such as the hydrogenations of 2-pentyne[271] and 2-butyne-1,4-diol.[272,273] Additionally Bio-films that incorporate this technique to produce a self-assembled catalytic layer have been shown by this group (working with Professor Lynne Macaskie, School of Biosciences, UoB)[274] to be active catalytically for the hydrogenation of dimethyl itaconate (work currently awaiting publication). If the material is pyrolysed a carbon based powder is formed containing PGM particles and this material has been used in preliminary studies as Bio-Pd fuel cell anode catalysts.[151,152,275] Alternatively the biomass-supported Pd has been mixed with carbon to produced catalyst layers in preliminary fuel cells studies[155]. Additionally, palladium nanoparticles have been shown to increase electron transfer across cell membranes electrochemically.[276]

With these demonstrations in mind the aim of this project was to investigate whether multiple microbial species and differing reducing agents could form PGM deposits from synthesized leachates. Whether the type of microbe and reducing agent used influenced the particle structures and whether without further pre-treatment this material exhibits any electrochemical behaviour.

2.2.2 Experimental

This section describes the techniques used to complete this study, exploring the methods used to culture the bacterial strains. The focus is on the bio-mineralization process and the effects various reducing agents and palladium precursor salts have on the process. The assessment of the process is completed through centrifugation and assays, to estimate the extent and rate of the reductive bio-

mineralization; electron microscopy to investigate the formation and characterization of the nano-particle deposits; followed by electrochemical techniques to evaluate any electro catalytic properties of the material produced. This part of the project was completed as a collaboration, with different parts experimentally carried out by others, such areas are highlighted, as they are included to allow understanding of the whole process however the author wishes to acknowledge and make clear the efforts of others within the overall project.

Bio-Pd production

The initial bio-Pd production was conducted by the functional bio-nano-material group headed by Professor Lynne Macaskie within the school of bioscience at the University of Birmingham. The author aided in all steps in the process of bio-mineralisation and growing the specific cultures, however the majority of the experimental work producing the deposits was conducted by Dr. K. Deplanche and Dr. A. Murray.

Biomass Culture

The project focused of three specific bacterial strains:

     1. E.coli MC4100

     2. M.luteus (Gram +)

     3. S.oneidensis mR1 (Gram -)

The initial cultures were grown in Luria-Bertani (LB) broth as with previously reported methods[274] (10 g.L^{-1} tryptone, 5 g.L^{-1} yeast extract, 10 g.L^{-1} NaCl) with the addition of ampicillin (100 µg.mL^{-1}).

Palladium mineralisation

A sample of cell suspension solution (25 mL) was taken and put anoxically (under oxygen free nitrogen, OFN) into 200 mL serum bottles. The synthetic leachate was added as 40 mL of degassed (OFN, 20 minutes sparging) 10mM Pd(II) with the exact salt used differing between experiments and discussed later. The concentration of the precursor salt can be altered to achieve differential loadings and the effect of precursor salt used is investigated; where this is the case it is highlighted in the results and discussion section. An example that achieves a 20 wt% loading is a solution of, 10mM sodium tetrachloropalladate, 0.01 M nitric acid in de-ionised water.

The mixed solution is left at 30^{0}C for 30 minutes with occasional shaking. The reducing agent is then introduced; either 5 mL of 50 mM formate solution (degassed, OFN, 20 minute sparging) or hydrogen gas is sparged through the solution (200 mL.min^{-1}, 20 min).

Assay assessment of biomineralisation

During the biomineralisation, the rate of reaction was measured through an assay of metal ions remaining in the residual solution. A spectrophotometry technique first described by Charlot[277] was used. Samples (1mL) were taken from the reaction mixture at predetermined times, and centrifuged (4 min, 12000 g, IEC bench centrifuge) to separate the biomass from the solution. 200 µl of sample was added to 800 µl of SnCl$_2$ solution in a plastic cuvette. The SnCl$_2$ solution was prepared through

dissolving 29.9g of $SnCl_2$ into 500 mL of concentrated HCl. The solution is incubated for 1 hour at 30^0C and the absorbance at 463nM compared against calibration curves of un-biomineralised samples. This method has previously been validated at a commercial laboratory (H2B, Capenhurst U.K.).

Electron microscopy

The imaging work conducted with the electron microscopes was completed within the centre for electron microscopy at the University of Birmingham. Sample preparation was conducted by the author, Dr K. Deplanche and Mrs Theresa Morris. Images were taken by the author and Dr K. Deplanche with all analysis completed by the author.

Several different electron microscopy techniques were used during the project. Standard Scanning Electron Microscopy (SEM) techniques are not applicable to these samples due to the inherent nature of bacterial samples. Trapped water and air within bacterial structure mean that during the ultra-low vacuum used for standard SEM these structures can 'erupt.' Therefore, the samples need to be investigated using environmental scanning electron microscopy (ESEM) (both backscattered and transmission as well as in-situ EDS spectroscopy). This technique allows for a minimal vacuum to be used, but can lead to a lower resolution. The use of Transmission electron miscroscopy (TEM) techniques, such as Scanning Transmission Electron Microscopy (STEM), is relatively unaffected due to the preparation of samples (explained below) needed for this technique.

Samples for ESEM were prepared relatively easily, bio-mineralised samples were removed, centrifuged and then dried. Samples of bio-mineralised biomass were taken as powder and

sprinkled onto carbon tape dots. Excess materials were knocked from the dot and collected along with any excess material from the sprinkling and kept for future studies. The modified dots were then mounted onto a standard SEM stub. These samples can be used within the SEM directly to obtain images and for EDS analysis. However, at times charging can occur at the surface due to the disperse nature of the biomass leading to poor conduction within the sample. This can lead to overexposure damage from the beam and images which are hard to interpret. For easier imaging carbon coating or gold coating can be used; this reduces charging effects on the surface but can make EDS analysis less reliable.

Preparation of Samples for STEM and TEM analysis was performed by the technical staff within the Electron Microscopy centre within the School for Materials and Metallurgy at the University of Birmingham. The samples are taken and embedded in resin allowing for ultra-thin sections to be taken using the same technique previously reported.[274]

The samples were examined using the Jeol JSM-7000f FE-SEM with Oxford Inca EDS, wave WDS and crystal EBSD; a Philips Tecnai with STEM, GAtan EELS and Oxford Isis EDS and a Jeol 1200EX with SEM and STEM.

Electrochemistry

To assess whether the biomineralised biomass had any electro catalytic activity electrochemical techniques were used to assess the samples. The most important part of this process is the production of electrodes for assessment and adequate layers allowing for characterization.

Electrode preparation

Electrode samples for assessment were produced by taking a polished glassy carbon electrode tip. The electrode tip was polished as has been described in previous section (2.1.2). In this example a 3mm (EDI101, Radiometer analytical, Salford) and a 5mm (afe2m050gc, Pine research instrumentation, Durham) GC electrode were used. Powders of biomineralised biomass (as described above) are taken and suspended in either water or IPA by sonication. The concentration (by weight %) was altered per experiment. In some samples (mentioned when used in the results and discussion section) 10 wt% Nafion® was added to the solution, this improves the durability of the electrode layer formed. 20 µl (5mm) or 10 µl (3mm) of this solution was taken and added as a droplet to the electrode surface. The electrodes were put under cover and left to dry for 24 hrs.

Electrochemical cell set-up

The set-up used in the analysis was a standard three-electrode electrochemical cell, with a surrounding water jacket kept at 25^0C. A normal hydrogen electrode (NHE) was used as a reference electrode and a platinum gauze (9 cm^2) was used as a counter electrode; the working electrode was prepared as above. The electrodes were connected to a Autolab (PGstat302N, Metrohm USA inc) potentiostat/galvanostat with the working electrode either connecting through a Pine modulated speed rotator (AFMSRCE, Pine Research Instrumentation, 5mm) or a EDI101 rotating disc electrode (Radiometer Analytical, 3mm). The electrolyte in all experiments was 75 mL of 0.1 M perchloric acid in de-ionised water.

Data recording

The electrodes were immersed in the Cell and the working electrode was 'cycled' to clean the surface; this technique is discussed below in the results and discussion section. The cycling involved exhibiting a voltage between 0-1.1 V Vs. NHE for 50 cycles at a scan rate of 0.1 v.s^{-1}. Different scan regions are used in the experiments with the 'standard' analysis scan range being between 0-1.1 V vs. NHE at various scan rates (0.1, 0.5, 0.05, 0.025 v.s^{-1}).

2.2.3 Results and discussion

This section discusses the results obtained investigating the effect of changing the microbe species, the reducing agent and the precursor salt (synthetic leachate) on the biomineralisation process, the particles formed and the electrochemical behaviour observed. The biomineralisation process is followed through a monitoring assay, electron microscopy is used to investigate the particle formation and the electrochemical behaviour is assessed with the use of cyclic voltammetry.

Reduction assay

The process of biomineralisation was completed in conjugation with Dr Kevin Deplanche from the functional bio-nanomaterials group at the University of Birmingham. The vast majority of the work producing the bio-cultures and the actual biomineralisation process was conducted by Dr Deplanche. As such the work is not presented in full within this thesis. It is important to mention the findings of the biomineralisation monitoring as it impacts on the conclusions drawn from the electron microscope imagery and the electrochemical analysis. It is important to note that although the author aided in the biomineralisation process and in the monitoring of its progression through

a UV/Vis assay, it is not claimed to be solely the authors work. All data associated with the biomineralisation and assays is shown in the appendix (10.2.1).

It was observed that the samples with hydrogen as a reducing agent showed complete biomineralisation after five minutes, whereas the samples with formate had a slower reaction rate showing completion after ten minutes. The trend was shown across all bacterial strains.

The strain of bacteria also affected the biomineralisation process with the difference in gram-strain defining the difference. E.coli and S.oneidensis strains completed biomineralisation within five minutes (with hydrogen as a reducing agent) whereas M.luteus showed a slower rate, with completion after ten minutes. This is assumed to be associated with the lack of a well-defined outer membrane in the M.luteus microbe, which leads to a slower diffusion to the active enzyme sites.

The same trends across reducing agent and microbe strain were seen when using both precursers Na_2PdCl_4 and $PdCl_2$. There was a slight difference between the two precursor salts with $PdCl_2$ showing a slower rate of biomineralisation.

These results indicate that there are differences across the microbe strains and the reducing agent but that the precursor salt used may not affect the process of biomineralisation.

Electron Microscopy

One of the key aspects of the project was to assess how the particles produced differed according to the microbe strains, the reducing agents and the precursor salts used. To assess particles formation, the samples were taken and examined with electron microscopy, using ESEM, STEM and TEM microscopes to produce images to compare. The images presented were taken in conjunction with Dr K. Deplanche (University of Birmingham) with the help of the technical staff at the centre for electron microscopy, in particular Mrs Teresa Morris.

E.coli – H_2 – $PdCl_2$

Figure 2.12 shows TEM images gathered on samples of the E.coli strain that used hydrogen as the reducing agent and $PdCl_2$ as the synthetic precursor. It highlights how large aggregations of particles are formed on both the inner and outer membrane as well as within the periplasmic space. The image on the left of the figure shows that not only do particles form on the cell walls but also within the bacterial structure. However, no large aggregates are formed within the cell and the particles observed are between 10-15 nm in diameter. Similar to particles in previous studies.[263,278,279]

It is thought that as the hydrogen gas is bubbled through the solution the bacteria interact with both dissolved hydrogen and the bubbles that are trapped as they cross the bacteria's surfaces. These bubbles cannot penetrate the cell walls and so large agglomerates tend to form on the outer surfaces.
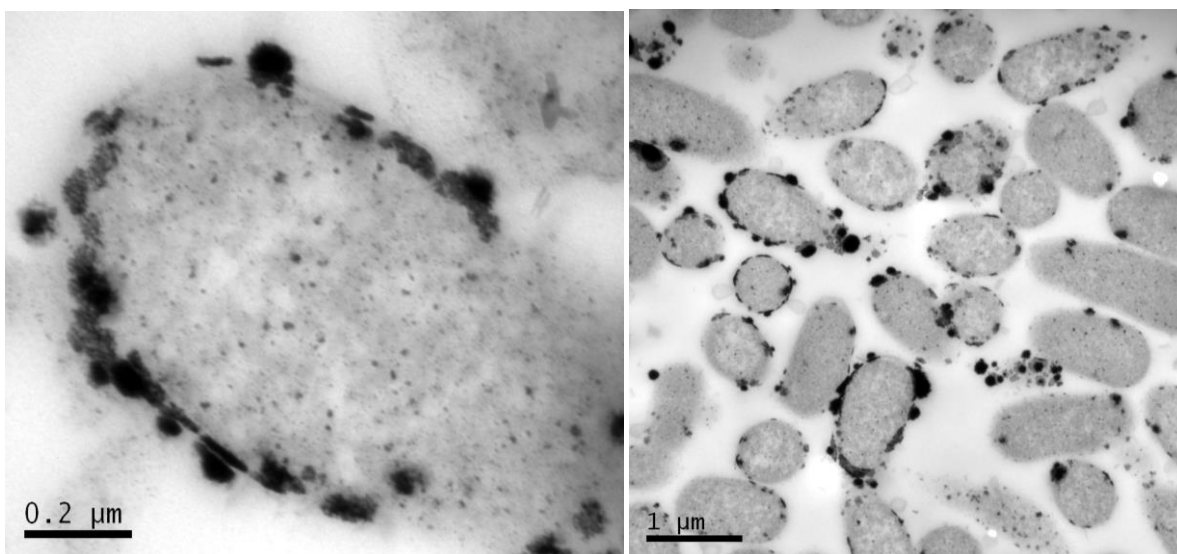
Figure 2.12 - TEM images of Pd deposits on E.coli bacteria using hydrogen as a reducing agent and PdCl₂ as a precursor salt. Image partly published by Courtney *et al*.[280] and reused through a creative commons license

E.coli – formate- PdCl₂

Figure 2.13 shows the images obtained of E.coli bacteria using formate as the reducing agent and PdCl₂ as the precursor salt. It can be seen that the particles produced are vastly different from the sample using hydrogen as the reducing agent with much smaller particles formed although some aggregates still exist.

The particles are in the 10-15 nm diameter range and the images show that although there is a thorough distribution throughout the cells, although there appears a preference to particle formation on the cell membranes. It is hypothesized that this is caused by the difference in the interaction between the reducing agent and the bacteria, with an even distribution throughout the solution rather than the chaotic situation caused by bubbles of hydrogen. These particles are similar in size and distribution to previous studies using PdCl₂ as the palladium source, formate as the reducing agent and S.Oneidensis bacteria.[155]

95
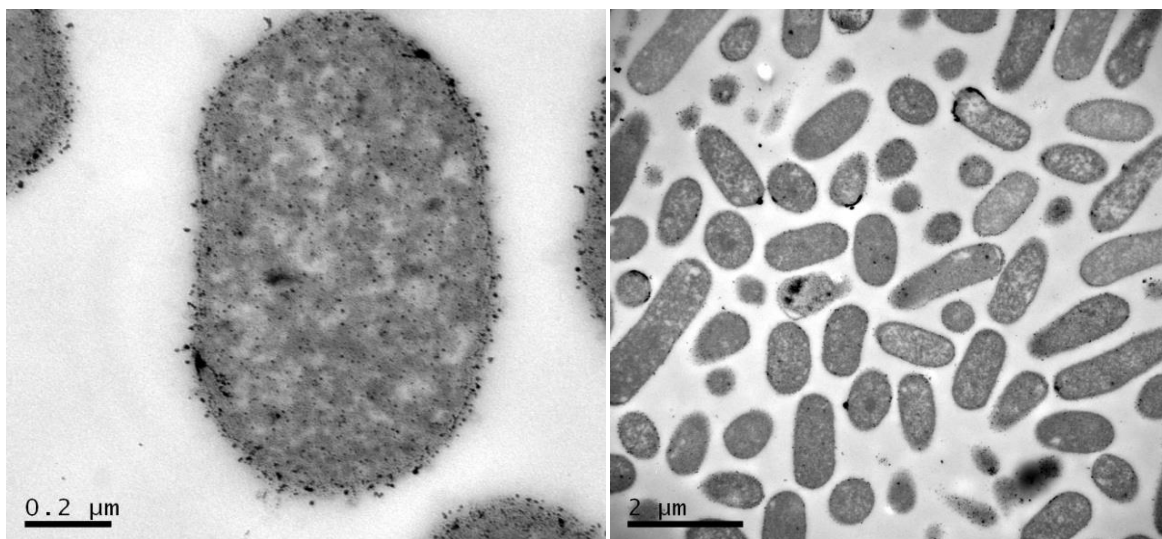
Figure 2.13 - TEM image showing Pd deposits on E.Coli bacteria when using formate as the reducing and PdCl$_2$ as the precursor salt.

E.coli – formate – Na$_2$PdCl$_2$

Figure 2.14 shows TEM images obtained of E.coli bacteria biomineralised using formate as the reducing agent and Na$_2$PdCl$_2$ as the synthetic leachate. The images show that the formation of particles is very similar to the particle formation of the sample using the PdCl$_2$ precursor but that there is arguably a slight preference for the formation of particles on the cell walls and within the periplasmic space.

The size of the particles is again in the 10-15 nm range and there are some observable larger aggregates with particles formed within the periplasmic space. The preference to form on the outer cell wall and the periplasmic space may be due to the larger the precursor species inhibiting diffusion. However, no observable difference in reaction rate was seen in comparison to the previous experiments, something which one would expect if this was caused by natural diffusion processes. This suggests a slight blocking of the reagent by the inner cell membrane
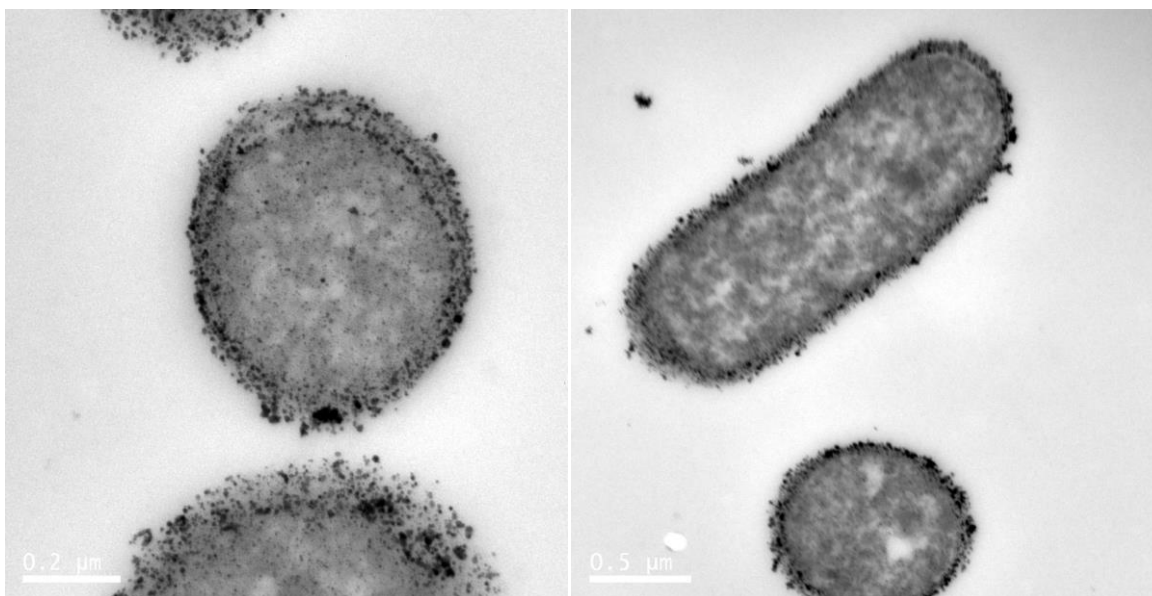
Figure 2.14 - TEM image of biomineralised E.coli when using formate as a reducing agents and Na_2PdCl_2 as the precursor salt. Image partly published by Courtney *et al.*[280] and reused through a creative commons license

M.luteus – hydrogen – $PdCl_2$

Figure 2.15 shows the images obtained from the M.luteus samples with hydrogen as a reducing agents and $PdCl_2$ as the precursor salt. The image shows how different the M.luteus samples are from the E.coli and the unshown S.oneidensis samples. Highlighting the effect that the lack of a defined outer cell wall has on the particle formation, as with previous studies[281]. It can be seen that particles form throughout the bacterial structure with large aggregates present.

It can be seen that there is a strong preference for particles to form on the inside surface of the inner cell wall and that unlike the previous samples, the large aggregates are formed throughout the structure. Agreeing with observations in previous studies of gram positive bacteria.[281]
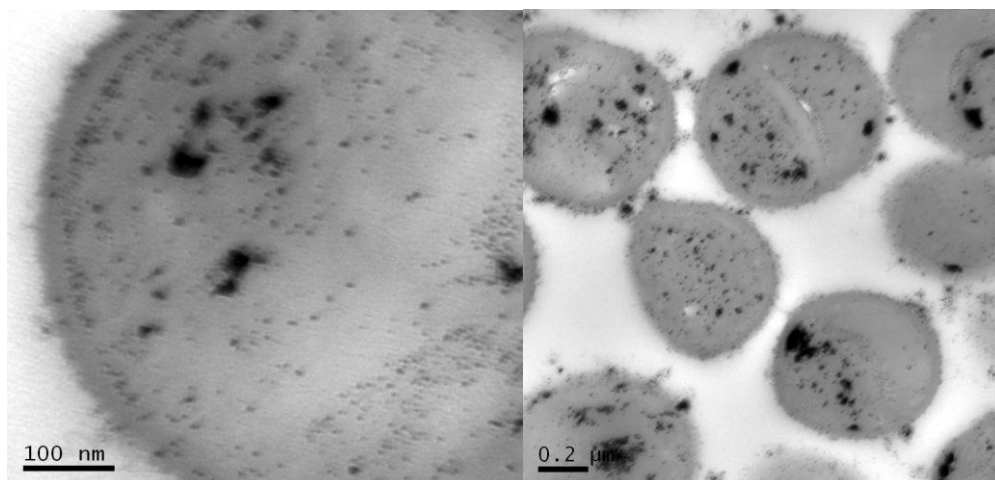
Figure 2.15 - TEM images showing Pd nano-deposit on M.luteous using hydrogen as the reducing agent and PdCl$_2$ as the palladium precursor salt

M.luteus – formate - PdCl$_2$

Figure 2.16 shows the images of M.luteus with a formate reducing agent and PdCl$_2$ precursor salt. It is observed that the particles are evenly distributed throughout the bacterial structure and as with the E.coli sample using a formate reducing agent it can be seen that no large single aggregations are formed. Unlike with the hydrogen M.luteus sample there seems to only be a slight preference for the formation of particles within the cell walls, with particles forming throughout the structure relatively evenly.
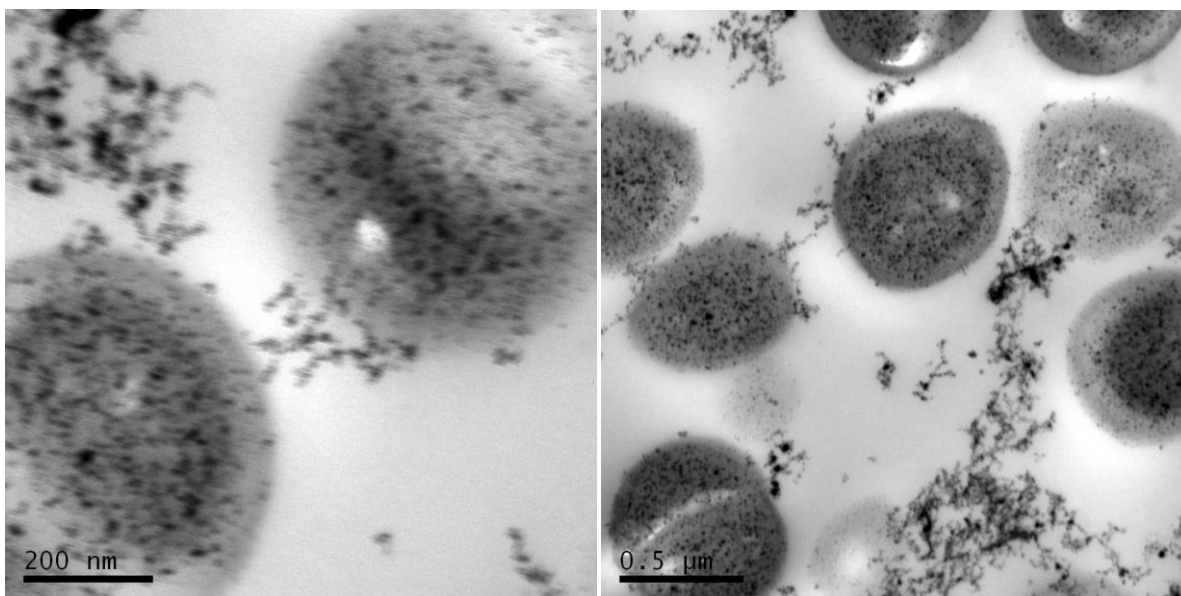
Figure 2.16 - TEM images showing nanodeposits on M.luteus bacteria using formate reducing agent and PdCl$_2$ palladium precursor

Conclusions on particle growth and formation

It has been observed that there is a clear difference between the microbial strains with the difference seemingly resulting from the structural differences between the strains. There has been a significant difference observed between the two reducing agents used.

Large aggregations are formed with the use of hydrogen gas bubbling through the solution, with a strong preference in the E.coli samples to form large aggregates on the outer surface of the bacterial structure.

Although a small difference was observed between the two synthetic leachates used, the images don't provide enough evidence to conclusively say that this difference will be seen in other

samples. The nature and the differences in the particles are predicted to have a large effect on any electrochemical behaviour.

Electrochemical results

The results from monitoring the biomineralisation process and from analysing the electron microscope images highlight that a range of bio-nanoparticles are formed. It was of interest to test whether before any further treatment were made, this material exhibits electrochemical behaviour. Previous studies have shown the material to be active following further treatment[143,148,282], either through removal of biomass via an acid treatment or through pyrolysis.

This study investigated whether any electrochemical activity was seen in 0.1M perchloric acid at the lower loadings (20 wt%) of metal and whether the different biomineralisation conditions and microbe strains, exhibited differing characteristics. Obtaining true results was difficult as simply forming electrodes from the raw material by dropcasting led to overly thick layers that were quickly removed once in solution. As such 10 % wt Nafion was added to the materials to form layers which did not delaminate from the electrode surface, as in previous studies.[283]

With these layers electrochemical responses were seen from the samples. This was encouraging as it was not previously known whether the layers would just act as insulating caps to the electrode or as a pseudo-capacitor layer with the increased surface area. This response can be seen in Figure 2.17.
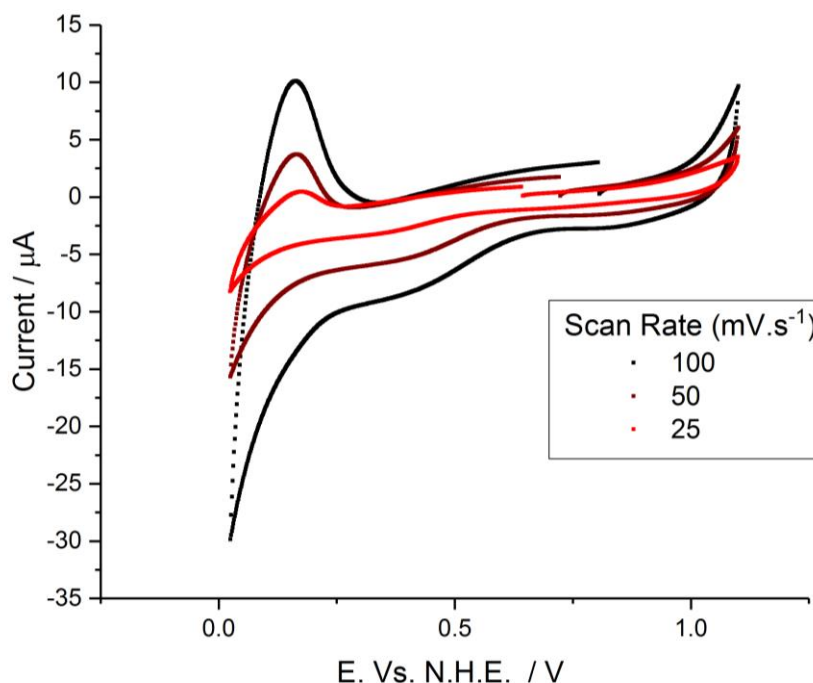
Figure 2.17 - cyclic voltammograms of a GC electrode modified with a 5 mg.cm^{-2} equivalent loading of Pd through Bio-mass material (e.coli) that was generated with a NaPdCl$_4$ synthetic leachate and formate as a reducing agent, taken in a solution of 0.1 M perchloric acid. Figure created with data published by Courtney *et al*.[280] and reused through a creative commons license

Figure 2.17 shows a typical CV under these conditions with peaks occurring at a similar potential to that of commercial Pt catalysts. However, the peaks are not well defined and the current magnitudes are very small compared with the same loadings of any commercial catalyst. The peak broadening may be due to the non-uniform nature of the particles as seen in the TEM images or alternatively may be due to the subsurface interactions that palladium particles have with protons. The relative magnitude of the current peak may be small due to much of the palladium mass being inaccessible in terms of active proton electrochemistry.

Although the particle sizes seen in the TEM were relatively small (although still larger then commercial fuel cell catalysts) a significant number of the particles were sub-surface, inside the

bacteria. However, as shown in the TEM the different reagents and microbial strains produced different particle distributions and sizes.

It was seen that the electrochemistry observed for samples differing in synthetic leachate were very similar as can be seen in Figure 2.18.
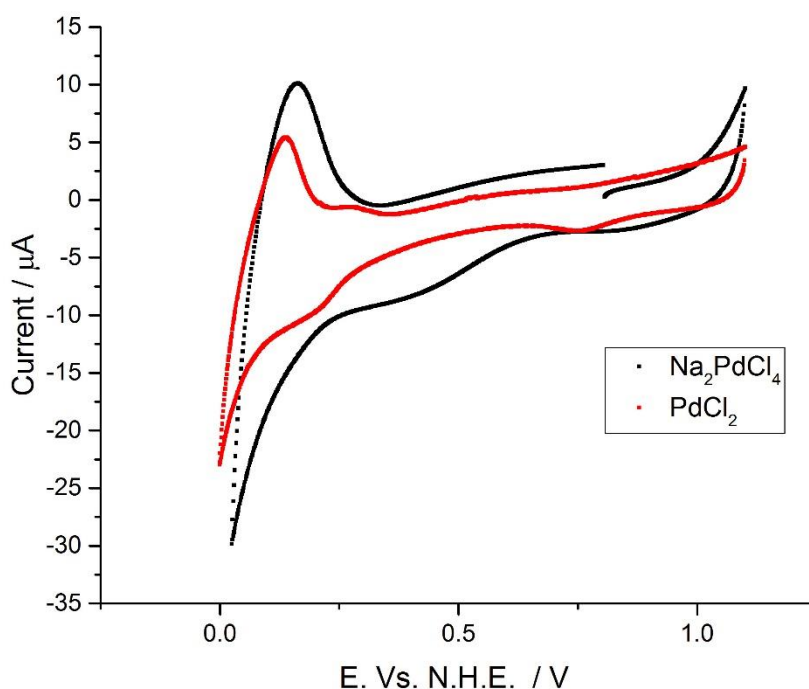
Figure 2.18 - cyclic voltammograms of two bio-Pd (e.coli) coated electrodes with an equivalent 5mg.cm^{-2} loading of Pd, one electrode using Na$_2$PdCl$_4$ and one with PdCl$_2$ as the synthetic leachate both samples using formate as the reducing agent, taken in a 0.1 M perchloric acid solution. Figure created with data published by Courtney *et al.*[280] and reused through a creative commons license

It is observed that there is a slight difference in the response, however, it must be noted that the technique used to analysis the samples, was is in its infancy and was difficult to keep consistent. There are arguments about the complete validity of the technique in the context of the amorphous non-uniform layer formation and thickness. This limits any direct conclusions that can be drawn

other than that both samples showed electrochemical responses that would be expected of a potential fuel cell catalyst.

It was interesting to see that there was also little difference between the two strains of microbes that were electrochemically tested as can be seen in Figure 2.19.
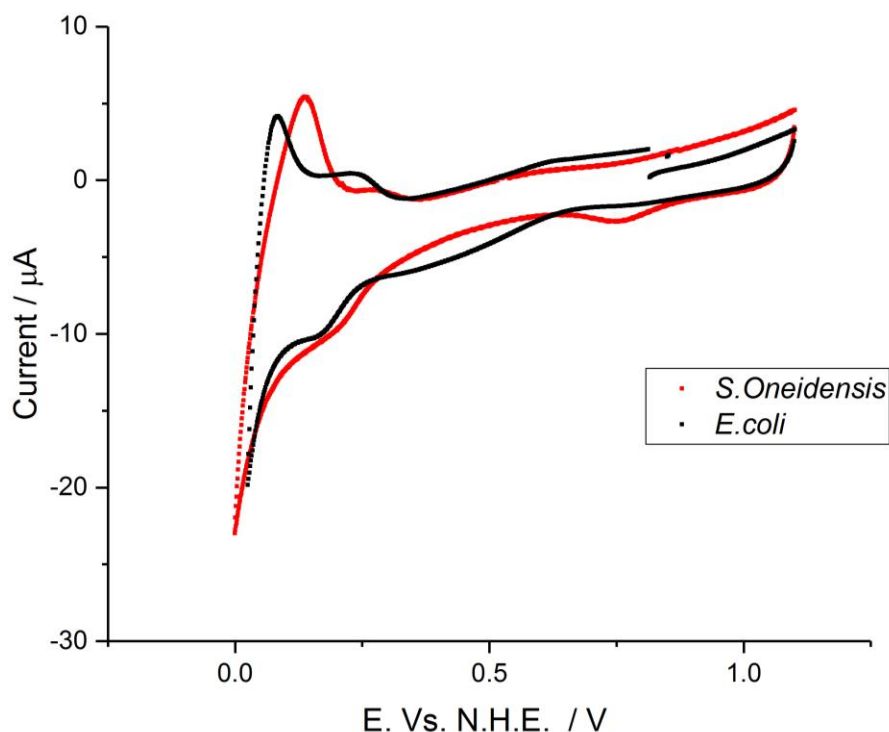
Figure 2.19 - cyclic voltammograms of electrodes coated with an equivalent 5 mg.cm^{-2} of Pd through bio-mass biomineralised with PdCl$_2$ as the synthetic leachate and formate as the reducing agent, taken in 0.1 M perchloric acid solution. The two electrodes are separated by the strain of bacteria used, one being S.oneidensis and one being E.coli. Figure created with data published by Courtney *et al.*[280] and reused through a creative commons license

It is observed that the responses of the two electrodes using two different microbe strains are remarkably similar, although slight differences can be seen in the figure. As with the change in synthetic leachate the experimental method does not allow for major conclusions to be drawn from the differences at this stage.

The main variable to cause a change in the electrochemical response was that of the reducing agent. A much more pronounced response was seen in samples using formate as the reducing agent rather than hydrogen. This is not necessarily surprising in the view of the data on the rate of biomineralisation and the images showing the particle nature.
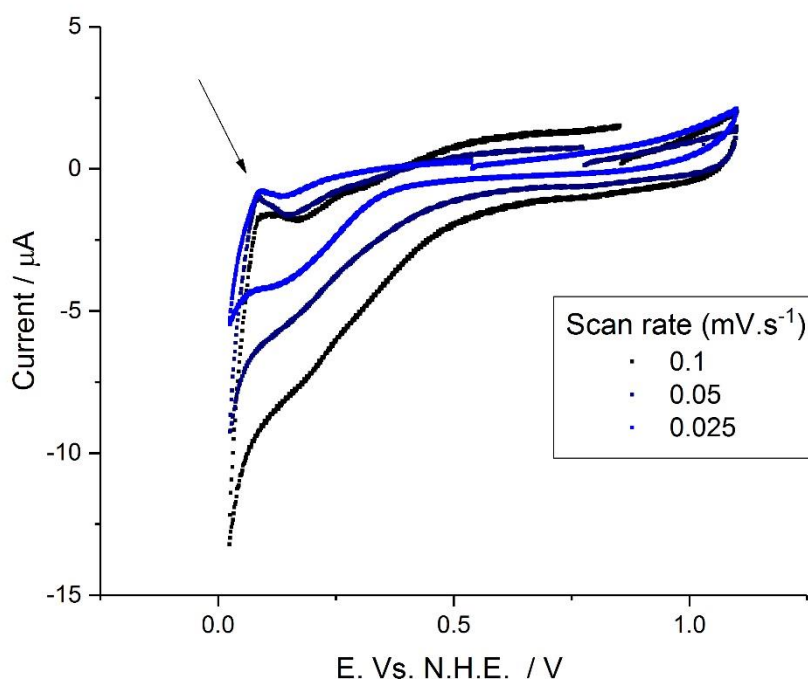
Figure 2.20 - Cyclic voltammogram of an electrode coated at an equivalent of 5mg.cm^{-2} of Pd through bio-mass biomineralised using the S.oneidensis microbe, PdCl$_2$ as the synthetic leachate and hydrogen as the reducing agent, taken on 0.1 M perchloric acid solution. igure created with data published by Courtney _et al._[280] and reused through a creative commons license

Figure 2.20 shows a typical electrochemical response for sample prepared using hydrogen gas as a reducing agent. At first glance it appears that no signal is formed. However, it can be observed that there is a wave present, but its reduction component is very broad and the oxidation (arrow in Figure 2.20) is very small.

The TEM showed that the largest difference in particles produced was between the samples using different reducing agents. This difference is confirmed in the electrochemical results. The electron micrograph showed that the particles formed with hydrogen were large and appeared at the edge of the bacterial cells, rupturing through the outer membranes. It looks as though this has had a large suppressive effect on the electrochemistry observed, whether this is due to a large subsurface interaction or whether there is less active palladium surface area available is not determinable at this stage.

Unfortunately, because palladium is the PGM being tested a formal assessment of the ECSA of the material is imprecise, as with palladium protons react both at the surface and subsurface rather than the primary surface reaction seen with platinum.

2.2.4 Conclusion

This project showed that the bacterial strain, reducing agent and the synthetic leachate used all had an effect on the biohydrometallurgical process and as such on the particles formed and the electrochemistry observed. The TEM imagery showed that there was a very large difference in the distribution and size of nanoparticles of Pd deposited when changing between bacterial strain and reducing agents used.

The largest difference in distribution of particles was caused by changing between a gram negative and a gram positive bacterial strain, agreeing with previous studies[281]. It is observed that due to the

lack of an outer membrane surface the distribution of particles within the M.luteous strain is very different from that of the S.oneidensis or E.coli strains.

The reducing agent used was shown to have a very large effect on the size of aggregates formed and on the distribution of particles across the bacterial structure. It is hypothesized that this is due to the interaction of the different reducing agents and the physical structure of the bacterial cells. For example that of the bubbles of hydrogen interacting with the cell walls of the E.coli bacteria leading to large aggregate formation.

The project showed that the distribution and size of the particles within the bacteria had a large effect on the electrochemistry and that the variables within biomineralisation had a large effect on the distribution and size of particles formed. Initial studies were started on turning qualitative data from TEM imagery into quantitative data. Image analysis of this type had begun to become available at the start of experimentation, however, with the large number of particles and large number of artefacts remaining from the bacterial cells often the automated image analysis proved inaccurate. These initial steps towards quantification and numerical relationships between nano-deposit formation and biomineralisation variables are shown in Figure 2.21 and developing this technique through programming and computer science formed a key part of the project moving forward.

The electrochemical results matched well with the TEM data showing a difference in electrochemical response with a change in reducing agent and suggesting subtle changes between the bacterial strains, E.coli and S.oneidensis. It was a significant finding that the un-treated biomass

obtained after biomineralisation showed electrochemical responses typical of palladium and of fuel cell catalysts as this had previously not been shown at the point of experimentation.

As the project had demonstrated this potential use for the biomass and the vast effect that the variables during biomineralisation had on the electrochemistry observed, a collaborative research project with Cardiff University was established. The project aimed at developing a much more consistent electrochemical test and to fully investigate the effect of biomineralisation on the electrochemical response, initially on palladium the platinum and eventually on to mixed metal alloy nano-deposits. In addition the work has now been published in biotechnology letters.[280]
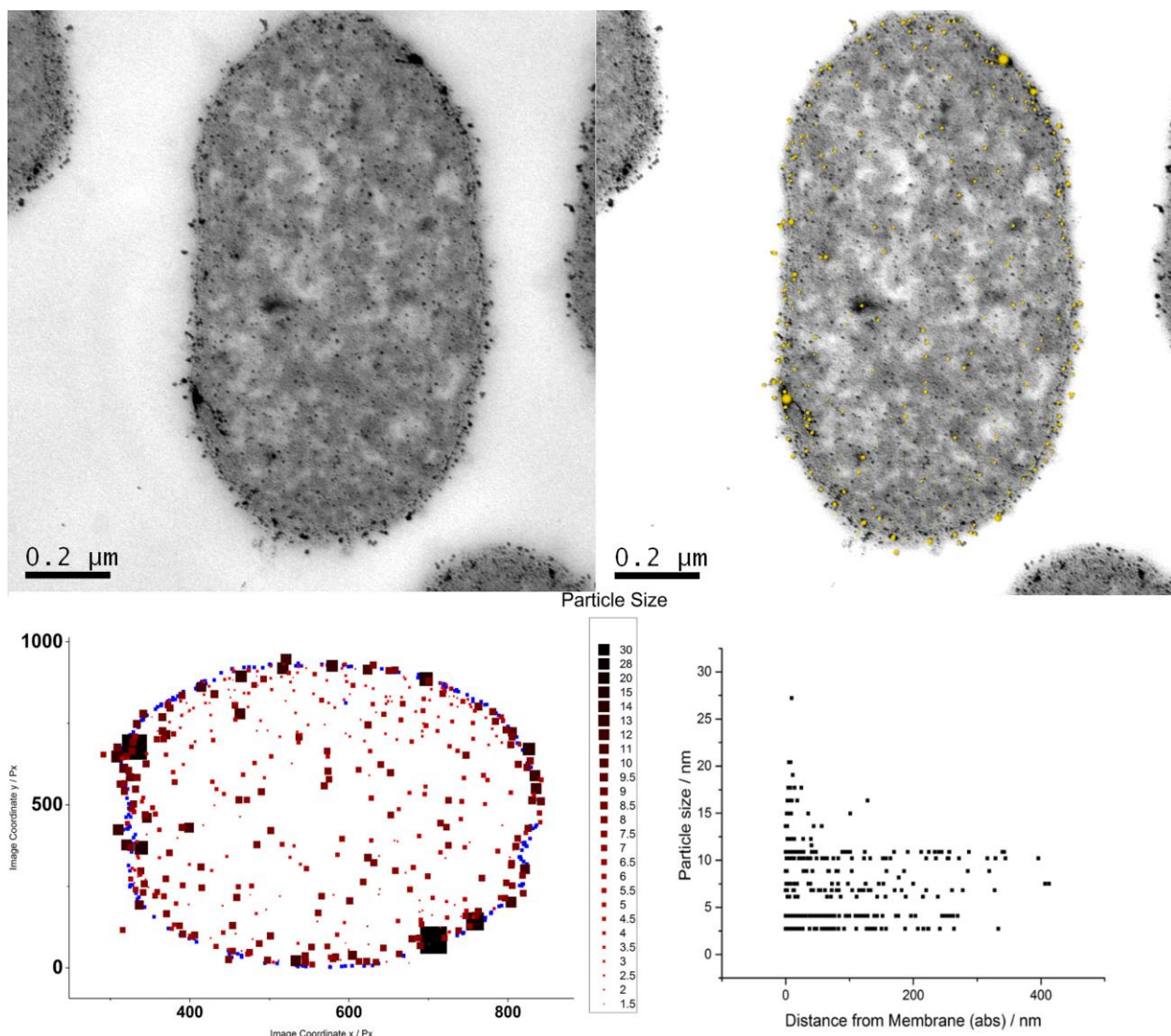
Figure 2.21 - images and graphs showing steps taken to quantify TEM data on particle position for a Biomineralised E.coli bacteria that used Hydrogen as the reducing agent and PdCl$_2$ as the synthetic precursor during biomineralisation

3. Removing platinum through alternative chemical architecture

3.1 Introduction

This chapter looks at the first steps investigating the electrochemical behaviour of adsorbed layers of phosphomolybdic acid and vanadium substituted subsidiaries. The electrochemical activity of phosphomolybdic acid (PMA) adsorbed layers has been studied and is used as a practical experiment in undergraduate laboratories.[284] The PMA adsorbed layer is used to set a precedent and to develop methodology before initial characterization of the singularly substituted vanadium phosphomolybdic acid (V1PMA).

3.1.1 Phosphomolybdic acid adsorbed layers

The adsorbed behaviour of PMA dominates much of its chemistry. It is a strongly adsorbing polyanion;[285,286] the redox behaviour of its adsorbed species; and in turn the relationship between the adsorbed and bulk species, is integral to its general electrochemical behaviour.

The multiple oxidation states of PMA species allow for its application as a catalyst in a multitude of reactions, involving both oxidations and reductions, examples are the oxidation of methanol[287] and oxidising benzene to phenol.[288] A review of these processes within organic synthesis was conducted by Heravi in 2009[289] and Zhou in 2014.[290]

The vanadium substituted species have also received a significant amount of research attention. A number of patents were filed in the 1970s with interest for their application towards the oxidation of organic compounds. Further, as discussed in chapter 1, the 90's saw a resurgence of research interest[291,292] that has increased recently with their application towards energy devices[293–296] as well as their traditional use in organic synthesis.[297]

These studies when taken together have shown an increased stability of the species with vanadium inclusion within the Keggin structure,[291] together with an increased affinity to oxygen and a widening of the redox potential window.[201,287] An increase in basicity of the compounds was also seen with increasing vanadium content.[287,291] Interestingly an enhanced regioselectivity is often observed in organic synthesis with the singularly substituted species.[297] These effects are observed both in solution and with adsorbed species.

In this chapter, initial experiments into the redox chemistry of the adsorbed polyanions is explored. It has been observed that these heteropolyanions willingly adsorb to the surface of many substrates.[298–302] Within this chapter the adsorption onto glassy carbon (GC) and edge plane pyrolytic graphite (EPPG) surfaces is used as a base example with the effect of different surfaces on this process is investigated in chapter 4. It has been shown that pH affects the equilibrium potential of observed redox phenomena.[190,303] Therefore, an in-depth differential pH analysis is performed on the analytes in chapter 4, to investigate the reaction mechanisms.

PMA has been shown to generally form a mono-layer coverage.[299,304] However, it has also been shown that through adaption of the adsorption procedure multi-layers can be formed on the

surface.[305] This aspect of adsorption is extremely important as it will greatly affect the interaction of species on the surface: determining whether polyanion exchange occurs between the bulk and surface concentrations and its rate; also determining the amount of charge that can be transferred during a redox process.

3.1.2 Model surface adsorbed species behaviour

The electrochemistry of surface adsorbed layers can be modelled and then compared to experimental data. A complete description of these equations was first derived in a series of papers by Laviron et al.[306–309] in the late 1970's and early 1980's. Additionally the equations described are applied to a similar example of self-assembled monolayers (SAMs) by Eckermann et. Al..[310]

Initial assumptions must be made to allow for the equations to be built. Primarily, that the surface reactions are in equilibria, with the net effect that the current is not influenced by the rate of reaction. In addition, it is assumed that all surface sites are equal, and that there are no net interactions between molecules on the surface, as such a Langmuir isotherm is presumed. As is discussed later this leads to an ideal case but allows of an initial description.

Laviron defines an expression for the surface standard potential ($E^{0'}$) as Equation 3.1,

Equation 3.1

$$E^{0'} = E^0 - \left(\frac{RT}{nF}\right) ln \left({b_O}/{b_R}\right)$$

Where, b_O and b_R are the respective adsorption coefficients for the oxidized and the reduced species and E^0 is the standard potential for the solution phase. Taking this forward and assuming Nernstian

behaviour for the reaction, Equation 3.2 can be formed with effective surface concentrations (Γ_O, Γ_R respectively).

Equation 3.2

$$\frac{\Gamma_O}{\Gamma_R} = \frac{b_O}{b_R} \; Exp\left[\left(\frac{nF}{RT}\right)(E - E^{0\prime})\right]$$

Laviron then further refines this equation to describe the free energy of adsorption for the oxidised and the reduced species. To form the equation to calculate the current response at a given potential, this equation is taken and combined with the general flux equation under the given conditions to produce Equation 3.3.

Equation 3.3

$$i = \frac{n^2 F^2}{RT} \frac{vA\Gamma_O^* \left(\frac{b_O}{b_R}\right) exp\left[\left(\frac{nF}{RT}\right)(E - E^{0\prime})\right]}{\left[1 + \left(\frac{b_O}{b_R}\right) exp\left[\left(\frac{nF}{RT}\right)(E - E^{0\prime})\right]\right]^2}$$

Subsequently this leads to the familiar equations for peak current (i_p) and peak potential (E_p).

Equation 3.4

$$i_p = \frac{n^2 F^2}{RT} vA\Gamma_O^*$$

Equation 3.5

$$E_p = E^{0\prime} - \left(\frac{RT}{nF}\right) ln \left(\frac{b_O}{b_R}\right)$$

Due to the assumptions made, if there are truly no molecular interactions and the surface adsorption holds to a Langmuir isotherm the reduction and oxidation peaks appear symmetrical about the potential axis leading to the equation of the half-peak height width.

Equation 3.6

$$\Delta E_{p,1/2} = 3.53 \frac{RT}{nF} = \frac{90.6}{n} \; mV$$

3.1.3 Application of adsorbed models

Equation 3.4 relates the peak current to the surface coverage of the redox active species and scan rate of the experiment. This allows for two test parameters to be established. First, a method for investigating the surface coverage of a species; secondly, a method to investigate whether the redox properties are truly dominated by adsorbed species or whether a diffusion regime dominates. A diffusion regime could dominate if the species has a high exchange rate, either in the oxidized or reduced form, or if counter ions/reactants must penetrate the layer to balance any charge within.

Recalling discussions in previous chapters, the Randles-Sevcik equation shows the relationship of peak current to scan rate in diffusion controlled regimes as being directly proportional to the square root of scan rate. Comparing this to Equation 3.4 a clear difference arises. This leads to the conclusion that a $\log |i_p|$ versus log (scan rate) graph should show a linear relationship in both cases if ideal behaviour is observed. Additionally, if the response is dominated by adsorbed layer behaviour the gradient of the linear relationship will equal 1 and if it is dominated by a diffusional aspect it will equal 0.5.

The surface coverage of phosphomolybdic acid has been well documented in previous studies which allows for a prediction of peak current values, and a measure of whether true ideal behaviour is observed. In addition, this information can show whether a monolayer of adsorbed material is formed. Even if the redox characteristics do not follow ideal behaviour, the charge transferred within a redox event should equal the charge needed to oxidise (or reduce) the number of adsorbed species (with respect to the number of electrons involved in the process) adsorbed to the surface.

This means that if the area under the peak is integrated, a value for the charge transferred to the surface species (if adsorbed behaviour is assumed) can be obtained. This in turn allows the calculation of the number of chemical units on the surface. As this surface coverage value is known, it can subsequently be established whether a true monolayer exists. When discussing the vanadium substitutions, the reference value for the surface coverage of phosphomolybdic acid can be considered. It must be noted that substitution will lead to a change in size of the chemical unit, however, the effect of substitution, especially in singularly substituted species will be relatively small in terms of magnitude.

3.1.4 Deviation from ideal behaviour for adsorbed species

It should also be noted that the description above based on Laviron's early work described the behaviour in ideal circumstances using the Langmuir isotherm, which does not account either for non-linear adsorption, or for interactions between chemical units on the surface. In subsequent work Laviron and others went on to describe multiple models with differential isotherms used to include these complications. The main effects of surface interactions between species are peak flattening, deviation from symmetrical peak shape and peak offset (where the peaks are offset from each other on the potential axis). Regarding the species considered here, multiple reduction and oxidation processes occur across the potential window and as such multiple multi-electron transfer processes occur leading to highly charged species on the surface. This in turn leads to considerable interaction between molecules on the surface.

3.1.5 Conclusion

There is a large volume of research material into the adsorbed layers of phosphomolybdic acid and its vanadium substituted derivatives. However the fundamental study of the electrochemical behaviour of adsorbed layers is incomplete.

This chapter covers the initial electrochemistry of the phosphomolybdic acid and singularly substituted vanadophosphomolybdic acid adsorbed layers. A key area missing from the literature is the rate of adsorption and how both species deviate from ideal behaviour with a developed systematic, reproducible approach to surface modification.

Chapter 4 covers the lack of information relating to the effect of graphitic surface, pH and cation used. Specific information on the interaction between the adsorbed layer and the solution phase has not previously been available, and is covered in chapters 5 and 6 of this thesis. Although ideas on the influence of increasing vanadium content within the heteropoly acid have been developed and explored, details of the relationship between the singularly and the doubly substituted species are not fully available due to previous synthetic routes, and incomplete studies. This subject area is covered in chapter 6.

3.2 Experimental

3.2.1 Electrode Preparation

Electrode preparation proved challenging due to PMA contamination, as such, repeatable and effective electrode cleaning and preparation procedure was developed specifically for this work.

After each experiment the electrode was polished for 50 cycles with 45µm diamond paste (Buehler, Germany) on a polishing cloth (Buehler, Germany). The electrode was then immersed in a stirred solution of 0.1M sodium hydroxide for ten minutes before rinsing and further polishing for 50 cycles with 15, 9, 6, µm diamond pastes on polishing pads subsequently followed by 1, 0.3 and 0.05 µm alumina slurries on polishing pads with the electrode rinsed in distilled water between each step. The electrode was then dried in a stream of nitrogen before further use. Where not specifically discussed the method used was to take an electrode as described above and immerse in 0.1 M aqueous solution of phosphomolybdic acid (diluted from 0.3 M solution provided by ACAL Energy Ltd), or phosphovanadomolybdic acid (diluted from 0.3 M solution provided by ACAL Energy Ltd), for 30 seconds before rinsing with ultrapure water and drying under blown nitrogen gas.

3.2.2 Cell preparation

To complete the electrochemical assessment a simple three electrode cell was constructed using a bright platinum as the counter electrode and a SCE reference. The beaker was filled with 50 mL of 0.1 M sulfuric acid then covered with parafilm[TM] and sealed. Holes were made in the parafilm[TM] to insert the 3 electrodes and to allow the cell to be purged with a nitrogen stream (20 minutes). A positive pressure of nitrogen was maintained above the solution throughout experimentation. A magnetic stirrer bar was inserted to allow agitation between experiments.

The electrodes were connected to an Ivium potentiostat, controlled through a PC driven by the Iviumsoft software (Alvatek Ltd. UK.). Standard cyclic voltammetry programs were used at the ranges and scan rate discussed in the results and discussion section.

3.3 Results and discussion

The system was found to be highly sensitive to self-contamination. It was not clear whether the contamination was residual adsorbed molecules or a reabsorption effect from the solutions and pads. This led to the development of a specific cleaning routine (detailed above), where the electrode was polished using highly abrasive slurry and soaked in alkali solution. The effect that alkali solution had on the adsorbed species is subject to further investigation in section 4.3.4 as this simple measure resulted in a distinct change in the behaviour of the layer with pH.

Having established a repeatable methodology for generating blank scans following active scans, the initial experiments focused on producing a repeatable layer on the electrode for experimentation and an initial study on the adsorption rate that was occurring.

3.3.1 Adsorption rates

A 3mm glassy carbon electrode was taken and dipped in a 0.1 M solution of PMA before rinsing with distilled water and being dried with compressed air. The electrode was then used as the working electrode in a 0.1 M sulfuric acid solution and the electrochemical response to cyclic voltammetry at 100 mV.s^{-1} was recorded. The length of time that the electrode remained dipped into the solution was varied to investigate whether a time dependence existed. These results are shown in Figure 3.1.
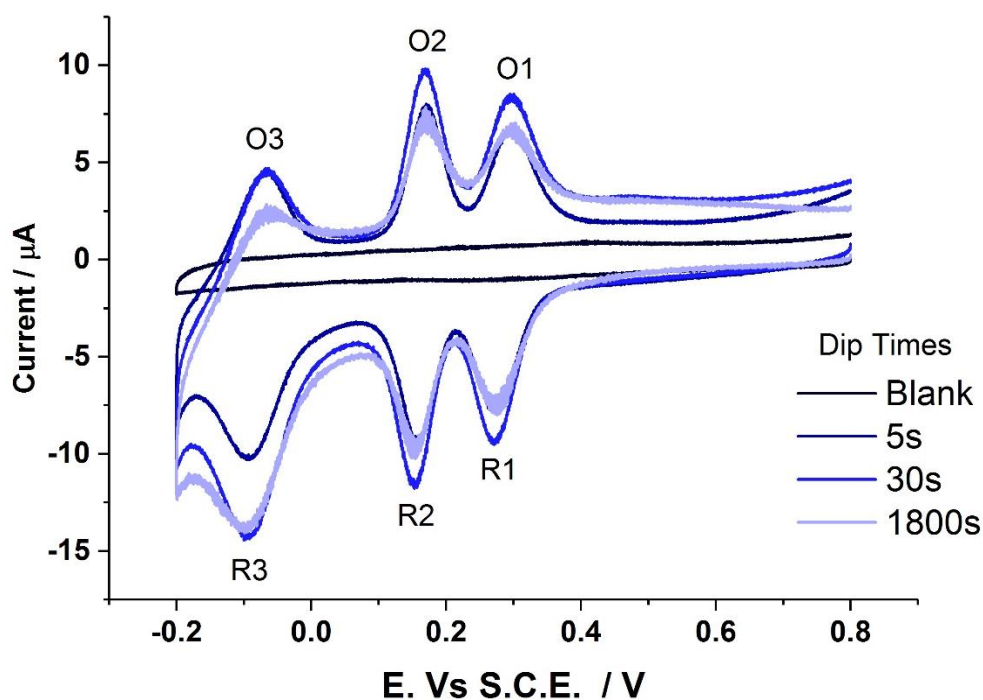
Figure 3.1 – Overlay of cyclic voltammograms obtained from 3 mm GC electrodes modified via dipping in 0.1 M PMA solutions and taken at 100 mV.s^{-1} in 0.1 M sulphuric acid solutions. Each electrode has been dipped for a differing length of time.

It was seen that the change in cyclic voltammetry was established after a very short dip time in the solution of PMA, Figure 3.1. Dip timings up to 3600 s were used on multiple GC electrodes (both 2 and 3 mm GC), to investigate whether a relationship between dip time and the magnitude of current existed. Peak current values were taken from cyclic voltammetry for reduction peaks, R1, R2 and R3, as denoted in Figure 3.1, and averaged to enable a plot of average peak current density versus dip time, Figure 3.2. The initial fast increase in magnitude appeared to take place within ten seconds. At this point, there was not enough information from this data to comment on any adsorption process, and it is explored in much greater detail in section 4.3.1.
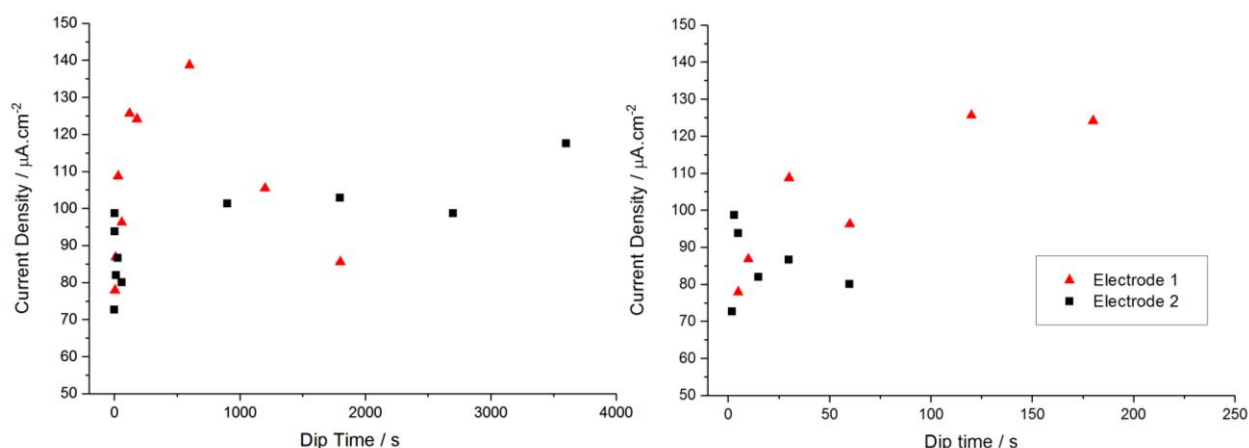
Figure 3.2 - Left, average reductive peak current density (across R1, R2 and R3) for GC electrodes modified by dipping in 0.1 M PMA solution, from cyclic voltammetry in 0.1 M sulphuric acid. Right, a highlighted section of quicker dip times using the same data as the left plot. Electrode 1 was a 3 mm GC electrode and electrode 2 was a 2 mm electrode.

Figure 3.2 shows a clear point at which an initial adsorption has taken place, however, that this is not repeatable enough at short dip times at this concentration. From this initial assessment, it was seen that dipping an electrode in the solution for 30 seconds produces a layer with a repeatable response, similar to previous studies.[311,312]The next step was to repeat the initial assessment with V1PMA. These results can be seen in Figure 3.3.
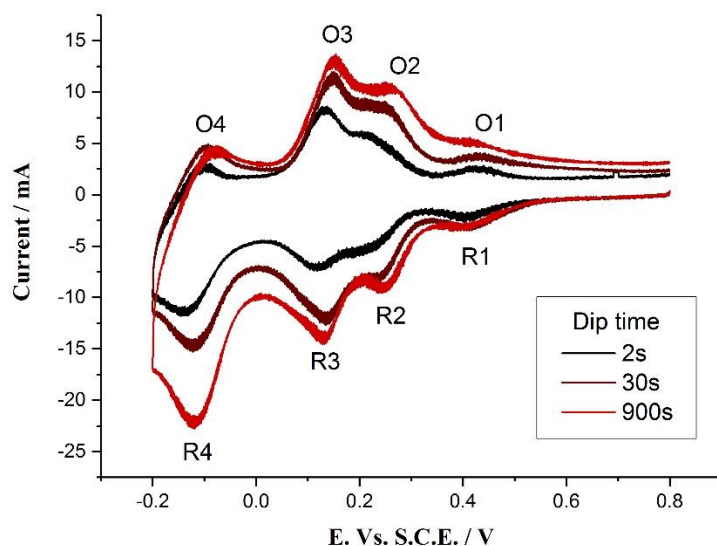
Figure 3.3 - Cyclic voltammetry of 3 mm GC electrodes modified with singular substituted vanado-phosphomolybdic acid at varying dip times at 100 mV.s^{-1} in 0.1 M sulphuric acid.

119

The dip-time response of singularly substituted vanado-phosphomolybdic acid was similar to that of phosphomolybdic acid, albeit the cyclic voltammetry is different. Taking the peak current values of R1 and R3, Figure 3.3, a plot of peak current density versus dip time can be plotted, Figure 3.4.
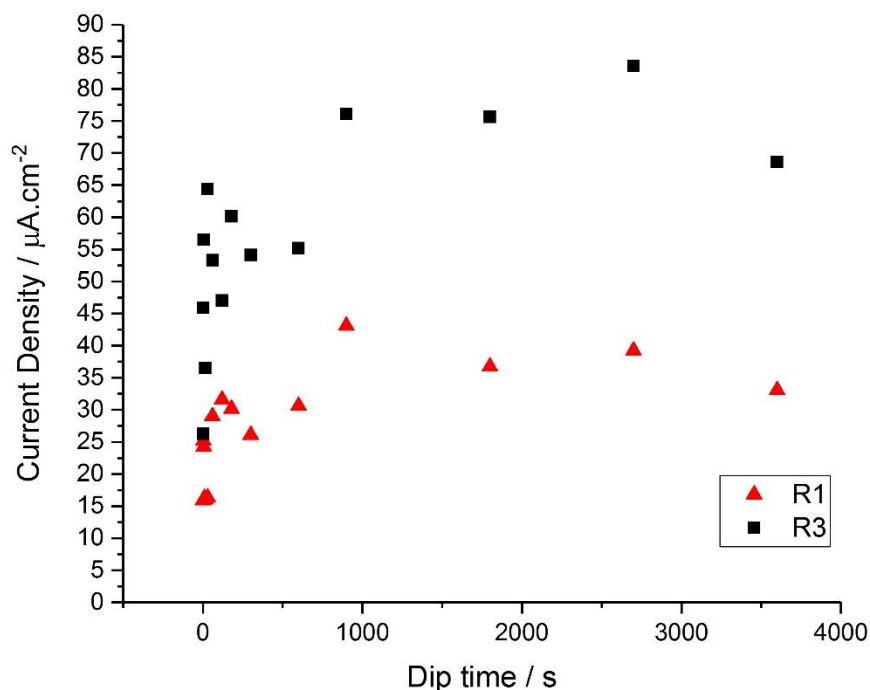
Figure 3.4 - Peak current density of R1 and R3, obtained from cyclic voltammetry of V1PMA modified 3 mm GC electrodes at 100 mV.s^{-1} in 0.1 M sulphuric acid, showing the magnitude versus dip time for the modification.

It can be seen that R1 in V1PMA is significantly lower in magnitude than R3. Also observed is that the response is observed with very short dip times, stabilising in magnitude within 15 seconds.

With the two cases supporting each other it was decided that in order to study the electrochemistry of the adsorbed layers, electrodes should be dipped for 30 seconds to ensure adsorption has occurred. Effects on this adsorption behaviour caused by changing concentration, pH and electrode surface are investigated further, in 4.3.1.

3.3.2 Signal degradation rates

The next experiments examined how these layers deteriorated. GC electrodes were taken, dipped for 30s in the phosphomolybdic acid solutions and the electrochemical response to repeated cycles was recorded, as shown in Figure 3.5.
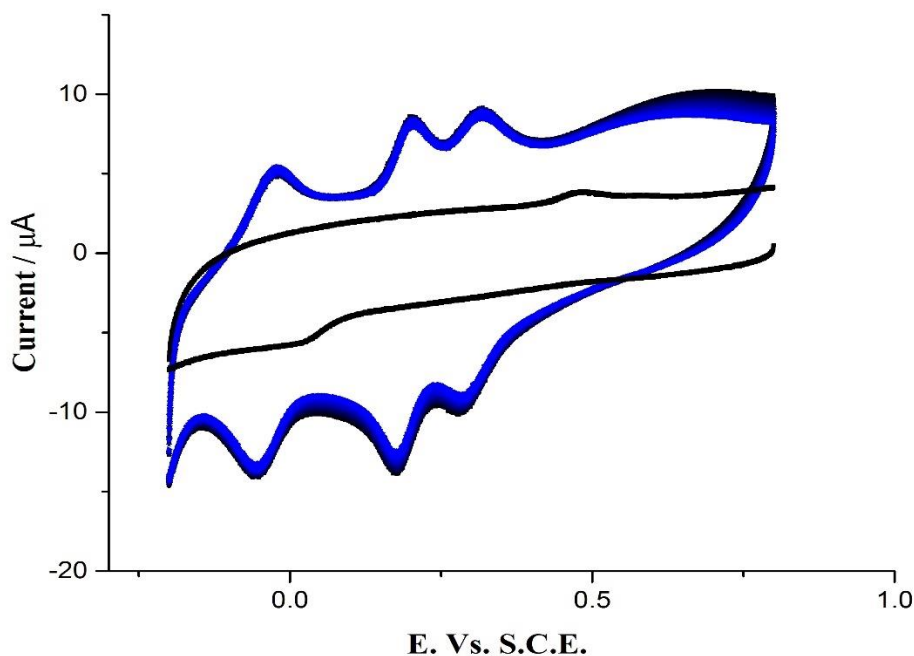
Figure 3.5 - repeated cycling (20 cycles at 100 mV.s⁻¹ in 0.1 M sulphuric acid) of a 3 mm GC electrode modified by dipping into a 0.1 M PMA solution for 30 seconds (blue) and an unmodified electrode (black)

It was observed that repeated cycling led to little deterioration in the magnitude of the current response. This was relatively unsurprising given the resilience of the layer during electrode polishing. It can be seen in the cyclic voltammograms that the GC electrode produced a relatively ill-defined electrochemical response with a large contribution from background capacitance. As such, an edge-plane pyrolytic graphite (EPPG) electrode was used to see if more pronounced

signals were observed. Response to repeated cycling of a phosphomolybdic acid modified EPPG electrode are shown in Figure 3.6.
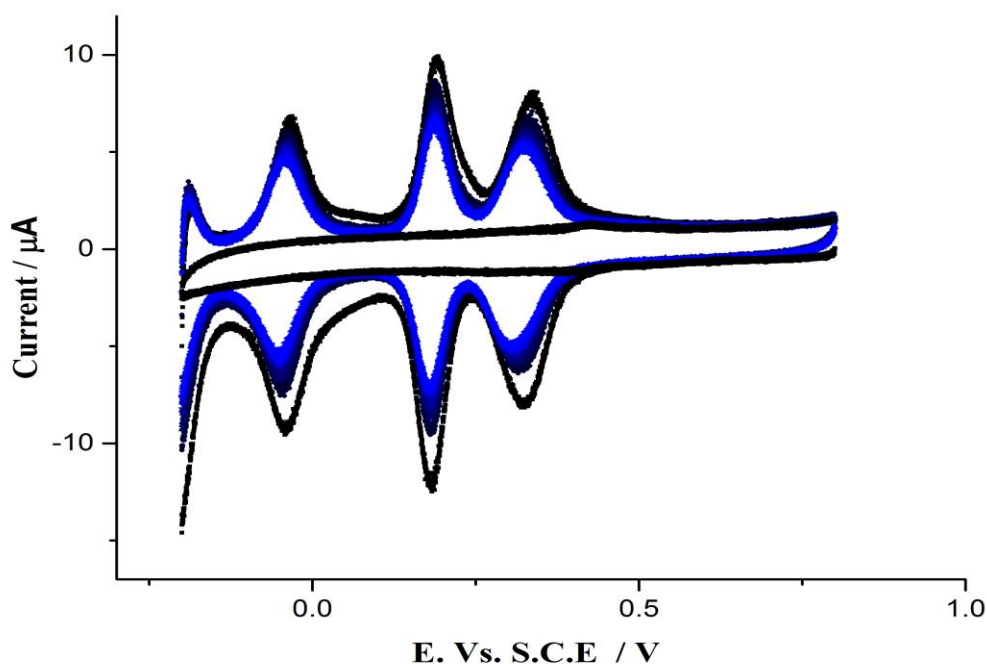
Figure 3.6 - repeated cycling (20 cycles at 100 mV.s⁻¹ in 0.1 M sulphuric acid) of a 3 mm EPPG Electrode modified by dipping in a 0.1 M PMA solution for 30 seconds (blue) and an unmodified electrode (black)

It was observed that indeed the signals are 'sharper' with a reduction in the contribution from background capacitance. A full investigation into the effects caused by the electrode material is covered in section 4.1.2. As with the GC electrode little reduction in the magnitude of the observed response was seen after repeated cycling across the selected potential window.

Within this window three reversible redox phenomena are observed. However, Figure 3.6 hints that further redox processes occur at lower (more negative) potentials, with the onset of a further redox process observable at around -0.2 V vs. SCE. It was also noted that the removal of the

modification from the surface is linked to a chemical change, this was achieved by exposing the surface to an alkaline pH. It is possible that further reduction of the surface species could lead to a structural change and a break-down in the structure.

3.3.3. Effect of potential scan range

To investigate whether this degradation could be induced at lower potentials, EPPG electrodes were modified with singularly substituted vanado-phosphomolybdic acid as has previously been described. These electrodes were subject to incrementally wider potential ranges, with a new electrode used for each increase in range, as in previous studies.[311]
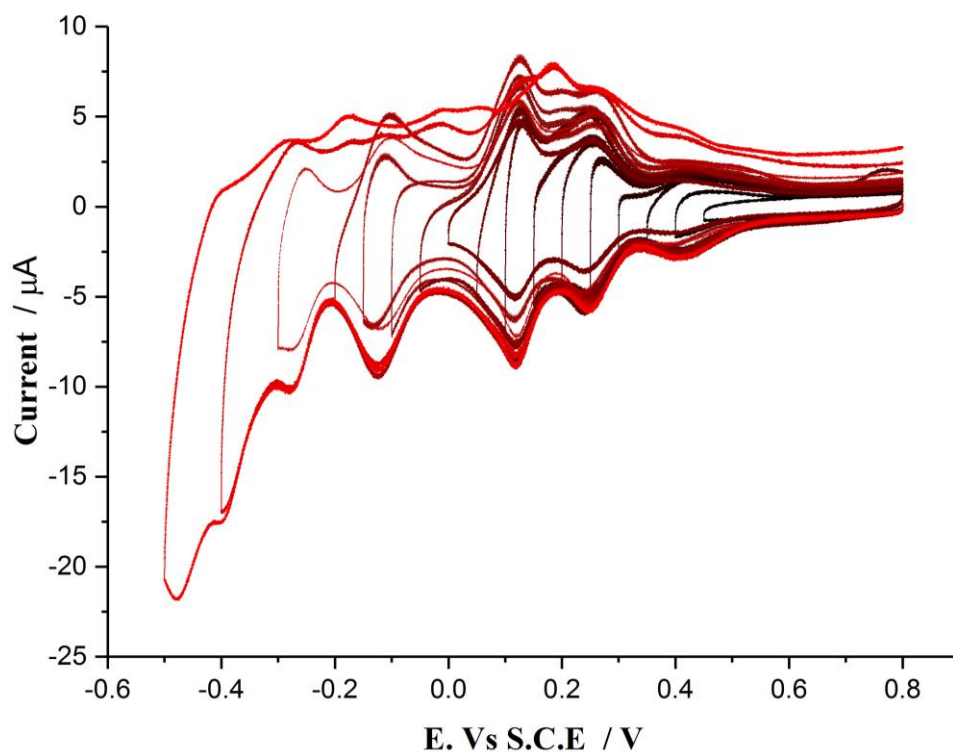
Figure 3.7 - Cycle voltammograms (taken at 100mV.s^{-1} in 0.1 M sulphuric acid) of 3 mm EPPG electrodes modified by dipping in 0.1 M V1PMA solution for 30 seconds at increasing potential ranges.

Figure 3.7 shows the initial scan of each increase in potential range. The first observation is that in total 7 reduction processes occur (peaks A-G in Figure 3.8) and that the return oxidations are not consistent across the increasing potential ranges. At potential ranges not venturing lower than -0.2 E. Vs S.C.E., four reduction processes occur and the reversible corresponding four oxidation process are present at this scan rate (100 mV.s^{-1}). Venturing below this potential range the oxidation processes are affected and break down into multiple events that are hard to decipher, as with previous polyoxometalate studies.[313] Figure 3.8 shows two selected potential ranges with repeated cycles alongside a plot of the current of the first reduction (peak) degrading with repeated cycles at the different potential regions.
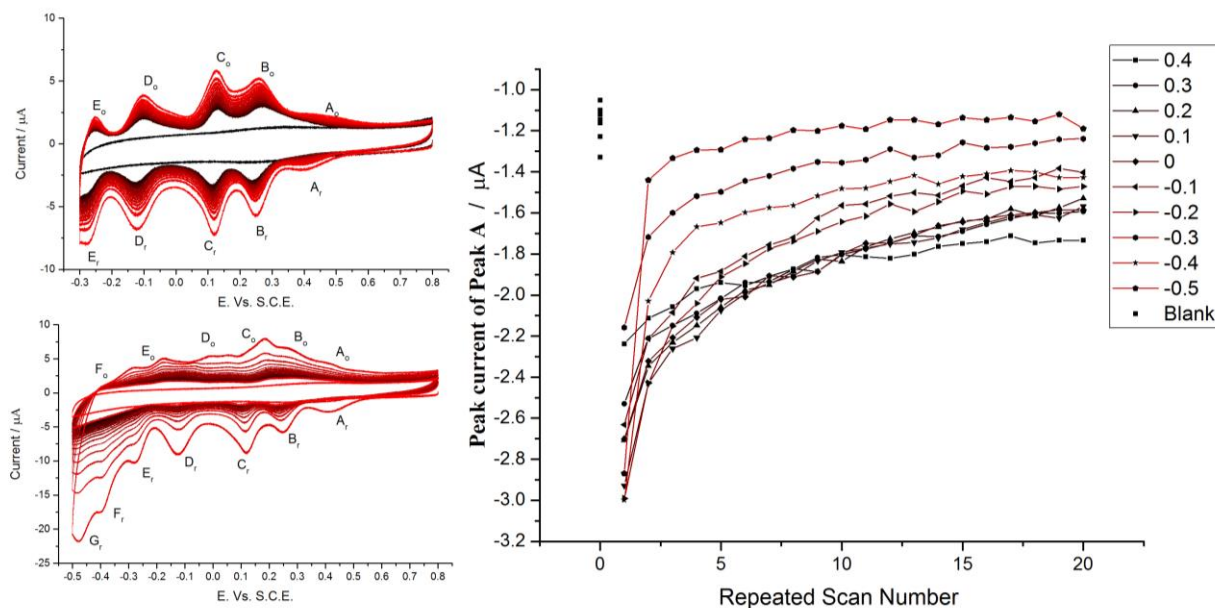
Figure 3.8 - cyclic voltammograms of repeated cycling (20 cycles at 100 mV.s^{-1} in 0.1 M sulphuric acid) at selected potential ranges of 3 mm EPPG electrodes modified by dipping in 0.1 M V1PMA solutions for 30 seconds, and the corresponding degradation in reduction peak (A) peak current at these extended potential windows, legend refers to lower potential limit.

Figure 3.8 shows that as the potential range is extended not only do the oxidation peaks become difficult to assign but that the degradation in peak magnitude occurs more rapidly. This indicates

that the layer is breaking down during these further reduction processes and it leads to the conclusion that when investigating the electrochemical behaviour of these layers, the potential window should stay above -0.2 Vs. S.C.E. to avoid the breakdown of the surface.

3.3.4 Analysis of phosphomolybdic acid electrochemical response

Peak Shape analysis

A phosphomolybdic acid modified EPPG electrode was taken and the electrochemical response to cyclic voltammetry between 0.8 and -0.2 E. Vs. S.C.E. was measured. The response from a blank electrode was recorded and then subtracted from the previously recorded data. This allows for assessment of the response from the layer without contribution from the background capacitance of the electrode. Subsequently the positive sweep data was taken and inverted so that oxidative and reductive sweeps overlay one another, resulting in the data seen in Figure 3.9.
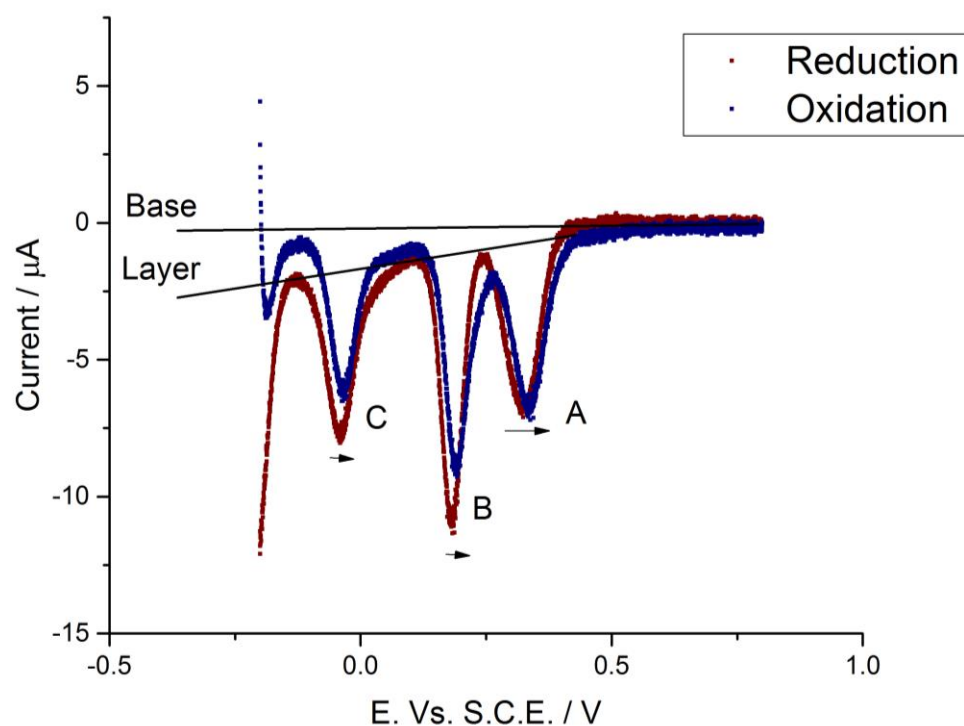
Figure 3.9 - overlaid oxidative and reductive cyclic voltammetry responses from a 3 mm EPPG electrode modified by dipping in a 0.1 M solution of PMA taken at 100 mV.s^{-1} in 0.1 M sulphuric acid, with a blank baseline removed

This way of presenting the data allows several characteristics to be observed. The deviation of the response from the baseline that takes place once the first reductive process (A) has been initiated shows that there is a resistive component to transferring electrons into and out of the adsorbed layer, as shown in the difference between the two lines labelled 'Base' and 'Layer' in Figure 3.9. It can also be observed that the peaks are not a perfect mirror image across the x-axis, meaning that the behaviour of the layer was not perfectly ideal. Table 3-1 lists the peak potentials and shows this non-symmetry, although it also highlights how small the shift in position is, being on average a shift of 10 mV.

	Reduction	Oxidation	Difference
A	**0.323**	**0.337**	**0.014**
B	**0.181**	**0.191**	**0.01**
C	**-0.04**	**-0.034**	**0.006**

Table 3-1 – Potential values of peak current for the oxidative and reductive process observed at a phosphomolybdic acid modified EPPG electrode in a 0.1 M sulphuric acid solution. Values are taken versus S.C.E.

Taking each peak individually the half peak height widths can be calculated and an idea of the symmetry can be obtained for the peak. This was achieved by separating the data associated with each peak and adjusting the potential so that it is referenced to the central peak height. The locations of the half peak height can then be found and the half peak height width calculated as is shown in Figure 3.10.
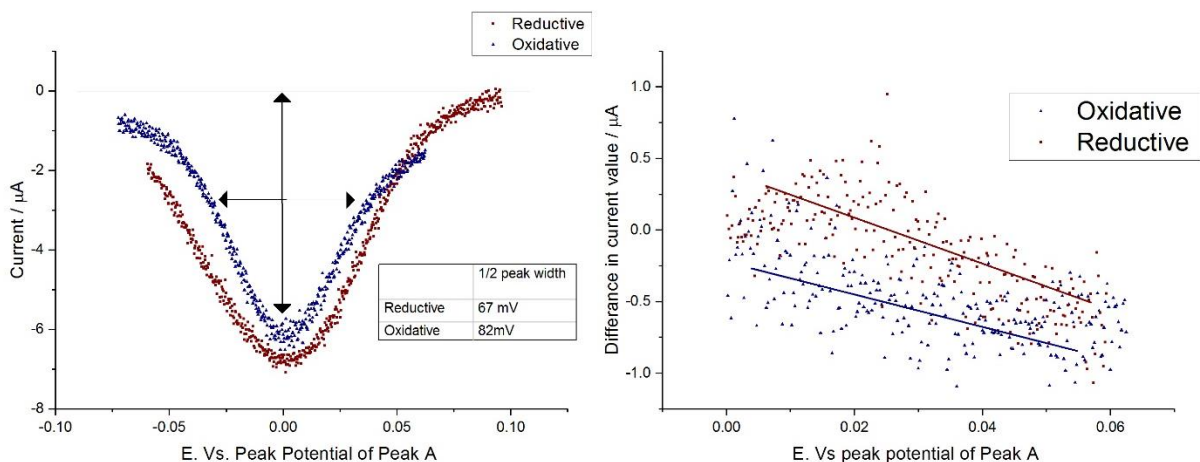
Figure 3.10 - Analysis of Peak A observed in cyclic voltammetry at 100 mV.s^{-1} in 0.1 M sulphuric acid for a 3 mm EPPG electrode modified by dipping in 0.1 M PMA solution for 30 seconds

Figure 3.10 also shows analysis of the symmetry of the peak. This can be represented by the difference in current response at equal distance from the peak centre, this is shown on the right-hand side of Figure 3.10. The data shows that for peak A, the reductive half peak width is 82 mV

and the oxidative half peak width is 67 mV. It has been shown in previous studies that the three peaks A, B and C are attributed to two electron redox processes. As such, and from Equation 3.6, the half peak height width should be 45 mV.

This deviation from ideal behaviour could be due to several possibilities. The data on the right-hand side of Figure 3.10 shows that the peak is not symmetrical and that the oxidative peak is less symmetrical then the reductive peak. However, the data is difficult to correctly baseline adjust. As can be seen in Figure 3.10 the peak is clearly not positioned on the baseline due to the contribution of the resistance within the layer and due to the overlapping of the peaks. This is also alluded to in the gradient shown in the right hand-side graph. If a second baseline adjustment is made, taken from the leading edges of the peaks it results in the data shown in Figure 3.11.
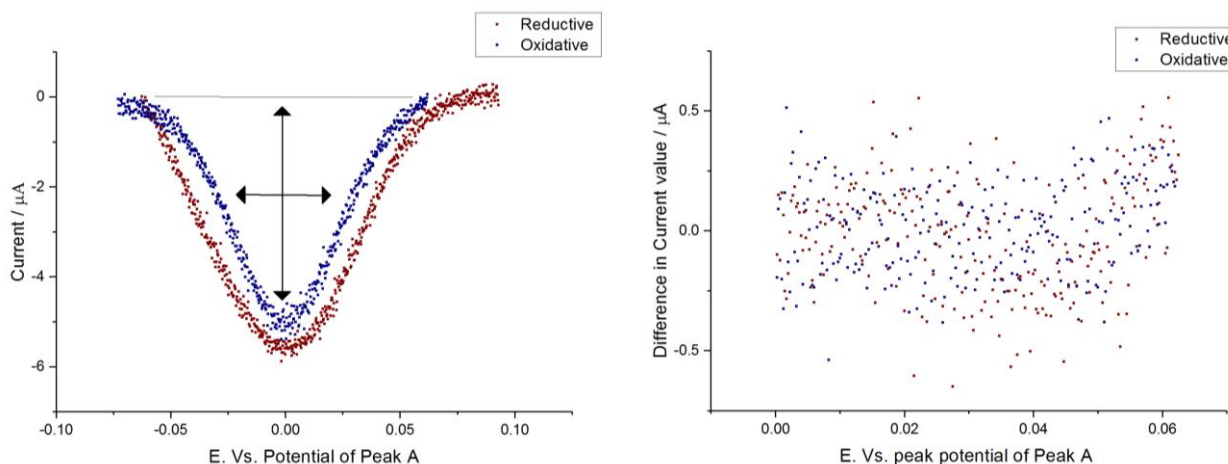
Figure 3.11 - Additional baseline corrected analysis of Peak A observed in cyclic voltammetry at 100 mV.s^{-1} in 0.1 M sulphuric acid for a 3 mm EPPG electrode modified by dipping in 0.1 M PMA solution for 30 seconds

With the data processed in this way the half peak height width for the reductive process is 71.5 mV and 54.5 mV for the oxidative process. It can also be seen that no gradient exists in the right-hand graph and that the data points surround a collective zero figure, showing that both peaks are very

symmetrical. The question of how to take correct baselines is a very important issue and is returned to frequently when analysing the electrochemistry of the adsorbed layer.

The same methods were applied to peaks B and C of Figure 3.9 leading to the data presented in Figure 3.12.
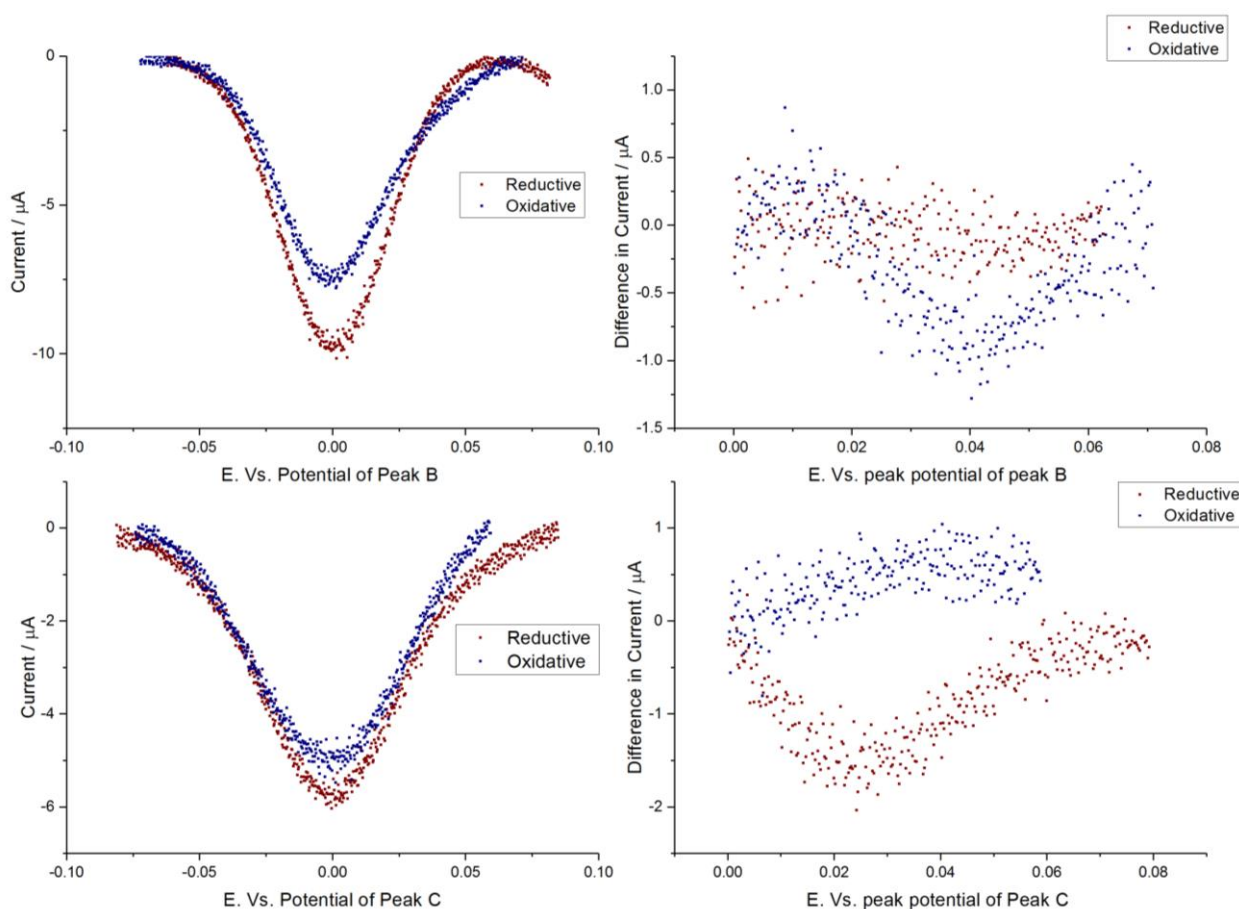
Figure 3.12 - Additional peak analysis for peaks B and C observed in cyclic voltammetry at 100 mV.s^{-1} in 0.1 M sulphuric acid for a 3 mm EPPG electrode modified by dipping in 0.1 M PMA solution for 30 seconds

Figure 3.12 shows that both peaks are symmetrical, with the reductive peak C showing the biggest deviation from symmetry. The negative deviation shows that the peak is biased to the negative

potential side, producing more current on the left hand side of the peak then the right. The reductive half peak width for Peak B was 47 mV with the oxidative being 49 mV. For peak C the values were 62 mV for the reductive and 63 mV for the oxidative process. Peak B shows the most ideal behaviour being very similar to the ideal calculated value, whereas, peak C shows some deviation. To ensure this deviation is not caused by the surface species exchange into solution or by the limitation of counter ion diffusion, scan rate analysis was used to determine whether the layer is exhibiting truly adsorbed layer behaviour.

Scan rate analysis

EPPG electrodes were modified with phosphomolybdic acid and their response to cyclic voltammetry and various scan rates recorded. These responses were plotted (Figure 3.13) and the peak heights were taken.
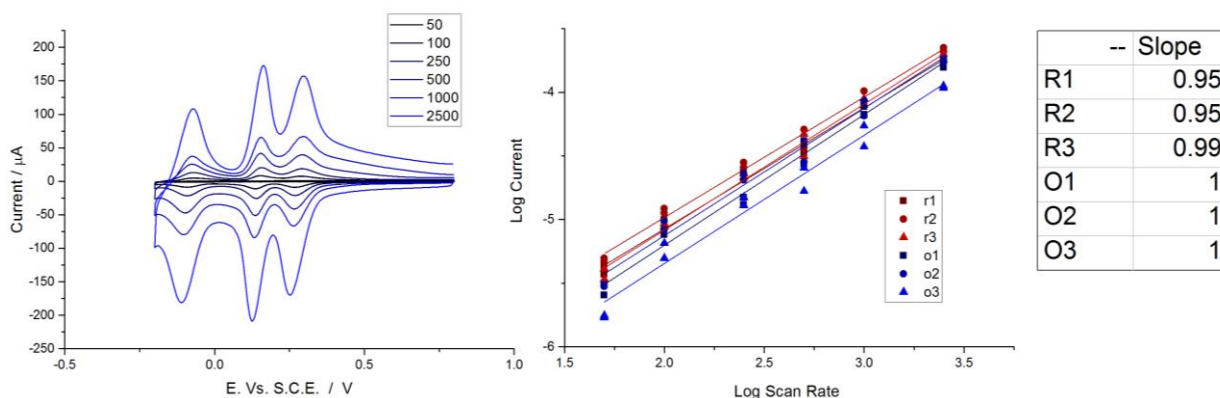
Figure 3.13 - Scan rate analysis of cyclic voltammetry in 0.1 M sulphuric acid of 3 mm EPPG electrodes modified by dipping in 0.1M PMA solution for 30 seconds

Logarithms were taken of the scan rate and corresponding peak height and plotted against each other (Figure 3.13). As can be seen the slope of this relationship is equal to 1 for each of the three redox process and their corresponding oxidation and reduction peaks. This information agrees very

well with the hypothesis that the electrochemical responses are all adsorbed layer behaviour and that deviation from ideal behaviour is due to physical parameters within the layer itself.

Charge transferred at each redox event

Having investigated the general shape and response of the redox peaks observed for phosphomolybdic acid modified EPPG electrodes and seeing how this relates to the ideal cases for two electron transfer processes it was decided to investigate the charge transferred to the layer in each redox process, relating this to the monolayer coverage of the electrode.

The size of a phosphomolybdic acid molecule reported in literature is between 10-12 Å,[304] this leads to a theoretical surface coverage of 1.7×10^{-10} mol.cm^{-2}. Using the equation that relates surface coverage to charge,

Equation 3.7

$$\Gamma = \frac{Q}{nAF}$$

A theoretical value for the charge passed to reduce or oxidise a complete layer of phsophomolybdic acid on the surface of the electrode can be calculated as 2.32 µC. In addition, when studies have factored in surface roughness they have found values of surface coverage of 2.0×10^{-10} mol.cm^{-2} leading to a charge of 2.73 µC. It must also be noted these studies were using ITO based electrodes which are inherently flat smooth surfaces compared with polished graphite.[217] In addition studies of silicone based vanadium substituted HPAs reported a maximum coverage of 1.4×10^{-10} mol.cm^{-2}.[314]

To obtain the charge values two EPPG electrodes were taken and for each scan rate they were prepared as previously described with phosphomolybdic acid. The data was taken with each peak treated to the same baseline correction as in previous sections and then integrated to calculate charge. The data was then plotted against the redox peak and results in Figure 3.14.
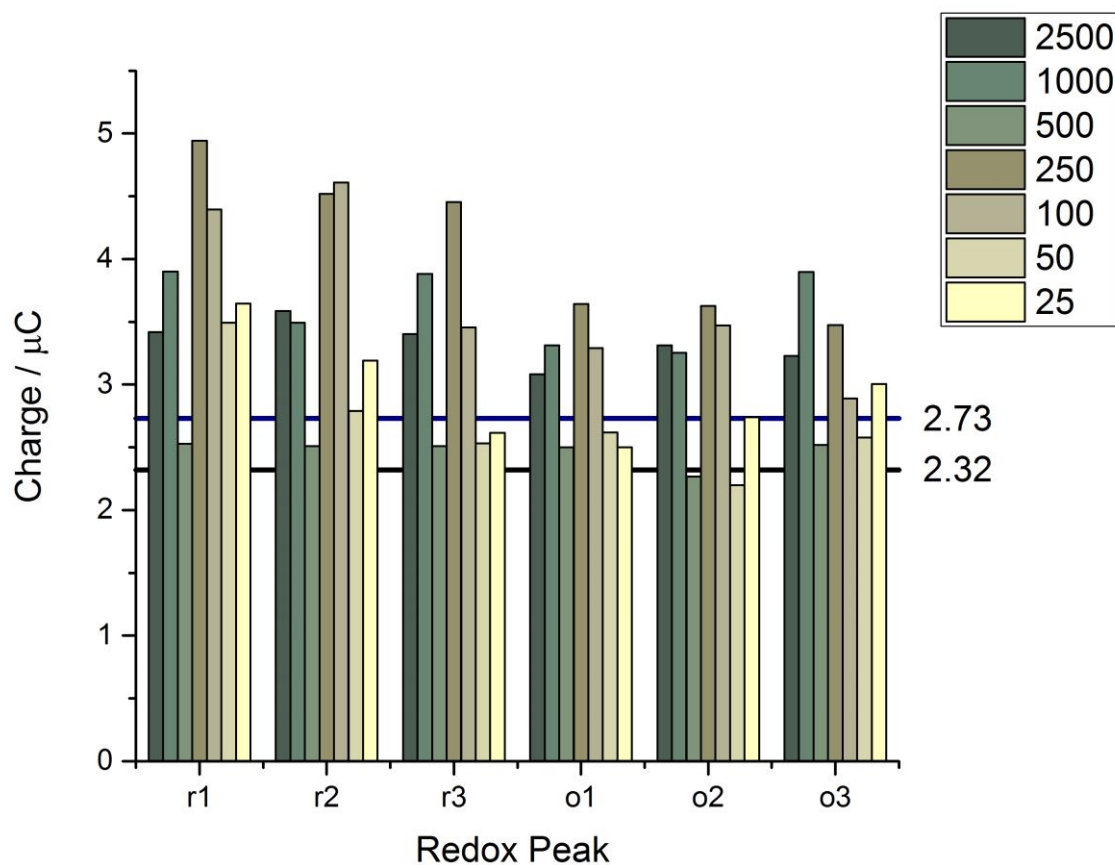
Figure 3.14 - Charge transferred in each redox process at each scan rate for a 3 mm EPPG electrode modified by dipping in a 0.1 M PMA solution for 30 seconds.

Figure 3.14 shows that the charge transferred for each layer is slightly larger than for the theoretical values for a monolayer coverage and slightly higher than previous reported studies using ITO.

However, considering the surface roughness of polished graphite when compared to ITO surfaces these values are reasonably similar.

3.3.5 Analysis of singularly substituted vanado-phosphomolybdic acid

The work into phosphomolybdic acid modified electrodes provided a baseline, and provided more information than is currently available from literature. The next step was to investigate the effect of substituting vanadium into the molecule.

Peak analysis

In the same way that the initial assessment of phosphomolybdic acid was conducted, an EPPG electrode was taken and modified with V1PMA. A blank scan was measured and subtracted, Figure 3.15.
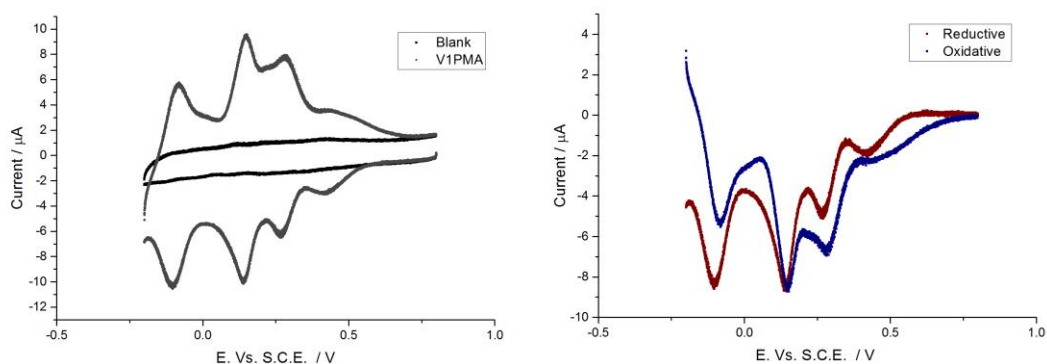
Figure 3.15 -Left, Cyclic voltammetry of a 3 mm EPPG electrode modified by dipping in a 0.1 M V1PMA solution for 30 seconds taken at 100 mV.s^{-1} in 0.1 M sulphuric acid, with a blank scan also shown. Right, the same data for the V1PMA modified EPPG electrode with the blank scan removed from the data and the oxidative portion inverted.

As with the phosphomolybdic acid electrode the oxidative signal is inverted and overlaid onto the reductive sweep (right, Figure 3.15). It can clearly be seen that the peaks are less symmetrical then

with the phosphomolybdic acid. Additionally, the onset of reduction has shifted positive and the first peak has appeared to be split into two separate peaks with 4 redox processes now evident. The initial redox peak is shown in Figure 3.16.
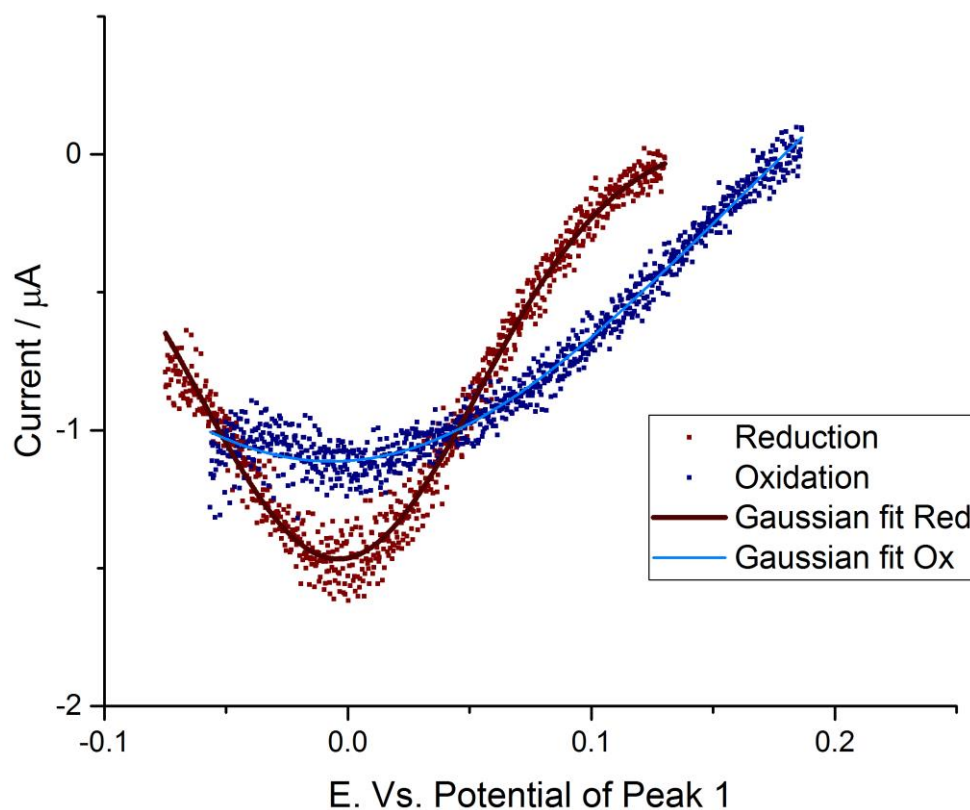
Figure 3.16 – Analysis of the first peak observed within cyclic voltammetry of a 3 mm EPPG electrode modified by dipping in a 0.1 M V1PMA solution for 30 seconds taken at 100 mV.s^{-1} in 0.1 M sulphuric acid

This first peak is attenuated and difficult to resolve. Its half height peak width can be determined by using the fitting function within Origin (Microcal Inc, USA) and using a Gaussian function to determine its statistical spread. Using this, the half-height widths are 135 mV for the reductive process and 381 mV for the oxidative. These greater than for any of the peaks in the

phosphomolybdic acid response and suggests that surface interactions are having an extremely significant effect on the process.

The second peak appears at the same position as the first peak for phosphomolybdic acid. It too looks diminished and asymmetric, however, in this case it appears this is due to overlaying peaks, Figure 3.17.
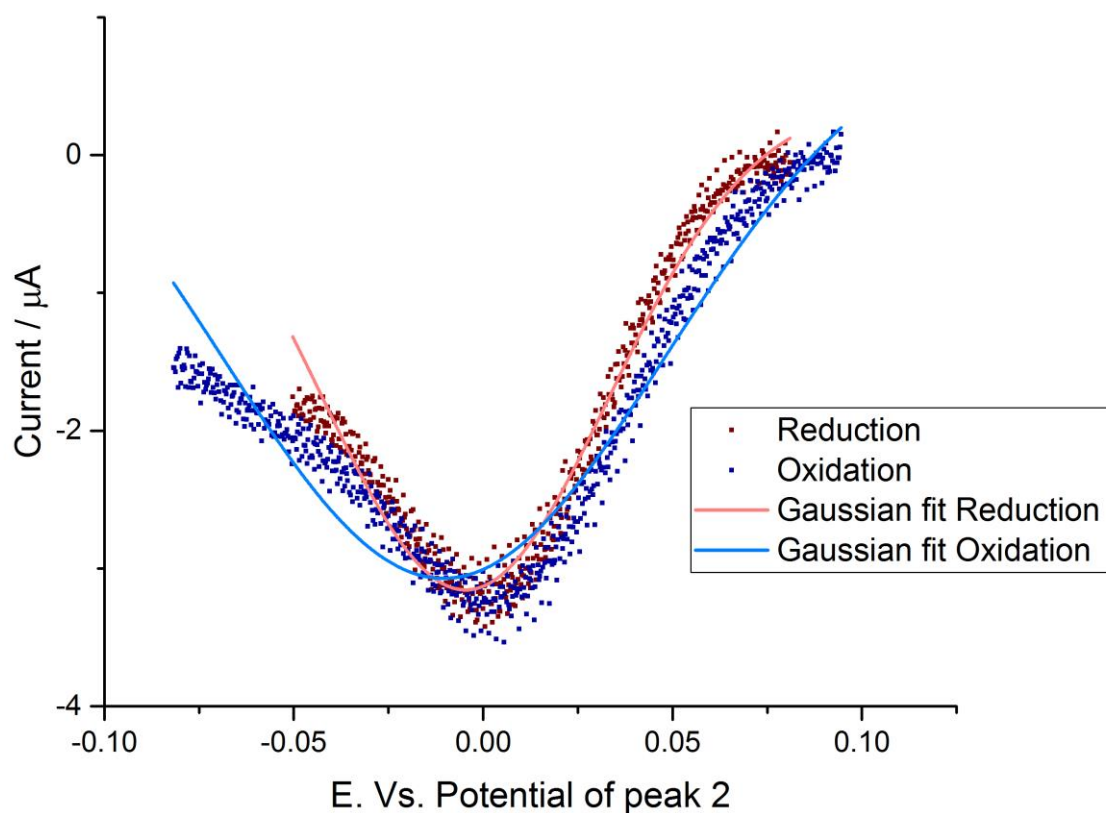
Figure 3.17 - **Analysis of the second redox peak observed within cyclic voltammetry of a 3 mm EPPG electrode modified by dipping in a 0.1 M V1PMA solution for 30 seconds taken at 100 mV.s^{-1} in 0.1 M sulphuric acid**

It can be observed that the peak is much more symmetrical then the first peak observed. Applying the same fitting protocol, it was determined that the reductive half height width was 89 mV and the oxidative was 116 mV. These values show an enlargement over the first peak observed in the phosphomolybdic acid modified EPPG electrode. This is indicative that this peak has become a one electron transfer process and allows for the hypothesis that the initial two electron redox process observed in the phosphomolybdic acid modified EPPG electrode has split into two, one electron processes, with one process occurring at higher potentials. The further two peaks are more symmetrical and are closer to ideal behaviour, Figure 3.18.
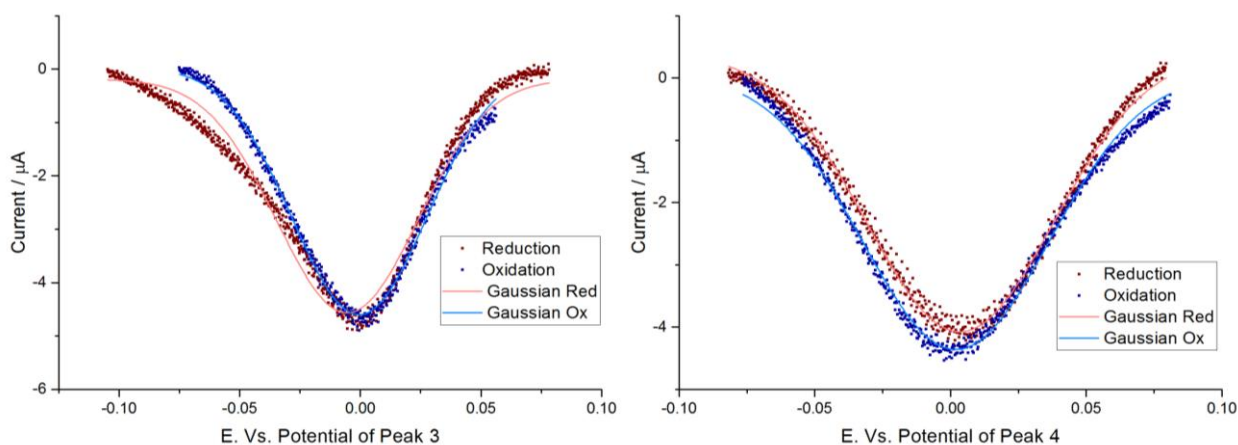
Figure 3.18 – Analysis of the 3rd and 4th observed peaks within cyclic voltammetry of a 3 mm EPPG electrode modified by dipping in a 0.1 M V1PMA solution for 30 seconds taken at 100 mV.s^{-1} in 0.1 M sulphuric acid

The half-height peak widths for peak 3 were 68 mV and 65 mV for the reductive and oxidative processes respectively and in the case of peak 4 both the oxidative and reductive peaks half height widths were 81 mV. These numbers indicate that these processes have been relatively un-perturbed by the substitution of vanadium. Similar to a reported 77 mV for the fourth reduction peak of silicon based vanadium substituted HPAs on gold electrodes.[314]

Scan Rate Analysis

The same scan rate analysis was performed for the singularly substituted vanado-phosphomolybdic acid modified EPPG electrodes as for the phosphomolybdic acid modified EPPG electrodes. This can be seen in Figure 3.19.
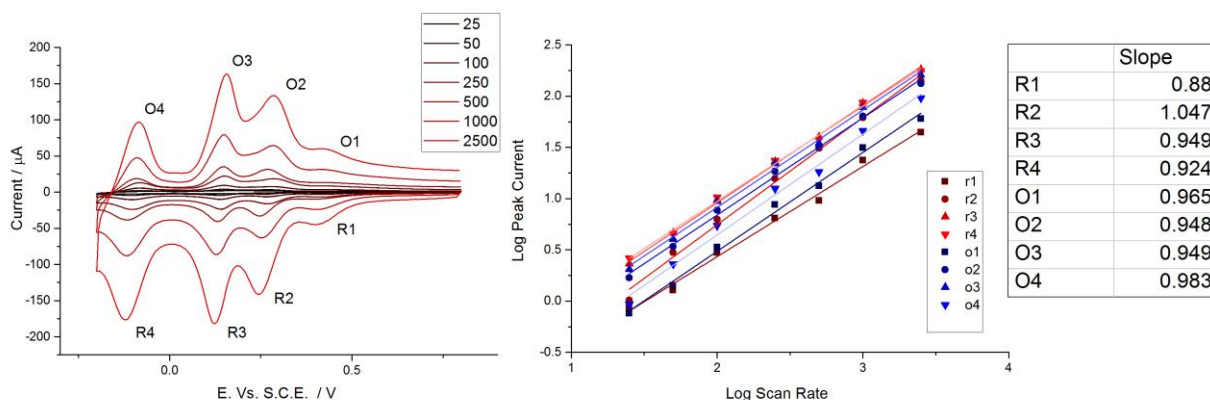
Figure 3.19 - scan rate analysis of cyclic voltammetry of a 3 mm EPPG electrode modified by dipping in a 0.1 M V1PMA solution for 30 seconds taken in 0.1 M sulphuric acid

The figure shows that the modified layer responds to cyclic voltammetry in a similar way to the original phosphomolybdic layer. All observable peaks generate a gradient in a log vs log plot of approximately one. It is interesting that the peaks become more defined at faster scan rates but that this also leads to increased asymmetry in the peaks. This is due to the rate at which the potential sweep increases, which may limit the time available for rearrangement on the surface making the surface interactions more evident.

Charge transferred at singularly substituted vanado-phosphomolybdic acid electrodes

Charge analysis was performed on the data obtained for the singularly substituted vanado-phosphomolybdic acid EPPG electrode. Additionally, a value of 1 for electrons transferred instead of two gives a theoretical value of 1.16 µC, and with the surface roughness factored in, of 1.37µC.
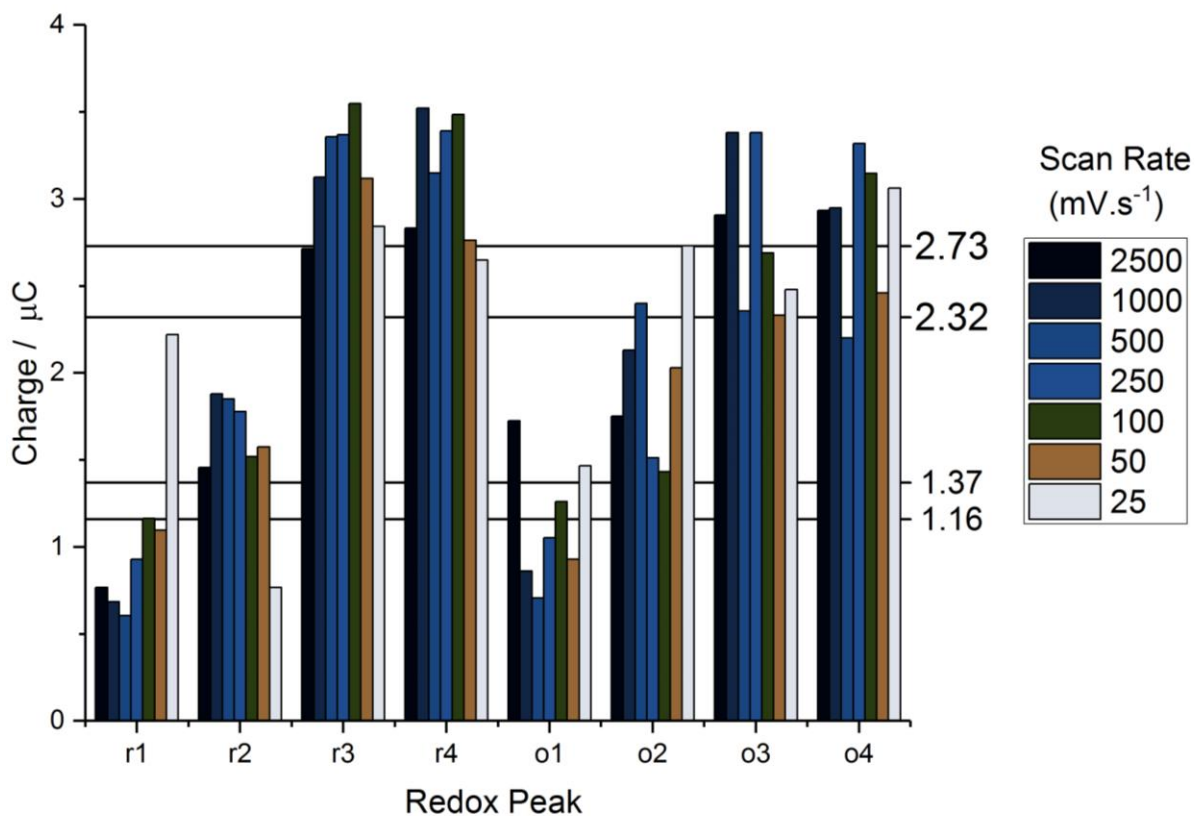
Figure 3.20 - charge transferred per redox process observed within cyclic voltammetry of a 3 mm EPPG electrode modified by dipping in a 0.1 M V1PMA solution for 30 seconds, taken in 0.1 M sulphuric acid

Figure 3.20 shows that the charge transferred in the first two redox process (R1, R2 and O1, O2) is representative of a one electron transfer process. This adds weight to the argument that the vanadium substitution has split the initial first peak of the phosphomolybdic acid layer into two separate peaks, with one peak occurring at a more positive potential.

3.3.6 Comparing Phosphomolybdic acid and singularly substituted vanado-phosphomolybdic acid modified EPPG electrodes

In previous studies the response of phosphomolybdic acid modified electrodes with three observable redox processes has led to the proposal that the phosphomolybdic acid molecule is reduced sequentially.[190] As proposed:

Equation 3.8

$$(PMo_{12}^{VI}O_{40})^{3-} + 2e^- \rightarrow (PMo_{10}^{VI}Mo_2^V O_{40})^{5-}$$

Equation 3.9

$$(PMo_{10}^{VI}Mo_2^V O_{40})^{5-} + 2e^- \rightarrow (PMo_8^{VI}Mo_4^V O_{40})^{7-}$$

Equation 3.10

$$(PMo_8^{VI}Mo_4^V O_{40})^{7-} + 2e^- \rightarrow (PMo_6^{VI}Mo_6^V O_{40})^{9-}$$
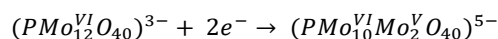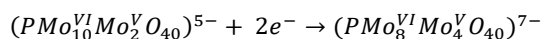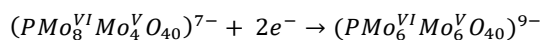
These individual two electron transfer processes correspond to the peaks 1, 2, 3 in Figure 3.1. It has been seen that the initial redox process (Equation 3.8) appears to split from a single two electron process into two, one electron processes and that these peaks no longer behave in a way that is true to ideal theoretical behaviour. It is hypothesized, due to the initial process being shifted much further positive, that the vanadium cluster within the molecule is the first metal centre to be reduced. As such,

Equation 3.11

$$(PV_1^V Mo_{11}^{VI}O_{40})^{4-} + e^- \rightarrow (PV_1^{IV} Mo_{11}^{VI}O_{40})^{5-}$$

Equation 3.12

$$(PV_1^{IV} Mo_{11}^{VI}O_{40})^{5-} + e^- \rightarrow (PV_1^{IV} Mo_1^V Mo_{10}^{VI}O_{40})^{6-}$$

Equation 3.13

$$(PV_1^{IV} Mo_1^V Mo_{10}^{VI}O_{40})^{6-} + 2e^- \rightarrow (PV_1^{IV} Mo_3^V Mo_8^{VI}O_{40})^{8-}$$

Equation 3.14

$$(PV_1^{IV} Mo_3^V Mo_8^{VI}O_{40})^{8-} + 2e^- \rightarrow (PV_1^{IV} Mo_5^V Mo_6^{IV}O_{40})^{10-}$$
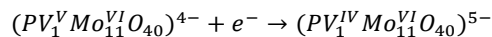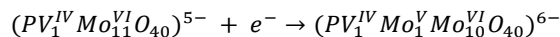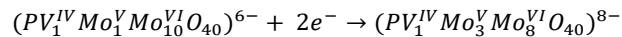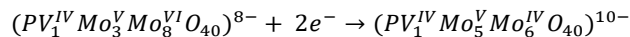
It must be noted that these equations are neither fully balanced nor have the associated counter ion species accounted for but are similar to those proposed in literature for solution phase species in organic media.[226]

Comparing cyclic voltammetry responses of phosphomolybdic acid EPPG electrodes and singularly substituted vanado-phosphomolybdic acid electrodes.

The first direct comparison of the two modified EPPG electrode types is an overlay of their corresponding responses to cyclic voltammetry, shown in Figure 3.21.
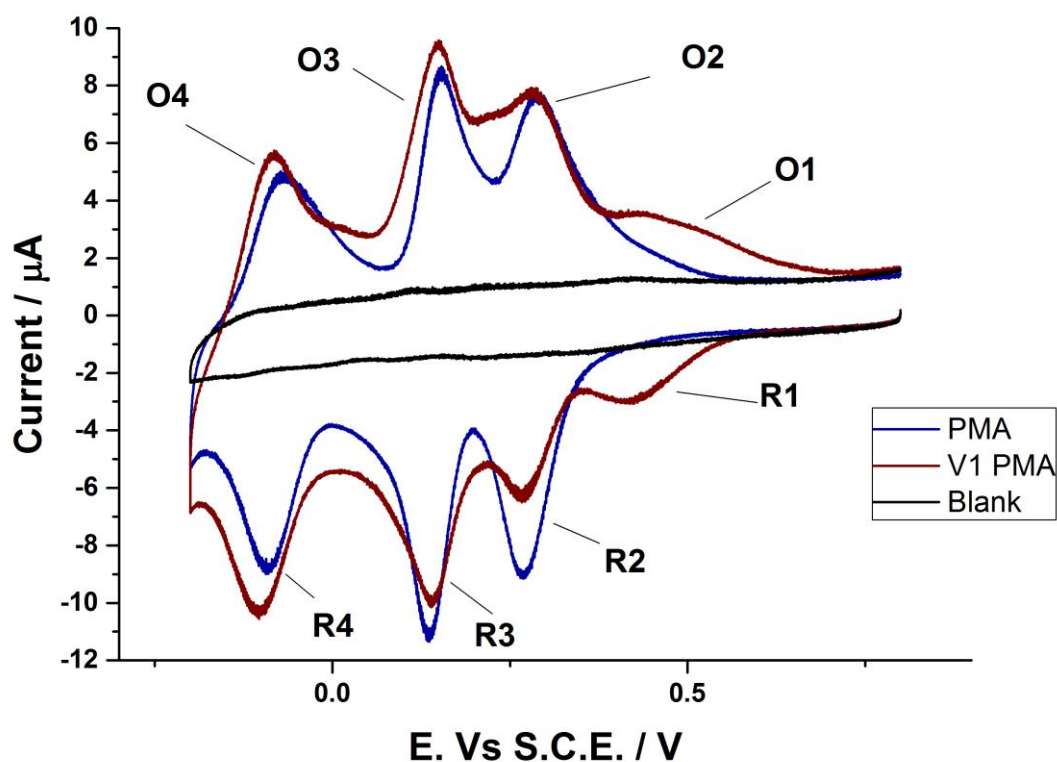
Figure 3.21 - CV responses of PMA and V1PMA modified (30 seconds dipped in 0.1 M solutions) 3 mm EPPG electrodes taken at 100 mV.s⁻¹ in 0.1 M sulphuric acid

It can be seen that the 3rd and 4th redox processes are approximately the same. However, it is evident that although the second redox processes (R2, O2) appear at the same potential a large drop in magnitude is observed. Additionally, the initial redox process (R1, O1) is not observed in the response from the phosphomolybdic acid modified electrode and present in the singularly substituted vanado-phosphomolybdic acid. This adds to the hypothesis and the equation scheme already put forward.

Comparison of charge transferred for PMA and V1PMA modified EPPG electrodes

The charge data was averaged (across scan rates) to enable a comparison, shown in Figure 3.22.
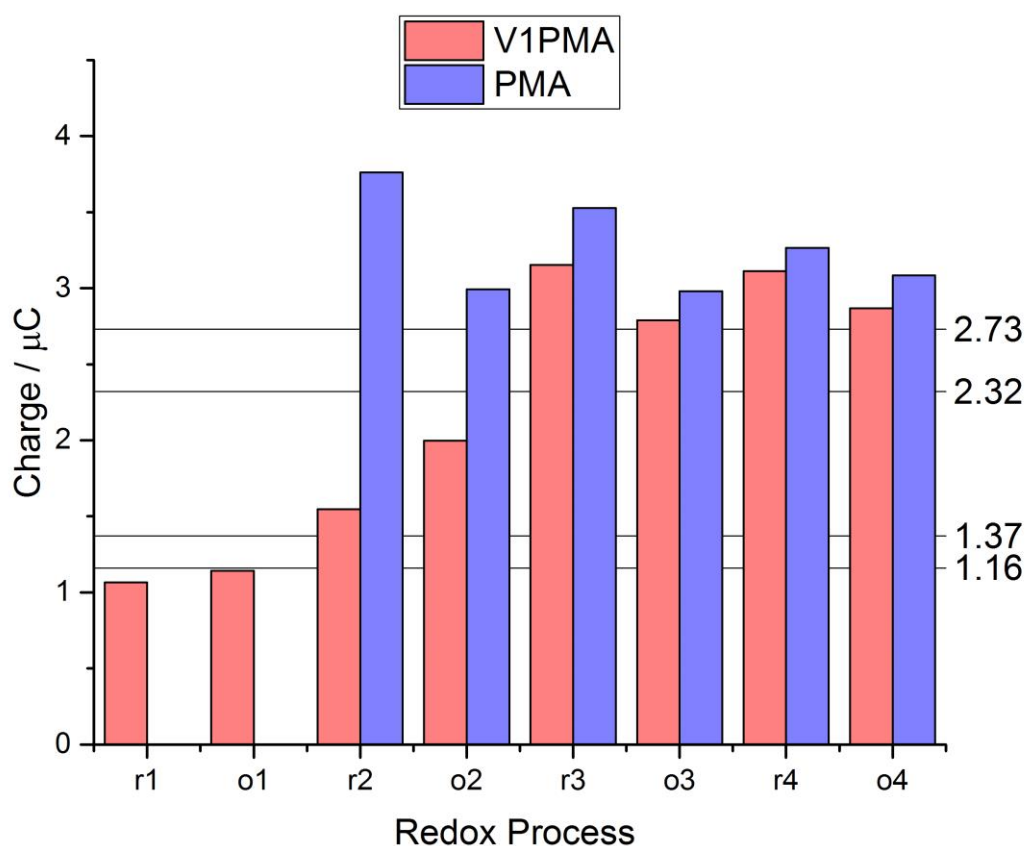
Figure 3.22 - charge comparison (averaged across scan rate) per redox process observed within cyclic voltammetry of PMA and V1PMA modified (30 seconds dipped in 0.1 M solutions) 3 mm EPPG electrodes in 0.1 M sulphuric acid

This data shows that the 1st and 2nd redox process for V1PMA modified EPPG transfers the charge associated via a one electron process. The 3rd and 4th (R3, O3, R4 and O4) are observable as two electron transfer processes matching the respective peaks in the PMA modified EPPG electrode. This data clearly supports the hypothesis for the change in redox processes, although more data would be beneficial to demonstrate this conclusively.

3.3.7 Conclusion on initial investigation

The cyclic voltammetry for phosphomolybdic acid matches previously recorded CVs. In addition, through analysis of charge transfer and peak current values it has been shown that the layer represents an approximate monolayer coverage of the surface.

Qualitatively, when comparing the two species it can be deduced that the first reduction wave has shifted. The magnitude of the shift suggests that a new reduction process has been introduced to the system with the substitution of vanadium into the species. The first reduction wave is more positive, approximately 200mV, and agrees with previous work suggesting vanadium would shift this potential in a positive direction.[190,215] It is also observed that the second wave of the substituted compound corresponds to the first of the original acid but is approximately half its peak current.

It has been shown that phosphomolybdic acid redox processes concur with ideal theoretical behaviour but upon substitution the peaks affected deviate significantly from described behaviour. This leads to the need for additional data to conclusively demonstrate that the mechanisms have shifted to those proposed. The difference in responses seen between EPPG and GC electrodes highlights the need to investigate the effect of electrode surface on the electrochemistry. With

additional data, accounting for counter ions and electrode surface, it may be possible to model the surface electrochemistry. It may also be possible with additional scan rate data and conclusive information on the shift in the electron transfer process to calculate the change in surface coverage between the two species. These aspects are the focus of investigations in Chapter 4.

4. Characterisation of Singularly Substituted Vanadophosphomolybdic acid adsorbed layers

4.1 Introduction

This chapter continues from chapter three, progressing from an initial investigation of the surface chemistry of phosphomolybdic acid derivatives to a characterization of the electrochemistry of the adsorbed layers. It considers the effect that a change in counter ion, a change in electrode material and a change of pH has on the adsorption and the subsequent electrochemistry of adsorbed layers formed by these species.

4.1.1 Effect on surface chemistry of vanadium inclusion

It has been observed that the heteropolyacid species undergoing reduction distorts but retains the polyanion structure and that this deformation increases with vanadium inclusion.[315] This may have implications for the adsorbed electrochemistry observed, leading to an increase in interaction between adsorbed species. As discussed, this can produce a peak suppression effect and a deviation from ideal behaviour, using a Langmuir isotherm (as described by Laviron[307]) and leads to the description using different isotherms, such as the Frumkin isotherm.

This effect on the electrochemistry of the species has not been fully investigated. Surface coverages of the material and the deviation caused by deformation from ideal behaviour have not been characterised.

4.1.2 Electrode Materials

The electrode material used has a large effect on these surface coverage values and in general the response of a system. It has been shown that V1PMAs have a periodicity on graphitic surfaces of 10-11 Å, these studies were performed on highly ordered pyrolytic graphite (HOPG) and additionally showed that the cation of choice effected the periodicity with caesium, and potassium increasing to 12-14 Å.[304]

Studies have shown that HPA species adsorb readily at a multitude of surfaces. Additionally, that the change in surface affects their effective surface coverages and subsequently the electrochemistry observed.[316–319] In particular, studies have used ITO, metals,[320,321] graphene oxide[294–296] and carbon nano-tubes (CNTs).[293] HPAs on titanium oxides have also received recent attention for use within photovoltaic cells.[322] It has been demonstrated that the electrode material can markedly affect the redox behaviour of the PMA and V1PMA species.[323] However, in fuel cells, batteries and other energy applications there is a need for understanding the behaviour on carbon based electrode materials.[324] As such, one aim of the chapter establishing the effects observed of changing the electrode material, several graphitic and carbon materials were chosen for investigation.

4.1.3 pH effects in surface electrochemistry

It has been observed in previous studies that the basicity of the species increases with the introduction of vanadium.[291] This has an important bearing on the effect that may be observed with pH variance. A full understanding of the role of protons within the electrochemistry of the adsorbed layers has not been developed, especially for the V1PMA species.

In general, the effect of protons within a mechanism can be first investigated by linking the equilibrium potential of an observed redox process to the pH of the experimental solution. This results, for this example, in information on the number of protons consumed for each electron transfer.

It was discussed in the conclusion to Chapter 3 that the likely reductive mechanism sees up to 6 electrons transferred to each molecule within the adsorbed layer. This leads to a large number of protons being needed to balance this charge transfer. It has been demonstrated and shown in previous literature that the mechanism and type of electron transfer observed with HPAs can often alter dramatically with pH.[190] Since data such as a Pourbaix diagram is unavailable for the particular species under investigation, it is an aim of this chapter to develop the understanding of how the electrochemical processes and the stability of the species changes across increasing pH values.

4.1.4 Effect of counter ion on heteropolyanion species

The counter ion alters many properties of the heteropolyanion.[325] Most commonly referred to in the literature is the ability to alter the solubility of the species through the cation. In addition, it has been shown that the cation affects the periodicity of the adsorbed species and as such the effective surface coverage.[304] To ensure that this effect was mitigated in these investigations, multiple cation species were used; the fully acidic PMA derivatives and the Na^+ cation derivatives.

4.2 Experimental

4.2.1 Electrode preparation

For general experimentation and where a different process is not specifically stated the electrodes were prepared as described in previous section 3.2.1.

Electrode preparation for adsorption rate experiments

To investigate the adsorption rates of the phosphomolybdic acid derivatives, the electrodes were prepared as in section 3.2.1., unless different surfaces were used as described below. The dip time was altered as described within the results and discussion section.

Basal-Plane Pyrolytic Graphite

BPPG electrodes (ALS, Japan) required a special preparation technique. This was investigated as part of the experimental work and is discussed in more detail in section 4.3.2. The standard preparation technique to produce a true basal plane was to wash the electrode in 0.1 M sodium hydroxide to chemically remove the adhered surface species. The electrode was then polished as described (section 3.2.1) however this creates a disordered multi-species terminated electrode surface. To investigate this effect adhesive tape (Sellotape, 3M) was used to remove the top surface by adhering it to the tip of the electrode and then removing; this was repeated 5 times. It was noticed that this sometimes left a 'sticky' residue on the surface which 'dulled' the electrochemical response. Therefore, numerous solvents and solutions were investigated to remove the residue without affecting the electrochemical response. Acetone was most effective at removing the residue but led to less reproducible results. The final procedure was to soak for 15 minutes in 0.1 M

sulphuric acid as it produced repeatable results and was most similar to experimental conditions. After the surface was prepared the modification step was performed identically to all other electrode experiments.

Cell Preparation

A standard three electrode electrochemical cell set-up was used throughout, connected to an Ivium compactstat potentiostat (Alvatek, UK) controlled by an external PC using IviumSoft (Alvatek, UK) software. The counter electrode was a high surface area bright platinum gauze. Two reference electrodes were used in experimentation, a saturated calomel electrode (ALS, Japan) and a saturated Ag/AgCl (CH Instruments, UK).

The electrolyte was varied with experiment where required. A stock solution of 0.5 M sulphuric acid was prepared for every experiment from concentrated sulphuric acid (s.g. 1.83, Sigma Aldrich) and ultrapure water of resistivity not less than 18.2 MΩ.cm (Milli-Q, Millipore). These solutions were diluted where required to 0.1 M as a standard electrolyte. pH was controlled through the addition of sodium hydroxide (Sigma Aldrich, UK) and the addition of the original 0.5 M stock solution, and monitored with a pH meter (Mettler-Toledo International Inc.). Other electrolytes were used such as 0.1 M perchloric acid (Sigma Aldrich, UK) and 0.1 M HCl (Sigma Aldrich) to ensure no effect of electrolyte was observed. Before each experiment electrolyte solutions were purged with nitrogen gas for 20 minutes.

4.3 Results and discussion

Chapter 3 focused on establishing a protocol for experimentation with PMA and V1PMA. This allowed for a basic hypothesis to be formed around the redox phenomena observed and the effect of substituting vanadium into the phosphomolybdic heteropolyanion.

This chapter develops this understanding, exploring the effects caused by changing the following: counter ion species, the electrode surface and pH. This allows for a much more detailed and comprehensive view on the adsorption behaviour at different surfaces, the nature of the adsorbed species and the mechanism involved in electron transfer.

4.3.1. Counter ions in singularly substituted vanado-phosphomolybdic acid

An area that was lacking in the initial study was the effect of the counter ion species on the redox process. ACAL Energy Ltd. have studied the effect in detail on the catalysts that they currently use and were able to supply a second sample of V1PMA. The studies in chapter three used the sodium version of the vanado-phosphomolybdic anion, formally, $[NaH_3][PV_1Mo_{11}O_{40}]$ and the protonated corresponding parent phosphomolybdic acid, $[H_3][PMo_{12}O_{40}]$. This first section of chapter 4 considers the fully protonated singularly substituted vanado-phosphomolybdic acid species, $[H_4][PV_1Mo_{11}O_{40}]$ to investigate the effect of a switch in counter ion. For ease and to clarify which species is being considered the denotation HV1PMA is used for protonated singularly substituted vanadophosphomolybdic acid and NaV1PMA for the sodium species.

It has been shown in several studies that the electronegativity and composition of the cation used to support the heteropolyanion has an effect on the chemistry of the anion.[326] Some debate remains about the ability of cation electronegativity to affect the redox potentials of phosphomolybdovanadic acid.[327]

EPPG electrodes were initially used, but additional electrode materials were investigated. The response of the modified EPPG electrodes is shown in Figure 4.1. It was a concern that the change in counter ion species could result in a difference in adsorption behaviour; this is discussed further in section 4.3.2. In this study the prerequisite 30 seconds dipping time is maintained.
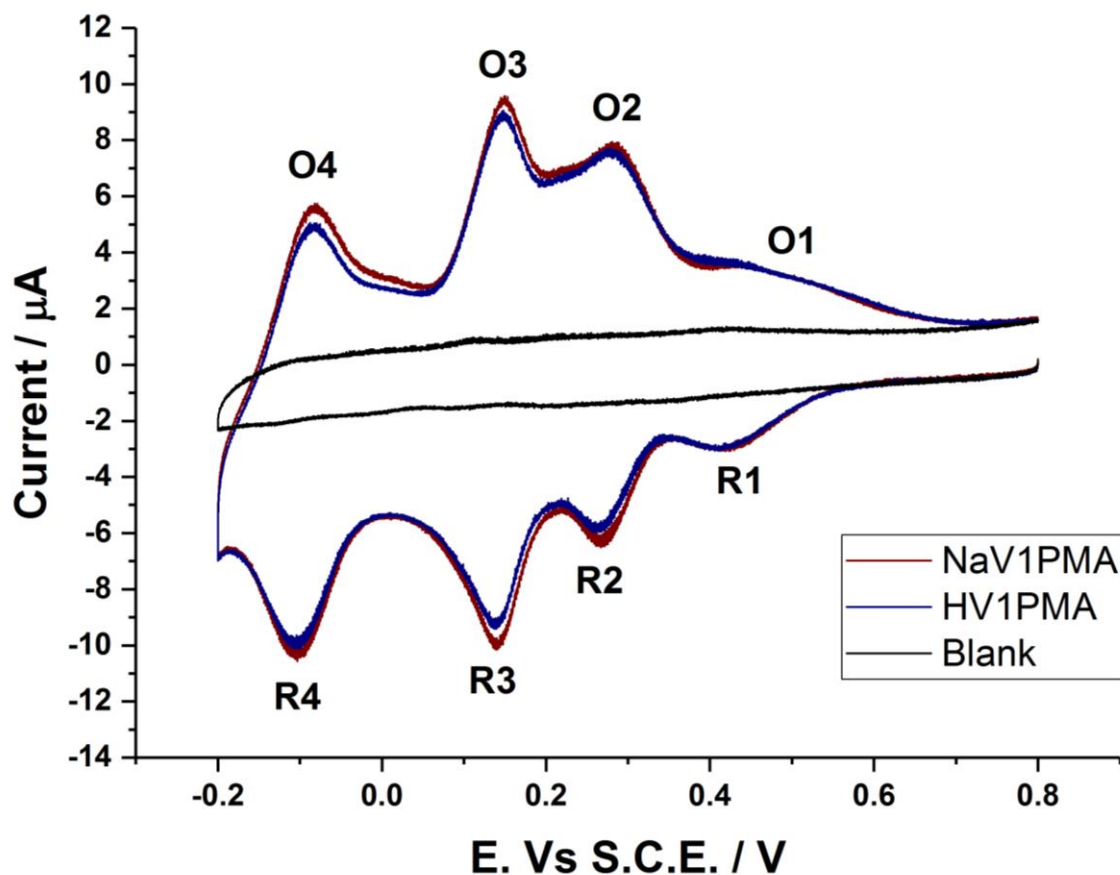
Figure 4.1- Cyclic voltammograms taken at 100 mV.s^{-1} in 0.1 M sulphuric acid of 3 mm EPPG electrodes, modified by dipping in solutions for 30 seconds of NaV1PMA and HV1PMA

150

Interestingly there is no observable difference in the two samples using different counter ions. This leads to the conclusion that the adsorbed layer response in unaffected by this switch in counter ion. The fact that no change is observed in subsequent electron transfers suggests that the species that acts to balance the charge transferred is not changed, as the diffusional rates must be (approximately) constant. This is expected under these conditions (at pH 1) as the number of protons available as part of the electrolyte support fair outweighs the effective presence of Na^+ ions.

It is surprising that no difference is observed as the change in size of the counter ion could have influenced the effective volume of the species to be adsorbed. However, this suggests that only the polyanion is adsorbed and the effective change in volume is negligible with a switch between Na^+ and H^+ counter ion species.

The previous chapter highlighted that the redox process denoted R4 in Figure 4.1 is relatively unperturbed and is the peak to follow closest to ideal redox behaviour. Using peak current values obtained for R4, through the same baseline correction applied in chapter 3, and plotting against dip time for the modification, it can be considered whether the switch in counter ion has produced any significant change in the adsorption rate.
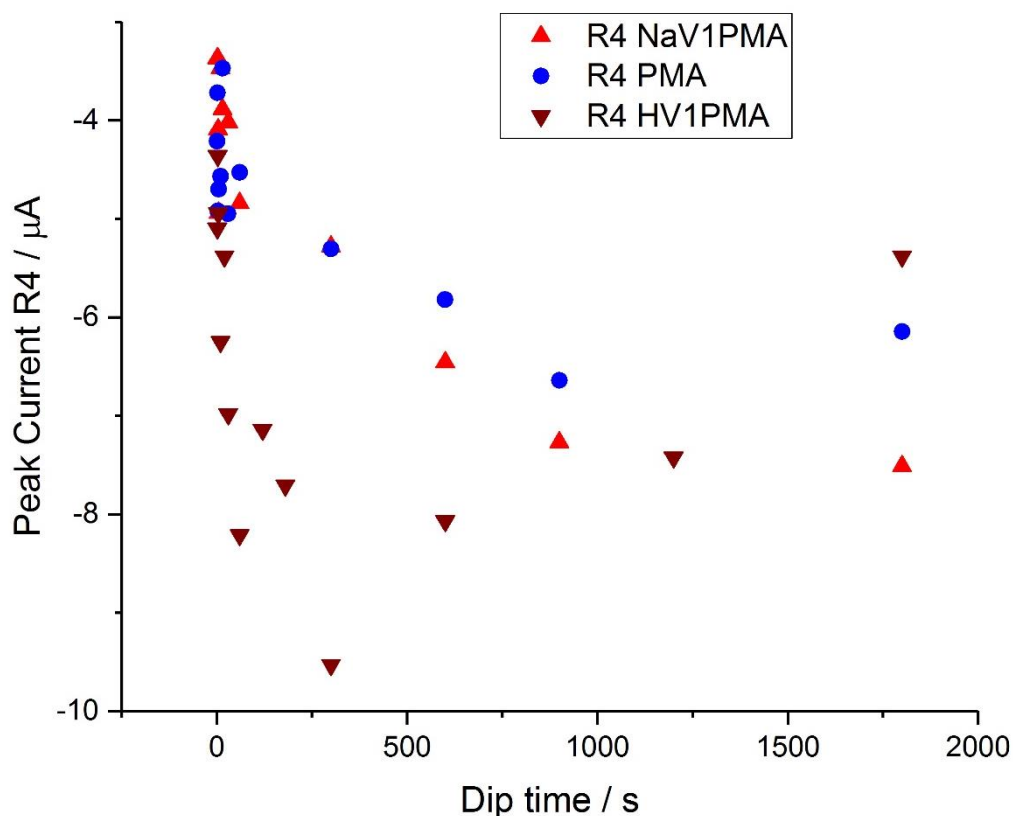
Figure 4.2 - Peak current of reduction process R4 obtained from cyclic voltammetry of 3mm EPPG electrodes modified by dipping in solutions of PMA, NaV1PMA and HV1PMA, taken in 0.1 M sulphuric acid at 100 mV.s⁻¹

The plot in Figure 4.1 shows that the adsorption process is similar across the PMA derivatives, in that the magnitude of the peak current establishes itself within a short dip time. There appears to be a small difference with the HV1PMA species, establishing a higher peak magnitude in a shorter dip time. However, the spread in values makes a conclusion difficult to draw.

4.3.2 Effect of electrode surface on the adsorption effects and the redox chemistry

In chapter 3 the difference between a GC electrode surface and an EPPG electrode surface was seen. Invariably when concerned with carbon surfaces the predominant bulk material discussed is

of a graphitic nature, due to its conductivity and relative ease of manufacture, even within its different forms. It is now possible to obtain graphitic materials with various densities and, when in electrode form, specific surface structures.

This section explores the effect of various carbon based electrode surfaces and the effect that these have on the electrochemical response of the adsorbed layers. Although not described here, metallic electrodes; platinum and gold, as well as semi-conductor materials such as indium doped tin oxide, were also trialled. These were trialled in early studies before rigorous protocols were in place and as such aren't shown.

An EPPG electrode was used extensively in chapter 3 and here it forms a baseline for comparison to other electrodes. It was seen in Chapter 3 that the cyclic voltammetry responses of layers produced on GC and EPPG were distinct although of similar magnitudes. The change did not affect the potential position of the redox processes but were closer to ideal behaviour for EPPG then for GC. The following sections widens to more carbon electrode surfaces.

Basal-Plane Pyrolytic Graphite Electrode

The Basal-Plane Pyrolytic Graphite Electrode (BPPG) is a particularly interesting case the basal plane provides a different surface structure, one that is parallel to the graphitic planes within the HOPG structure. In addition, the plane is highly stable with few defects across the plane and low-energy surface groups. The low concentration of oxygen containing terminal groups (when

compared to EPPG) was of interest to this project as the adsorption of the heteropolyanion may be associated with the outer sphere oxides of the Keggin species.

To render a true Basal-plane the electrode must be cleaned electrochemically and then sellotape used to remove the top layer of material to reveal a 'fresh' basal-plane. In practice this was not sufficient to generate a clean electrochemical response from the electrode surface. This is suspected to be a result of ingress of the PMA and its derivatives into the graphitic layers.

In order to obtain a 'clean' electrochemical response, with no residual redox phenomena relating to PMA species, the electrode had to be soaked in NaOH and polished, following the same procedure as with other electrode materials. It could be argued that this methodology could fracture the basal-planes leading to an increasing character of an edge-plane pyrolytic graphite electrode. Unfortunately, this was the most effective method to obtain a blank scan and so the reduction in reliable basal-plane character had to be accepted and noted when analyzing the data.

Figure 4.3 shows the response of PMA modified BPPG electrodes with various pre-treatments before modification with PMA. It can be seen that when the surface was produced by using sellotape to remove the top basal-plane layers a significant reduction in electrochemical response resulted. However, it was observable that significant residue was left on the surface on the electrode after using the sellotape, effectively reducing the size of the electrode surface area, which would lead to the effective suppression in the peaks. Several types of sellotape where trialled, with 3M sellotape leaving the least observable residue, and producing the data shown in Figure 4.3.
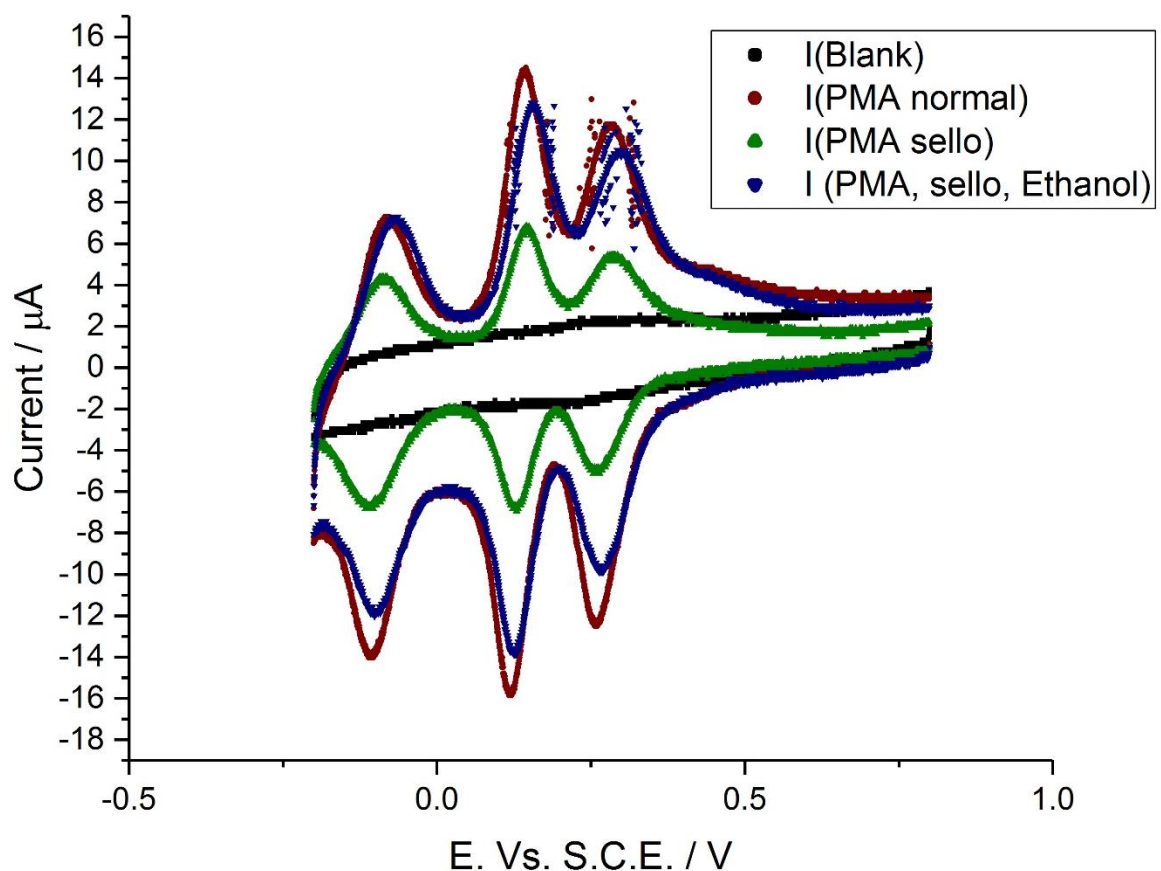
Figure 4.3 – Cyclic voltammetry taken in 0.1 M sulphuric acid at 100 mV.s^{-1} of 3 mm BPPG electrodes modified by dipping in 0.1 M PMA solution for 30 seconds. The BPPG surfaces have been prepared with slightly different techniques. The blank electrode is unmodified. The normal electrode has been prepared via the same preparation as all other electrodes. The sello electrode has been polished then the surface prepared with 3M sellotape. The ethanol electrode has been prepared with polishing, 3M sellotape and then a wash in ethanol.

To try and overcome the issue with surface residue the BPPG electrodes were exposed to organic solvents after the use of sellotape but before modification to remove the residue. The results for a BPPG electrode that was soaked in ethanol is presented in Figure 4.3. Acetone and acetonitrile resulted in vastly suppressed responses and left a visible sheen on the surface.

It can be observed from the data that using ethanol results in a response which is not vastly depressed but is still significantly reduced. The most significant observation is the apparent shift

in peak position. The onset values for reduction are the same but the peak position is shifted positive. These two observations lead to a hypothesis that the surface coverage has reduced but the surface possess a more ordered structure.

Once a methodology for preparing a repeatable surface was established, the modified electrode's response was compared to the EPPG electrode. Figure 4.4 shows the difference in electrochemical response.
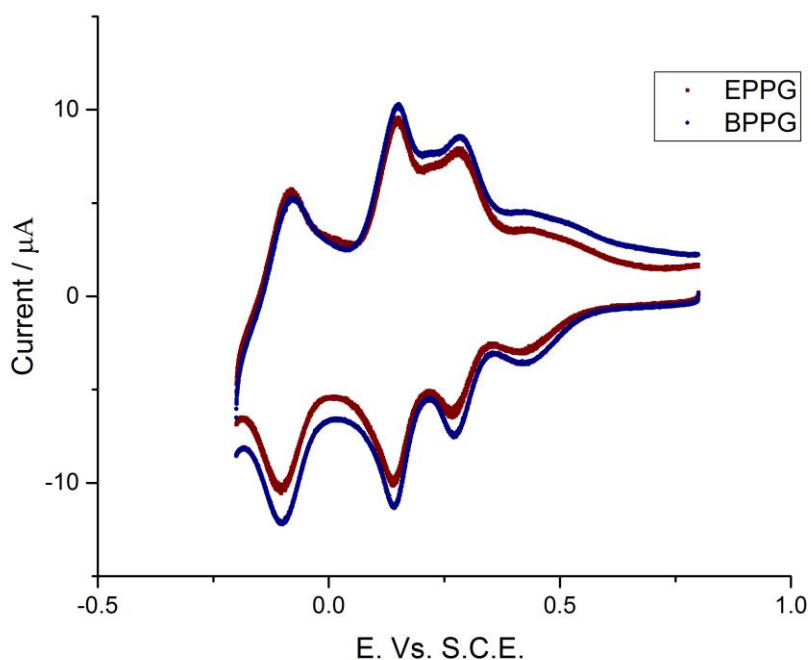
Figure 4.4 -Cyclic voltammetry of 3mm EPPG and BPPG electrodes modified by dipping in 0.1 M NaV1PMA solution for 30 seconds, taken in 0.1 M sulphuric acid at 100 mV.s^{-1}

It can be seen from the figure that the two electrodes behave remarkably similarly but that it appears the BPPG electrodes produce a slightly higher current response. This goes against what might be expected for BPPG electrodes, as theoretically it is a lower energy surface and a more difficult

surface for the phosphomolybdic acid derivatives to adsorb to. However, the difference is within the error of electrode surface area and so if the adsorption of the phosphomolybdic acid species is the same on both electrodes the data would suggest there is no real difference once the two electrode surface types have been modified.

Monitoring the electrochemical response against dip time to elucidate adsorption behaviour for BPPG, the same behaviour was observed as has been seen for EPPG surfaces (Figure 4.5).
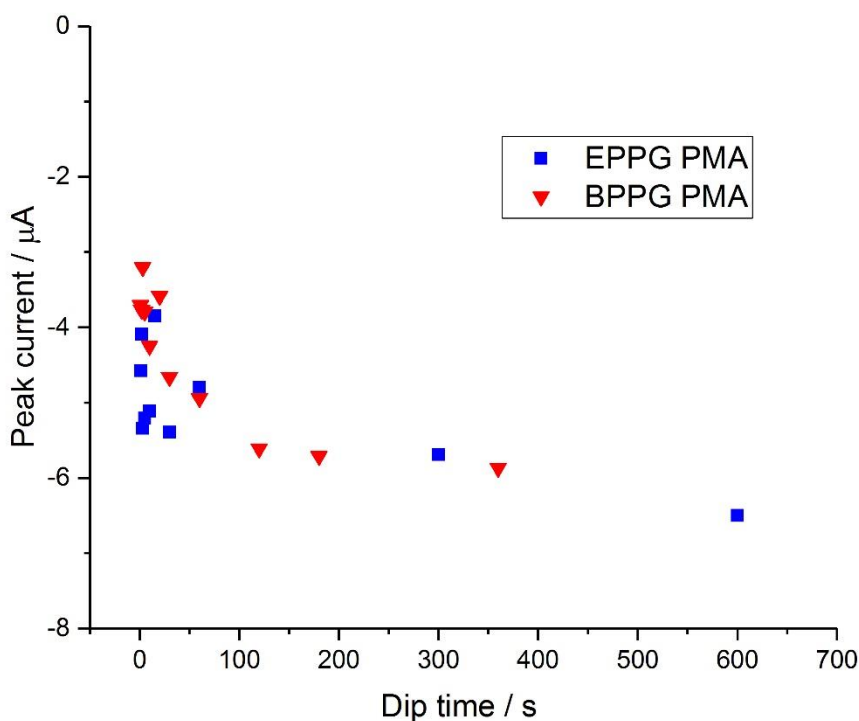
Figure 4.5 – Peak current responses for reduction process R4 within cyclic voltammetry for EPPG and BPPG electrodes modified by dipping in 0.1 M PMA solution, taken at 100 mV.s^{-1} in 0.1 M sulphuric acid.

The adsorption behaviour of PMA on BPPG were remarkably similar to that of EPPG. When also comparing the effect with NaV1PMA the similarity is again observed, Figure 4.6.
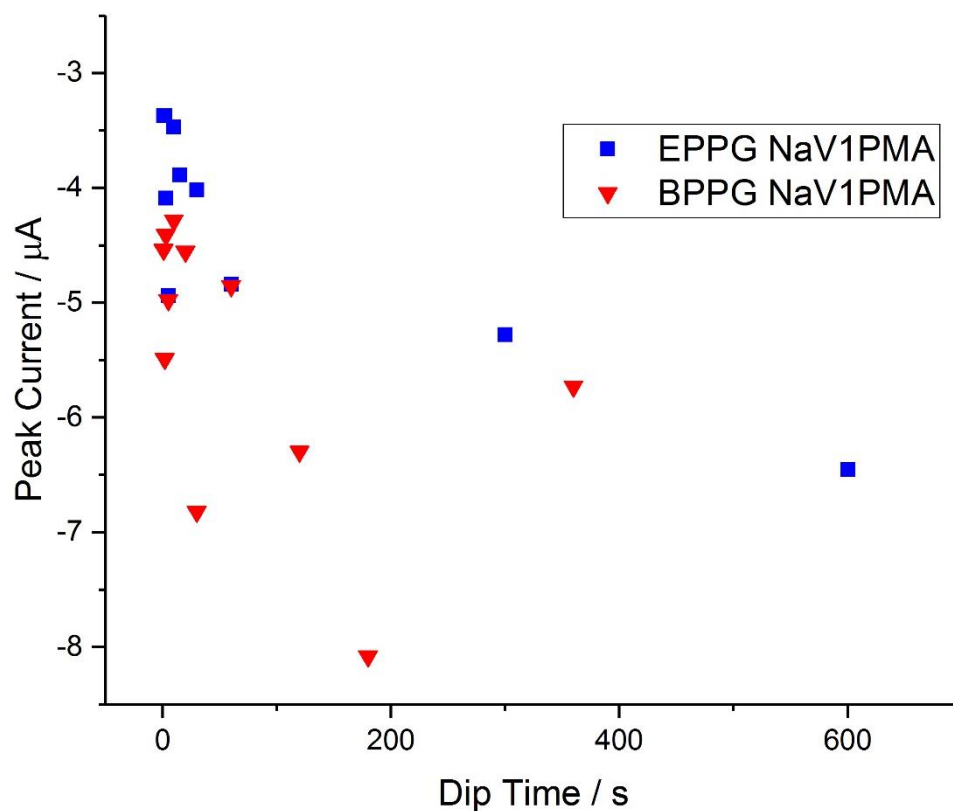
Figure 4.6 - Peak current responses for reduction process R4 within cyclic voltammetry for EPPG and BPPG electrodes modified by dipping in 0.1 M NaV1PMA solution, taken at 100 mV.s⁻¹ in 0.1 M sulphuric acid.

Figure 4.6 shows a greater spread of peak current values for the R4 reduction of NaV1PMA layers on BPPG. It is possible that the difficulty in preparing surfaces has contributed to this spread in values. In addition, it makes it difficult to fully characterise the process of adsorption at this stage.

Plastic Formed Carbon Electrode (PFCE)

PFCE electrodes are a different type of carbon electrode from either the GC electrode surface or the HOPG electrodes. The method used to create the surface forms a very dense material with an irregular surface compared to HOPG and GC when it has been tested in previous studies.[328,329]

Qualitatively it was an easier electrode material to handle then BPPG, and the same methods used to obtain a clean scan as for GC and EPPG could be used. The electrochemical response was markedly different in magnitude then for the previously explored electrodes as can be seen in Figure 4.7.
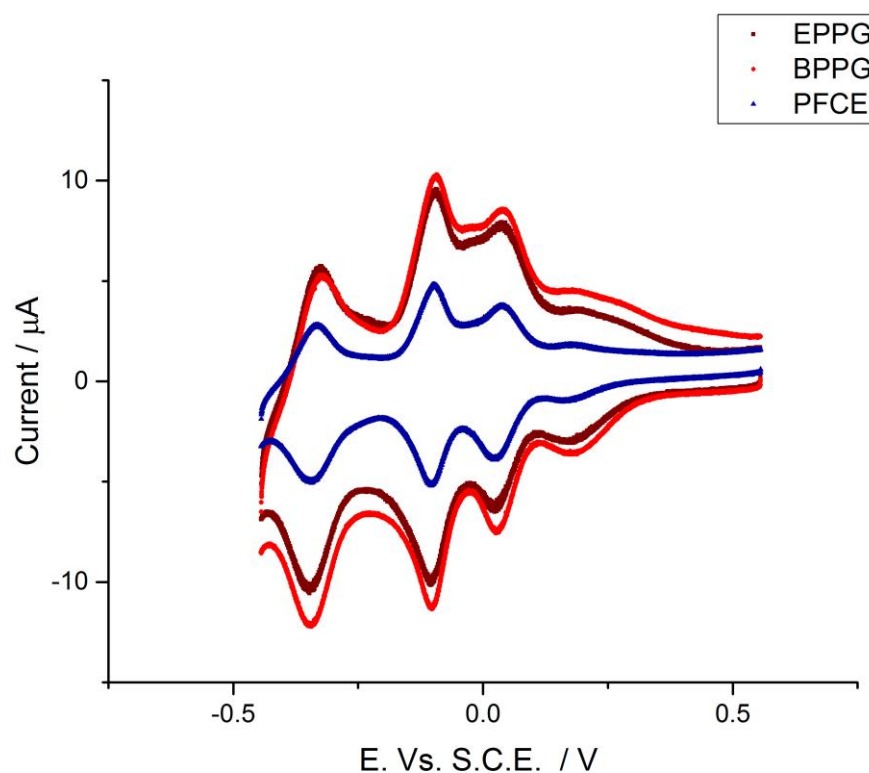
Figure 4.7 Cyclic voltammetry of 3mm EPPG, BPPG and PFCE electrodes modified by dipping in 0.1 M NaV1PMA solution for 30 seconds, taken in 0.1 M sulphuric acid at 0.1 mV.s^{-1}

However, the ratio of charge transferred in each process is maintained, and charge values are not as disparate as the peak current magnitudes. It is also observable that the capacitance and layer

resistance values are contributing as much to the peak current magnitude and that after baseline correction the values become much more similar.

It is apparent that the surface coverage of species is slightly reduced and this is explored when calculating values for surface coverage, in a later section, after the number of electrons transferred in each process is confirmed. The PFCE was also 'easier' to clean then other electrodes, with fewer scans being affected by residual electrochemical responses after cleaning. This may be a sign that due to the denser material, the ingress effect is reduced and that this effectively reduces the size of the electrochemical response. The effect of dip time was also affected in the same way, Figure 4.8.
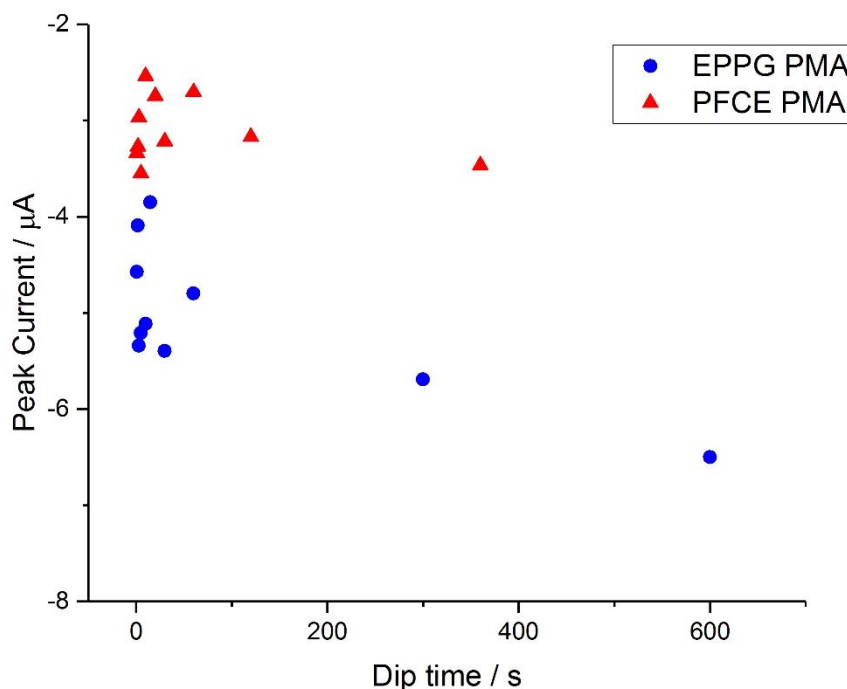
Figure 4.8 – Peak current of reduction R4 taken from cyclic voltammetry of 3mm PFCE electrodes modified by dipping in 0.1 M PMA solution, taken in 0.1 M sulphuric acid at 100 mV.s[1].

Figure 4.8 shows the adsorption effect seen at the PFCE surface. It is the same pattern as previously seen with GC, EPPG and BPPG electrodes, in that the magnitude of current response is established

at fairly low dip times. The peak current was considerably less than for other carbon electrodes for both PMA, Figure 4.8 and NaV1PMA, Figure 4.9, modified electrodes.
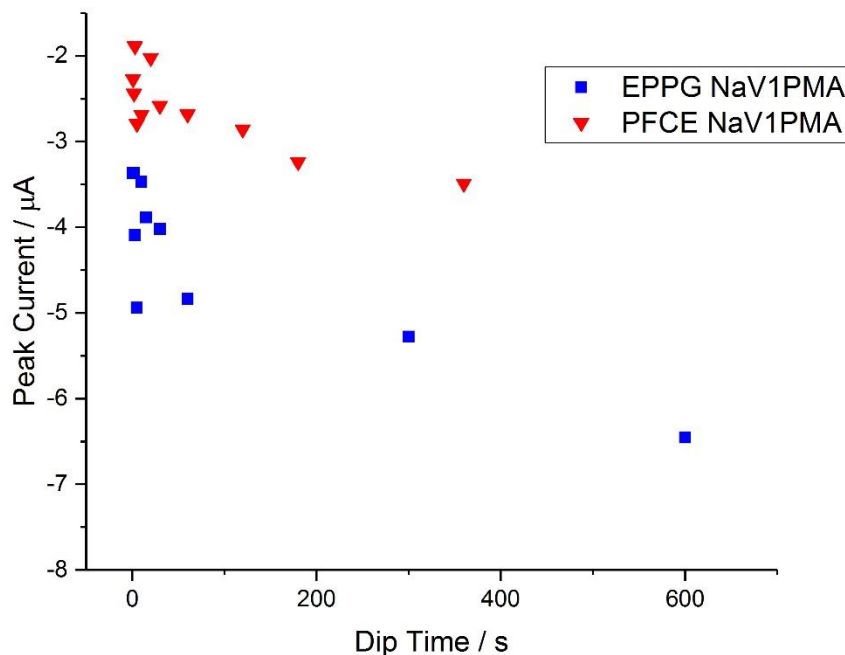
Figure 4.9 Peak current of reduction R4 taken from cyclic voltammetry of 3mm PFCE electrodes modified by dipping in 0.1 M NaV1PMA solution, taken in 0.1 M sulphuric acid at 100 mV.s^{-1}.

Comparing Adsorption Rates across electrodes

The sections above have covered the separate adsorption seen at each of the surfaces. Although the magnitudes are slightly different between the different electrodes the predominant patterns remain. The magnitude of peak current is quickly attained before settling to an apparent slow increase of response with dip time. It is also observable that there is little difference between the two counter ion species of singularly substituted vanado-phosphomolybdic acid.

It is difficult to fully analyse this relationship due to the time periods used for the dip time. This leads to a large uncertainty and an observable spreading in experimental values. The need to rinse

and dry the electrode after dipping introduces a large uncertainty in the time that the electrode is exposed to a certain species, and adds a disproportionate error, the error being larger at shorter dip times. To help analyse this relationship, different concentrations of dipping solutions was used, shown in Figure 4.10.
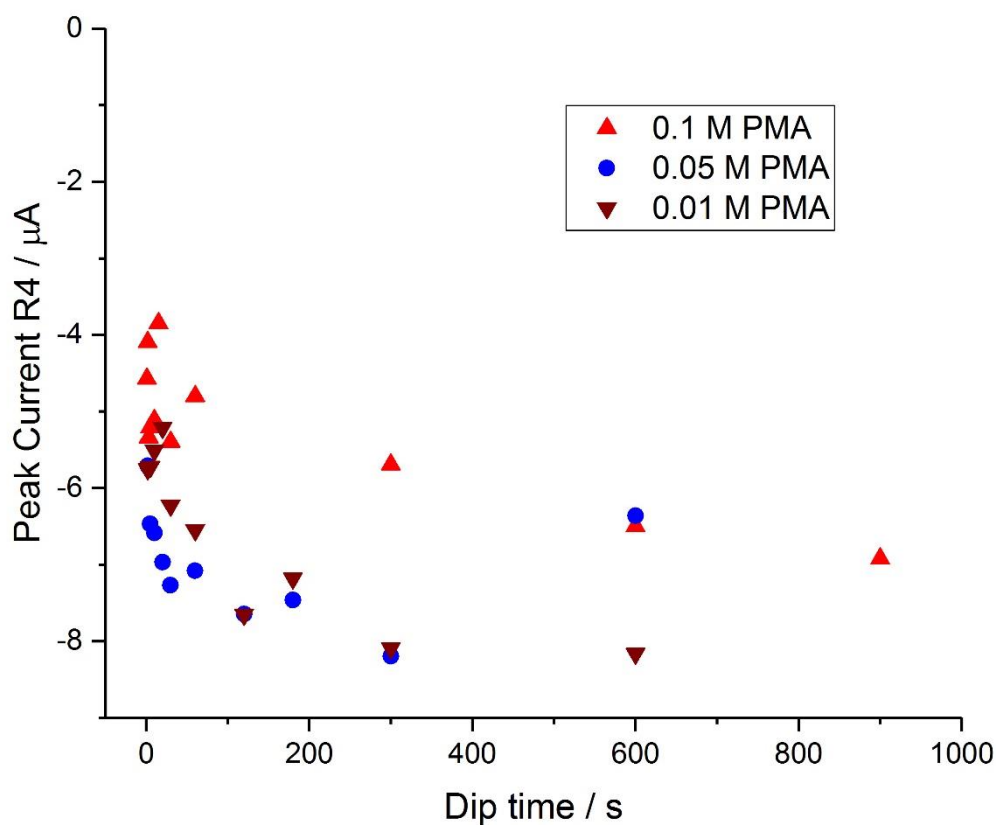
Figure 4.10 – Peak current for reduction process R4 for 3 mm EPPG electrodes modified by dipping in 0.1 M, 0.05 M and 0.01 M PMA solution, taken at 100 mV.s^{-1} in 0.1 M sulphuric acid

The data in Figure 4.10 shows that the concentration of the dipping solution seemingly has little influence on the rate in adsorption response. It was deemed that extending to lower concentrations would neither add any additional insight, without a higher degree of error, nor bear a resemblance to real-life conditions inside a fuel cell.

Charge Transfer at different electrodes

Chapter 3 showed that by calculating the charge transferred through each redox process an idea of the number of electrons for each process can be attained. Each species was put through a series of scan rates as adsorbed layers on each graphitic surface. The charge transferred under each peak was calculated as in chapter 3. The oxidative and reductive charge for each process was averaged and this allows for a plot of scan rate normalized, absolute charge per redox process, as shown in Figure 4.11.
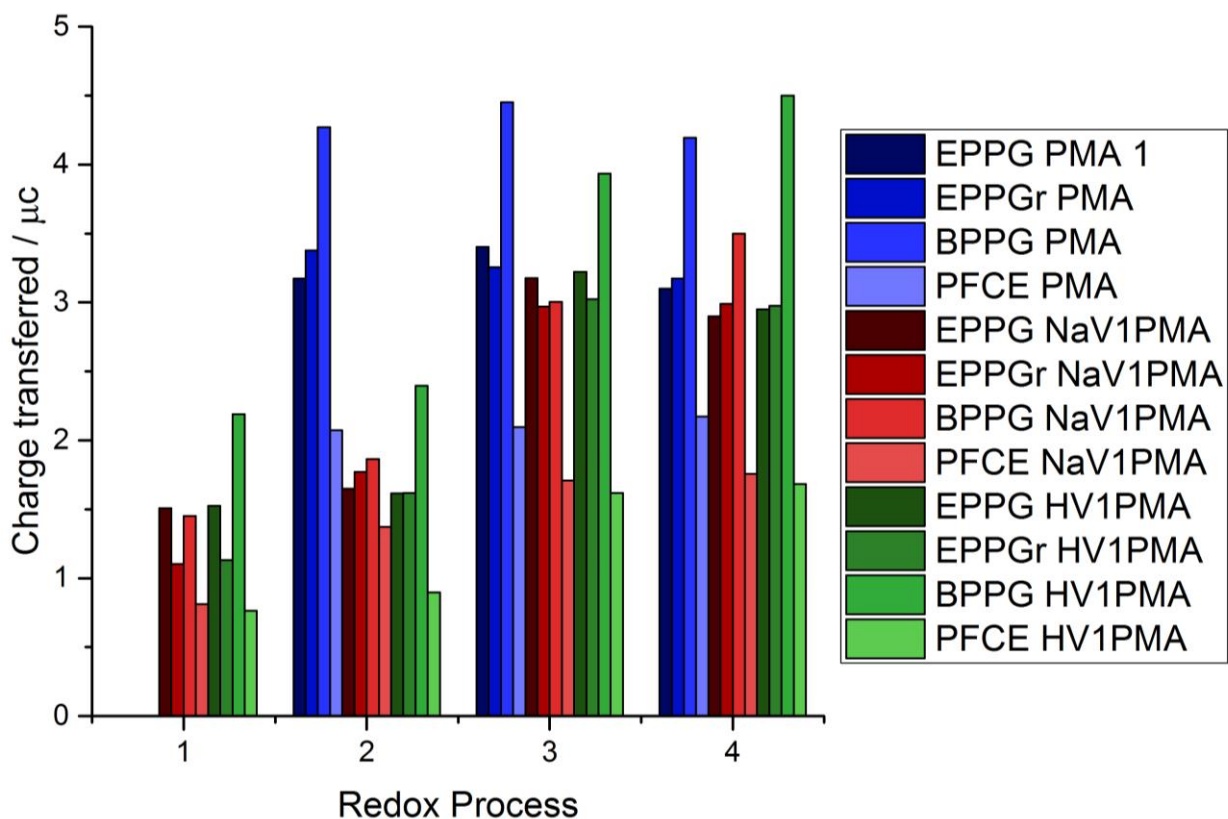
Figure 4.11 - Charge transferred through each redox process across the phosphomolybdic acid species and electrode surfaces normalised for scan rate

It can be seen from the data (Figure 4.11) that clearly the initial redox process (1) and the second redox process (2) of the vanadium substituted species is about half of the initial redox process (2) of the parent phosphomolybdic acid. It is also clear that the pattern seen across the electrode materials is still present in the data, once normalized for scan rate. To remove this pattern from the data, to allow for electron number comparisons, the data is averaged across electrode material (left, Figure 4.12). As has been shown in previous studies, each redox process in the parent phosphomolybdic acid anion is a two electron process.[217,285] It has been seen in previous section that the second redox process exhibited by phosphomolybdic acid is the process which most closely follows ideal behaviour. The charge transferred through this process is factored to reference two electrons (as all other factors are constant across the samples, once all the averages have been applied), this allows for a comparison to see how many electrons are transferred in the other processes and in the cases of the vanadium substituted species (right, Figure 4.12).
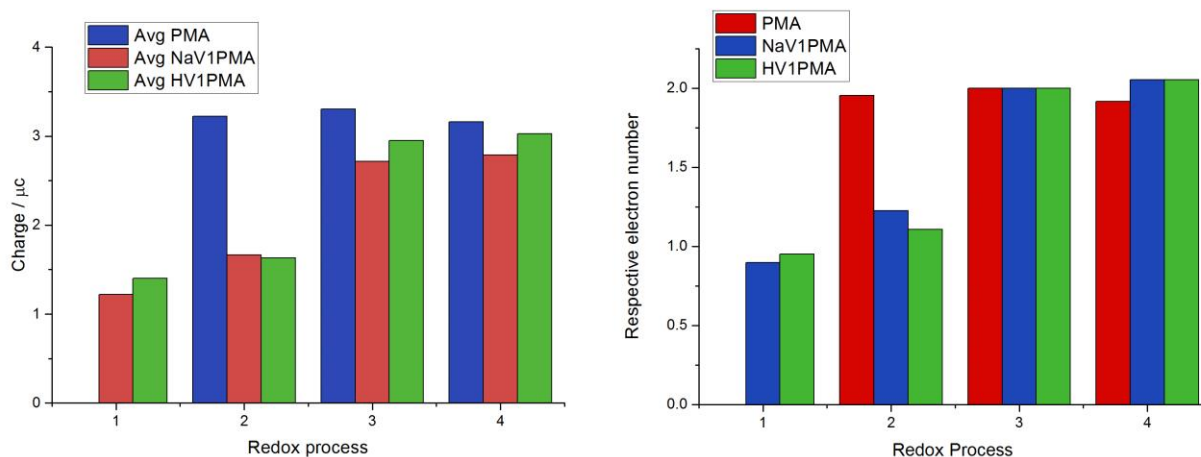
Figure 4.12 - collected and averaged charge values for phosphomolybdic acid derivatives (left) and the referenced charge values to represent a two electron transfer process for PMA at process 3 (right)

164

Figure 4.12, helps to conclusively show that the mechanism put forward in chapter 3 (and shown below) involves the correct number of electrons in each process.

Equation 4.1

$$(PV_1^V Mo_{11}^{VI} O_{40})^{4-} + e^- \rightarrow (PV_1^V Mo_{11}^{VI} O_{40})^{5-}$$

Equation 4.2

$$(PV_1^V Mo_{11}^{VI} O_{40})^{5-} + e^- \rightarrow (PV_1^{IV} Mo_1^V Mo_{10}^{VI} O_{40})^{6-}$$

Equation 4.3

$$(PV_1^{IV} Mo_1^V Mo_{10}^{VI} O_{40})^{6-} + 2e^- \rightarrow (PV_1^{IV} Mo_3^V Mo_8^{VI} O_{40})^{8-}$$

Equation 4.4

$$(PV_1^{IV} Mo_3^V Mo_8^{VI} O_{40})^{8-} + 2e^- \rightarrow (PV_1^{IV} Mo_5^V Mo_6^{IV} O_{40})^{10-}$$
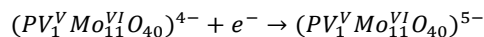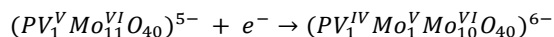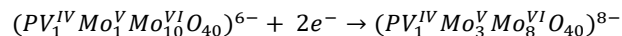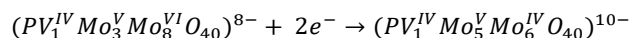
This shows that the adsorbed layer redox processes follow the same mechanisms observed in similar HPAs in organic media and those for the vanadium species proposed in solution by Nambu.[226]

Surface coverage determination through charge transfer

Through taking the values of charge transferred in each redox process above, the surface coverage can be calculated. This is done through taking the charge transferred and dividing it by, the number of electrons transferred in the process, surface area and then the Faraday constant, for each species on each surface.

	PMA (10^{-10} mol.cm^{-2})	NaV1PMA (10^{-10} mol.cm^{-2})	HV1PMA (10^{-10} mol.cm^{-2})
EPPG	2.38	2.21	2.20
BPPG	3.16	2.41	3.23
PFCE	1.55	1.44	1.21
Average	2.37	2.07	2.21

Table 4-1 surface coverage for each species at each surface calculated through charge

As can be seen most of these surface coverage values are close to those previously observed,[217,304] especially when surface roughness is taken into consideration. It must be noted that all values for the BPPG are higher than would be expected, this may come from the imperfect surface.

4.3.3 Effect of pH on surface redox chemistry

One important variable in experimentation is the pH of the electrolyte solutions. In experiments, multiple electrolytes were trialled, the data so far has been presented using sulphuric acid as the supporting electrolyte. Phosphoric acid, hydrochloric acid, potassium chloride, potassium nitrate, sodium hydroxide, and sodium phosphate were all used to investigate the effect of the electrolyte. It was found that the supporting electrolyte did not affect the redox behaviour seen, as long as the pH was kept constant. However, a dramatic shift in behaviour was observed with pH. Indeed, the most effective method for 'cleaning' the electrodes was to immerse the electrode in 0.1 M sodium hydroxide solution.

This dramatic shift points to a change in stability of the adsorbed species, as has been seen with similar heteropolyacids in previous studies.[190] Several electrolyte solutions were prepared at various pHs and the electrochemical response to cyclic voltammetry was recorded for all phosphomolybdic species on all electrode surfaces. In addition, at several points full scan rate analysis was conducted and degradation studies performed. Finally, several studies were completed starting either at very low or very high pH, with additions made to the solution to sequentially raise or lower the pH to give data across the whole pH range and with multiple electrolyte species.

General observations on the effects of pH

As described above all phosphomolybdic species were investigated on all the graphitic electrodes surfaces mentioned. The data was collected and sorted by scan rate, phosphomolybdic acid type and electrode surface. Figure 4.13 shows the example CVs at a pH of 0.8 and at 2.6.
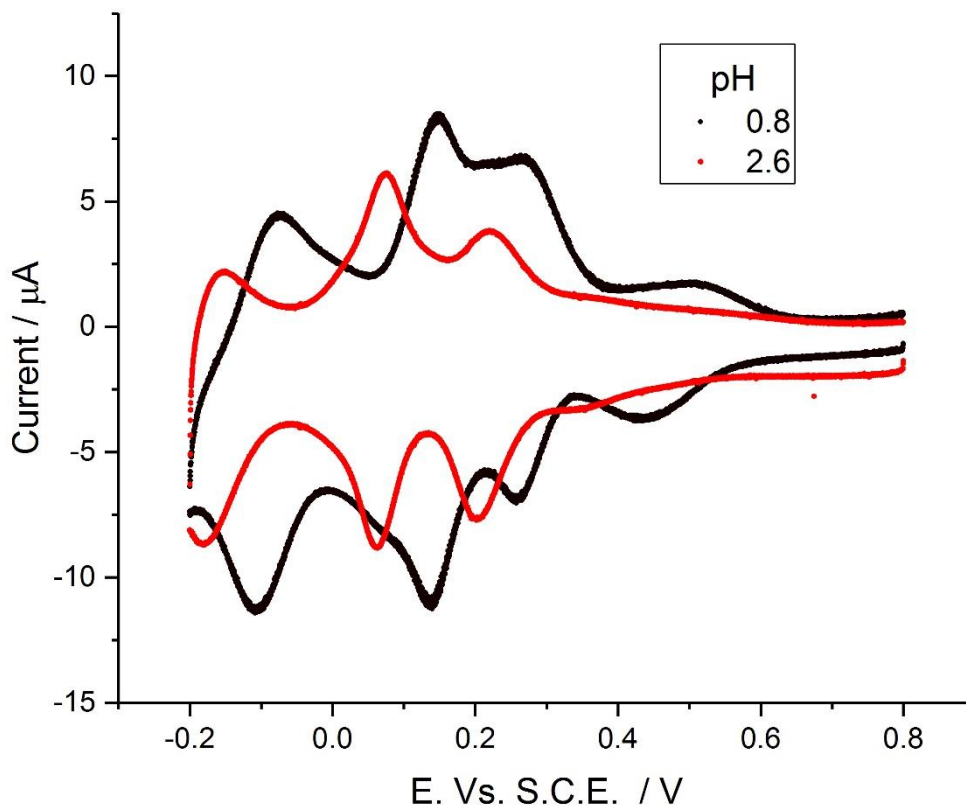
Figure 4.13 – cyclic voltammetry of two 3 mm EPPG electrodes modified by dipping in 0.1 M NaV1PMA solution for 30 seconds, taken at 100 mV.s⁻¹, at a pH of 0.8 and a pH of 2.6. The electrolyte is 0.1 M sulphuric acid, with added aliquots of 0.1 M NaOH and 0.5 M sulphuric acid to achieve the desired pH which was measured with an in-situ pH meter.

Figure 4.13 shows the dramatic effect on the response that a change in the electrolyte pH has on the redox processes, similar to previous studies.[226] The plots demonstrate that as pH increases there is a significant shift negative and a fall in current. The response is further altered at higher pH, moving towards alkaline conditions as shown in Figure 4.14
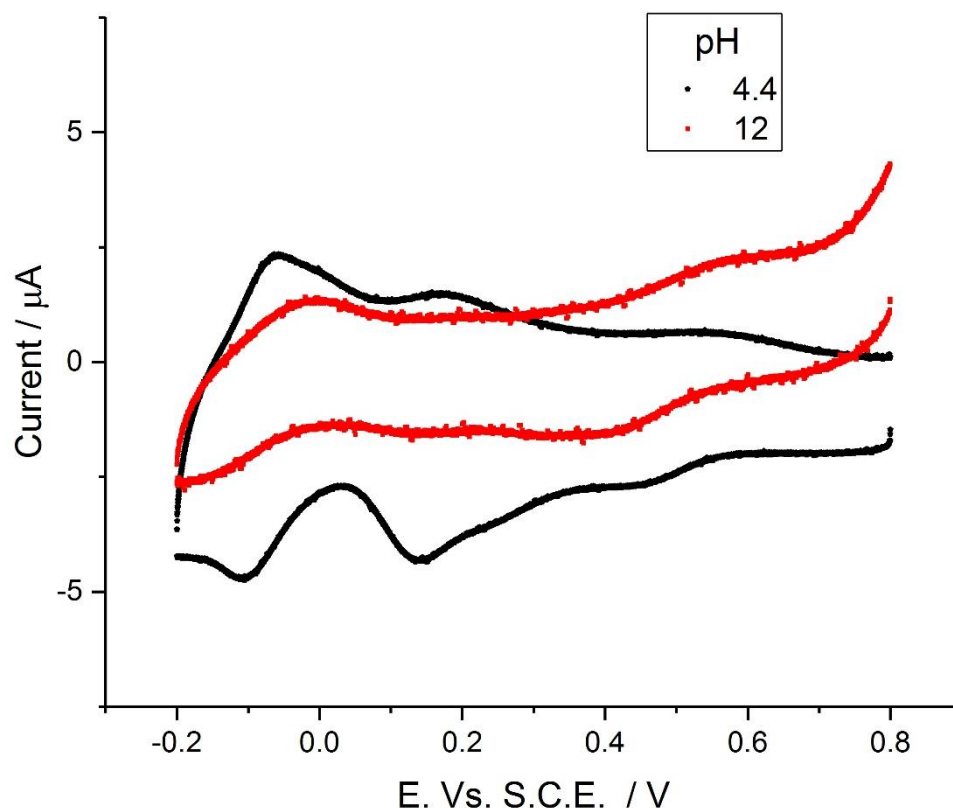
Figure 4.14 - cyclic voltammetry of two 3 mm EPPG electrodes modified by dipping in 0.1 M NaV1PMA solution for 30 seconds, taken at 100 mV.s^{-1}, at a pH of 4.4 and a pH of 12. The electrolyte is 0.1 M sulphuric acid, with added aliquots of 0.1 M NaOH and 0.5 M sulphuric acid to achieve the desired pH which was measured with an in-situ pH meter.

It shows that as pH proceeds towards alkaline pH values the response tails off, no longer representative of the redox behaviour at low pHs. This trend was observed across all phosphomolybdic acid derivatives at all electrode surfaces, and is different from behaviour of larger crown polyoxometalates[330] but similar to other heteropolyacids.[286,300,331,332]

Figure 4.15 shows the effect of altering pH on electrodes modified with phosphomolybdic acid. Showing the same general trend in cyclic voltammetry response as for electrodes modified with NaV1PMA.
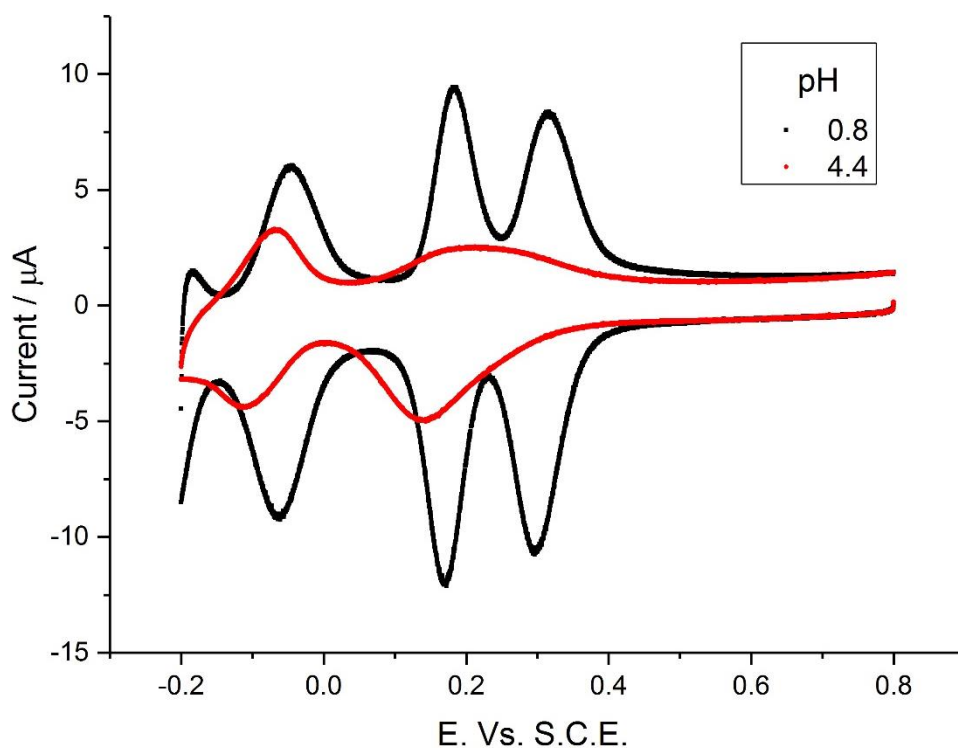
Figure 4.15 - cyclic voltammetry of two 3 mm EPPG electrodes modified by dipping in 0.1 M PMA solution for 30 seconds, taken at 100 mV.s^{-1}, at a pH of 4.4 and a pH of 12. The electrolyte is 0.1 M sulphuric acid, with added aliquots of 0.1 M NaOH and 0.5 M sulphuric acid to achieve the desired pH which was measured with an in-situ pH meter

Important information alluding to the stability of the adsorbed layer across the pH range is the magnitude of the peak current for each redox process, which varies dramatically across the full pH range. However, a general pattern emerged for both V1PMA and PMA modified electrodes. There was an initial area of stable peak current, followed by a constant reduction in peak current with an increase in pH of the electrolyte. This is observable for the example of process O2/R2, shown in Figure 4.16, for both PMA and NaV1PMA.

169
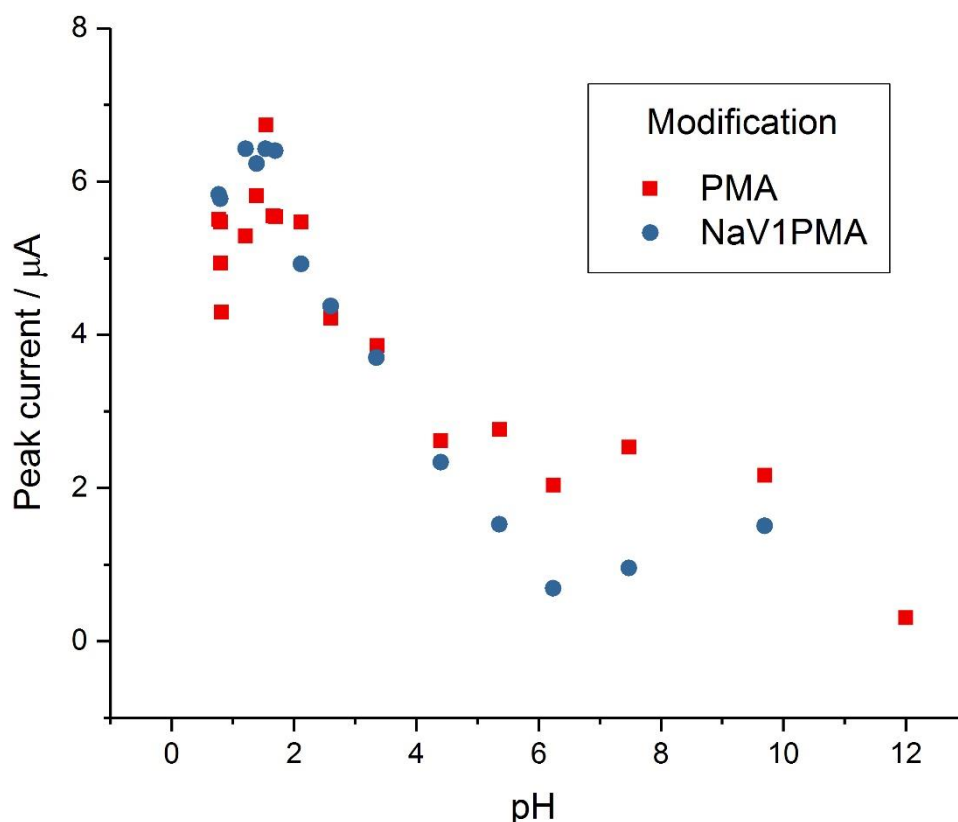
Figure 4.16 – Averaged absolute peak current values for O2/R2 in previous figures, recorded from baseline corrected cyclic voltammetry at 0.1 mV.s^{-1} of 3 mm EPPG electrodes modified with by dipping for 30 s in either 0.1 M PMA or 0.1 NaV1PMA solutions plotted against the pH of the electrolyte.

At high pH the currents drop dramatically until no current response is seen that can be described as arising from one of the aforementioned redox processes. At mid pH values a general decrease in current response is observed, agreeing with previous studies with phosphomolybdic acid, showing a transition from a two electron process at low pH to a one electron process at higher pH values.[226,227] This is attributed to a gradual change in structure at the surface with increasing pH. It has been seen in previous studies that multiple polyoxometalate species exist at these pH values and that the Keggin structure is no longer the dominant species within higher pH regions.[190,333] This transitional decrease represents a general decline in the dominance of the Keggin species at the surface which is observed by the change in shape of the CV response as seen in, Figure 4.13,

Figure 4.14 and Figure 4.15. The transitions in peak current agree well with previously established

Pourbaix diagrams for vanadium and molybdenum oxides as described in detail by Sadakane.[190]

The exact relationship between pH and $E_{1/2}$ potential for each redox process is examined further in

the subsequent section, however if it is viewed across the full pH range, Figure 4.17, it shows a

characteristic transition in relationship at pH 4, further agreeing with previous studies on these

types of species.
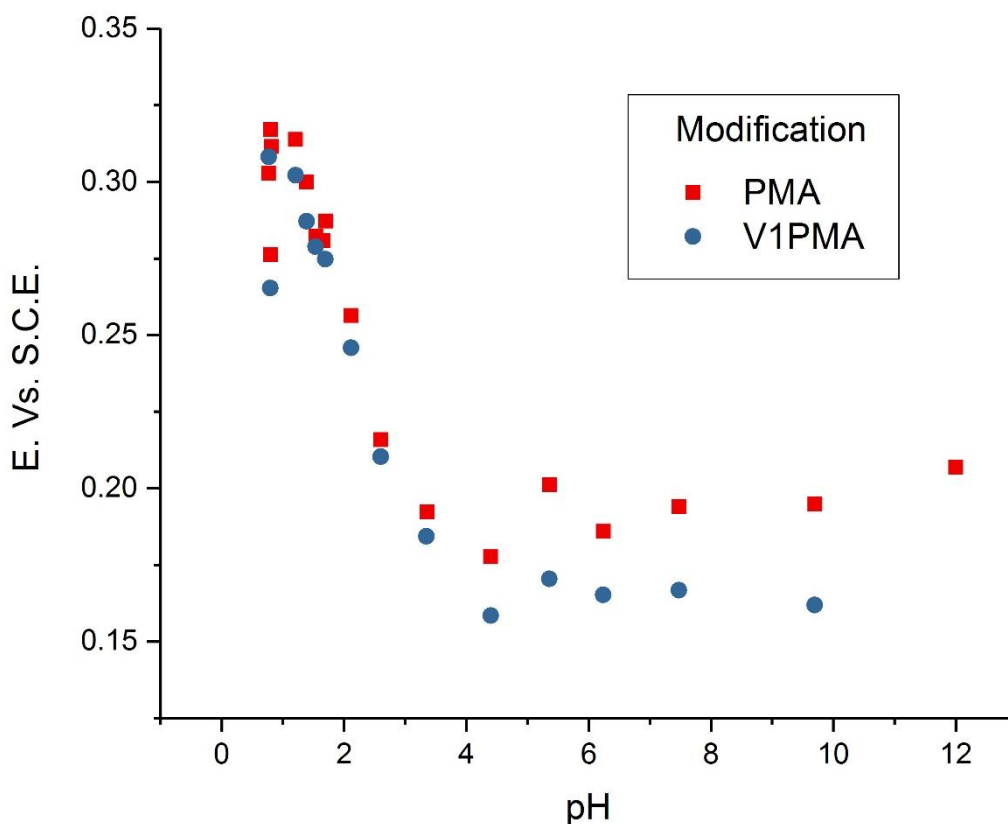
Figure 4.17 - Observed $E_{1/2}$ potential for redox process R2/O2 recorded from cyclic voltammetry at 100 mV.s^{-1} of 3mm EPPG electrodes modified by dipping for 30 s in either 0.1 M PMA or 0.1 M NaV1pma versus pH of electrolyte solution.

At a pH value of 2 and below the current is much more stable and slowly increases. In acidic

conditions the keggin structure is the most favourable with, the loss of metal centers at higher pH

possible.[190,200,333] As has been discussed the relation to ideal behaviour of an adsorbed species is affected by inter-molecular interactions within the surface species and the need for balancing counter ions to diffuse through any such layer. If a species is tending towards more ideal behaviour the peak becomes less suppressed leading to an increase in peak current, even though the charge transferred in each process is the same. This can be seen when analysing individual peaks. As shown by the example, of a PMA modified EPPG electrode, with the data corresponding to reduction peak three highlighted at a very low pH and then at an increased pH, Figure 4.18.
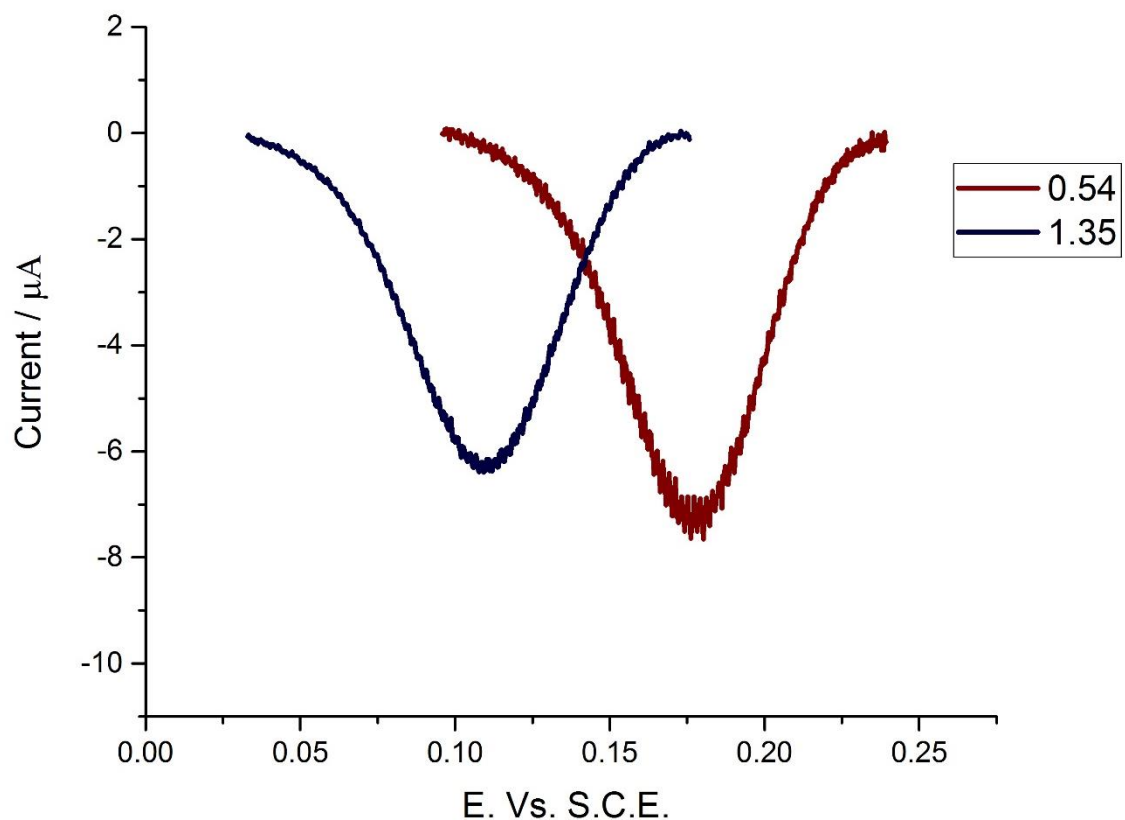
Figure 4.18 - Reduction R3 for a 3mm EPPG electrode modified by dipping for 30 seconds in a 0.1 M PMA solutions, at pH 0.54 and a pH 1.35. Data selected from cyclic voltammetry taken at 100 mV.s^{-1}.

This data shows that at pH 1.35 the half peak width is 58 mV which is close to ideal behaviour for a two electron process but that at 0.54 pH it is 48 mV, a lot closer to the 45mV of ideal behaviour

for a two electron process. The data at these peaks can be analysed using a simple model built on

Laviron's equation based on the Langmuir isotherm (described in chapter 3). This is shown in

Figure 4.19.
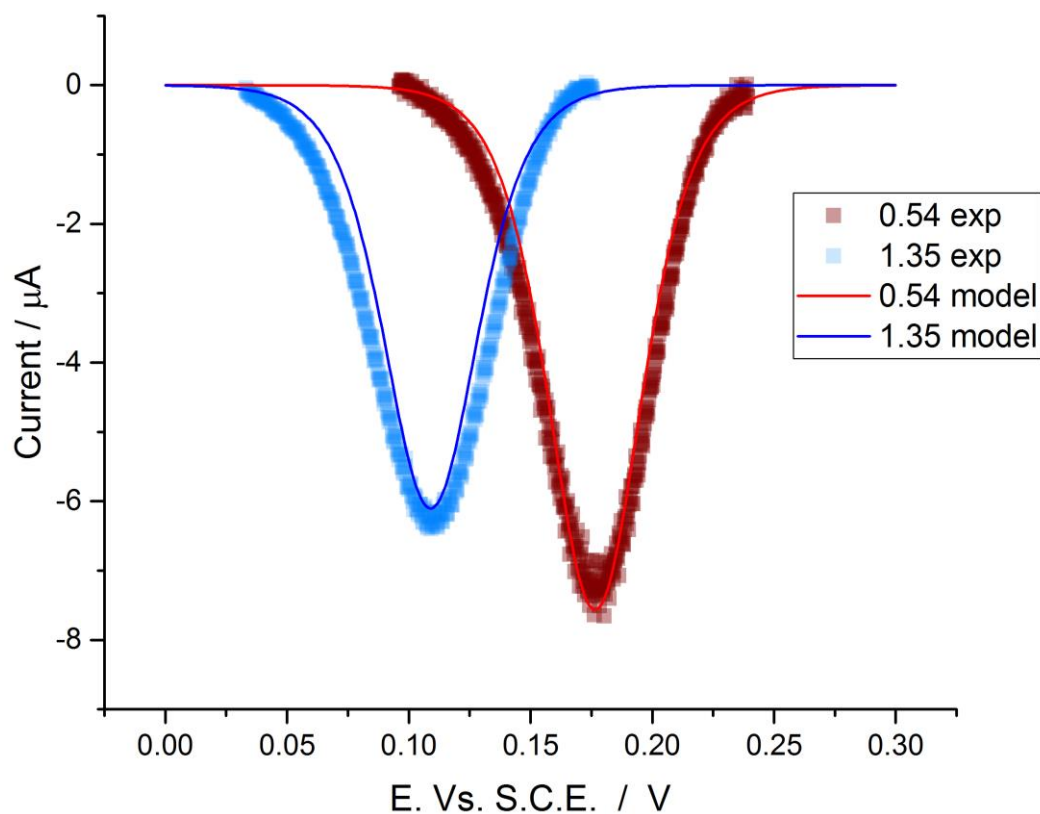
Figure 4.19 - Reduction R3 for a 3mm EPPG electrode modified by dipping for 30 seconds in a 0.1 M PMA solutions, at pH 0.54 and a pH 1.35. Data selected from cyclic voltammetry taken at 100 mV.s^{-1}pH compared to modelled behaviour

It can be seen that the peak at pH 0.54 is more closely aligned to ideal behaviour. In addition, the

peak at pH 1.35 uses a surface coverage of 2.3×10^{-10} mol.cm^{-2} and the peak at pH 0.54 uses a

surface coverage value of 2.85×10^{-10} mol.cm^{-2}.

Shift in redox equilibrium with pH

To obtain information relating pH to the electron transfer process at the adsorbed layers, lower pH values were focused on. The experiments so far have provided data that suggests multiple electron transfer reactions occur across the pH range. It has also clearly demonstrated that these reactions are dominated by the influence of pH. When considering two electron transfer mechanisms there are multiple pathways these mechanisms can take. Before the nature of the mechanistic pathway can be addressed the exact dependence on proton concentration must be established.

The Nernst equation can be used to aid in establishing the ratio of protons to electrons transferred to the adsorbed layer. As discussed in chapter 1, a gradient of 59 mV.dec^{-1} in a plot of equilibrium potential versus pH would indicate a direct 1:1 correlation of proton concentration to electron transfer.

Equation 4.5 is an example reaction quotient in the phosphomolybdic acid derivatives. It shows the proposed reaction quotient for the R2/O2 redox process in singularly substituted vanado-phosphomolybdic acid. Within this equation, because we are considering the transfer of electrons and an adsorbed species, the activity of these species can be considered to be 1 within the quotient. This leads to Equation 4.6 and the relationship of a 59 mV shift per pH unit. However, if the relationship is not 1:1, for example if the mechanism deviates from ideal behaviour then an additional factor needs to be added, z in Equation 4.7.

This relates to the ratio of protons to electrons, (z/n). Subsequently it can be seen that plotting pH versus redox potential yields this ratio from the gradient and any deviation away from a gradient of 59 mV.dec^{-1}.

Equation 4.5

$$Q = \frac{[H_6 PV_1^V Mo_1^V Mo_{10}^{VI} O_{40}]\,[e^-]^2 [H^+]^x}{[H_{6+x} PV_1^{IV} Mo_3^V Mo_8^{VI} O_{40}]}$$

Equation 4.6

$$E_{red} = E_{red}^{\emptyset} + \frac{RT}{nf} \ln([H^+])$$

Equation 4.7

$$E_{red} = E_{red}^{\emptyset} + \frac{zRT}{nf} = \ln[H^+]$$

As has been discussed in a previous section the layer's response has not been demonstrated as ideal behaviour. This introduces a difficulty in establishing the exact redox potential for each process as the peaks are not perfectly symmetrical. With this in mind, data was gathered for the oxidation and reduction peaks and an average value was taken for the redox potential to be plotted versus pH. This data is shown for the example of PMA and NaV1PMA modified EPPG electrodes in Figure 4.20.
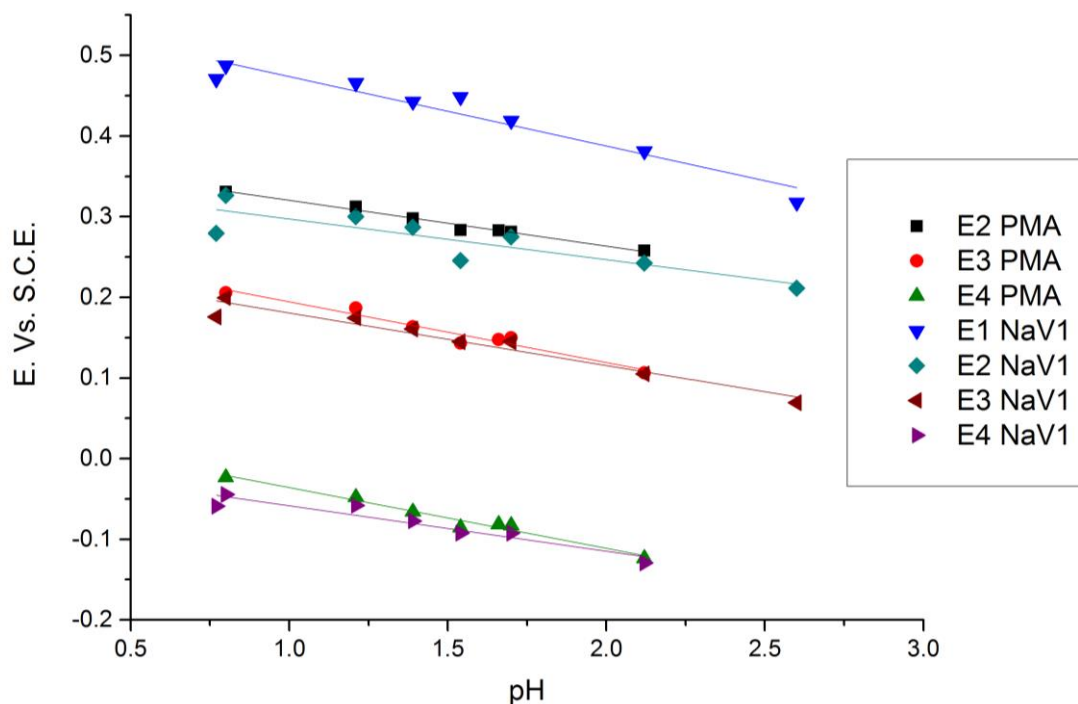
Figure 4.20 – Observed $E_{1/2}$ for the redox processes observed during cyclic voltammetry at 100 mV.s^{-1} of 3mm EPPG electrodes modified by dipping for 30 s in either 0.1 M PMA or 0.1 M NaV1PMA versus pH of electrolyte species.

The data allows for the calculation of the z/n values, as presented in Table 4-2.

	PMA BPPG	PMA EPPG	NaV1PMA BPPG	NaV1PMA EPPG
1			1.22	1.22
2	0.95	1.07	0.95	1.09
3	1.44	1.35	1.38	1.22
4	1.24	1.30	1.23	1.27

Table 4-2- z/n values calculated from figure 4.21 for redox processes on PMA and NaV1PMA on EPPG and BPPG

The figures for z/n are all close to a value of one, indicating that the mechanism proceeds with one proton for each electron transferred. However, most values are larger than one, showing that there is a non-ideal relationship, dominated by the concentration of protons available, and are similar to previous studies on similar heteropolyacid species[334,335] and phosphomolybdic acid within an layer-by-layer assembled layer.[332] This indicates that the mechanism is more reliant on proton diffusion

than electron transfer. However, the values are also slightly misleading as the effective pH surrounding and within the monolayer may differ from the bulk. This difference may be caused by the position at which reduction takes place within the species and the decreasing concentration of protons within the layer as they are consumed.

4.4 Conclusion on the characterization of singularly substituted vanado-phosphomolybdic acid

This chapter has completed the investigation into the adsorbed layers of phosphomolybdic acid and its singularly substituted vanadophosphomolybdic acid derivatives. It has analysed the effect that the surface of an electrode has on the electrochemical response observed and the surface coverage of the species on that surface.

The work has shown that the layers adsorbed onto EPPG and BPPG electrodes behave very similarly, that the layer on GC produces slightly depressed responses and that PFCE has the lowest surface coverage value. With the additional data it can be concluded that for V1PMA species the redox processes show two, one electron transfers followed by two, two electron transfers.

Additionally, with the data produced through varying pH the ratio of protons to electrons transferred can be calculated and the full reaction mechanisms can be put forward, as in the example for sodium phosphovanadomolybdate below,

Equation 4.8
$$NaH_3(PV^V Mo_{11}^{VI} O_{40}) \ + e^- + H^+ \rightarrow NaH_4(PV^{IV} Mo_{11}^{VI} O_{40})$$

Equation 4.9

$$NaH_4(PV^{IV}Mo_{11}^{VI}O_{40}) \quad + e^- + H^+ \rightarrow NaH_5(PV^{IV}Mo_1^V Mo_{11}^{VI}O_{40})$$

Equation 4.10

$$NaH_5(PV^{IV}Mo_1^V Mo_{11}^{VI}O_{40}) \quad + 2e^- + 2H^+ \rightarrow NaH_6(PV^{IV}Mo_3^V Mo_9^{VI}O_{40})$$

Equation 4.11

$$NaH_6(PV^{IV}Mo_3^V Mo_9^{VI}O_{40}) \quad + 2e^- + 2H^+ \rightarrow NaH_8(PV^{IV}Mo_5^V Mo_7^{VI}O_{40})$$
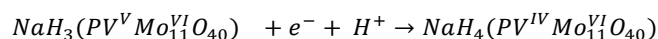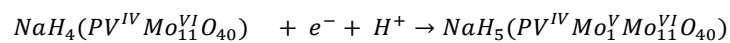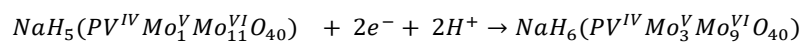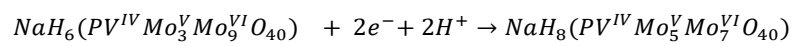
5. Solution Phase Chemistry of substituted vanadophosphomolybdates

5.1 Introduction

Chapter 3 and chapter 4 explored the electrochemistry and redox mechanism of the adsorbed layers of phosphomolybdic acid and the singularly substituted vanadium phosphomolybdic acid. In the FlowCath® system, liquid catholytes are used and so information relating to the electrochemical behaviour of the solution phase is of particular interest. As has been discussed in chapters 1 and 3, a volume of research exists on the solution phase of phosphomolybdic acid and singularly substitution vanadophosphomolybdic acid. However, much like the research available on the adsorbed layer equivalents, important characteristic information is missing from the literature.

Similarly, the information that is required is the effect of electrode surface used, the cation and the exact effect of pH, the same gaps that exist for the adsorbed species. Additionally, the effect of the concentration of the solution and the interaction between the adsorbed and solution phase is an area specifically requiring understanding.

5.1.1 Solution phase electrochemistry

It has been seen that solutions of phosphomolybdic acid and its singularly substituted vanadium derivatives have numerous applications from imagery, medicine and organic synthesis.[199,200,318,333]

The redox properties of these solutions are the source of their great application range. However, stability of these solutions has long been a concern in their commercial application.[200,288]

The electrochemical behaviour of these solutions has been explored by previous studies, but gaps remain in the literature regarding a full understanding of the effects the parameters of electrode surface, pH and concentration. Due to the formation of adsorbed layers the electrochemical response is often difficult to interpret.[333]

It has been observed that due to the heterogeneous nature of the reaction the adsorbed species of polyoxometalates show inferior catalytic performance to their homogeneous solution phase equivalents.[290] Their ability to mimic the redox shuttles within biology leads them to be attractive catalysts within fuel cells. The inclusion of vanadium within the keggin phosphomolybdic acid structure, increasing oxygen affinity and widening its redox properties[190,201,336] means that a full understanding of its electrochemistry may further develop their application as redox mediators.

5.1.2 Concentration effects in electrochemistry

It is clear from the Butler-Volmer equation and the Randles-Sevcik equation the effect that concentration has on the electrochemical behaviour of solution based systems. However, with this specific case concentration plays a more important role than in standard solution phase electrochemistry.

It has been shown that the stability of HPA's is dependent on concentration and that at low concentrations the molecule is more susceptible to dissociation and pH shifts.[200] Additionally, due to the formation of adsorbed layers which have been shown to still form at fast time scales (chapter 3) at low concentrations the electrochemical response may be difficult to interpret. This is because at low concentrations the effective surface concentration (due to the surface coverage of any adsorbed layer) may be larger than the bulk concentration.

The effect that this will have on the system is unclear, whether the response seen will effectively be that of the adsorbed layer alone, or that at low concentrations the mediating effect of the solution may become clearer and more determinable.

5.1.3 Interactions between solution phase and surface bound redox active species

Possibly the largest hole in the literature reflects the interaction of adsorbed phosphomolybdic acid derivatives with the solution phase and the effect it has on the observed electrochemistry. There are several possible ways the layer-solution interaction could appear. It is possible that the layer acts as a catalyst/mediator to the reduction of the solution phase species, which would appear as a catalytic wave in the cyclic voltammetry. It is also possible that the adsorbed layer inhibits the electrochemistry of the solution phase acting as a resistor to the electron transfer across the layer, although previous solution phase electrochemical studies are not suggestive of this.

5.1.4 Effect of pH on solution phase phosphomolybdic acid derivatives

The multiple reactions that the heteropolyacids can partake in have been highlighted in numerous research papers. Also highlighted has been the possibility of disproportionation (Equation 5.1) reactions in the vanadium substituted species and protolysis (Equation 5.2) occurring in strong acids.[226,337]

Equation 5.1 [337]

$$2H_{x-1}PV_xMo_{12-x}O_{40}^{4-} \rightleftarrows 2H_xPV_{x+1}Mo_{11-x}O_{40}^{4-} + 2H_{x-2}PV_{x-1}Mo_{13-x}O_{40}^{4-}$$

Equation 5.2 [337]

$$(13-x)H_{x-1}PV_xMo_{12-x}O_{40}^{4-} + 16H^+$$

$$\leftrightarrows (12-x)H_{x-2}PV_{x-1}Mo_{13-x}O_{40}^{4-} + 16H^+ + 12VO_2^+ + H_3PO_4 + 12H_2O$$
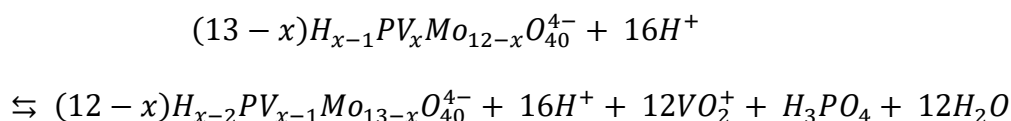
These reactions, particularly the possibility of increasing protolysis at increased pH need to be considered when conducting solution based electrochemistry.

5.2 Experimental

5.2.1 Electrode preparation

The electrodes used in experimentation were prepared as has previously been described, predominantly without prior-modification through dipping in the phosphomolybdic acid derivatives.

5.2.2 Analyte preparation

This experimental series looks at the solution phase electrochemistry of the phosphomolybdic acid derivatives. All vanadium substituted phosphomolybdic acids were supplied as 0.3 M aqueous

solutions by ACAL Energy ltd. These were diluted to the required concentration with either stock electrolyte solution (as described in chapter 4) or distilled water. Phosphomolybdic acid solutions were produced by diluting stock phosphomolybdic acid (Sigma-Aldrich) or sodium phosphomolybdate (Sigma Aldrich).

5.2.3 Cell preparation

Standard three electrode electrochemical cells were used as described in previous chapters (3 and 4). The pH was altered in the same way that the pH was altered and described in chapter 4. Due to the presence of the phosphomolybdic acid derivative species in the solution, extra care was taken in preparing the platinum gauze counter electrode and the reference electrode (described in section 5.2.4). The platinum gauze was flame cleaned after each experiment, to avoid a build up of adsorbed species affecting measured results.

5.2.4 Reference electrode preparation

With the increase in phosphomolybdic acid derivative species in solution, an issue of contamination with the reference electrode arises. It can be seen visually that the frit and solution of the reference electrode can become stained and that the potential of the electrode can drift. Therefore, an S.C.E and Ag/AgCl reference electrode were permanently kept separate from any contaminants to function as an in-house reference to check against the reference electrodes used with the phosphomolybdic acid derivatives. The S.C.E. did not show any drift during experimentation and the solution was changed frequently within the electrode, commonly with saturated (or 0.3 M, depending on reference electrode used) KCl solution made with KCl crystals (Sigma Aldrich) and

ultrapure water. The Ag/AgCl electrodes were less stable but the ease of remaking the electrode held an advantage.

To construct an Ag/AgCl reference electrode a glass pipette is taken and a molecular sieve is flame sealed at one end of the pipette so that it is exposed. The pipette is filled with degassed (oxygen-free nitrogen for 20 minutes) KCl solution. A silver wire is polished and placed within the pipette which is then sealed with either blu-tack (WHSmiths) or epoxy resin. A layer of AgCl is then formed on the wire by driving an oxidizing potential (0.9 V Vs S.H.E) within a standard electrochemical cell (prepared as previously described) with a 0.1 M KCl solution as an electrolyte. Finally it's potential was checked against a commercial electrode.

5.3 Results and Discussion

The study of the bulk solution phase electrochemistry is made more complicated due to the knowledge that whatever concentration of phosphomolybdic species was used, an adsorbed layer would form on the electrode. As such all experiments were conducted thirty seconds after the electrode had been introduced into the cell. This was done in order that any layer formed on the electrode would be similar to the layers that have been examined in previous sections allowing for identification of any redox processes arising from the adsorbed layer. In addition, it has already been identified that after thirty seconds of dip timing the adsorption of additional material to the electrode dramatically reduces, meaning that any layer already formed should be less dynamic than if the experiment were conducted immediately.

The effect that the adsorbed layer has on the bulk solution electrochemistry is subject to study in a later section of this chapter; this initial section aims to characterize the bulk solution phosphomolybdic species at analytical concentrations (1-10 mM). A later section looks at the electrochemistry as the phosphomolybdic concentration approaches self-supported electrochemistry, where the concentration of active species, approaches the same and exceeds the concentration of the supporting electrolyte species.

5.3.1 Initial assessment of low concentration solution phase electrochemistry

As with the adsorbed layers, multiple redox processes are evident in the bulk solution electrochemistry. At lower concentrations some of these redox processes are of the same current magnitude as the adsorbed layer electrochemistry. Figure 5.1 shows an increasing potential range experiment for a 1 mM solution PMA in 0.1 M sulfuric acid at an EPPG electrode. A series of redox processes are clearly visible.
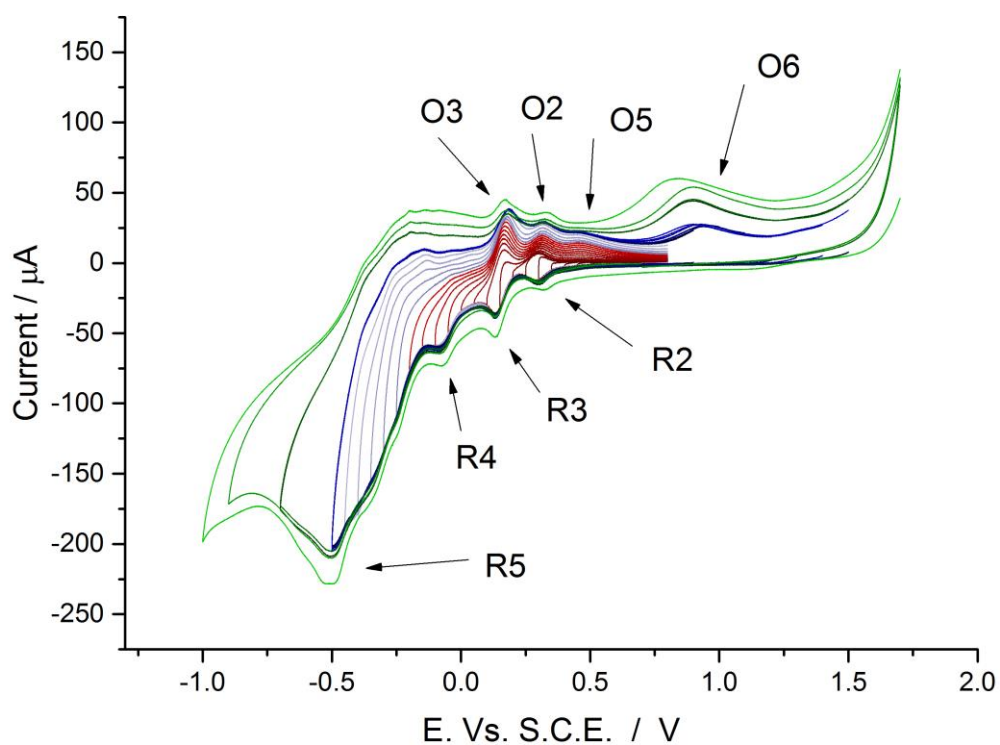
Figure 5.1 - Cyclic voltammograms at differing potential ranges of 1mM PMA in 0.1 M sulphuric acid at a 3mm EPPG electrode at 100mV.s^{-1}

Although it can be seen that the electrochemical response is clearly different to that of adsorbed layers, differentiating a contribution from the adsorbed layer is difficult at this concentration. For example, the peak labelled R2 has a current peak of -12.9 μA which is not dissimilar to the adsorbed layer's response at EPPG, which saw current magnitudes of around -10 μA. Whereas, peak R3 has a current magnitude of -38 μA which is a four-fold increase on current magnitudes seen for adsorbed layers.

This is clearly visible when using the potential range established for the adsorbed layer, seen in chapters 3 and 4. Figure 5.2 shows an overlay of a cyclic voltammogram of an adsorbed layer response and of a 1mM PMA solution, on EPPG at 100mV.s^{-1}. It can clearly be seen that the first reduction peak (labelled as R2) is smaller for the solution phase than for the adsorbed layer, whereas the peaks for R3 and R4 have doubled.
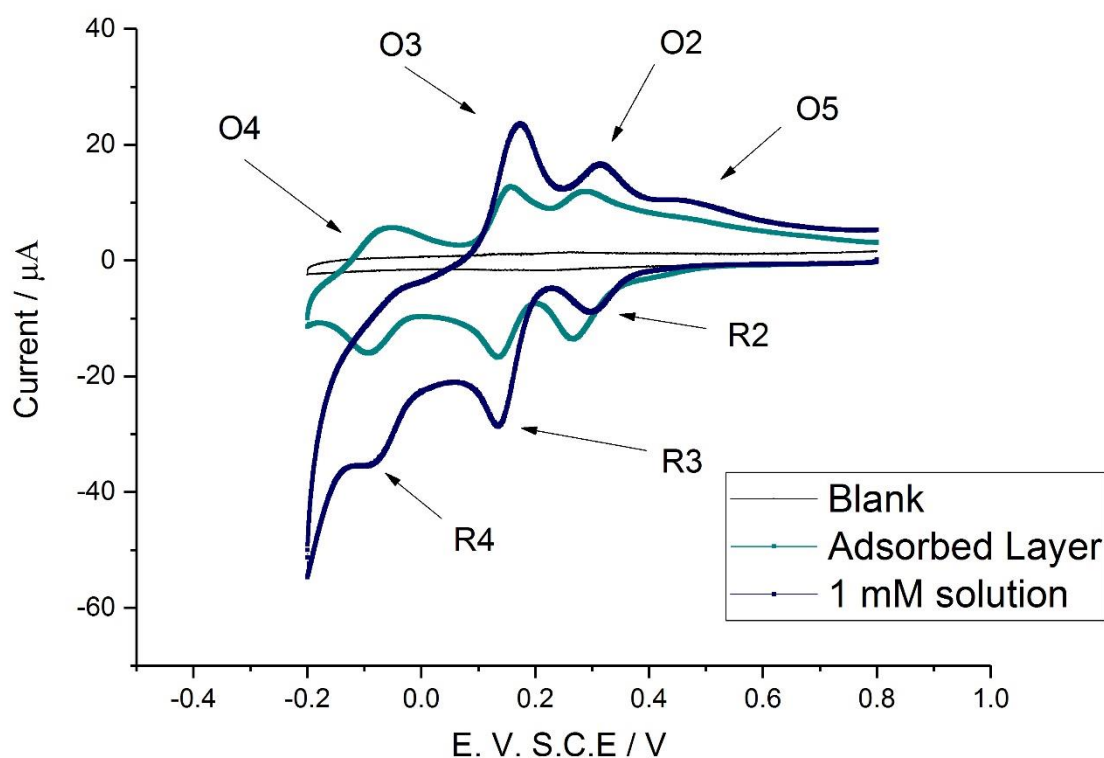
Figure 5.2 - Cyclic voltammograms of 3mm EPPG electrodes, in 'blank' 0.1 M sulphuric acid, in 1mM PMA in 0.1 M sulphuric acid and a modified 3mm EPPG electrode, modified by dipping in 0.1 M PMA for 30 s in 0.1 M sulphuric acid at 100mV.s^{-1}

Responses like those shown in Figure 5.2 are difficult to interpret and almost impossible to characterise. It is a similar situation when examining the vanadium substituted species. Figure 5.3

shows similar potential range experiments conducted on a 5mM NaV1PMA solution. It can be observed again that there are multiple redox processes that are difficult to interpret.
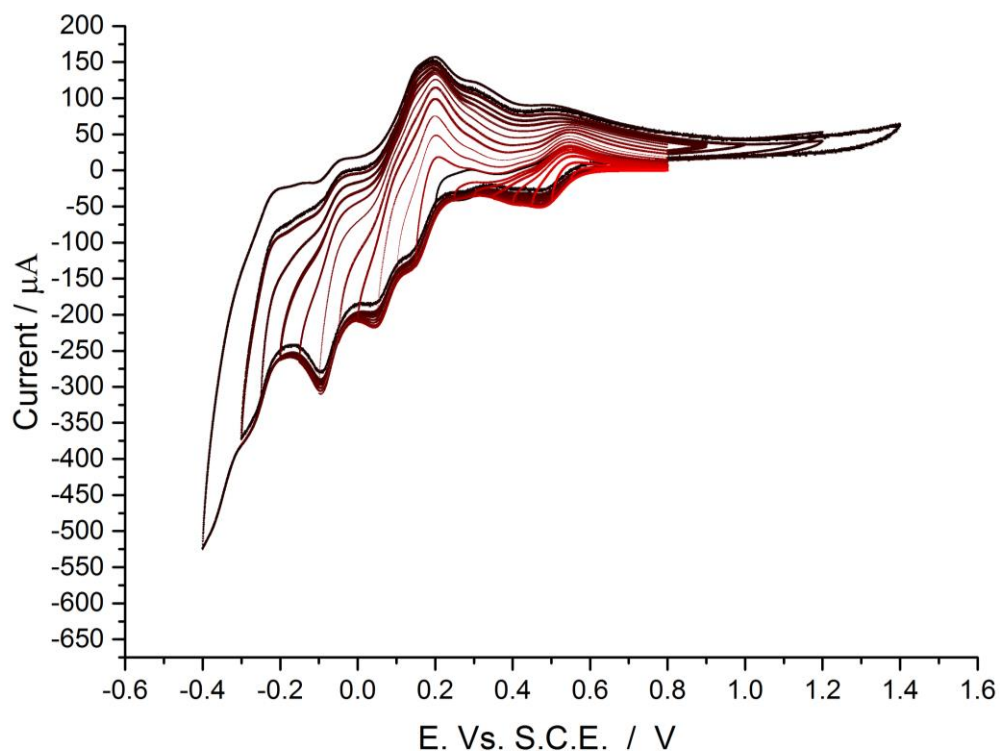
Figure 5.3 - Potential range cyclic voltammetry of 5 mM NaV1PMA in 0.5 M sulphuric acid and 0.55 NaOH at a 3mm EPPG electrode at 100mV.s^{-1}

The two figures, Figure 5.1 and Figure 5.3, shows the difficulty is assessing the multiple redox processes in the solution phase. Whilst studying the adsorbed species, the species are not subject to diffusion and so the data is relatively clear to analyse. In the bulk phase, diffusion and interaction between the bulk and adsorbed species make the data harder to interpret. However, whilst in the adsorbed phase, concentration was not a variable available to use in analysis.

As well as concentration being utilized to discern the electrochemical properties, the same variables as in previous chapters of, electrode, scan rate, derivative type and pH were used. This enabled a picture, although qualitative, of the electrochemical behaviour.

5.3.2 Electrode surface effect on the solution phase electrochemistry

As with the analysis of the adsorbed layer, the electrode surface can be changed and the effect of different surfaces investigated. It has been noted above that the adsorbed layer has a strong influence on the solution phase electrochemistry. Chapter 4 discussed how the electrochemical response of the adsorbed layers did change subtly between the graphitic electrode surfaces. Figure 5.4 shows the cyclic voltammetry of 1mM solutions of phosphomolybdic acid on a range of graphitic surfaces.
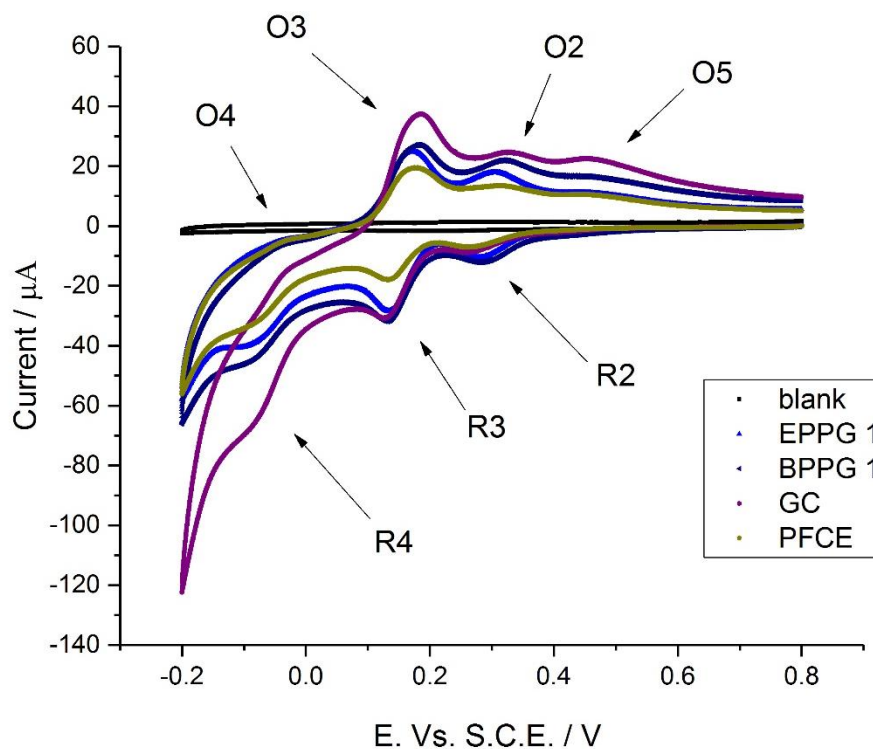
Figure 5.4 - Cyclic voltammetry of 1 mM PMA in 0.1 M sulphuric acid taken with 3mm, EPPG, BPPG, GC and PFCE electrodes at 100mV.s⁻¹

It can be seen in the figure that the response on most surfaces is the same, but that the GC electrode has a slightly exaggerated response. It is not surprising that the responses are similar, as there was little difference between the electrode surfaces when analyzing the adsorbed layer. It has already been seen that the electrochemistry at these concentrations is dominated by the interaction between the bulk and the surface species. As the adsorbed layers were similar on these electrodes it would be expected that the solution phase electrochemistry would further tend to an average response.

This is confirmed when looking at the response of the NaV1PMA species, shown in Figure 5.5. The cyclic voltammograms are virtually identical across the electrodes.
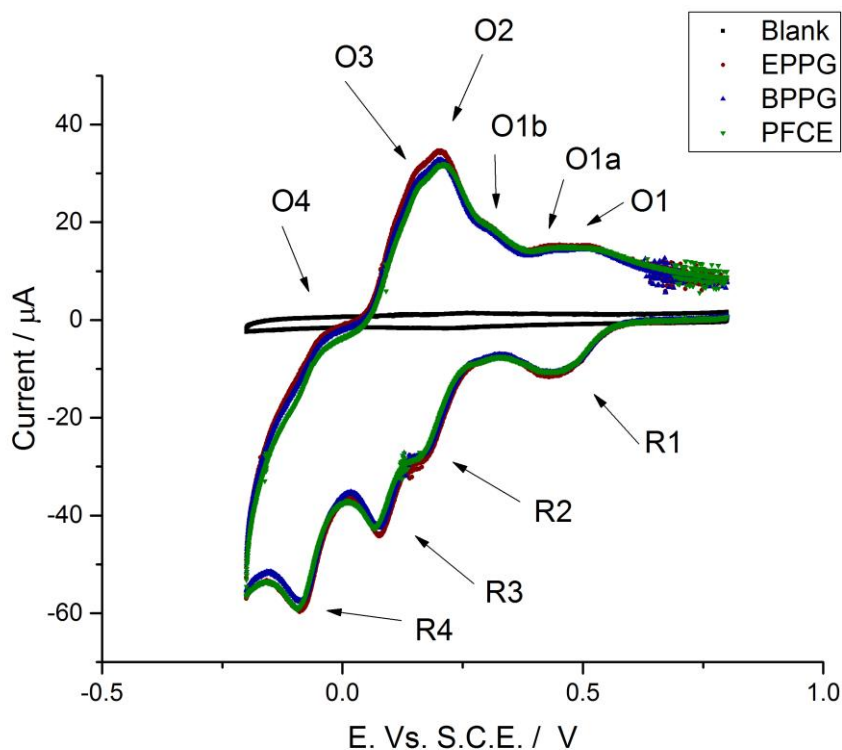
Figure 5.5 - cyclic voltammetry of a 1mM NaV1PMA in 0.1 M sulphuric acid solution at 3mm EPPG, BPPG, PFCE electrodes and a 'blank' scan taken at a 3mm EPPG electrode in 0.1 M sulphuric acid at 100 mV.s^{-1}

It can be observed from the cyclic voltammetry displayed so far in the bulk phase that the electrochemistry is dominated by the adsorbed layer and that it is very different in nature from the simple three step process (PMA) or the four step process (V1PMA) of the adsorbed layer. This difference is most likely created by the effect of a much more active environment, with diffusion and surface-bulk interactions leading to a more complicated response.

5.3.3. Counter Ion effect

Chapters 3 and 4 showed that there was little difference when changing the counter ion when studying the adsorbed layer. In the bulk phase the supporting counter ion may play a bigger role in supporting the anion species before and after the redox process. Figure 5.6 shows the cyclic voltammetry response for the different phosphomolybdic acid derivatives at an EPPG electrode at $100mV.s^{-1}$. It can be seen in the figure that as with the adsorbed layer changing the counter ion of the substituted phosphomolybdic acid from Na^+ to H^+ has little effect on the electrochemical response. The small effect of cation on solution phase electrochemistry has previously been seen in acetonitrile for phosphomolybdic acid.[336]
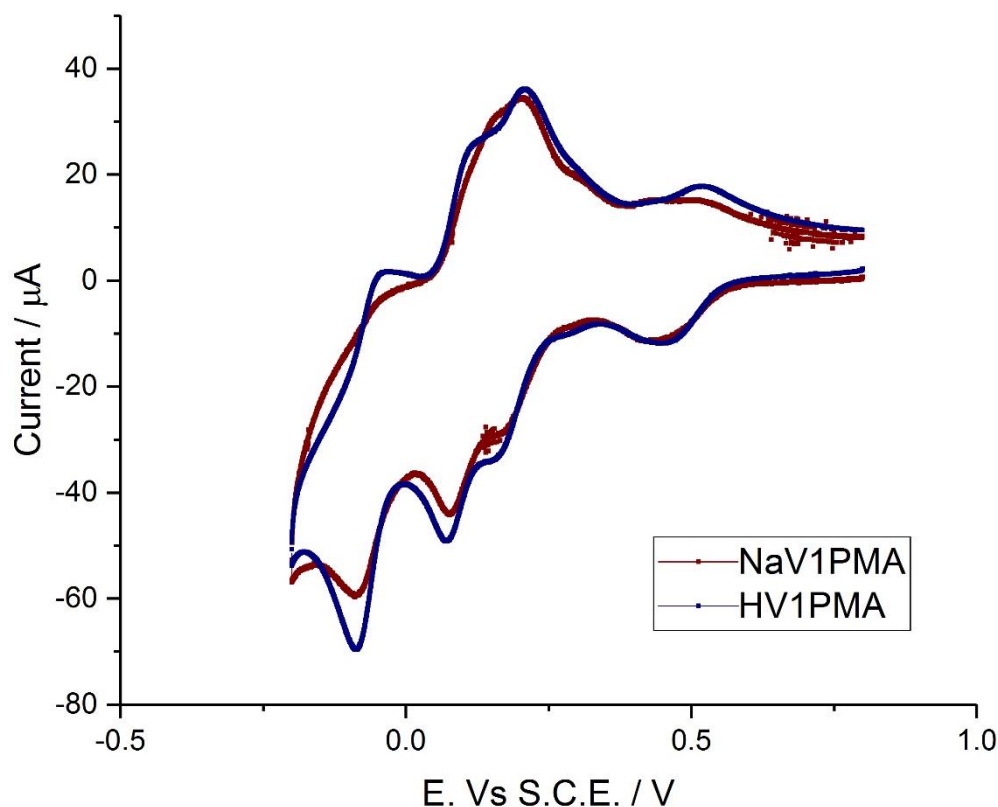
Figure 5.6 - Cycle Voltammograms of 1 mM NaVlPMA and 1 mM HV1PMA both in 0.1 M sulphuric acid at a 3 mm EPPG electrode at 100mV.s[1]

Figure 5.6 quite clearly shows that although there is little difference when changing the counter ion in the substituted species, there is a large difference between the PMA and its substituted derivatives. It also shows that the change that comes from substituting vanadium into the keggin structure is similar to that seen on the adsorbed layer, with the initial reduction shifted positive and a subsequent change in the redox processes that occur at a lower potential. Also included in Figure 5.6 is the effect of using an electrode with a pre-established adsorbed layer being introduced to the cell. This shows no discernible difference at these concentrations.

5.3.4 Concentration effect on the redox behaviour of the redox couples

As has been discussed, if the electrochemical response is dominated by the bulk solution phase and follows ideal behaviour then the peak current will grow linearly with concentration. As can be seen in the cyclic voltammetry already presented the initial reduction process does not follow ideal behaviour. As such the second redox process labelled R2/O2 in Figure 5.7 is used to plot absolute peak current versus concentration.
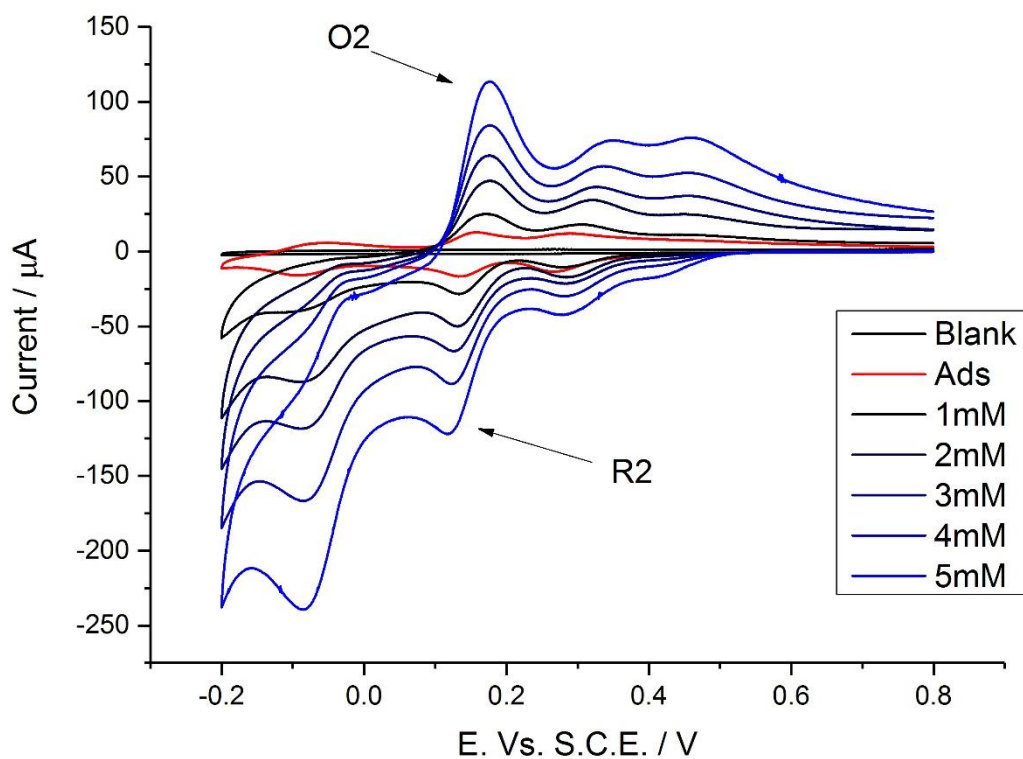
Figure 5.7 - Cyclic voltammetry of 1-5mM PMA solutions in 0.1 M sulphuric acid meter taken at a 3mm EPPG electrode at a pH of 1.23 and 100 mV.s^{-1}

Figure 5.7 shows the increases in current response seen with increasing concentrations of PMA solutions at 1.23 pH. Values were also calculated at several other pH values, (the effect of pH is

discussed in section 5.3.6). It can be seen in this figure (and in data not shown) that the initial peak, is somewhat unpredictable at low concentrations. Taking the absolute peak current at the R2/O2 (as labelled above) redox couple and plotting it against concentration gives Figure 5.8. This figure also includes the peak current data for the equivalent (pH considered) CV response of the adsorbed layer of PMA on EPPG labelled as concentration 0 for this representation.
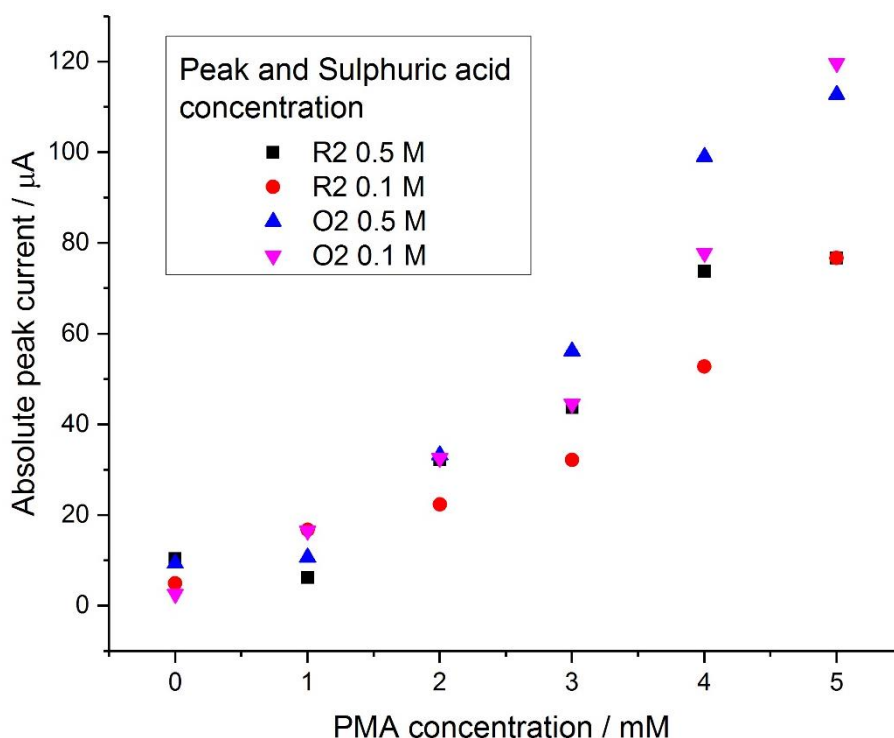
Figure 5.8 - Peak current versus concentration for peak R2/O2 (labelled in plot 5.7) for PMA solutions in 0.1 M sulphuric acid and additionally 0.25 M sulphuric, taken at 3mm EPPG electrodes at 100mV.s⁻¹.

It can be seen in Figure 5.8 that peak current grows linearly with concentration. The effect that the adsorbed layer is having on the solution phase electrochemistry is evident, especially at low concentrations. This can be observed in Figure 5.9. The linear growth of current gives a gradient value which can be used to calculate an experimental diffusion coefficient for the species through rearranging the Randles-Sevcik equation. For these experiments with PMA solutions it gives a

coefficient of 1.83×10^{-6} cm^2.s^{-1} and 1.48×10^{-6} cm^2.s^{-1} for the 0.73 pH and 1.23 pH samples respectively. These are smaller than would be expected, following similar previous studies on Keggin species,[227]f further indicating the adsorbed layer interaction is dominating the electrochemical response.
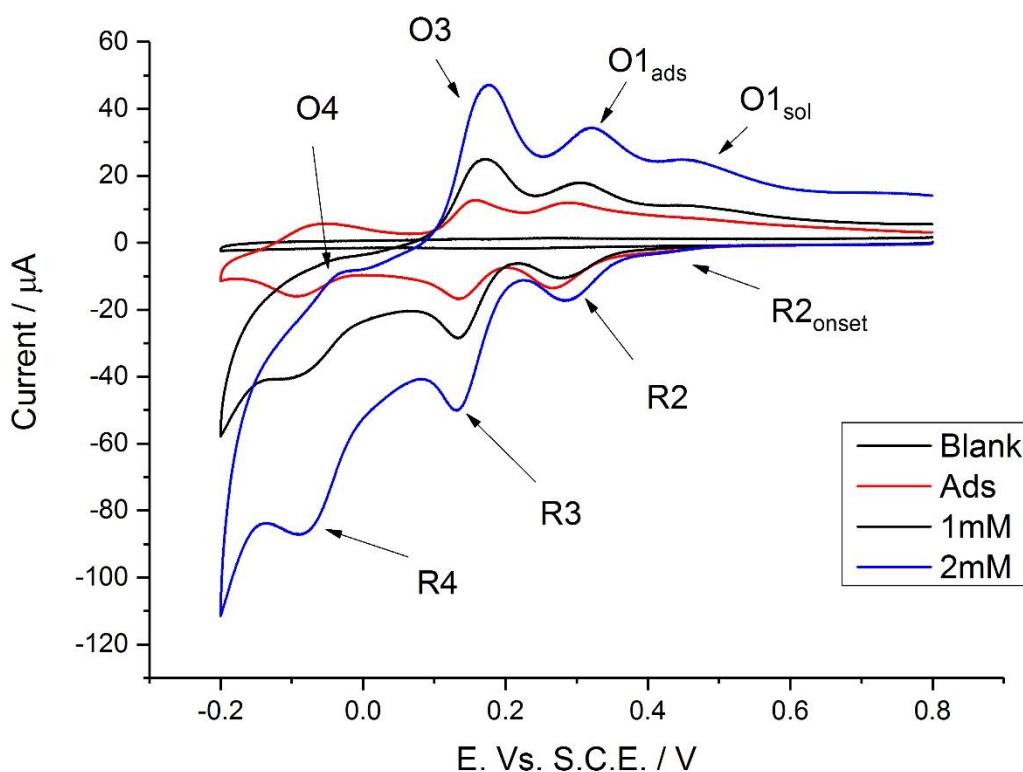
Figure 5.9 – Cyclic voltammetry of 1 mM PMA solution and 2 mM PMA solution in 0.1 M sulhuric acid at a 3 mm EPPG electrode, with the corresponding 'blank' eppg electrode and a 3 mm EPPG electrode modified by dipping in PMA solution for 30 s taken in 0.1 M sulphuric acid. All scans shown have been taken at 100 mV.s^{-1}.

Figure 5.9 shows this effect by highlighting the very low concentrations of PMA. It is possible to determine the three redox processes that were observed at the adsorbed layer and how these correspond to the solution phase. It is shown that no redox processes occur before the initial adsorbed layer reduction, an onset only being seen at the higher 2 mM concentration However, on

the return oxidation it can be seen that this initial process has split into two peaks, the solution phase and the adsorbed responses. This leads to the idea that at these pHs the initial reduction equilibrium potential for the adsorbed layer is lower than that of the solution phase, but for the solution phase to be reduced, first the adsorbed layer must be reduced to then mediate the electron transfer. With initial reduction of the V1PMA this may not be observed due to the higher reduction potential and it may be possible to separate these peaks by altering pH.

The same effect of concentration was studied for the vanadium substituted species. In this study concentrations as low as 0.1 mM and as high as 100 mM were used and are shown in Figure 5.10. This was to investigate whether the behaviour deviated at ultralow concentrations, affecting the adsorbed layer, or at high concentrations, as the electro active species became self-supporting.
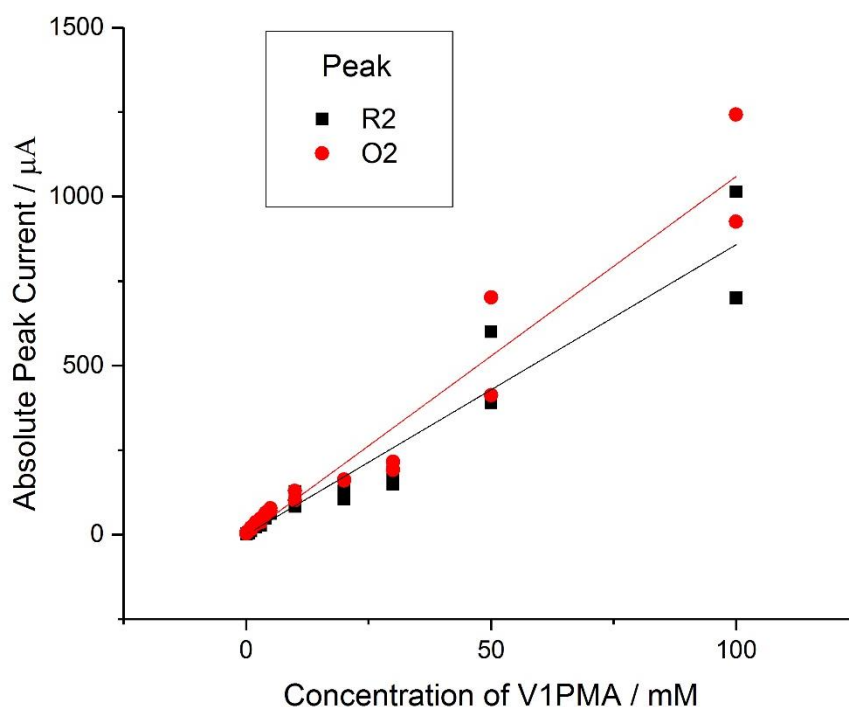
Figure 5.10 – The absolute peak current values taken for the R2 and O2 peaks (as labelled in figure 5.11) taken from cyclic voltammetry of different concentrations of V1PMA in 0.1 M sulphuric acid at a 3 mm EPPG electrode at 100 mV.s⁻¹. The trendlines show a 'hypothetical' linear fit

Figure 5.10 shows that the peak current in general increases linearly with peak current even at the extreme lower and upper concentrations, although with significant deviation. The figure shows a hypothetical line of linear best fit, and highlights that the behaviour is not truly linear acros the range but may have areas of different relationships. Using the Randles-Sevcik equation this data yielded diffusion coefficient values of 3×10^{-7} cm^2.s^{-1}. This value is much lower than for the PMA sample and is smaller than may be expected, indicating that the adsorbed layer is still having a large influence over normal behaviour. This can again be seen when highlighting the lower end of the concentrations used as shown in Figure 5.11.
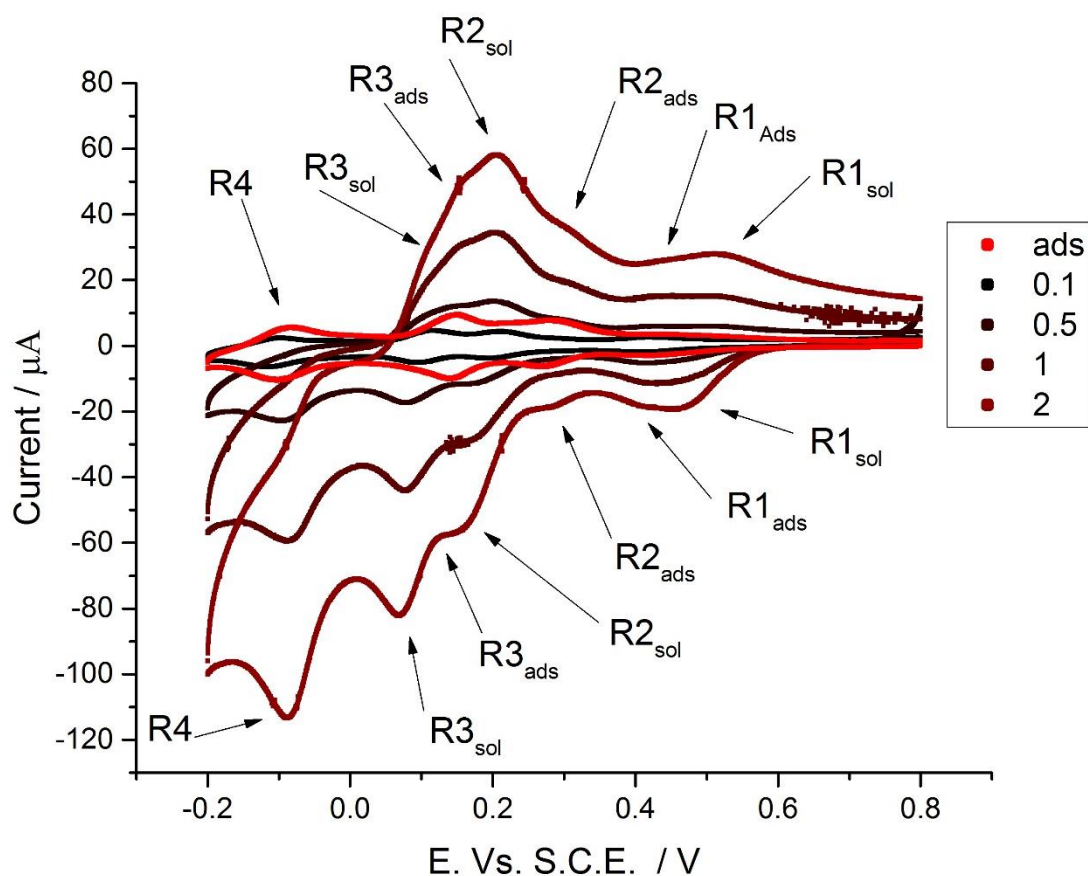
Figure 5.11 - Cyclic voltammogram showing low concentrations (0.1, 0.5, 1 and 2 mM) of NaV1PMA in 0.1 M sulphuric acid at 3 mm EPPG electrodes as well as a modified 3 mm EPPG electrode, dipped in 0.1 M NaV1PMA solution for 30 s taken in 0.1 M sulphuric acid, all scans taken at 100 mV.s^{-1}.

Figure 5.11 shows that as with the PMA solution the adsorbed layers response is superimposed on the solution electrochemical response, but that the peaks are much more clearly separated (with the exception of R4/O4). It also appears that the main peak for adsorbed R1 appears at a more negative potential then the main peak height for the solution based R1 peak. However due to the non-ideal nature of the adsorbed peak R1/O1 the onset of reduction occurs at a similar potential to that of the solution based reduction, meaning reduction of the adsorbed layer has begun at a higher potential than that of the solution. This is evident when the data is processed to produce a pseudo Tafel plot, indicating the position of reduction onset, shown in Figure 5.12. Figure 5.11 also shows that at the very low concentration of 0.5 mM the response is different from the adsorbed layer and the peak currents are lower than the adsorbed layer, this may indicate that the adsorbed layer is incomplete, or not fully formed.
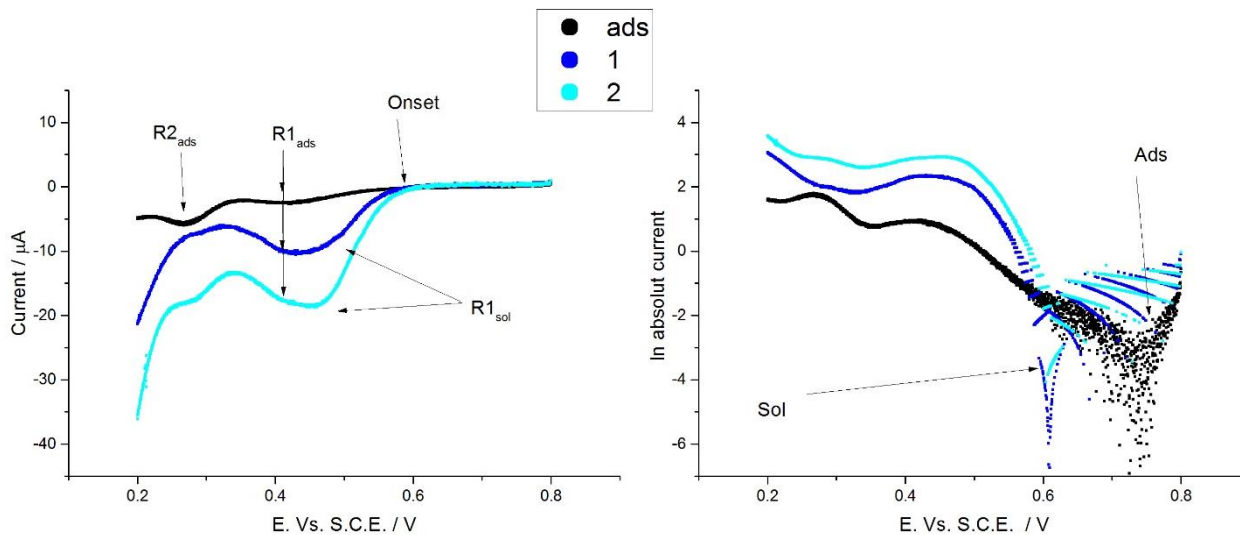
Figure 5.12 – Left, Selected R1 reduction taken from cyclic voltammetry at 3 mm EPPG electrodes in 1 and 2 mM NaV1PMA in 0.1 M sulphuric acid and a 3 mm EPPG electrode modified by dipping in 0.1 M NaV1PMA for 30 s taken at 100 mV.s^{-1}. Right, the corresponding pseudo-tafel plot.

5.3.5 Scan rate analysis of solution phase phosphomolybdic acid derivatives

The effect of scan rate on diffusion controlled and mediated electron transfer can provide mechanistic detail. The ability to out run reactions with scan rate exceeding the rate of reaction can yield information on those processes. As has been seen in previous sections there is a considerable interaction with the adsorbed layer from the solution, making analysis difficult and potentially confusing.

The diffusion coefficients have been relatively small compared to what one might expect and hint at these additional processes. When analysing the concentrations above, scan rates of $100 mV.s^{-1}$ were used. If the same analysis is completed at $10 mV.s^{-1}$ and $1000 mV.s^{-1}$ different values are calculated. Figure 5.13 and Figure 5.14 show the effect of concentration at these scan rates.
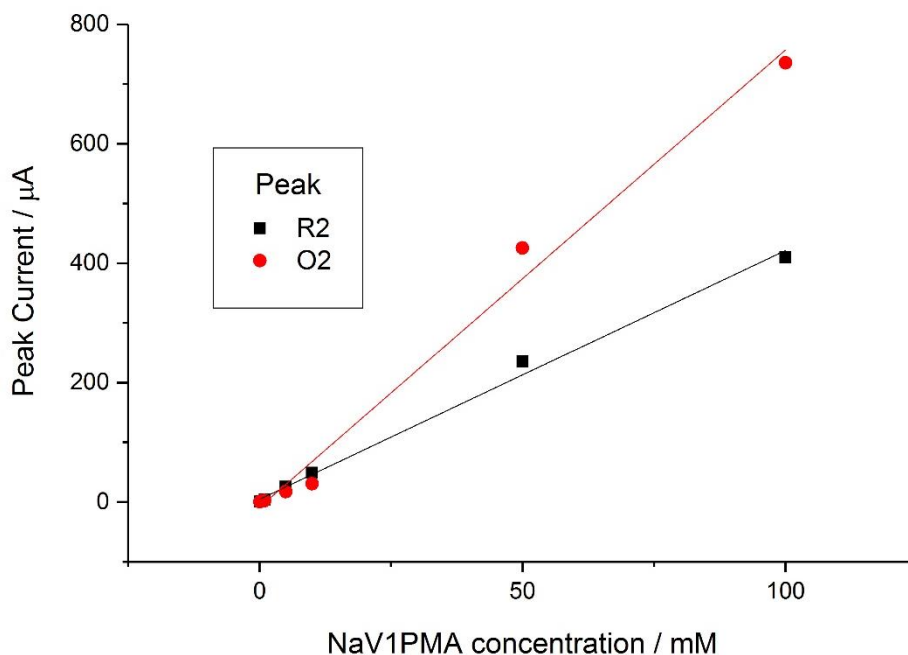
Figure 5.13 – Absolute Peak current versus concentration for the R2 and O2 peaks (labelled on previous figures) taken from cyclic voltammetry at 3 mm EPPG electrode with differing concentrations of NaV1PMA in 0.1 M sulphuric acid, taken at 10 mV.s⁻¹.
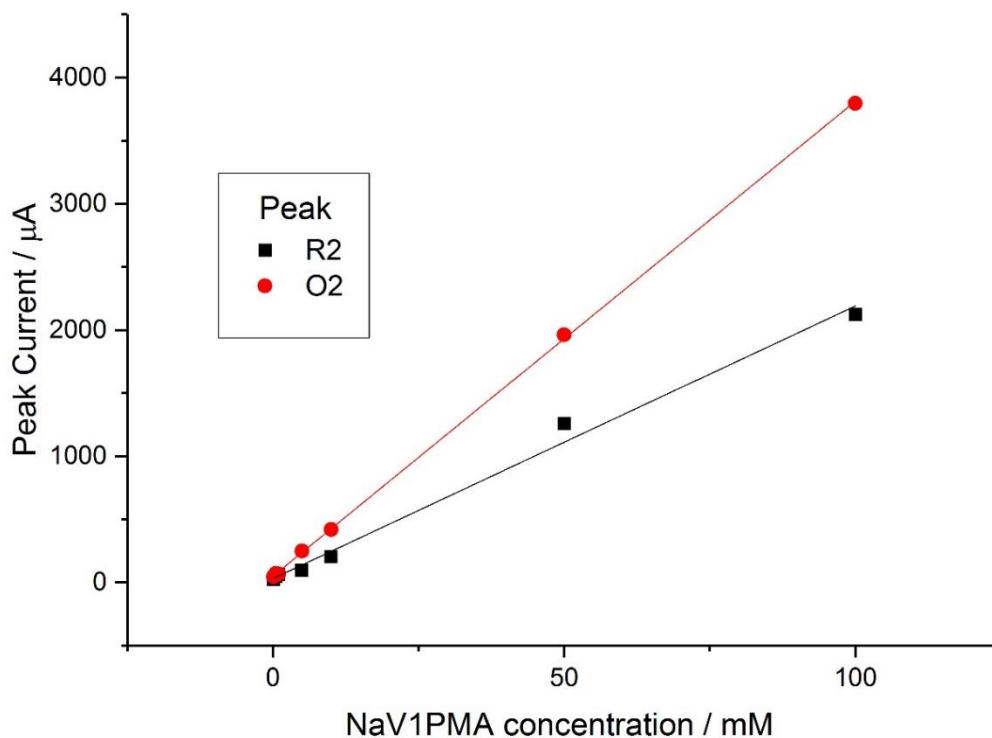
Figure 5.14 - Absolute Peak current versus concentration for the R2 and O2 peaks (labelled on previous figures) taken from cyclic voltammetry at 3 mm EPPG electrode with differing concentrations of NaV1PMA in 0.1 M sulphuric acid, taken at 10 mV.s^{-1}

From this data, using the same derivation for the Randles-Sevcik equation, diffusion coefficients at these scan rates can be calculated. At 10mV.s^{-1} the calculated diffusion coefficient is 1.32×10^{-6} cm^2.s^{-1} and at 1000 mV.s^{-1} it is 3.13×10^{-6} cm^2.s^{-1}. The diffusion coefficient of a substance in a given environment is independent of scan rate and so the effect that is really being observed is the change in the timescale used to observe a given process. A method to resolve the confusing effect of dominance of adsorbed layer electrochemistry at low concentration and also the change in observed process with increased scan rate is to create a plot incorporating both components. Within this study complete scan rate ranges were taken across a complete concentration range. Figure 5.15 and Figure 5.16 show variable scan rate graphs and the difference between the plots shows how the relationship with scan rate changes across the concentrations.
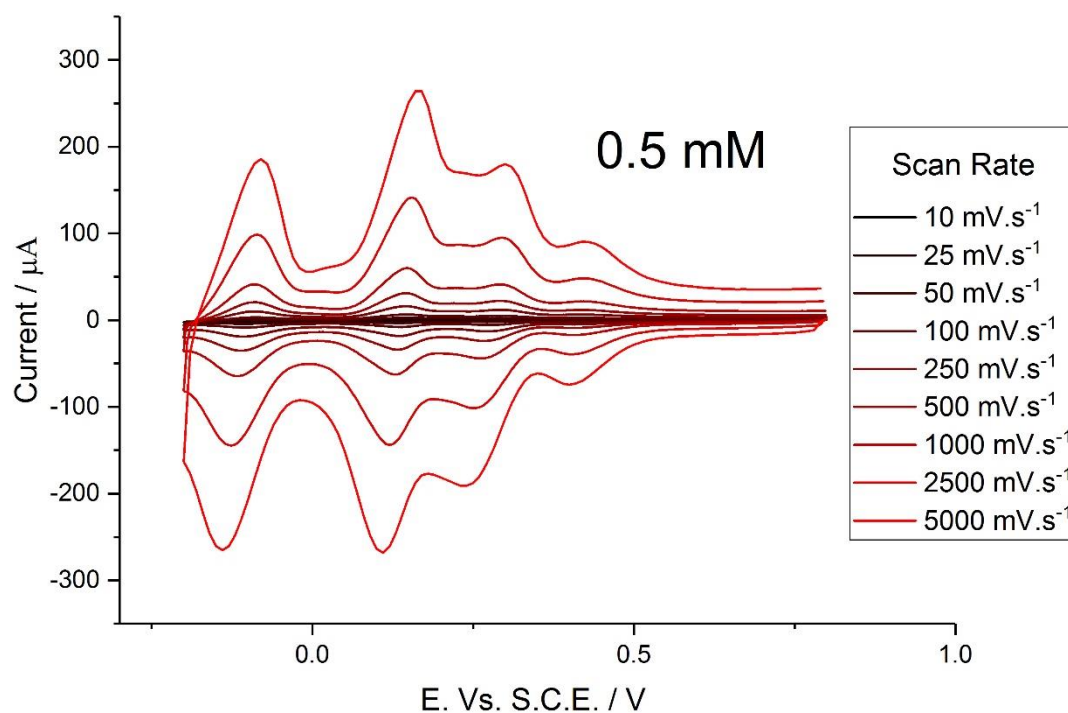
Figure 5.15 – Cyclic voltammetry at variable scan rates of 0.5 mM NaV1PMA in 0.1 M sulphuric acid at 3mm EPPG electrodes
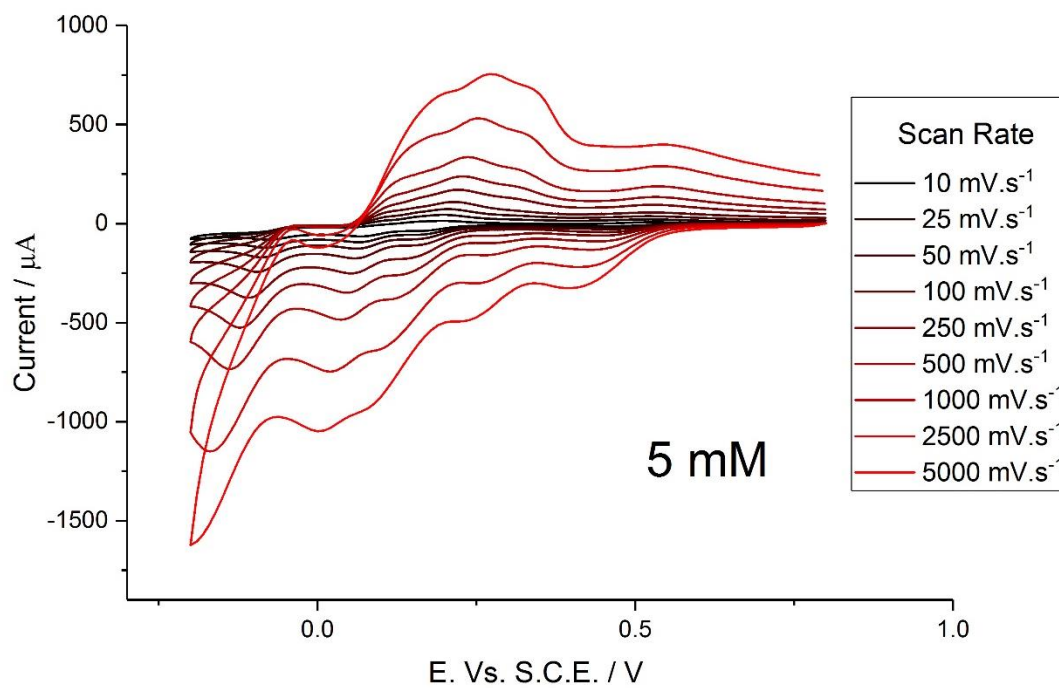
Figure 5.16 - Cyclic voltammetry at variable scan rates of 5 mM NaV1PMA in 0.1 M sulphuric acid at 3mm EPPG electrodes

Taking this data and processing it to give peak current vs concentration vs scan rate, allows for a multitude of graphs to be compiled. The scan rate vs peak heights can be used to plot normal Randles-Sevcik graphs to calculate diffusion coefficients, as shown in Figure 5.17. It is important to remember that these diffusion coefficient values are not truly valid across the whole range.
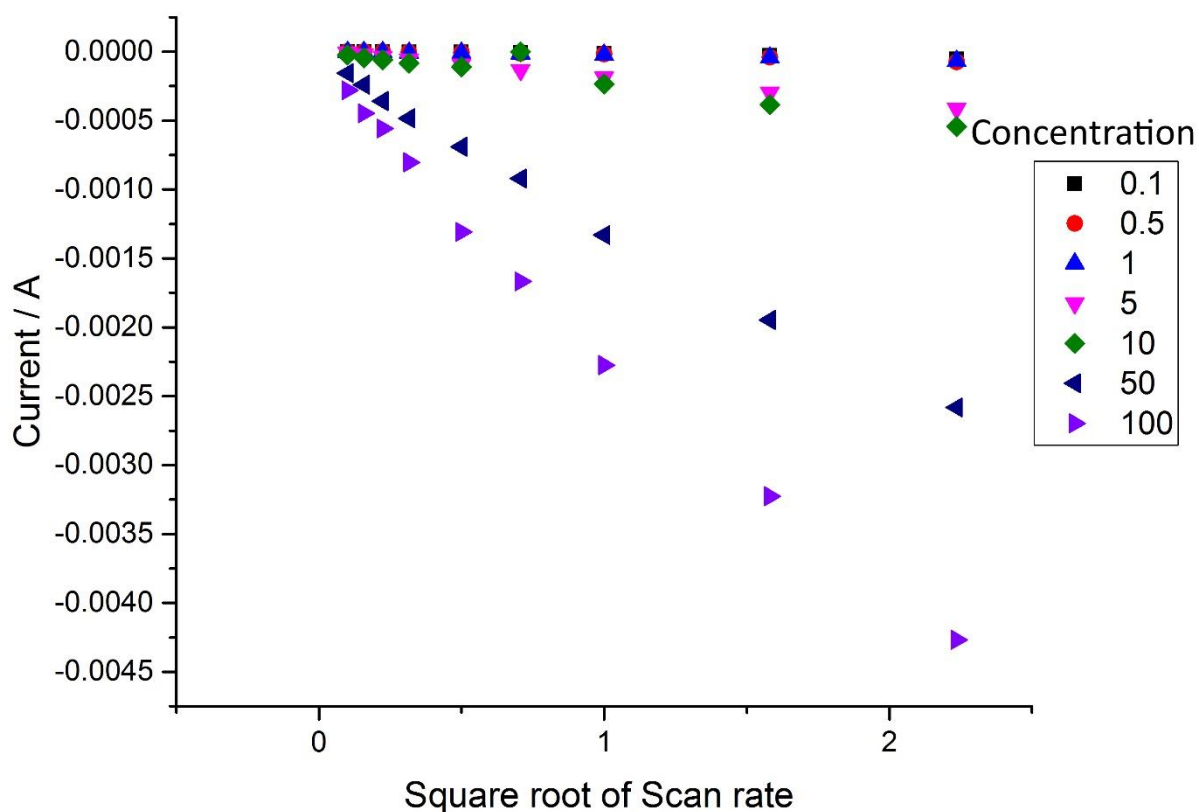
Figure 5.17 - Square root of scan rate versus peak height for the initial reduction process of V1PMA at 3 mm EPPG electrodes taken at various concentrations (mM) in 0.1 M sulphuric acid.

The data can also be used to plot concentration versus peak height to calculate diffusion coefficients as shown in Figure 5.18.
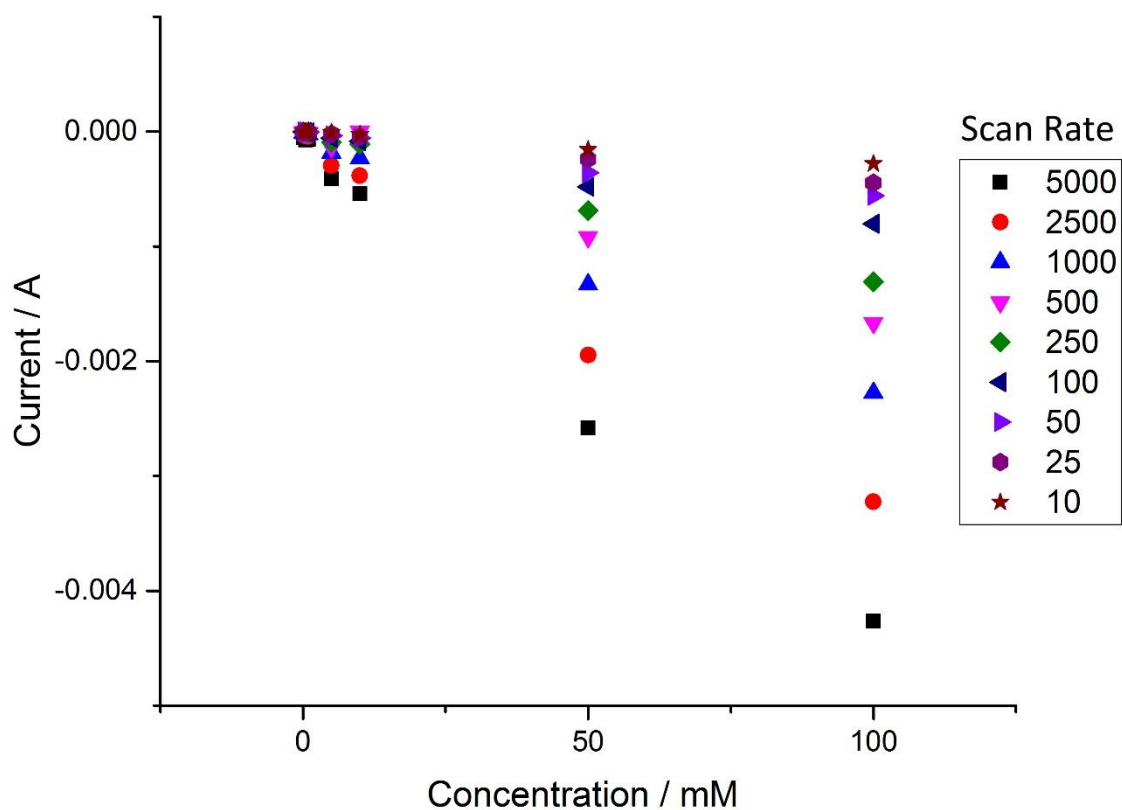
Figure 5.18 - Concentration versus peak height for the initial reduction process for V1PMA at EPPG electrodes taken at various scan rates (mV.s^{-1}) in 0.1 M sulphuric acid

As has been discussed these values are not valid across the whole range of scan rate and concentration and this leads to a huge variation in the calculated diffusion coefficient across the range. This is shown in Table 5-1.

Scan Rate (mV.s^{-1})	Diffusion Coefficient (cm^2.s^{-1})	Concentration (mM)	Diffusion Coefficient (cm^2.s^{-1})
5000	1.03	0.1	162.57
2500	1.19	0.5	11.92
1000	1.48	1	2.63
500	1.62	5	1.64
250	1.93	10	1.45
100	1.88	100	0.97
50	1.87		
25	2.28		
10	2.30		

Table 5-1- table of calculated diffusion coefficients for the initial reduction process for V1PMA

It can be seen in Table 5-1 that a relatively large spread of values exists. The data can be taken and plotted as a surface plot, together with a calculated plot for a given diffusion coefficient, shown in Figure 5.19.
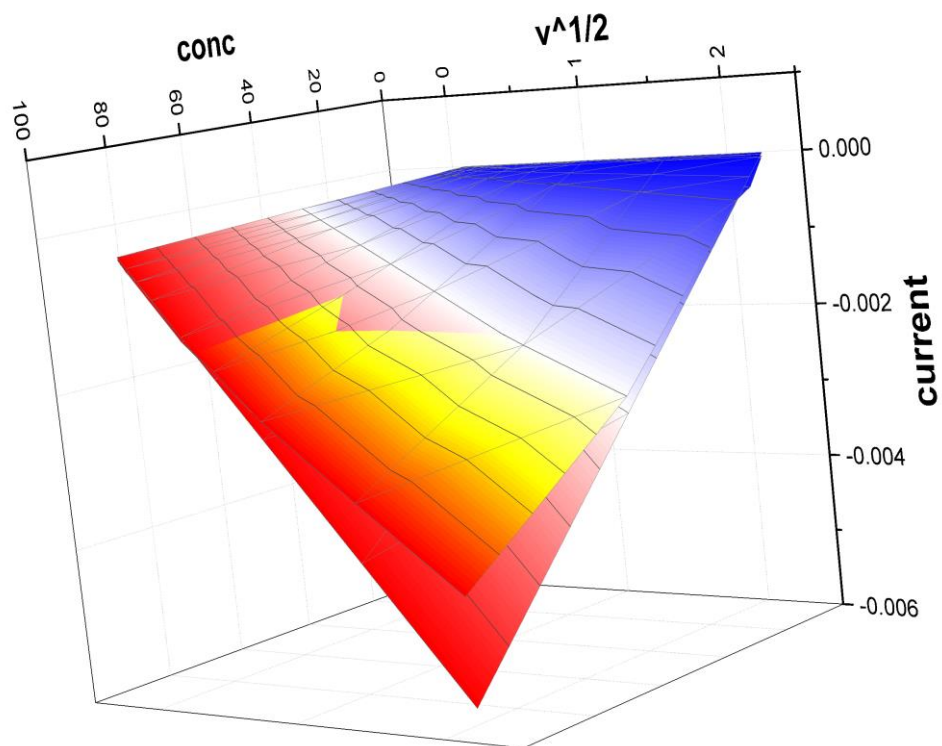
Figure 5.19 - Surface plot of peak current versus the square root of scan rate versus concentration for the initial reduction process of V1PMA solutions in 0.1 M sulphuric acid at 3mm EPPG electrodes

Figure 5.19 allows for a visualization of where the experimental data deviates from a theoretical flat sheet plot using an input diffusion coefficient. The diffusion coefficient used was fitted through progressive iterations reducing an average error in the calculated and theoretical current values. These errors can also be plotted to highlight the deviation from theory, as shown in Figure 5.20.
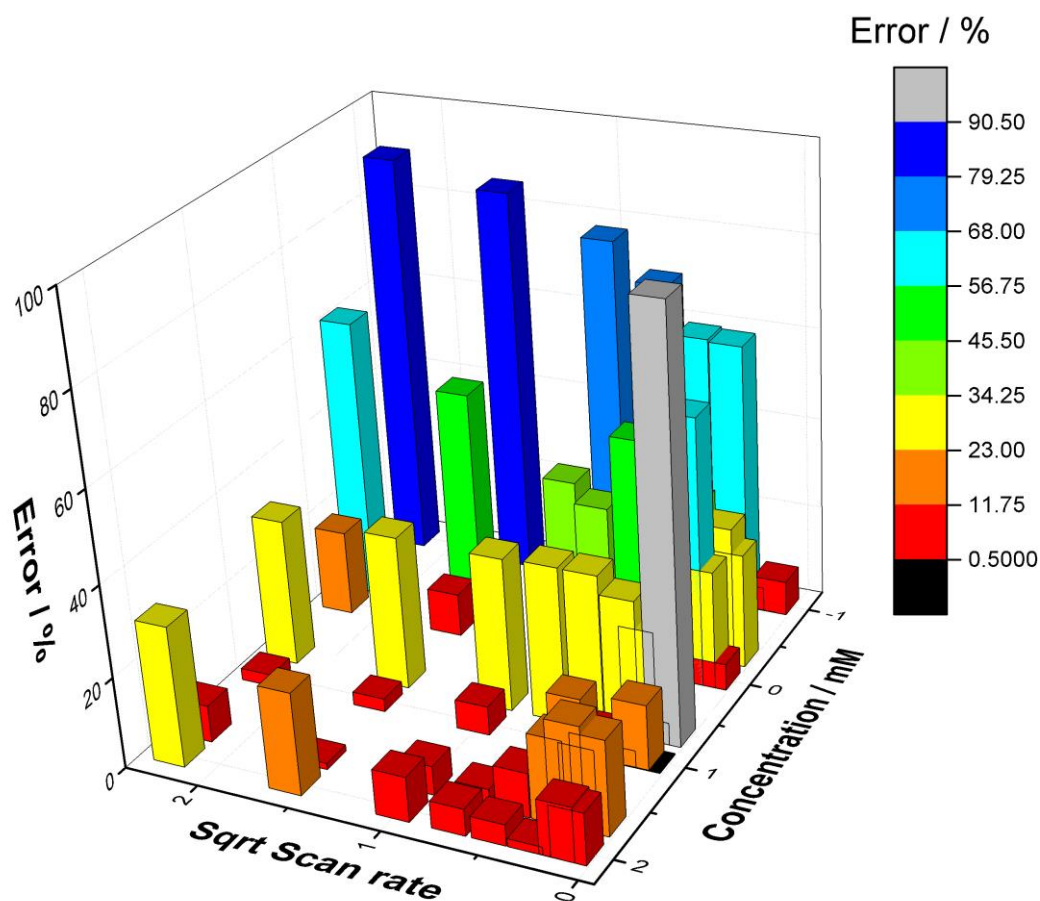
Figure 5.20 - 3d plot showing error in calculated and experimental current peaks versus the square root of scan rate and the concentration (logarithmic scale) for the initial reduction process in V1PMA solutions in 0.1 M sulphuric acid at 3mm EPPG electrodes

The lowest average error across the plane reached 24.8 % when using a coefficient of 1.73×10^{-06} $cm^2.s^{-1}$. It can be seen that at low concentrations and high scan rates the maximum error occurs. This is because at these conditions the largest percentage contribution of the adsorbed layer is seen and the scan rate is faster than the mediation process between the solution phase and adsorbed layer phase.

Using the same process as laid out above, diffusion coefficient values can be calculated for all the redox process across the cyclic voltammograms. These are shown Table 5-2. As discussed, using this methodology is not ideal to produce valid diffusion coefficients. Different methods including simulation using DigiElch^{TM} were also trialled, however, due to the complicated multi-step, multi-electron transfer and non-ideal behaviour, issues with over-parameterisation occurred.

	Diffusion Coefficient $(10^{-6}$ cm^2.s$^{-1})$	number of electrons
R1	1.73	1
O1	0.35	1
R2	2.3	1
O2	1.05	1
R3	0.65	2
O3	1.1	2
R4	2.3	2
O4	2.15	2

Table 5-2 - Diffusion coefficient values for all redox process in V1PMA at EPPG electrodes

5.3.6 Effect of pH on the redox couples

As with the adsorbed layer electrochemistry in chapter 4, pH adjustment can be used to identify attributes within the reaction mechanism. It has already been seen how the electrochemistry of the

solution phase involves interaction with the adsorbed layer and that the redox processes exhibited by the adsorbed layer shift with pH.

The sequence of redox processes is not as clear within the solution phase due to the interaction with adsorbates. Sections 5.3.4 and 5.3.5 showed how the degree of this interaction was affected by scan rate and concentration. Additionally, it was thought this interaction would be affected by pH. Figure 5.21 and Figure 5.22 show the effect of changing pH on the cyclic voltammetry seen when conducted variable scan rate assessment of PMA solutions.
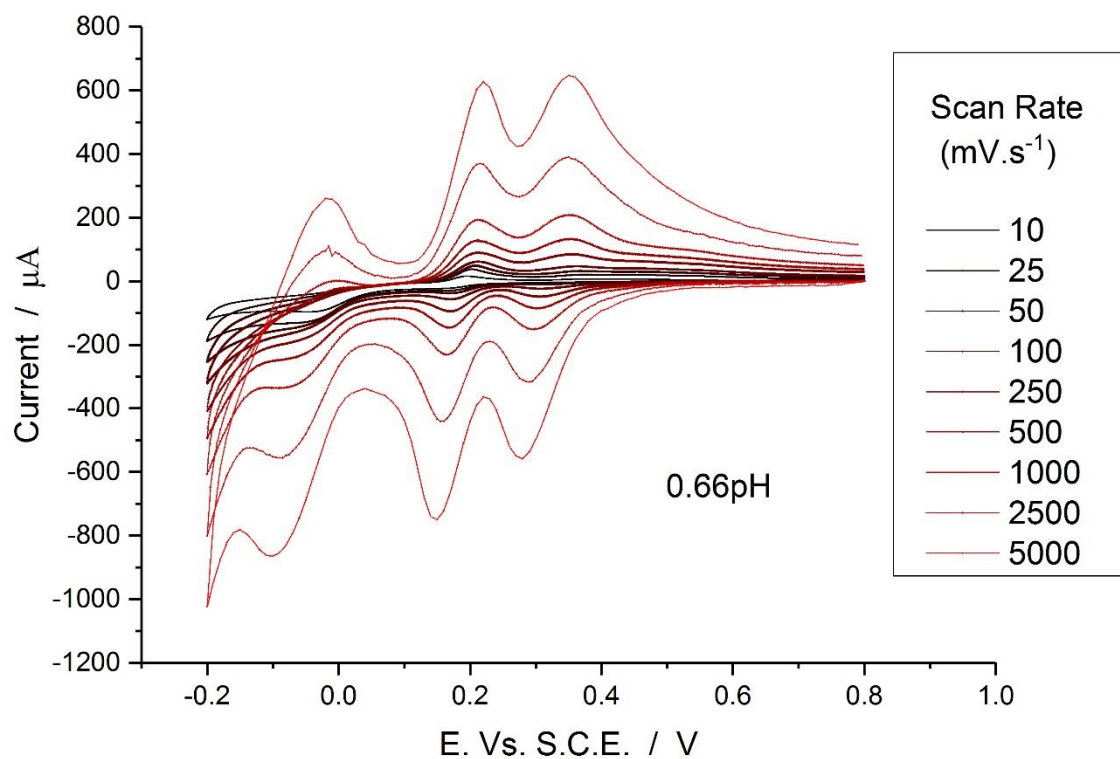
Figure 5.21 – Cyclic voltammetry of 5 mM PMA in 0.5 M sulphuric acid at 3 mm EPPG electrodes at variable scan rates
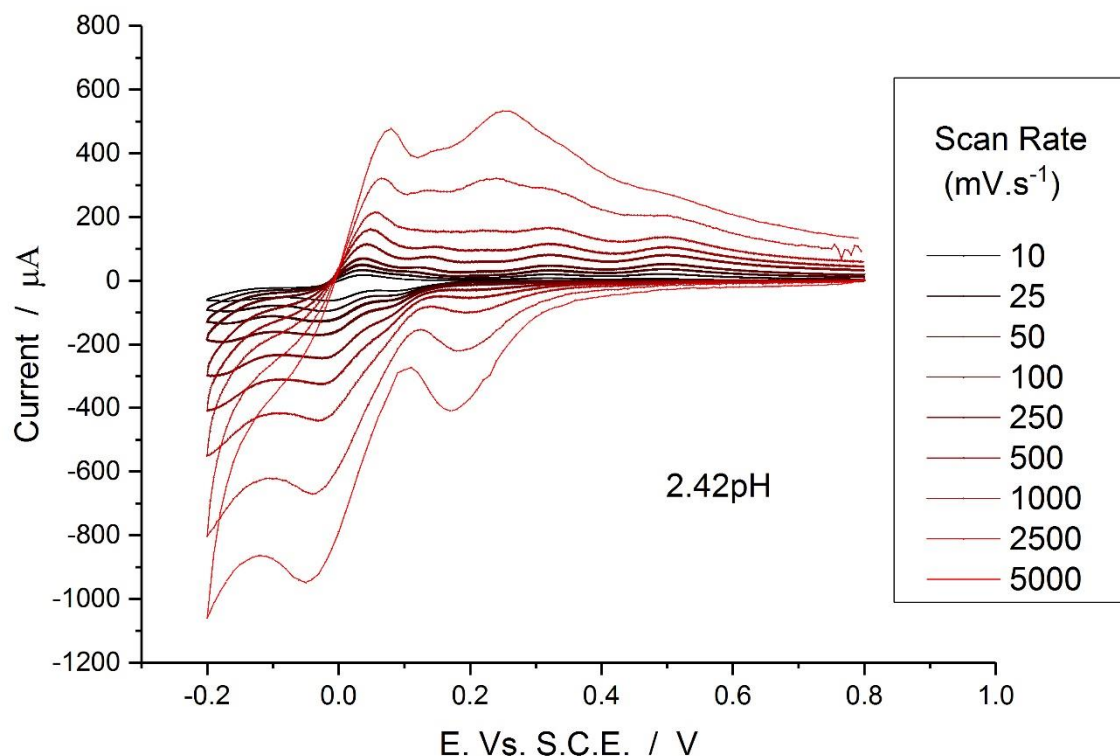
Figure 5.22 – Cyclic voltammetry of 5 mM PMA in 0.5 sulphuric acid adjusted with NaOH to reach 2.42 pH (measured with a pH meter) taken at 3 mm EPPG electrodes at variable scan rates.

By analyzing these plots and comparing to literature, it can be deduced that a similar overall reaction scheme to that of the adsorbed layer is dominating, of three two electron reductions. However, when analysing slow scan rates additional processes are seen which do not shift in the same manner with pH. In particular, R1/O1 labelled in Figure 5.23 is an additional feature that does not shift with pH. Additionally, the reduction is particularly difficult to observe, often appearing as an onset feature rather than a full peak.
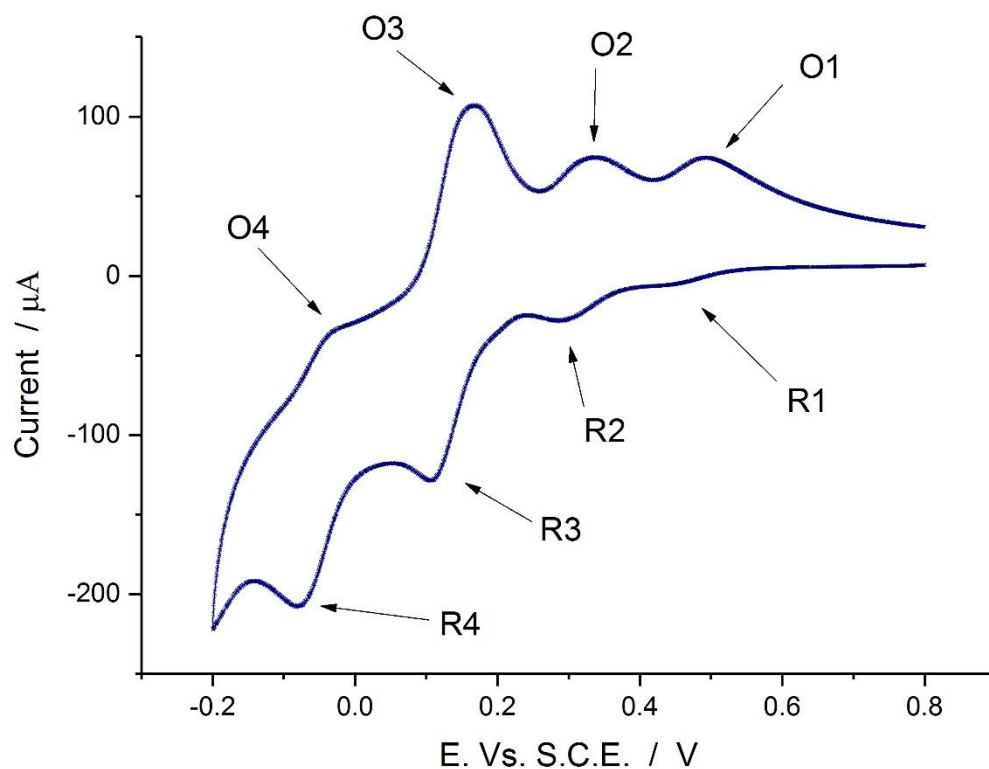
Figure 5.23 – Cyclic voltammetry at 3 mm EPPG electrode at 100 mV.s^{-1} of 5 mM PMA solution in 0.5 sulphuric acid with aliquots of 0.1 M NaOH solution to adjust pH, the pH in this example was 1.14.

This makes a full pH analysis difficult and as such it makes any information obtained about the proton to electron ratio highly susceptible to error. However, the analysis can still provide insight into the redox process, as shown in Figure 5.24.
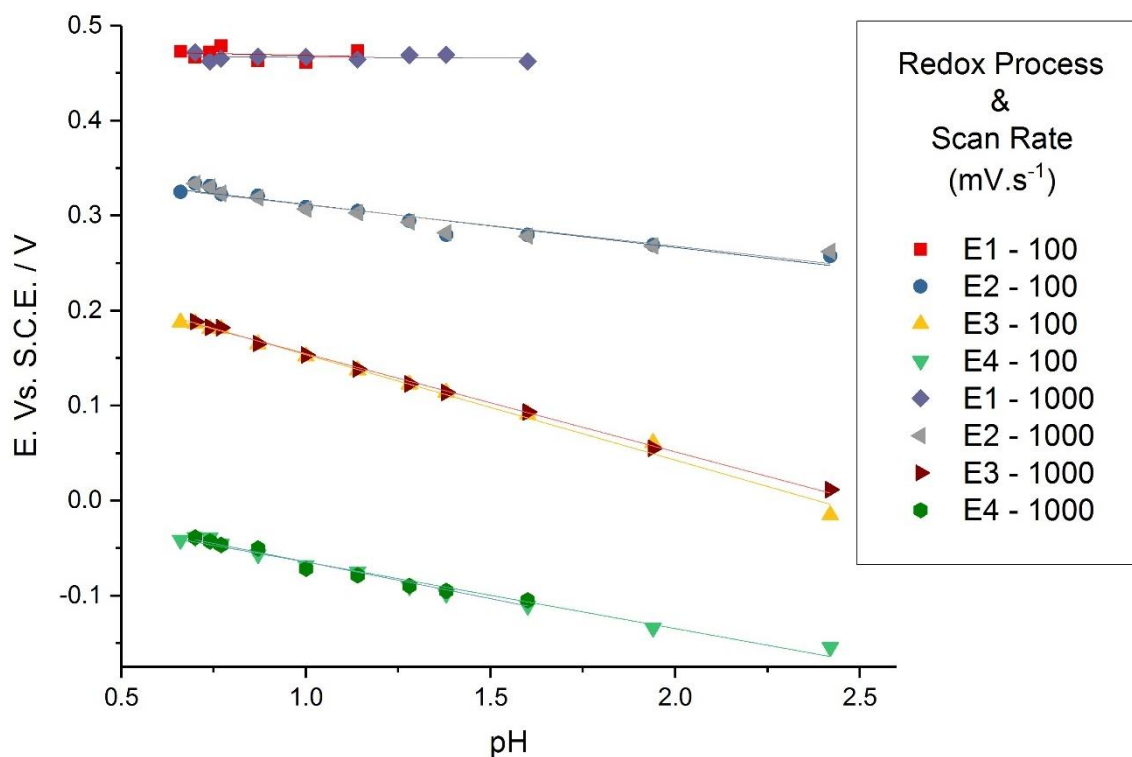
Figure 5.24 – Observed $E_{1/2}$ versus pH for redox processes (labelled in figure 5.23) observed during cyclic voltammtry of 5 mM PMA solution in 0.5 M sulphuric acid adjusted with aliquots of NaOH solution to achieve pH taken at 3 mm EPPG electrodes at 100 mV.s^{-1} and 1000 mV.s^{-1}.

The data shows that the redox equilibrium positions for most processes observed are dependent on pH and so that the reactions are dependent on proton concentration with processes 2, 3 and 4, having slopes of 44, 106.5 and 73.5 mV.dec^{-1} respectively. However, the initial redox process' equilibrium is independent of pH with a slope of 4 mV.dec^{-1}. This indicates that this is a mediated reduction, where the layer is being reduced and 'passing' the electron onto the bulk solution phase. This interpretation is supported by the shift in this peaks equilibrium position with concentration, as the reduced species in the layer is being oxidised by a reduction in the bulk solution and as such is more dependent on the concentration of the bulk solution.

It is a similar situation with the more complex redox processes observed within the V1PMA solutions, Figure 5.25.
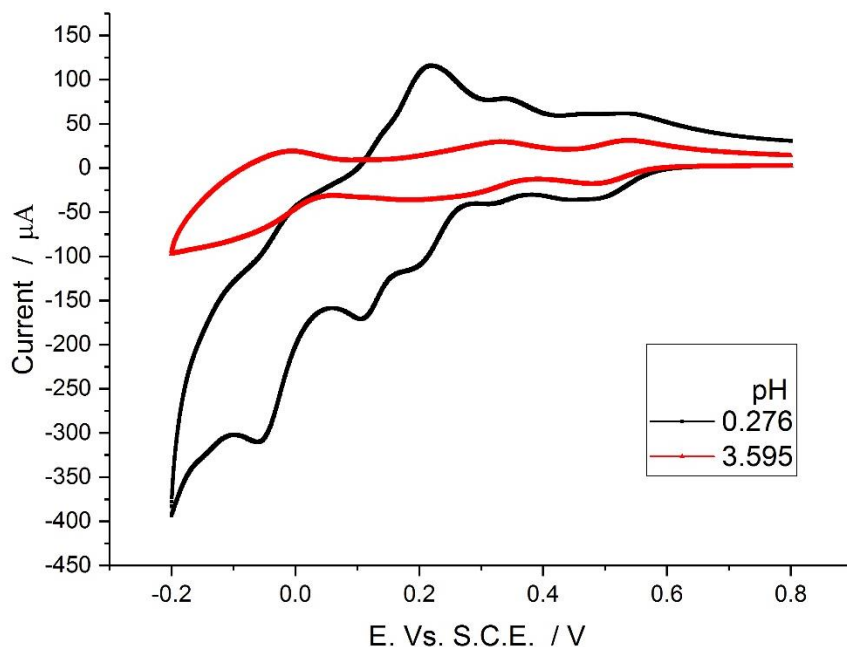
Figure 5.25 - Cyclic voltammetry at 3 mm EPPG electrode at 100 mV.s^{-1} of 5 mM NaV1PMA solution in 0.5 sulphuric acid with aliquots of 0.1 M NaOH solution to adjust pH, the pH in these examples were 0.276 and 3.595.

At low concentrations, it is possible to see evidence of the shifting underlying redox processes of the adsorbed layer, although at higher concentrations, the main processes exhibited by the bulk solution (R1/O1, R2/O2, R3/O3 and R4/O4, in following figures) are clearer. However, there are additional peaks (R1a/O1a and R1b/O1b, in Figure 5.26 and Figure 5.27), which are superimposed upon these waves.
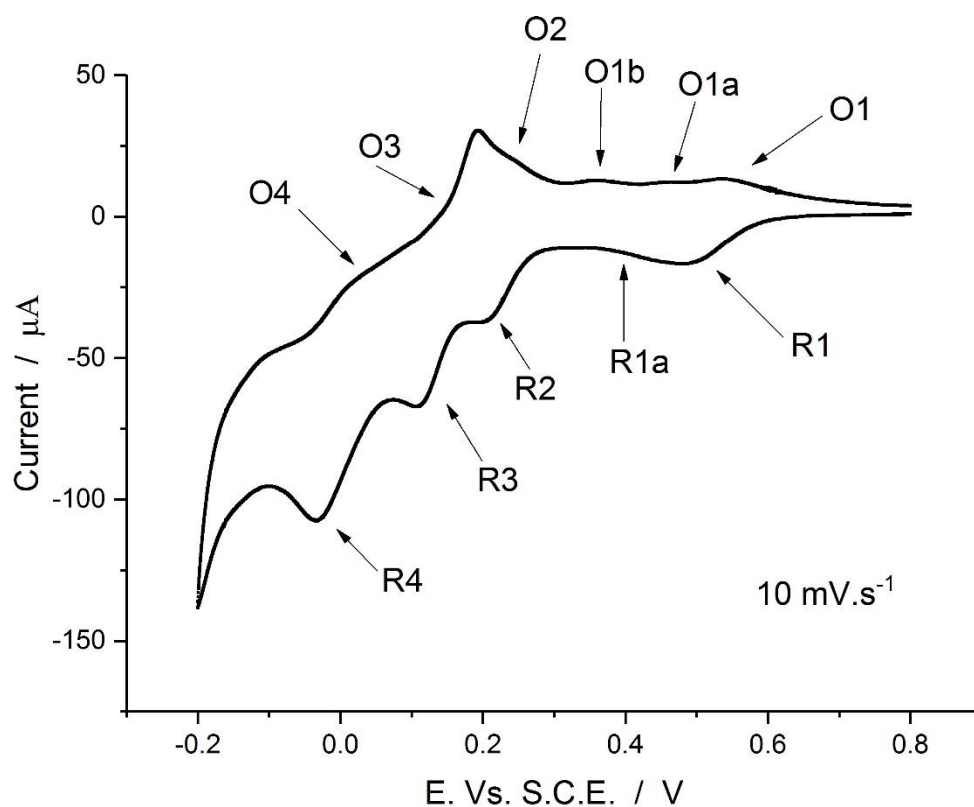
Figure 5.26 – Cyclic Voltammetry at 10 mV.s⁻¹ of 5 mM HV2PMA in 0.5 M sulphuric acid adjusted to a pH of 0.47 with NaOH taken at 3 mm EPPG electrodes.

These additional redox features are especially difficult to identify. Additionally, changing in prominence with scan rate and pH, as can be seen comparing Figure 5.26 with Figure 5.27. This suggests that the difference in scan rate is again 'out-running' some redox mechanisms at fast scan rates.
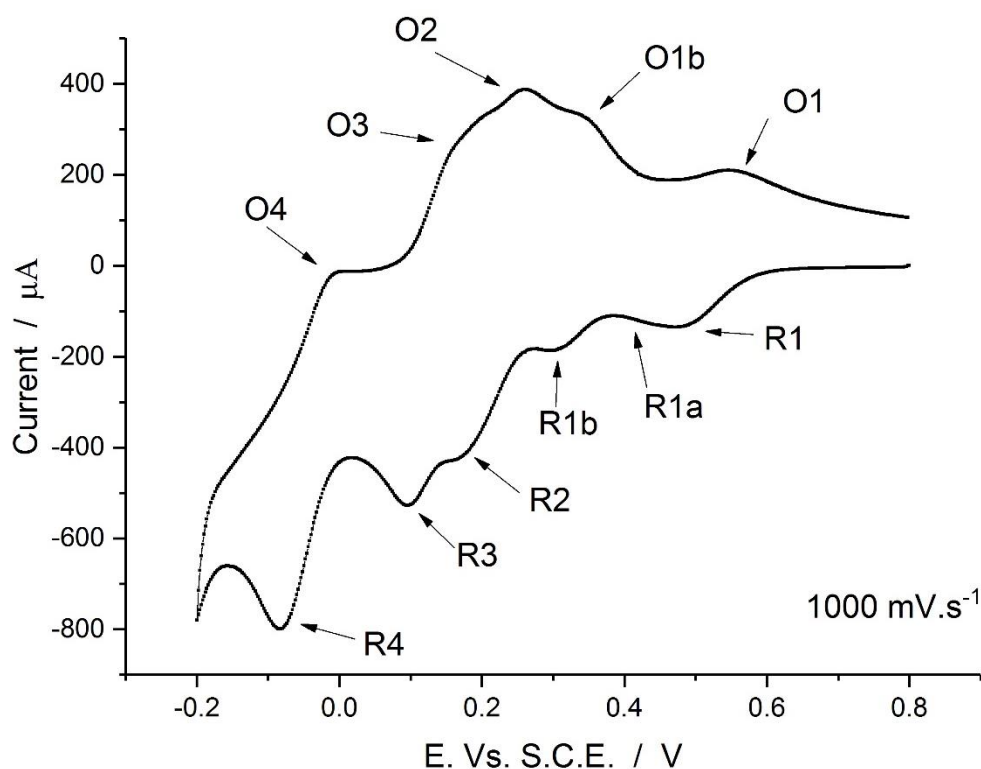
Figure 5.27 - Cyclic Voltammetry at 1000 mV.s^{-1} of 5 mM HV2PMA in 0.5 M sulphuric acid adjusted to a pH of 0.47 with NaOH taken at 3 mm EPPG electrodes.

This difference across the scan rates led to the determination of the shift with pH to be conducted across different scan rates. This allowed for the difficulty identifying peaks to be mitigated against, although it must be incorporated when assessing the results. Figure 5.28 shows an example of results determined at 100 mV.s^{-1}.
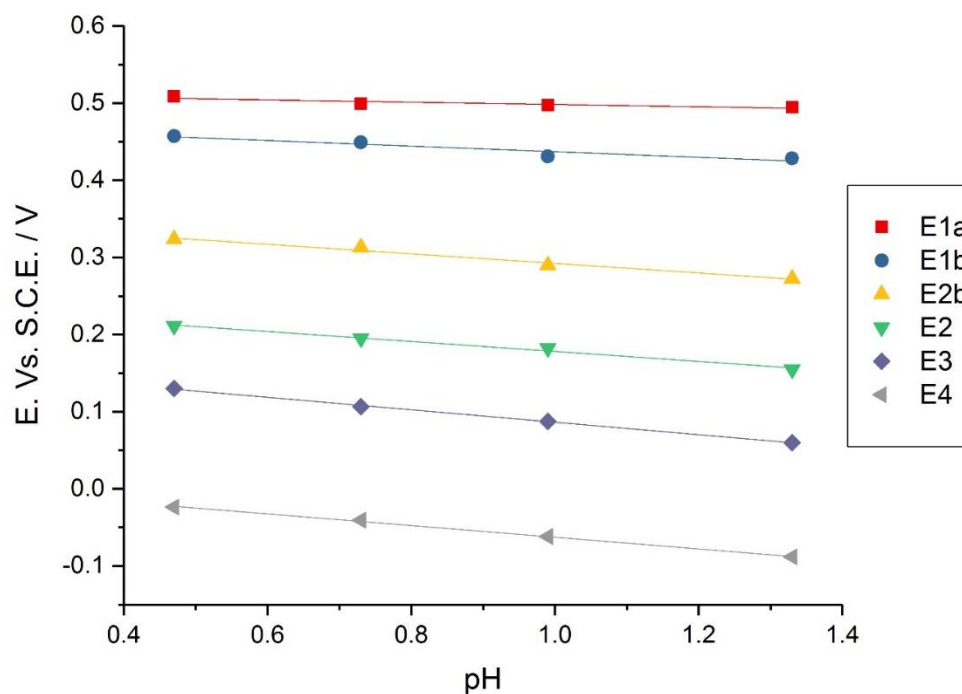
Figure 5.28 – Observed $E_{1/2}$ versus pH for HV2PMA, values taken from cyclic voltammetry at 100 mV.s^{-1} of 5 mM HV1PMA in sulphuric acid adjusted for pH with NaOH taken at 3 mm EPPG electrodes.

This data was collected and tabulated into Table 5-3 showing that the ratio of protons to electrons in the redox reaction taking place changes with each process. It is especially evident that the ratio is no longer purely 1:1.

Scan Rate (mV/s)	E1	E1a	E1b	E2	E3	E4
10	0.42	0.44		1.09	1.32	1.38
50	0.42	0.46	1.26	1.55	1.34	1.26
100	0.25	0.62	1.05	1.10	1.37	1.28
500	0.41	0.98	0.96	1.28	1.57	1.44
1000	0.51	0.70	1.00	1.16	1.62	1.65

Table 5-3 – tabulated proton to electron ratios of the different redox process, labelled in previous figures, for cyclic voltammetry of 5 mM HVIPMA at 3 mm EPPG electrodes in sulphuric acid adjusted for pH with NaOH.

The same pattern was observed between the two species of V1PMA using the H^+ and the Na^+ counter ions. A much more detailed study at $100\,mV.s^{-1}$ was undertaken, using multiple scan ranges to allow the identification of the different peaks easier.

From the previous data, Table 5-3, the first and second redox processes where still unclear, especially regarding the ratio of proton to electrons in the reaction. Figure 5.29 shows the highlighted R1/O1 peak and demonstrates clearly that the $E_{1/2}$ does not change but the shoulder R1a/O1a does change with pH.
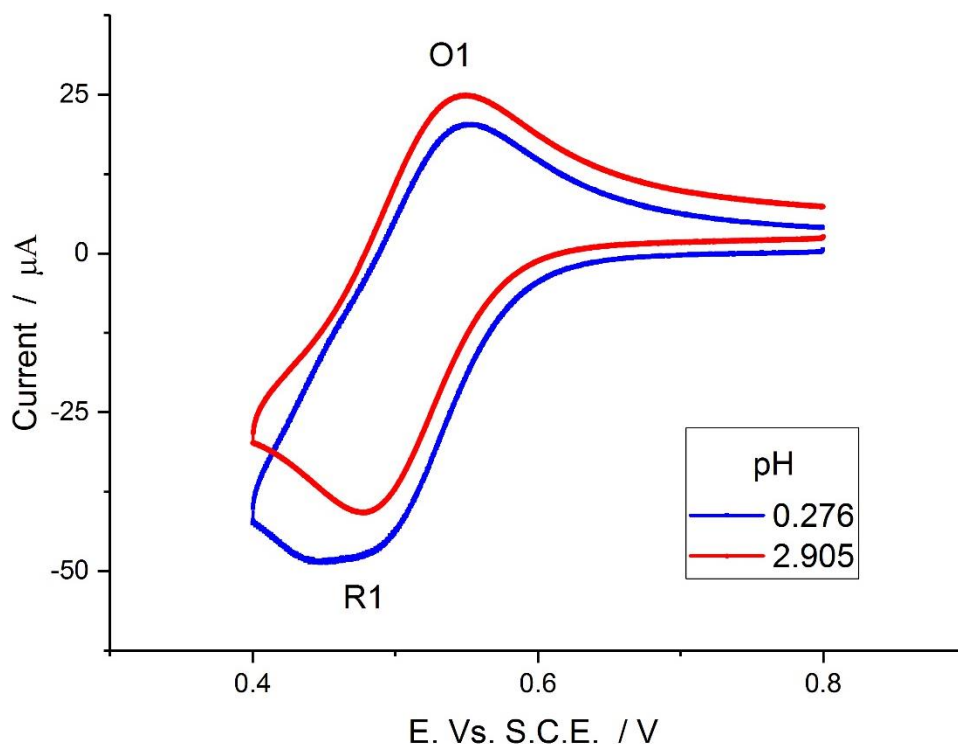
Figure 5.29 – Cyclic voltammetry of 5 mM NaV2PMA in 0.5 M sulphuric acid adjusted for pH with NaOH taken at 100 mV.s^{-1} at 3 mm EPPG electrodes.

216
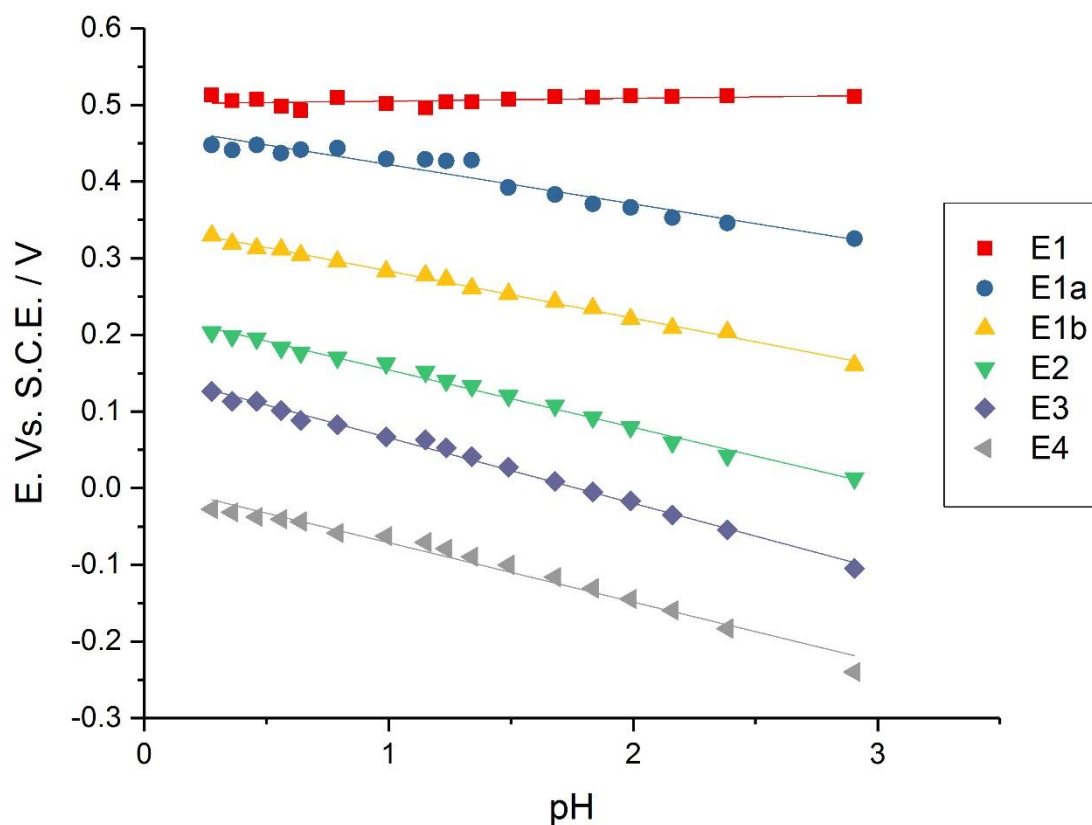
Figure 5.30 - Plots of observed $E_{1/2}$ versus pH for the redox process observed (E1-E4, labelled figure 5.25) for cyclic voltammetry of 5 mM HV1PMA and NaV1PMA 5mM solutions in 0.5 M sulphuric acid with aliquots of NaOH solution to adjust pH taken at 100 mV.s^{-1}

The slope values for processes, E1, E1a, E1b, E2, E3 and E4, taken from Figure 5.30, of 3.6, 51.4, 61.5, 75, 85.6 and 77.4 mV.dec^{-1}. These again indicates that the first redox process is independent of pH but that the following processes are much closer to the 1 electron 1 proton ratio observed previously and in literature.[223,332] However, it infers that the processes are no longer simple processes and have been complicated deviating away from 1:1 ratios, possibly mixing mechanisms or the existence of multiple species at higher pH, as seen previously with HPAs.[338,339]

5.4 Conclusions on solution phase electrochemistry for phosphomolybdic acid and singularly substituted vanado-phosphomolybdic acid

It has been observed that the bulk solution phase electrochemistry of phosphomolybdic acid derivatives is much more complex than the adsorbed layer or of standard redox processes. It has been shown that this is due to the interaction between the bulk phase and the adsorbed layer phase of the species. The same redox processes, of three two electron transfers for phosphomolybdic acid and two, one electron and two, two electron transfers for singularly vanadium substituted phosphomolybdic acid are observed.

However, the initial reduction process is dominated by the mediation of the adsorbed layer reduction by the bulk phase and hence is no longer showing a 1:1 proton to electron dependence. It is almost impossible to tell from the data the rate at which the mediation occurs but, it can be shown that it is the dominant process at low concentrations and low scan rates. Additionally, at high scan rates the mediation rate is out run by the rate of excitation increase and as such is not observed. It is also noted that at higher concentrations, the interaction has been dominated by the bulk solution electrochemistry so that the interaction with the layer is no longer observable, even though the process is underlying.

6. The effect of further vanadium substitution into the keggin structure of phosphomolybdic acid.

6.1 Introduction

The surface adsorbed and the solution phase electrochemistry of phosphomolybdic acid and singularly substituted vanadophosphomolybdic acid has been investigated in chapters 3, 4 and 5. The clear difference between the surface electrochemistry between the mother phosphomolybdic species and the singularly substituted vanadium derivative has been shown with the effect of electrode surface and pH in chapters 3 and 4. The influence of the adsorbed layer on the solution phase electrochemistry was demonstrated in chapter 5 with the effect of concentration, pH and electrode structure.

Often the research has focused across species containing multiple substitutions into the keggin structure of vanadium.[222,223] This is because it has been difficult to isolate one derivative from another due to disproportionation of the species in previous studies. ACAL Energy Ltd. supplied two cation variants of the doubly substituted vanadium species of phosphomolybdic acid, which was shown to be pure (by their in-house analysis). This presents the opportunity to investigate the effect of increasing the substitution of vanadium into the structure by one atom and observing its effects on the electrochemistry of the adsorbed layer and in solution.

6.1.1 Multi-substituted keggin species

Additionally to the increased oxygen affinity[222,331] and the volcano curve of activity, the increase in vanadium concentration also leads to the possibility of increased rates of disproportionation (Equation 5.1 [337]).[291,331,337] It has also been observed that only V1PMA solutions can truly be described as a single species solution but the increased disproportionation at higher vanadium inclusion values leads to mixed species.[291] However, discussions with the synthetic chemists within ACAL Energy Ltd suggests that with modern synthetic routes (the previous references are all prior 1995) that V2PMA is also a solution of a single species.

It was discussed in chapter 1 and further in chapter 3 that the adsorbed layers of PMA and V1PMA show catalytic, electrochemical and electrocatalytic behaviour. Similar behaviour is observed in V2PMA. Which has been shown to catalyse dye molecules,[340] perform oxidations[341,342] and chemical synthesis,[343,344] as adsorbed layers.

The effect of further inclusion of vanadium within the phosphomolybdic species has been well documented in terms of its affinity to oxygen, its increased stability and its effect as a solution based catalyst.[190,200,336] However, its electrochemistry remains relatively unexplored as a separate entity. As such this chapter aims to address this gap in knowledge and perform the same characterisation that has been seen for phosphomolybdic acid and its singularly substituted derivative in chapter 3, 4 and 5.

This chapter will explore the adsorbed layer and the solution phase electrochemistry of doubly substituted vanadophosphomolybdic acid, including the effect of electrode surface, pH and concentration on the redox processes observed.

6.2 Experimental

The equipment and techniques used to assess the surface species electrochemistry of doubly substituted vanadophosphomolybdic acid was the same as that described in chapter 4. The solutions used for modification consisted of aqueous 0.1 M doubly substituted vanado-phosphomolybdic acid diluted from 0.3 M solutions provided by ACAL Energy Ltd. Similarly, the solution phase electrochemistry of doubly substituted vanado-phosphomolybdic acid was investigated using the same methods described in chapter 5. The solution used to make the analyte solutions being the aqueous 0.3 M doubly substituted vanadophosphomolybdic acid.

6.3 Results and discussion

After analysing the change in redox processes introduced by substituting a single vanadium atom into the phosphomolybdate heteropolyanion, the effect of substituting two vanadium atoms into the species was investigated. The aim was to see how this affected the redox behaviour and whether it led to a higher first potential at which reduction would take place. If so, this would lead to a higher open circuit potential within a fuel cell application. Additionally, if this was not the case a second question was whether it would increase the current density observed within the first reduction wave seen at singularly substituted species.

6.3.1 Surface redox behaviour of doubly-substituted vanado-phosphomolybdic acid

The previous chapters investigated the formation of adsorbed layers by the singularly substituted phosphomolybdic acid derivatives and subsequently how the formation of these layers significantly affected the electrochemistry of the solution phase. Having established techniques to investigate the adsorbed layers and solution phases in previous chapters the same techniques were used to investigate the adsorbed layers formed by doubly substituted vanado-phosphomolybdic acid (V2PMA).

Adsorption rates of doubly substituted vanado-phosphomolybdic acid

The first step was to study whether the extra substitution had affected the rate of layer formation. As with previous experiments a 0.1 M dip solution was used and a variety of graphitic electrodes were tested, Figure 6.1 shows initial cyclic voltammetry.
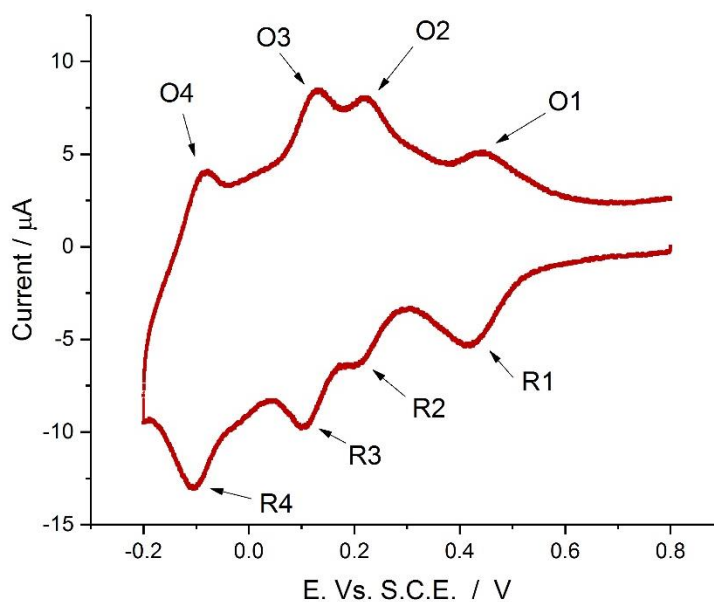
Figure 6.1 – Cyclic voltammetry in 0.1 M sulphuric acid at 100 mV.s^{-1} of a 3 mm EPPG electrode modified by dipping in 0.1 M V2NaPMA solution for 30 s.
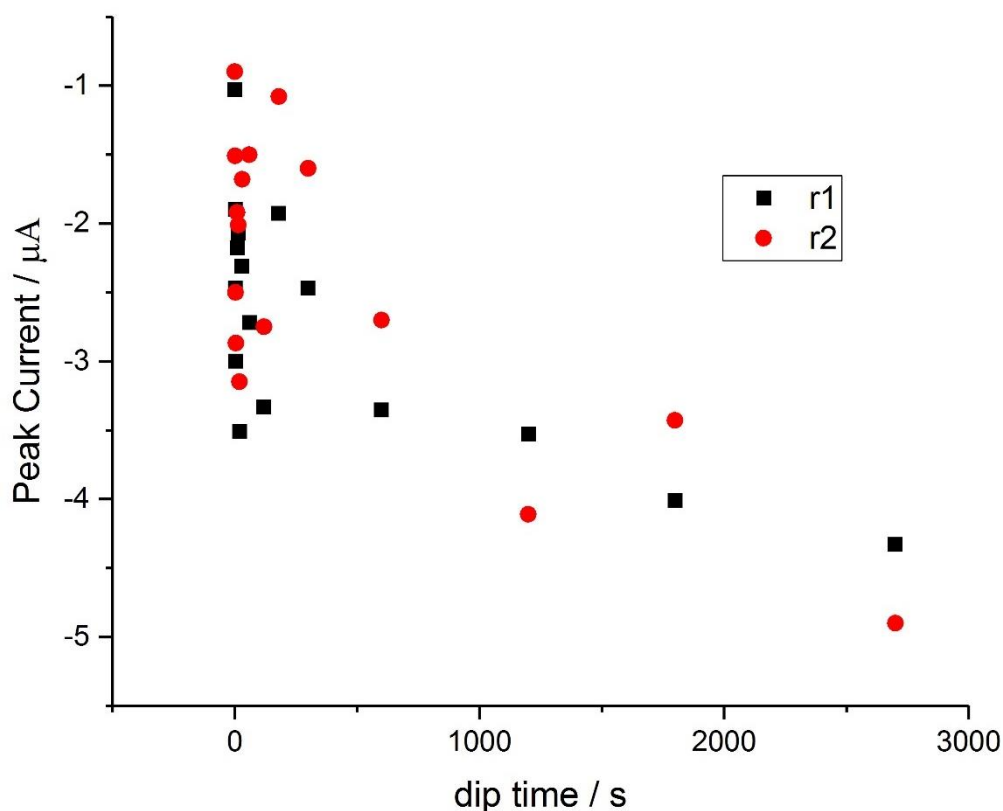
Figure 6.2 -Peak current of the R1 and R2, as labelled in figure 6.1, observed in cyclic voltammetry in 0.1 M sulphuric acid at 100 mV.s⁻¹ of 3mm EPPG electrodes modified by dipping in 0.1 M NaV2PMA for variable timings, versus the time that the electrodes were dipped for.

It can be seen from Figure 6.2 that the same pattern in the development of the layer exists, with an initial dramatic rise in current that then reduces. This suggests that the process of adsorption has not been affected by the extra substitution. This validates using the same methods for analysing the electron transfer processes as previous experiments.

Figure 6.1 also highlights the slight switch in the magnitudes between the electron transfer processes. The substitution appears not to have shifted the initial reduction more positive but does seem to have increased its magnitude whilst the third reduction wave has seemingly reduced in

223

magnitude. The effect on the redox processes is much clearer when viewing a direct comparison with PMA and NaV1PMA, Figure 6.3.
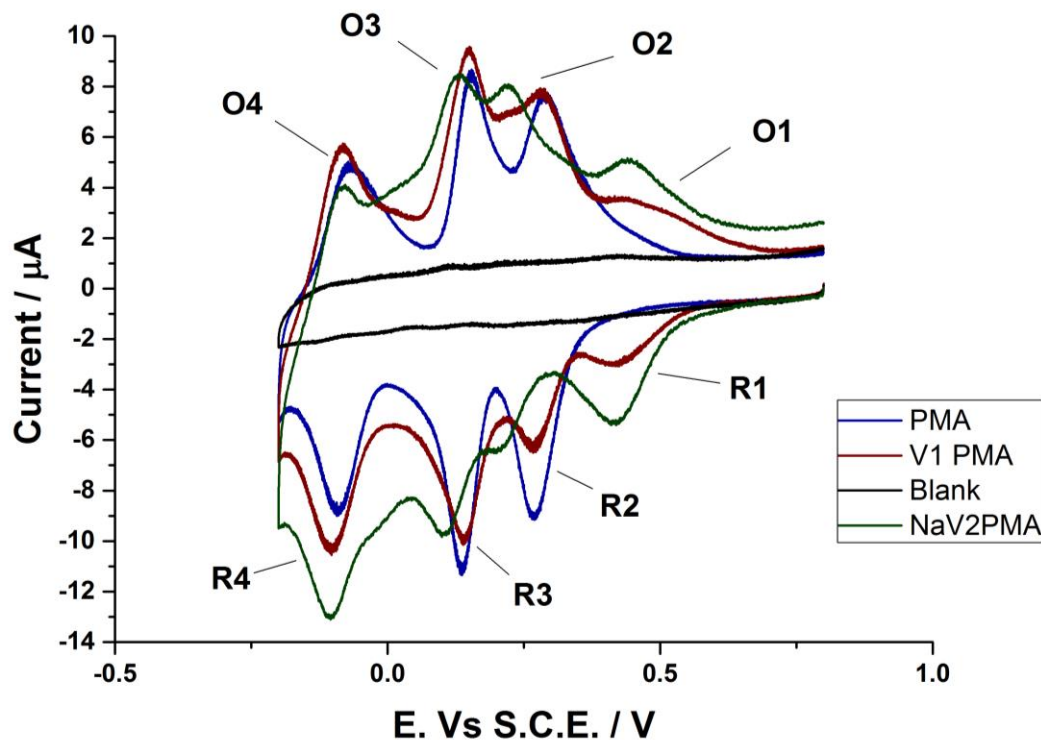
Figure 6.3 - cyclic voltammetry at 100mV.s^{-1} of phosphomolybdic acid derivatives

Figure 6.3 shows the transition of redox processes with the inclusion of vanadium within the phosphomolybdic heteropolyanion Keggin structure. The R1/O1 redox process doubles in magnitude between the singularly and doubly substituted species. It can also be seen that the R2/O2 peak seems to stay stable in terms of magnitude but that its equilibrium potential shifts negative. Additionally, the R3/O3 process reduces in comparative current magnitude as well as shifting slightly negative. This is suggestive that the redox processes have changed and now proceeds through a two electron process at R1/O1 followed by the two single electron transfers, R2/O2 and R3/O3 and then by a two electron transfer process R4/O4. It is clear that four processes exist,

contrary to a study suggesting three, two electron transfers took place at immobilised V2PMA species within a polypyrrole layer.[345]

Scan rate analysis of doubly substituted vanadophosphomolybdic acid adsorbed layers

This hypothesis was investigated using scan rate analysis and the charge transferred through each process. The initial scan data can be seen in Figure 6.4 and Figure 6.5.
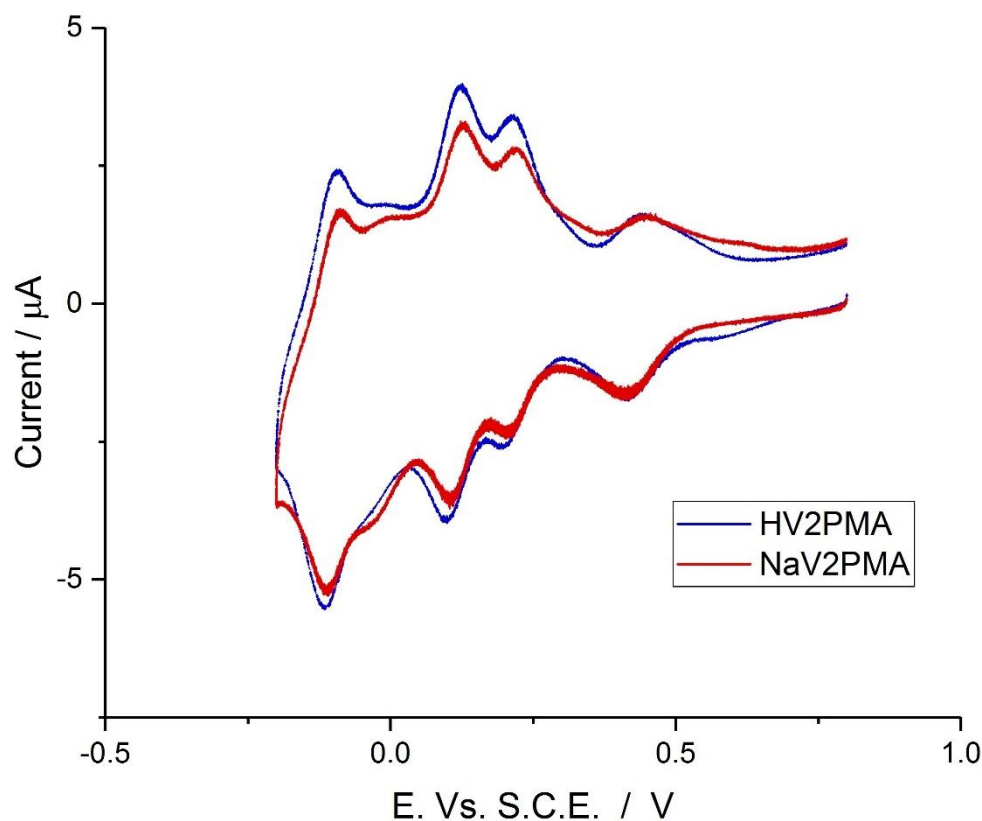
Figure 6.4 – Cyclic Voltammetry at 50 mV.s^{-1} of 3 mm EPPG electrodes modified by dipping in either 0.1 M HV2PMA or 0.1 M NaV2PMA solutions for 30 seconds taken in 0.1 M sulphuric acid

It can also be seen in Figure 6.4 and Figure 6.5 that as with previously seen examples in singularly substituted species the change between H$^+$ and Na$^+$ cations does not cause a significant difference in the observed cyclic voltammetry.
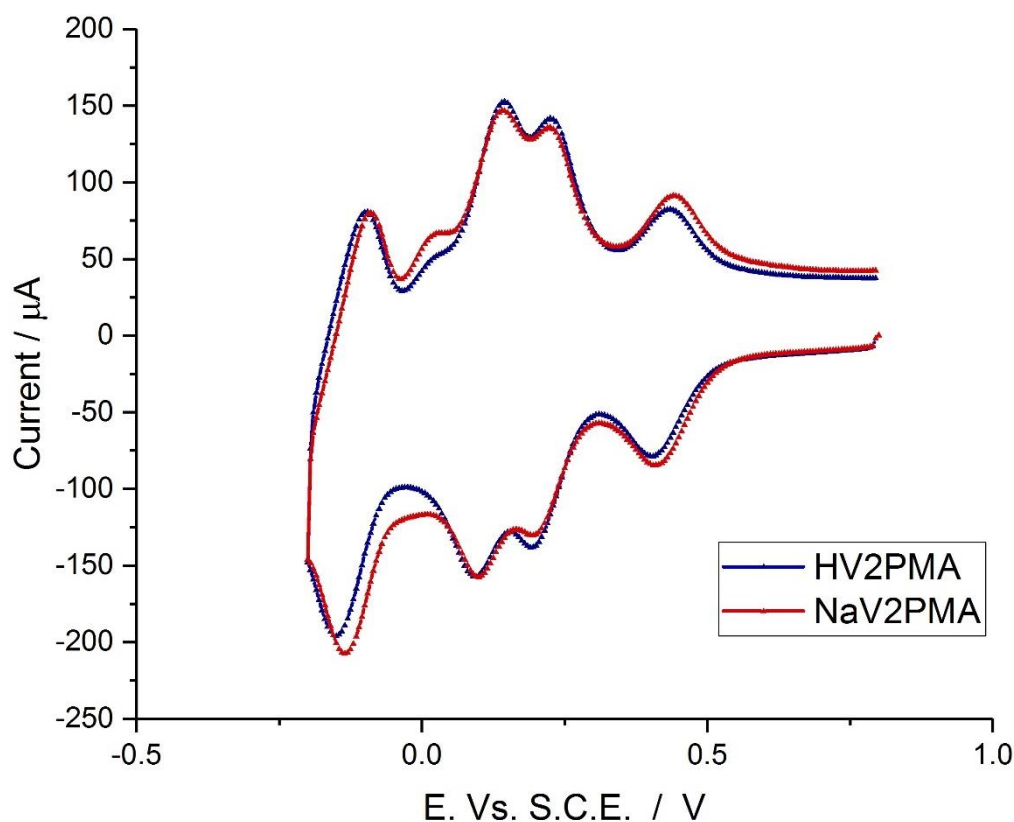
Figure 6.5 - Cyclic Voltammetry at 2500 mV.s-1 of 3 mm EPPG electrodes modified by dipping in either 0.1 M HV2PMA or 0.1 M NaV2PMA solutions for 30 seconds taken in 0.1 M sulphuric acid

This cyclic voltammetry data was used to plot log of peak current versus log of scan rate plots, as shown in Figure 6.6. The gradients from these plots showed that as with previous examples of phosphomolybdic acid derivative adsorbed layers the redox processes are adsorbed layer electrochemistry, similar to other V2PMA adsorbed layers.[341,346]

Process	R1	R2	R3	R4	O1	O2	O3	O4
Gradient	1.039	1.163	1.023	0.986	1.038	0.973	0.986	0.96

Table 6-1 – Gradient values taken from log peak current versus log scan rate, as figure 6.6, for cyclic voltammetry of 3 mm EPPG electrodes modified by dipping in 0.1 M HV2PMA for 30 s, taken in 0.1 M sulphuric acid across a range of scan rates.
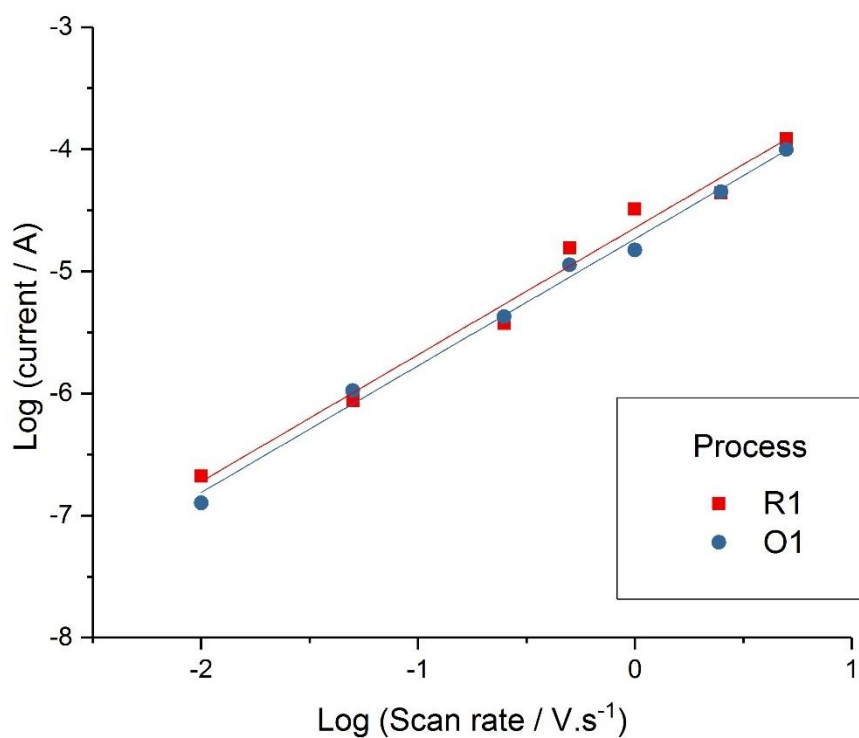
Figure 6.6 -Example plot of log peak current versus log of scan rate for the R1 and O1 redox process, labelled in figure 6.3, obtained from cyclic voltammetry at 3 mm EPPG modified by dipping in 0.1 M HV2PMA solution for 30 s taken in 0.1 M sulphuric acid at the defined scan rates.

In addition to information on whether the electrochemistry is dominated by diffusion or the adsorbed species the cyclic voltammetry data across the scan rates can be used to calculate the charge transferred at each process. Following the same procedure laid out in chapter four the average charge transferred through each process was calculated, Figure 6.7..
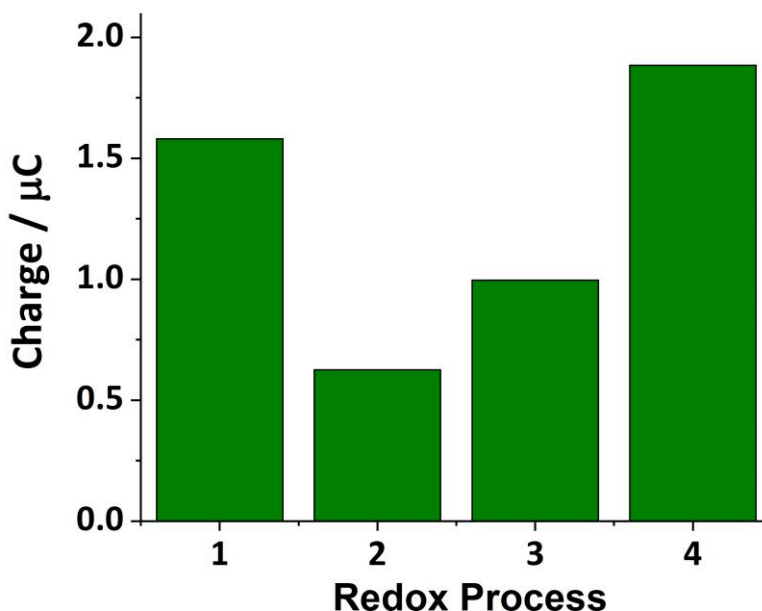
Figure 6.7 - Charge transferred for each redox process during cyclic voltammetry at a 3 MM EPPG electrode modified in 0.1 M NaV2PMA solution for 30 s, taken in 0.1 M sulphuric acid, averaged across scan rates.

As can be seen in the figure this data adds to the evidence suggesting that when moving from singularly to doubly substituted vanadophosphomolybdic acid derivatives the initial process R1/O2 has become a two electron process, whilst R3/O3 has become a one electron process. However overall the charge values are much smaller than previously seen.

Effect of pH on the electrochemistry of doubly substituted vanado-phosphomolybdic acid

As with previous investigations into adsorbed layers, pH variance was used to understand the effect on the electron transfer processes. The same experiments across scan rates were conducted across the graphitic electrode types at varying pHs leading to the data in Figure 6.8.

The behaviour of the redox processes for the adsorbed layer of V2PM|A is very similarly to that of the previously examined adsorbed layers. It shifts towards more negative potential with decreased pH and reduces in magnitude to become unrecognizable at high pHs. This is supported by the data collected on the equilibrium potentials of each process, shown in Figure 6.8.
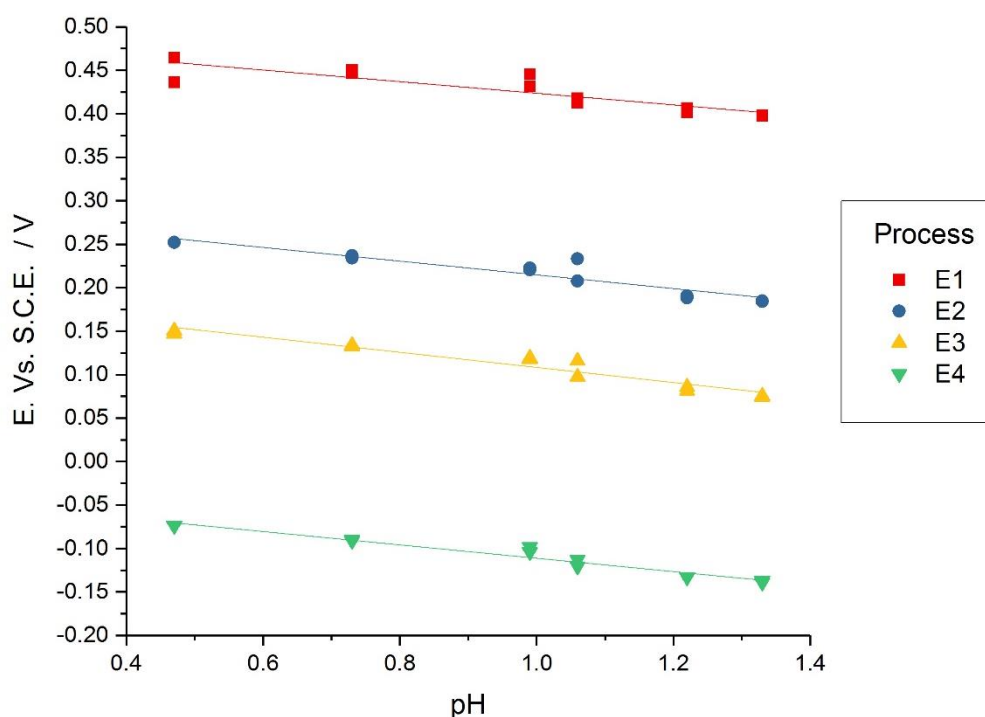
Figure 6.8 – Observed $E_{1/2}$ versus pH, during cyclic voltammetry at 3 mm EPPG electrodes modified by dipping in 0.1 M NaV2PMA for 30 seconds, taken at 100 mV.s^{-1} in different concentrations of sulphuric acid adjusted with NaOH to achieve desired pH.

The slope values of, 67, 79, 87 and 77 mV.dec^{-1} for the 1st, 2nd 3rd and 4th redox processes suggest that, just like the processes for PMA and V1PMA adsorbed layers and a limited previous study,[346] they proceed with a 1 electron: 1 proton ratio. However, these values are much larger than one might expect and are certainly larger than the 59 mV.dec^{-1} normally indicative of a 1:1 ratio.

Conclusions on the surface adsorbed electrochemistry of doubly substituted vanado-phosphomolybdic acid

The gathered data shows how the adsorbed layer electrochemistry has changed from singularly to doubly substituted vanado-phosphomolybdic acid, and indicates that the doubly substituted derivative adsorbs in the same manner as both PMA and the singular substituted species. It has also been shown that changing the counter ion from H^+ to Na^+ has no effect on the surface electrochemistry. Additionally, the V2PMA species shows the same change in behavioural characteristics across the graphitic electrode surfaces as V1PMA.

Through scan rate analysis and charge association it can be seen that the number of electrons associated with each electron transfer process has changed. Combining this with pH variance experiments allows the equations below to put forward as responsible for each redox process.

Equation 6.1
$$Na_2H_3(PV_2^V Mo_{10}^{VI}O_{40}) + 2e^- + 2H^+ \rightarrow Na_2H_5(PV_2^{IV} Mo_{10}^{VI}O_{40})$$

Equation 6.2
$$Na_2H_5(PV_2^{IV} Mo_{10}^{VI}O_{40}) + e^- + H^+ \rightarrow Na_2H_6(PV_2^{IV} Mo^V Mo_9^{VI}O_{40})$$

Equation 6.3
$$Na_2H_6(PV_2^{IV} Mo^V Mo_9^{VI}O_{40}) + e^- + H^+ \rightarrow Na_2H_7(PV_2^{IV} Mo_2^V Mo_8^{VI}O_{40})$$

Equation 6.4
$$Na_2H_7(PV_2^{IV} Mo_2^V Mo_8^{VI}O_{40}) + 2e^- + 2H^+ \rightarrow Na_2H_9(PV_2^{IV} Mo_4^V Mo_6^{VI}O_{40})$$
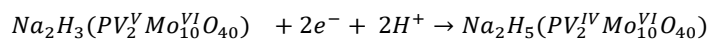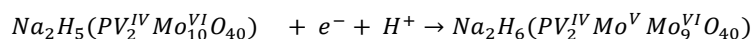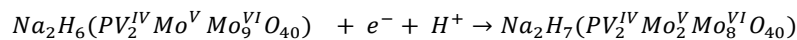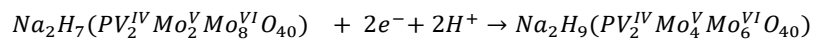
6.3.4 Solution based electrochemistry of doubly-substituted vanado-phosphomolybdic acid.

The electrochemical response for the solution phase of the V2PMA species is further complicated by the shift caused by the additional substitution of vanadium into the heteropolyanion. This can be seen in the cyclic voltammetry of 1mM and 5mM solution when compared to the V1PMA and PMA species which can be seen in Figure 6.9.
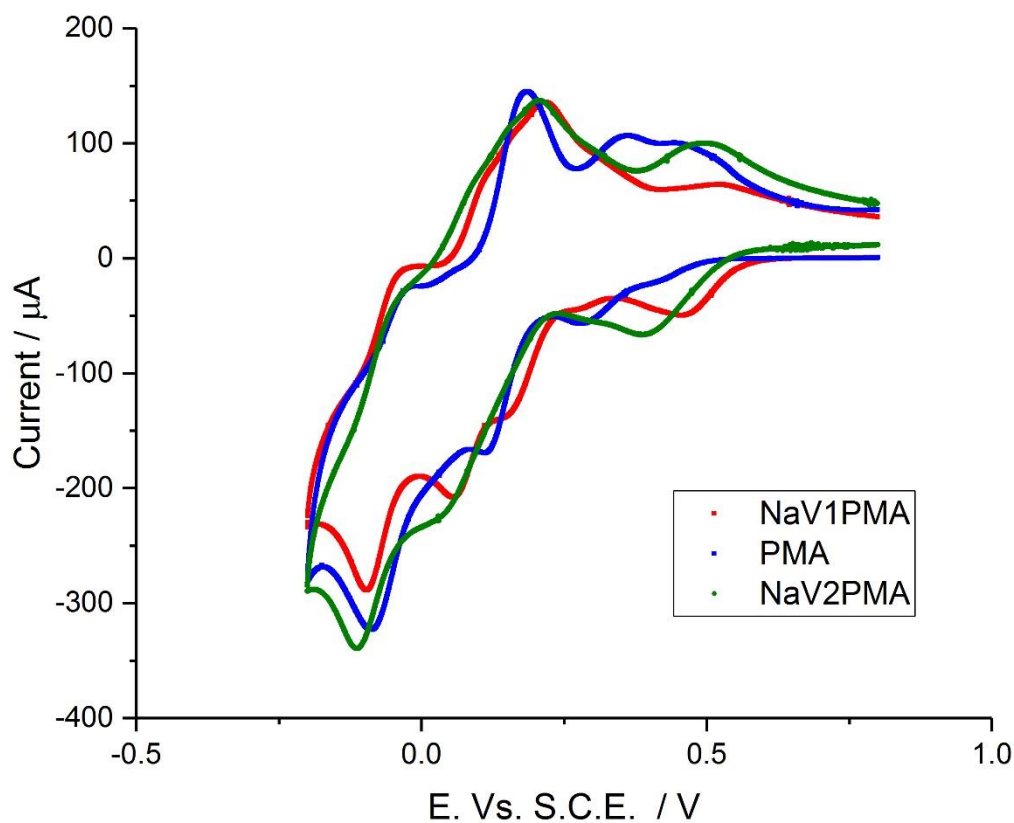
Figure 6.9 - cyclic voltammetry at 100mV.s^{-1} of solutions of 5 mM NaV2PM, 5 mM NaV1PMA and 5 mM PMA in 0.1 M sulphuric acid at 3 mm EPPG electrodes.

From these cyclic voltammetry responses, very little quantitative information can be obtained further than the qualitative view of the increasing and shifting redox processes being similar to the adsorbed layer. It can be seen that the initial redox process, R1/O1, enlarges, as with the adsorbed layer. The second redox process shifts negative and the third, R3/O3, reduces in magnitude. This is indicative of the same shift in redox processes seen in the adsorbed layer, although it is difficult to draw any definitive conclusions.

Effect of scan rate on doubly substituted vanadophosphomolybdic acid derivative solution phase electrochemistry

Previous experimental work into the solution phases of the phosphomolybdic acid showed that by altering the concentration and scan rate, some separation of the peaks could be identified. Variable scan rate experiments of a 5 mM NaV2PMA solutions is shown in Figure 6.10. The figures show both the effect that it is much harder to elucidate quantitative information for the V2PMA samples than for the previous V1PMA or PMA
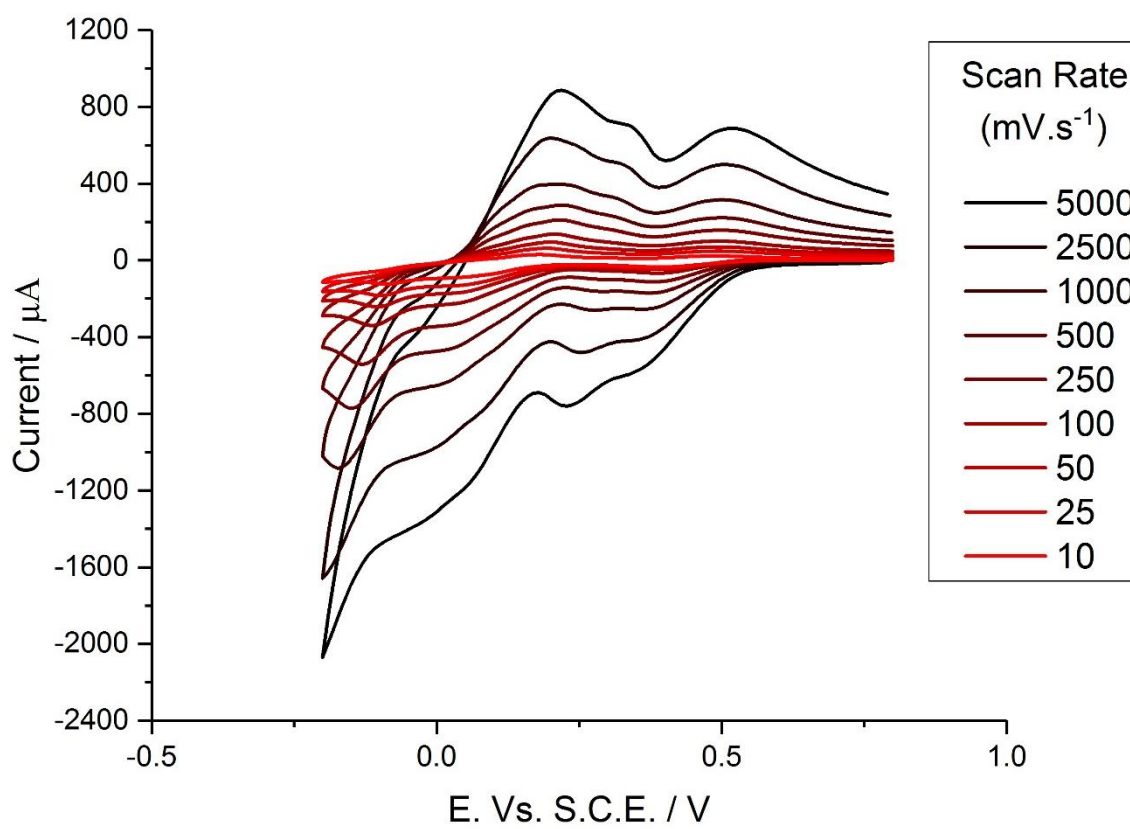
Figure 6.10 – Variable scan rate cyclic voltammetry of 5 mM NaV2PMA in 0.1 M sulphuric acid at 3 mm EPPG electrodes

However, to gain any additional information the scan rate data, must be viewed alongside the cyclic voltammetry obtained across the concentrations of HV2PMA and NaV2PMA. This is evident when comparing Figure 6.10 with Figure 6.11 and Figure 6.12.
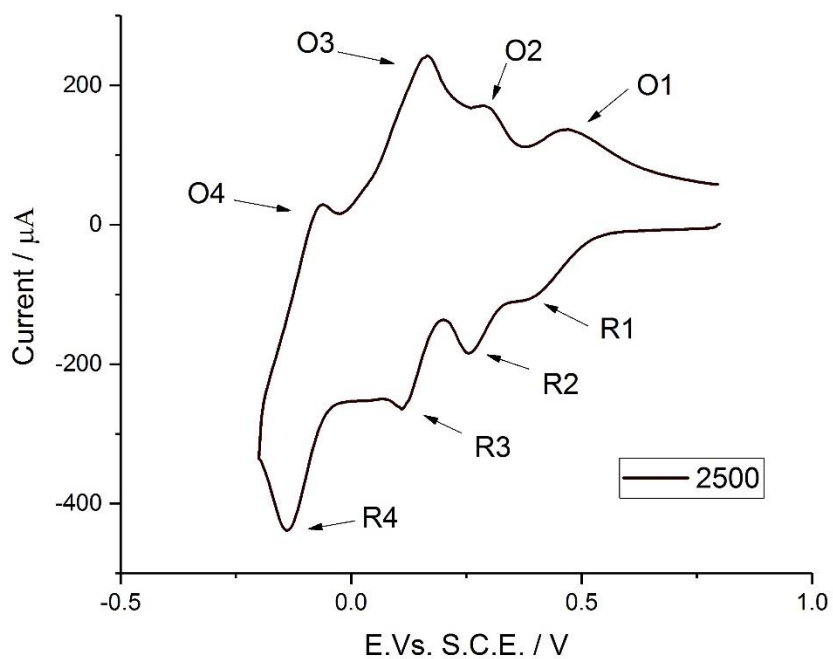
Figure 6.11 – Cyclic voltammetry at 2500 mV.s⁻¹ at a 3mm EPPG electrode in 1 mM NaV2PMA in 0.1 M sulphuric acid.

Figure 6.11 shows that at low concentrations and at high scan rates the redox processes R1-4/O1-4 are more evident that at higher concentrations and high scan rates.
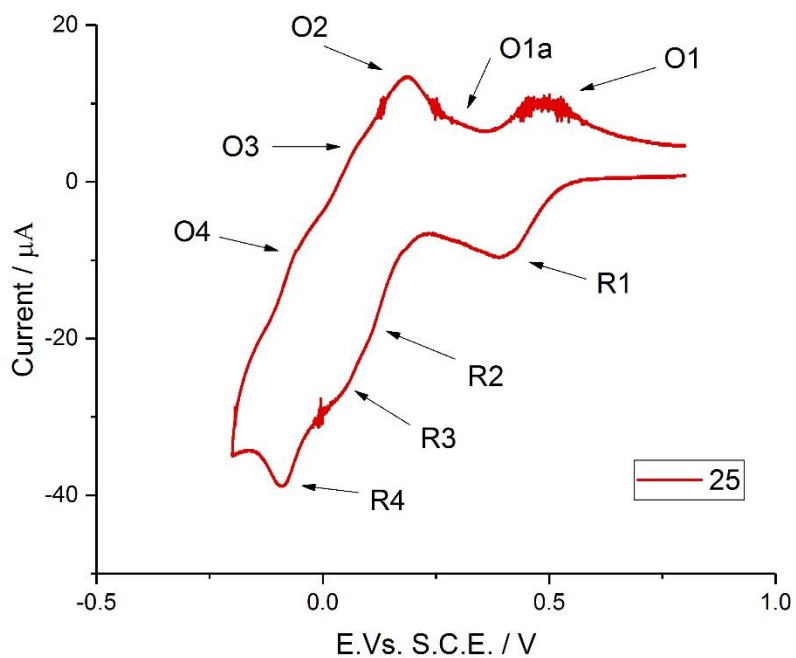
Figure 6.12 - cyclic voltammetry at 25 mV.s⁻¹ of 1 mM NaV2PMA in 0.1 M sulphuric acid at a 3 mm EPPG electrode

Figure 6.12 shows that at reduced concentrations and slow scan rates the cyclic voltammetry is less discernible again. Additionally, an extra feature, labelled O1a, hinting at an interaction with the adsorbed layer is evident. Plotting the square root of the scan rate versus peak current, Figure 6.13, can sometimes be used to calculate diffusion coefficients for solution based systems, as in chapter 5.
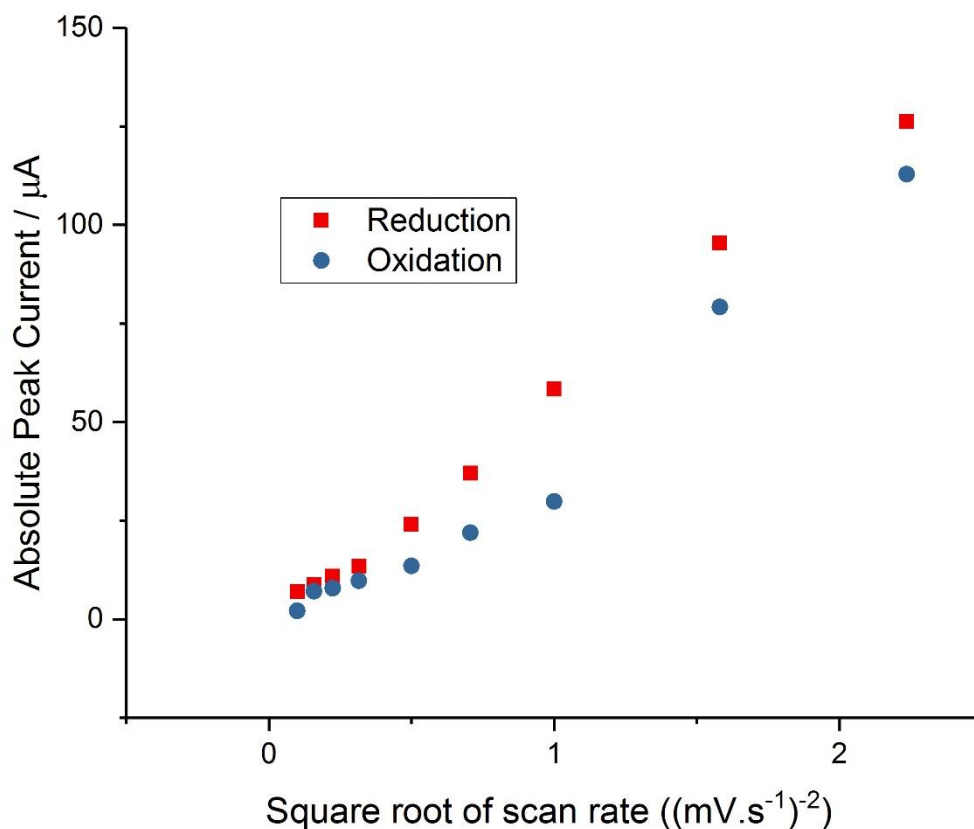
Figure 6.13 – Absolute peak current of the R1/O1 process, previously labelled, versus the square root of scan rate, values taken from cyclic voltammetry of 1 mM NaV2PMA in 0.1 M sulphuric acid at 3 mm EPPG electrodes.

However, as can be seen from Figure 6.13, the relationship is not linear with a significant kink between scan rate of 100 mV.s^{-1} and 250 mV.s^{-1}. Using a Log (peak current) versus log (scan rate) plot the gradient can be used to indicate if the electrochemistry is diffusion controlled, with a value of 0.5, or associated with the adsorbed layer, with a value of 1. In this case the gradient

for scan rates below 100 mV.s^{-1} is 0.46 and above 250 mV.s^{-1} is 0.65. This may indicate that below 100 mV.s^{-1} the system is behaving more as a traditional solution based system, possibly mediated through the adsorbed layer. However, above 250 mV.s^{-1} the contribution from the adsorbed layer is greater. This change in behaviour with concentration has previously been seen with HPAs in acetonitrile.[336]

Effect of concentration on doubly substituted phosphomolybdic acid derivatives solution phase electrochemistry
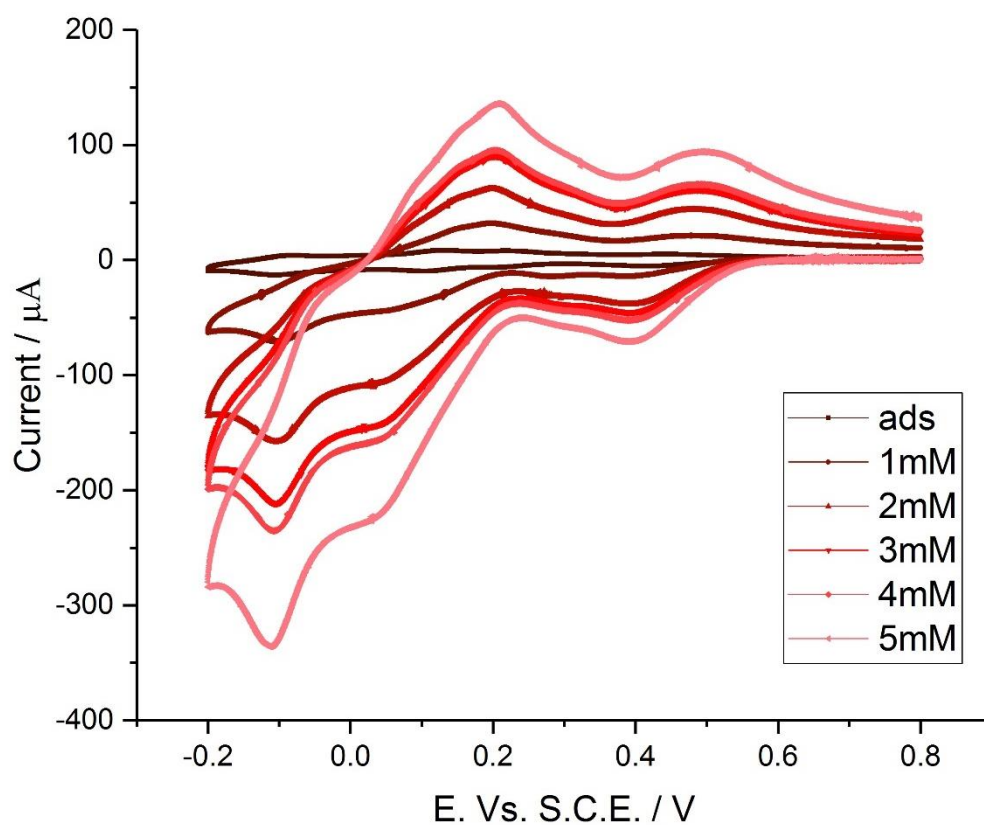
Figure 6.14 – Cyclic voltammetry at 100 mV.s^{-1} of solutions of NaV2PMA in 0.1 M sulphuric acid at 3 mm EPPG electrodes, as well as an additional plot of a 3 mm EPPG electrode modified by dipping 0.1 M NaV2PMA solution for 30 s in a blank 0.1M sulphuric acid solution.

Figure 6.14 shows that although the redox processes are hard to distinguish, the general trend is similar to previous PMA derivatives. The only redox process which can be reliably isolated is that of the R1/O1 process labelled in previous figures. When this is plotted against absolute peak current for this process a linear relationship exists as shown in Figure 6.15.
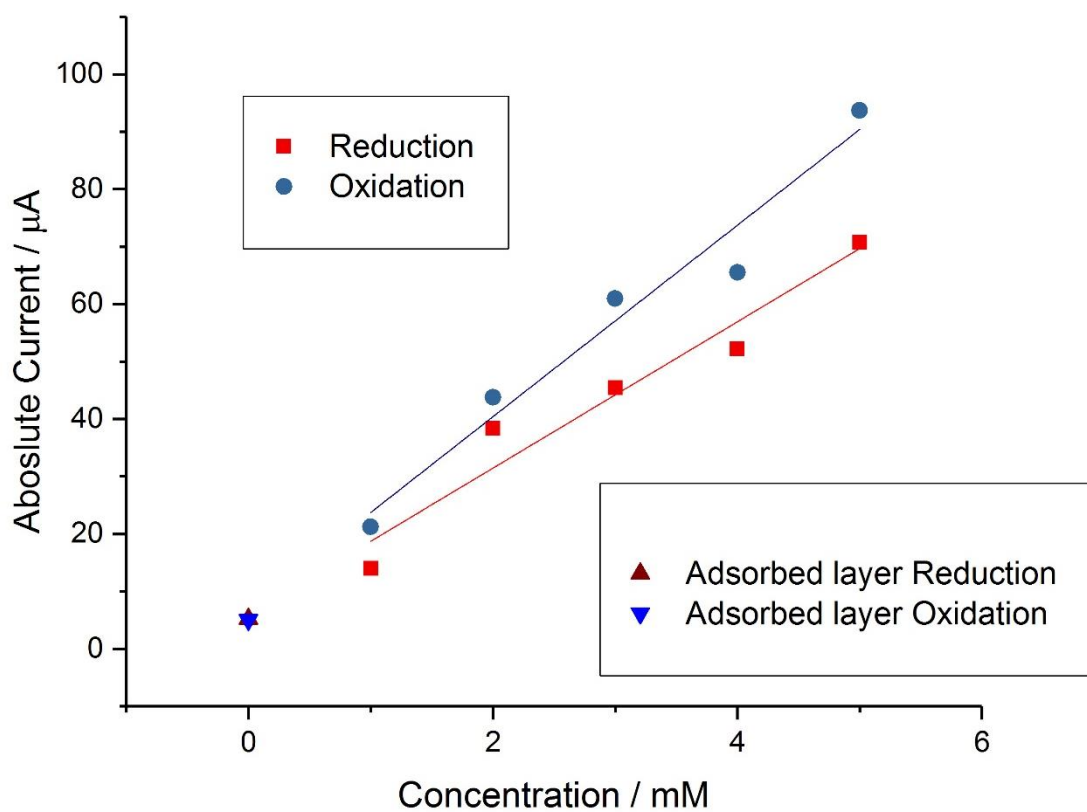
Figure 6.15 – Absolute current of the peaks R1 and O1, as previously labelled, versus concentration, taken from cyclic voltammetry at 100 mV.s^{-1} of different concentrations of NaV2PMA in 0.1 M sulphuric acid at 3 mm EPPG electrodes, additionally including results taken from a 3 mm EPPG electrode modified by dipping in 0.1 NaV2PMA for 30 s in 0.1 M sulphuric acid.

By analysing different concentrations at different scan rates, it can be seen that at low concentration and low scan rates the adsorbed layer behaviour is dominant but at high concentrations and high scan rates the bulk solution electrochemistry is dominant. Similar to the singularly substituted species. This can be seen in Figure 6.16.
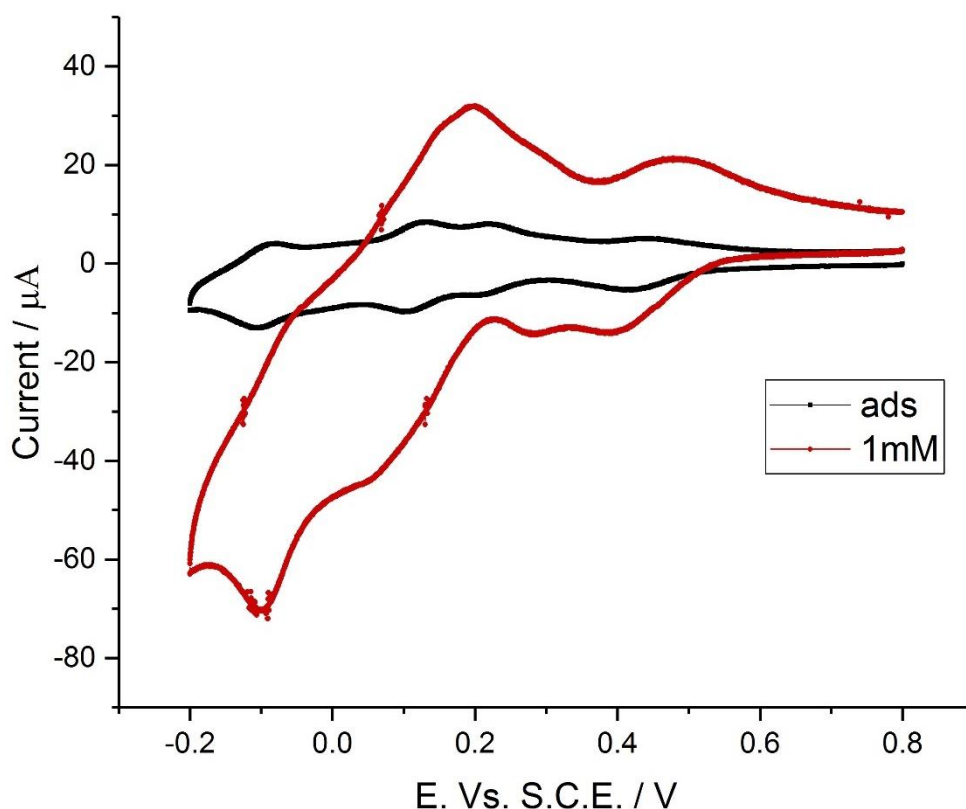
Figure 6.16 - Effect of concentration at low and high scan rates for NaV2PMA cyclic voltammetry on EPPG electrodes showing the splitting in the R1/O1 peak at fast scan rates

In addition, the mediation effect of the adsorbed layer that was clearly seen in the singularly substituted derivative is observable in the doubly substituted species. The appearance of a semi-catalytic reduction at R1 at low scan rates and a non-catalytic and separated double peak at R1 at fast scan rates is seen.

Effect of pH on the solution phase electrochemistry of doubly substituted vanado-phosphomolybdic acid derivatives

The electrochemistry of the solution phase doubly substituted vanado-phosphomolybdic acid has been difficult to quantitatively analyse. Altering pH has been a useful way of analysing the electrochemistry of the previously seen derivatives in the adsorbed and solution phase.

238

Altering the pH of the solution had a dramatic effect on the electrochemistry observed for the solution phase of the doubly substituted species and allowed a much greater insight into the splitting of the first reduction process. At higher pH values this split in the peak was not observed, the process occurring at the highest potential was only activated at lower pH values. Additionally, the process occurring at the highest potential did not seem to shift with pH whilst the lower process of the split process did shift with pH. This can be seen in Figure 6.17.
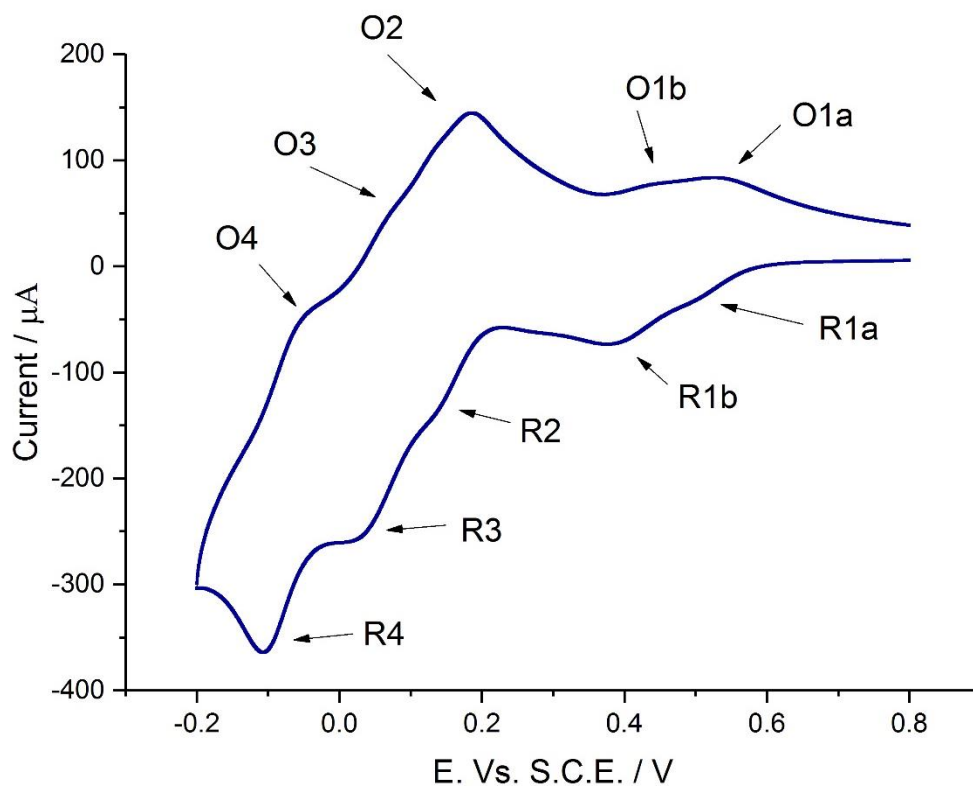
Figure 6.17 – cyclic voltammetry of 1 mM NaV2PMA in 0.5 M sulphuric acid solution adjusted to a pH of 1.23 with NaOH, taken at 100 mV.s^{-1} at a 3 mm EPPG electrode

This R1$_a$/O1$_a$ process is very similar to the R1 process highlighted for the solution phase of the V1PMA derivatives with the R1$_b$/O1$_b$ process behaving like the rest of the observable processes in

its shift with pH. This indicates that the initial two electron reduction process observed in the adsorbed layer is replaced by two separate one electron processes when considering the solution phase. Additionally, when considering the different scan rates and concentrations, the mechanistic route to this overall two electron transfer changes from being an adsorbed layer mediated process to a solution phase process across these variables.
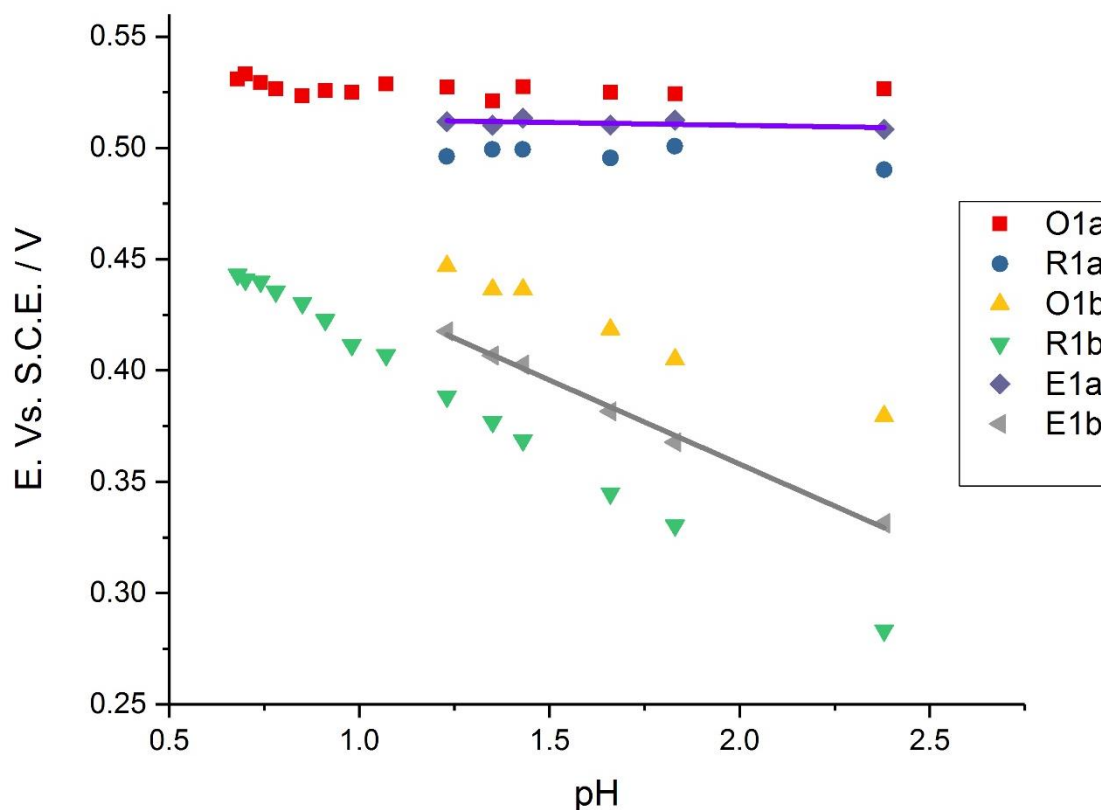
Figure 6.18 - Observed peak current potential plotted against pH, taken from cyclic voltammetry at 3 mm EPPG electrodes in 1 mM NaV2PMA in 0.5 M sulphuric acid, adjusted to pH with NaOH, taken at 25 mV.s^{-1}

When plotting the equilibrium position versus pH to obtain the ratio of protons to electrons within the mechanism it can be seen that the two processes proceed through differing mechanisms, as shown in Figure 6.18.
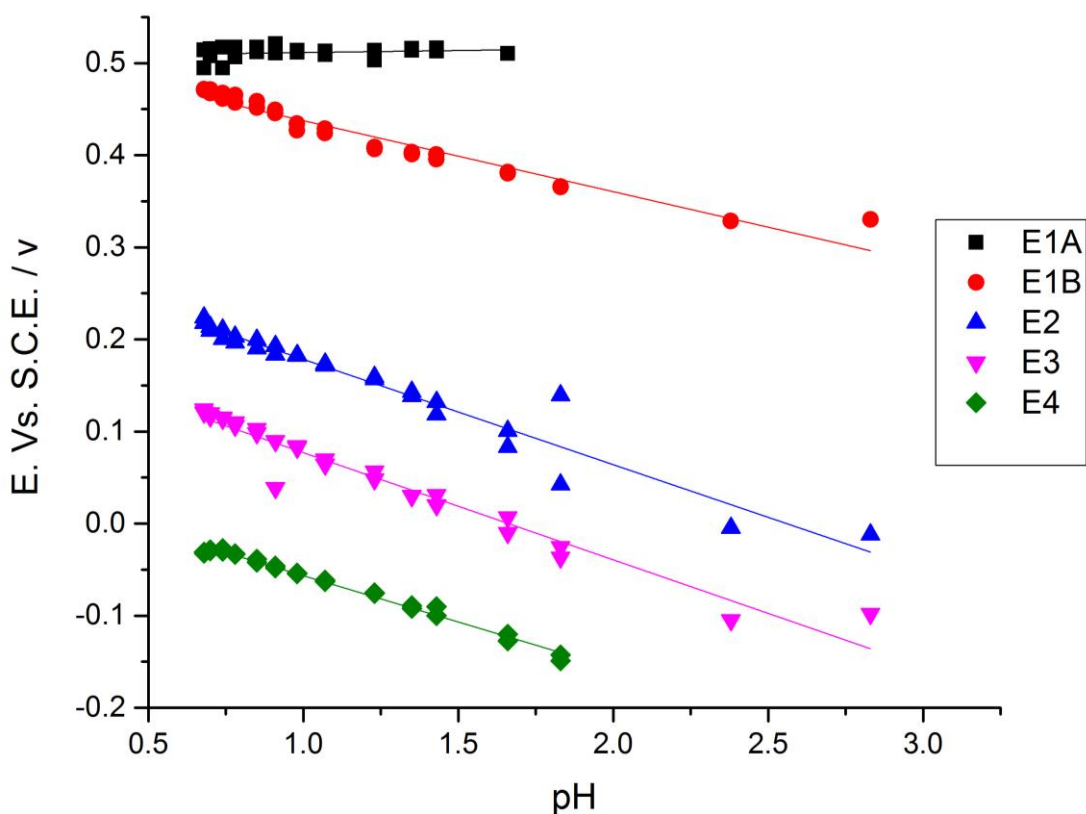
Figure 6.19 - Equilibrium position versus pH for V2PMA 5nM solution phase electrochemistry

The slope values obtained from Figure 6.19, of 4, 86, 125, 129 and 100 mV.dec^{-1} for the processes E1$_a$, E1$_b$, E2, E3 and E4 respectively show that this first process is not dependent on pH, where-as, all other processes are and that these mechanisms do not proceed with a simple 1:1 proton to electron ratio with processes E2-4 approaching and exceeding 2:1 at 100 mV.s^{-1}.

Scan Rate	E1a	E1b	E2	E3	E4
100	0.08	1.45	2.12	2.18	1.70
25	0.03	1.28	1.86	2.22	1.78

Table 6-2 – tabulated values of Proton to Electron ratio for the different redox processes as previously labelled. Calculated from Cyclic voltammetry of 1 mM NaV2PMA in 0.5 M sulphuric acid adjusted to pH with NaOH, taken at 100 and 25 mV.s^{-1}

Conclusion on the solution phase electrochemistry of doubly substituted vanadophosphomolybdic acid.

It has been seen that the solution phase electrochemistry of doubly substituted vanadophosphomolybdic acid is difficult to interpret. Through scan rate and concentration variation it can be seen that as with the singularly substituted species adsorbed layer domination and mediation is observed at low concentrations and slow scan rates and this is reversed when at high concentration and high scan rates.

It is apparent that when transitioning from singularly to doubly substituted species, the same increase in the initial redox process is observed in the solution phase as with the adsorbed layer phase. However, it is observed that at low pHs this initial process is in fact two processes and not a single two electron transfer and that these two individual processes behave differently when altering pH, indicating a difference in mechanism.

The other observable process all exhibited a slope of close to 100mV.dec^{-1} when plotting equilibrium position versus pH. This indicated that they proceed with a 1:1 proton to electron ratio.

7. Extra experimental work into the development of cathodic flow fuel cells.

7.1 The use of image analysis in analysing fuel cell electrodes

Previously, the surface area of an electrode has been used to 'normalize' a current response to allow comparisons and to analyse catalytic and kinetic parameters. However, when designing a device to generate power, and therefore, inherently increase the total current density of a device, the surface area of an electrode per volume unit is a key design concern.

There are many ways to produce a larger surface area within a given electrode type, often with an associated 'trade off' cost. In the example of liquid catholyte cells this 'trade off' cost is often an increase in the pressure drop across the electrode through greater turbulence, or physical path length. This in turn leads to an increase in parasitic loss in the extra energy needed to produce fluid pressure across the cell. Typically, in large surface area electrodes such as foams, felts or expanded structures the flow channels are small in relation to the fluid velocity leading to a mainly laminar flow. Laminar flow across an electrode surface leads to an increase in the electrochemical double layer size down the length of the electrode, and as such a lower overall current density compared to the electrochemical surface area.

Methods to increase the surface roughness and induce turbulence could increase the total volumetric current density of a device. Many methods have been tested, such as dip coating in

carbon, to add additional material to the surface of these electrodes. The physical surface area increase obtained by using such techniques can be measured through several methods, such as BET adsorption or electrochemical surface area measurements.

This section of the thesis deals with the assessment of some of these techniques through image analysis. SEM images were taken and compiled to form cross sections of the whole electrode structure, allowing for a complete depth analysis of the deposition.

A sample of untreated RVC (reticulated vitreous carbon), a sample of high density heat treated RVC, a sample of high density dip-coated RVC and a sputter coated sample of RVC were investigated. The principle reasons for investigation were both to see the effects of each treatment technique and to assess the use of imaging techniques to produce usable design data. The exact electrodes used and the exact production parameters of each sample were of proprietary commercial value. The experiments were designed for physical characterization and development of the analysis technique; it was considered that the ultimate methodologies in production should not be revealed to the author as this would not inhibit the relevant goals of the experiment.

7.1.1 Introduction

ACAL Energy Ltd has been developing liquid catholyte technology through their Flowcath system. Recently they have installed commercial units[347,348] for in-situ testing[349] and announced plans to develop units for the automotive market.[350] As has been previously discussed the technology allows for a reduction of up to 90% in the platinum content within the PEMFC unit.[351] However, the liquid catholyte system is still in need of development.

The liquid system relies on a mediatory catalyst, in solution, which is reduced at a solid cathode electrode and oxidised within a separate 'lung', Figure 7.1.
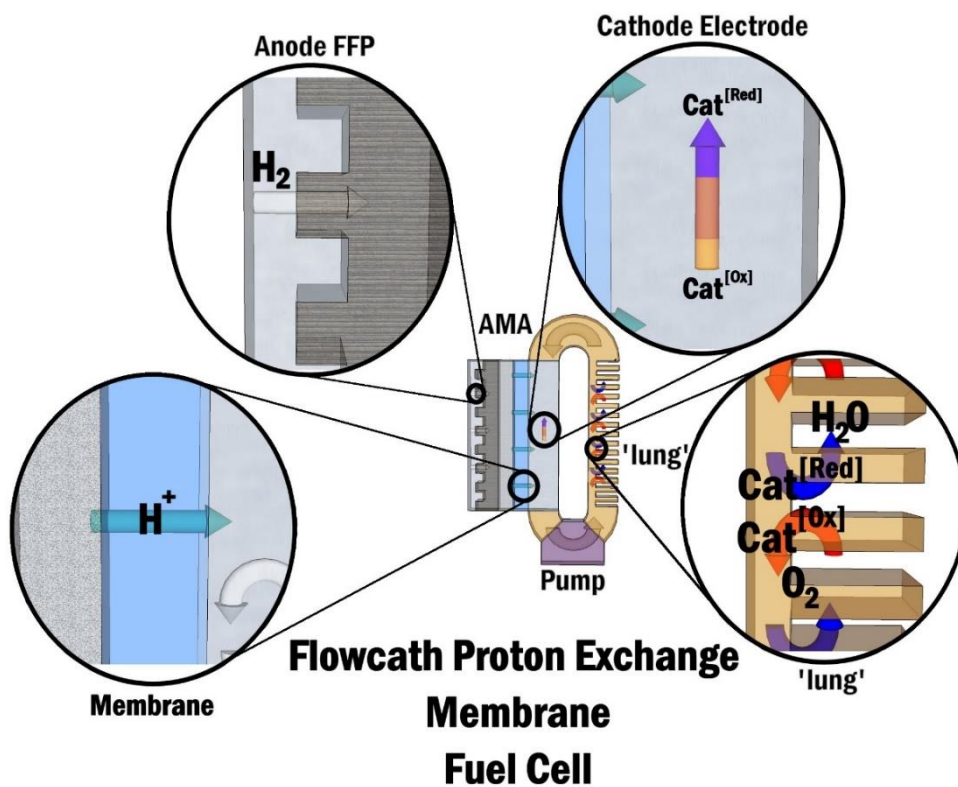
Figure 7.1 - Flowcath Proton Exchange Membrane Fuel Cell.

The anodic side of the cell operates in the same way as a regular PEMFC. However, the cathode is designed differently to allow a flow of catalyst solution over the solid cathode section. Therefore, the cathode electrode must be designed and constructed from material allowing the greatest transport of electrons from the solid cathode to catalyst in solution.

Reticulated vitreous Carbon

RVC is a promising electrode material and has been used since its discovery in the 1950's.[352] The manufacture of RVC is achieved by the polymerisation of a resin combined with a foaming agent preceding a carbonisation step.[352,353] The process produces a material highly resistant to chemical attack (especially to acids and bases), highly porous and possessing little electrical resistance.[352]

It is an ideal substance for use as the solid electrode component in a liquid catholyte system as the pressure drop across the structure is relatively small and has led to its use in, diesel engine exhaust cleanup,[354] removal of metal ions from solutions[355] and noise reduction within liquid systems.[356] The structure exhibited is of interlocking tetrahedral structures, with the 'strut' dimensions affecting the pore size and as such the density of the material. The typical characterisation of an RVC sample is either, strut length or pores per inch (ppi).[352]

In addition, the temperature at which the material is 'carbonised' or heat treated after carbonisation can have considerable effect on the properties of the material. For example, heat treatment above 315 ^{0}C in air can lead to significant oxidation and enhanced adsorption properties.[352]

The carbon structure within the RVC is still under debate. It was initially thought to contain a mixture of sp^2 and sp^3 bonds this was followed by a general consensus that 'glassy carbon' possesses a complete sp^2 bonding structure,[353] however, some now conclude that glassy carbon exhibits a fullerene type structure.[357]

The reason for its use within the liquid catholyte system is the high surface area (65 cm^2.cm^{-3} for a 100ppi RVC sample),[352] low resistivity and low pressure drop across the structure. In this investigation, different treatment techniques have been assessed through SEM to try to determine the effect that the different treatments have had on the structure and any potential changes caused to the surface.

The use of image analysis techniques and image data representation is explored to be able to quantify the images, and therefore making the technique more quantitative then the qualitative nature of SEM imagery.

7.1.2 Experimental

Materials

The samples of treated RVC were supplied by ACAL Energy Ltd. Four separate sample types were given:

Sample 1 was a dense RVC sample which had been put through a heat-treatment process.

Sample 2 was a dense RVC sample that had an additional coating of carbon added through a dip coating technique.

Sample 3 was a normal density RVC sample that has had additional carbon added through a sputter deposition process.

Sample 4 was a normal density control sample of RVC.

Techniques

Several sample preparation techniques were trialled. The sample was taken, a fresh cross section cut with a razor blade, it was then mounted with carbon tape onto a standard SEM Stub, ensuring that the cross section was perpendicular to the beam direction. The samples were imaged using a Jeol JSM-7000f FE-SEM with Oxford Inca EDS, wave WDS and crystal EBSD and a XL-30 FEG ESEM (Cambridge Instruments, Cambridge, UK).

Afterwards the images were assessed and grafted together using Jasc Paint Shop Pro 7, or GIMP software. Areas which were identified as modified were highlighted and differential colour analysis allowed for a percentage covering of modification. This then could then be plotted versus a distance from the leading edge.

7.1.3. Results and discussion

Heat treated RVC samples

Heat treatments of RVC have been shown to greatly reduce the resistivity of RVC, decreasing rapidly up to 700^0C, before decreasing more gradually until reaching a constant value at 1500^0C for samples derived from phenolic resin). This relates to the removal of heteroatoms on the surface, specifically removal of water (up to 400^0C), removal of CO_2 (up to 700^0C), removal of CO (up to 1200^0C), H_2 and CH_4 (above 950^0C) and nitrogenated and sulfonated forms (above 1800^0C).[8]
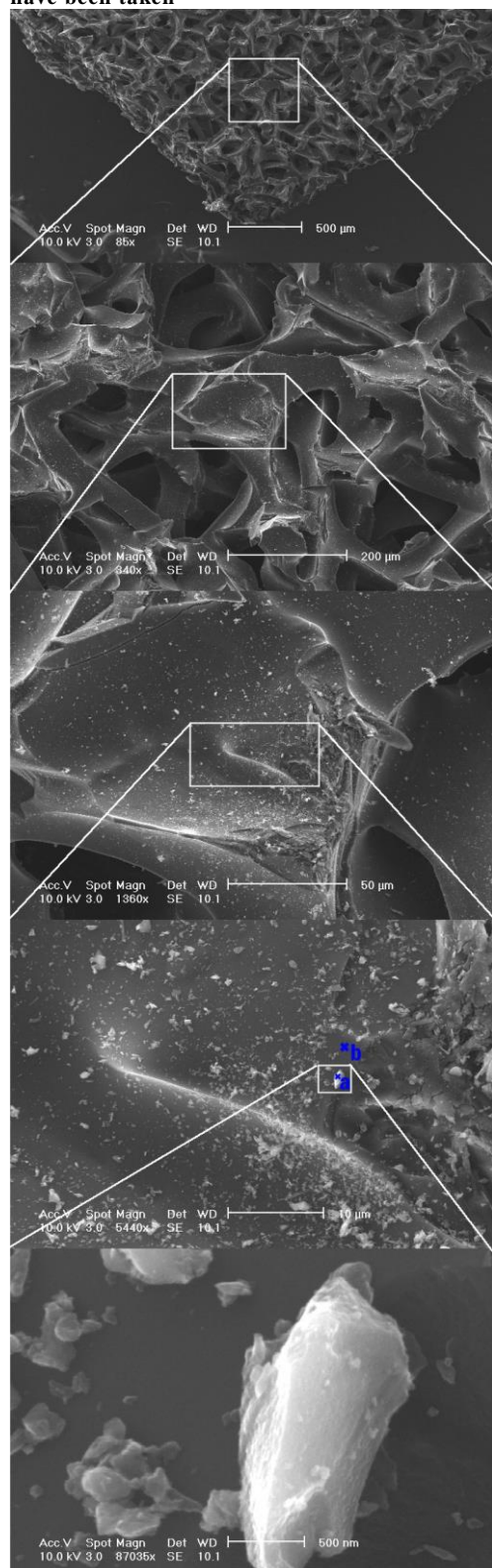
These effects are presumed to be related to electron delocalization across the surface as the bonding structure tends towards sp^2 hybridization.

However, as previously stated heat treatments above 350^0C in a non-controlled atmosphere can lead to oxidisation of the surface.[352] Additionally, one might expect to see the results of mechanical stresses on the structure, although RVC has a high tolerance to heat, some cracking might be expected.
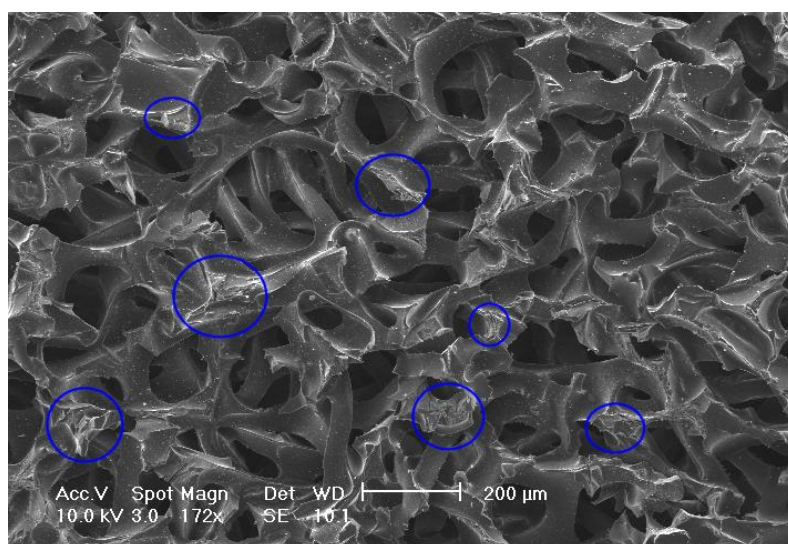
Figure 7.3 SEM Image showing cracking of RVC 'tips' in the RVC structure

The purpose of the investigation was to see the effect of the treatment procedures and detect any cracking or

249

deformation that had occurred. Figure 7.2 shows the path taken to the inspected area with the blue x's highlighting areas inspected by the adjacent EDX spectra (Figure 7.5). Figure 7.3 shows one area of interest with the blue circles indicating area of damage and cracking to the RVC structure.

Figure 7.4 shows a higher resolution area of interest with arrows labelled a, showing areas of what looks like compressive or damaged tips and circles labelled b showing possible cracks in the structure.
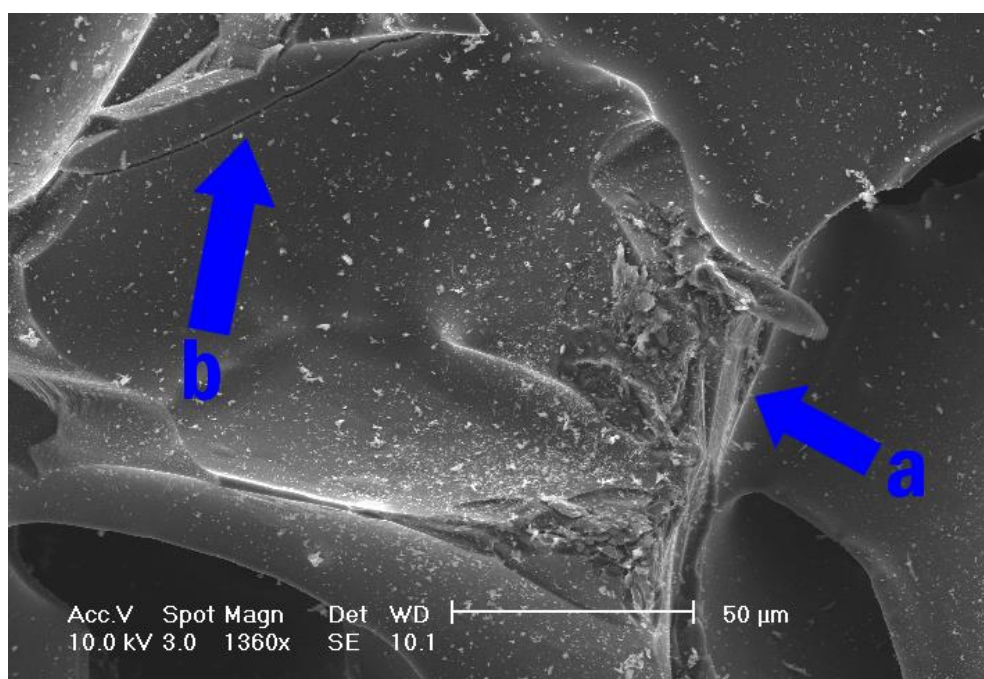
Figure 7.4 - High resolution image of heat treated RVC sample, highlighting a cracked area and broken 'tip of the RVC structure

The spectra, shown in Figure 7.5, indicate that no contaminants are present. Oxygen has been detected within the spectrum but at a very small level. Interestingly the spectra of the small particles present are the same as the base material. It has previously been reported that RVC sample contain up to 0.1%-0.5%[358] ash presence remaining from the carbonisation process. It is possible that these

particles on the surface are these remaining ash particles or debris left from the damage to the RVC tips.
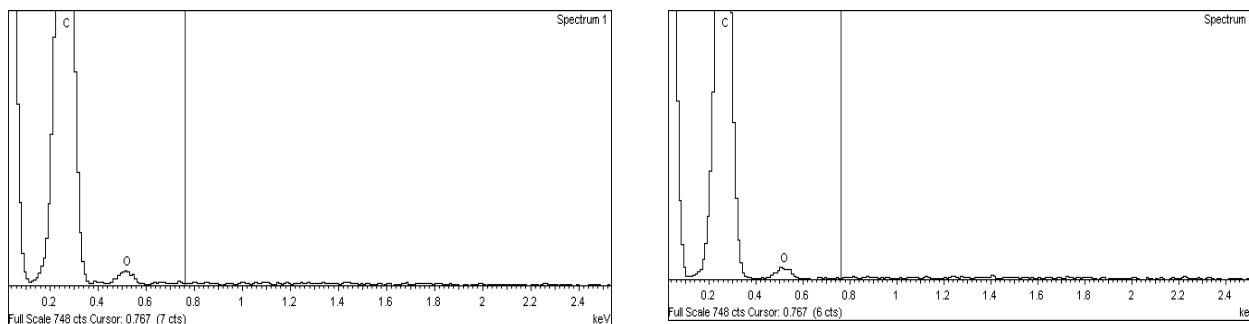
Figure 7.5 EDX Spectra of heat treated RVC sample, the Left Spectra represents area a, with the right spectra representing area b from Figure 7.2.

Dip Coated RVC sample

Dip coating can be a precise method for producing a layer on a material. It has been used to form layers in electrode preparation,[359] carbon nano-tube formation[360] and many more applications. However, despite the process being simple to perform, it is complex to correctly adjust each variable to achieve a particular layer. The solvent used, method of ink preparation, speed, shear
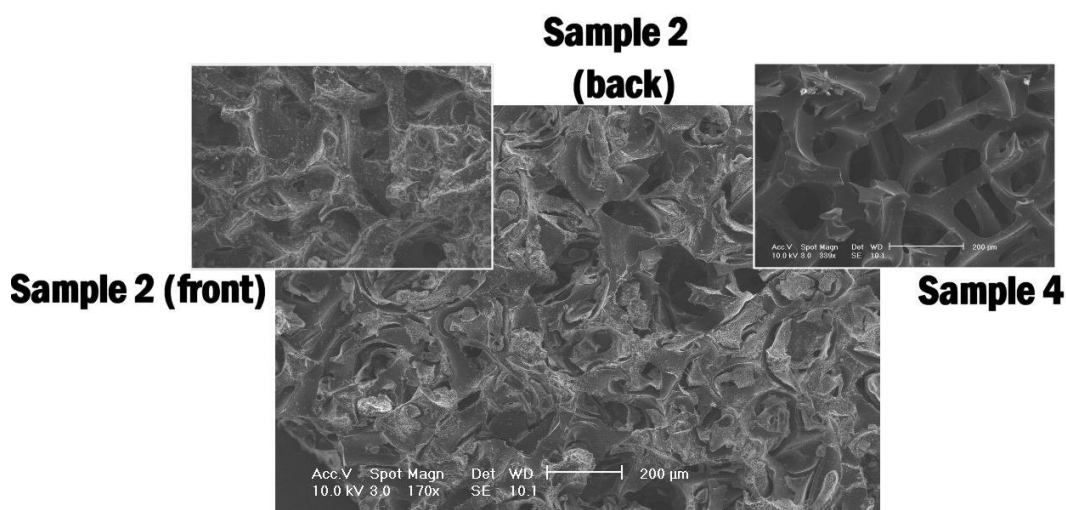
Figure 7.6 - Dip coated RVC sample showing the back and front of the sample and a comparison against a control sample (sample 4).

force and pre-treatment can all affect the formation of a layer and the nature of its surface structure and chemistry.

Figure 7.6 shows a comparison of the 'front' and 'back' sides of the dip coated RVC compared against the control RVC sample. It shows a clear difference between the two sides. The 'back' side shows significant blocking of pores and coating of the RVC. The front side shows coverage of the RVC surface but much less material filling the void space within the struts of the tetrahedral RVC structure. Figure 7.7 shows a much higher resolution image of the material on the surface of the RVC showing the long needle crystalline shape.
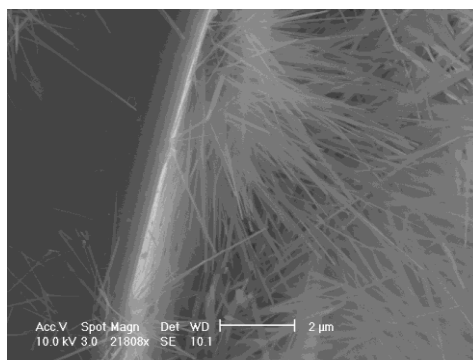
Figure 7.7 - high resolution SEM image of the crystal formation on the RVC surface.

Figure 7.10 shows one of the areas that was investigated on the back of the dip coated RVC sample. It highlights where the crystal growth occurs on the surface of the RVC and the blocking of the void space with the RVC strutted structure.

Figure 7.8 - EDX spectra position a, of crystalline formations
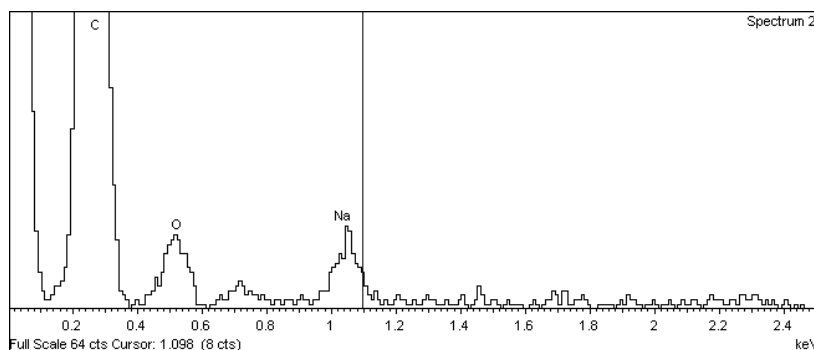
Figure 7.9 - EDX spectra position b, showing RVC surface

Figure 7.10 - SEM image of the 'back' side of the dip coated RVC sample, highlighting the areas that EDX spectra were taken and where the crystal structures occur

Combining this imagery with the EDX spectra of Figure 7.8 and Figure 7.9 demonstrates that the ratio of peak intensities shows the crystal to have a much higher composition of silicon. This is somewhat unexpected.

253
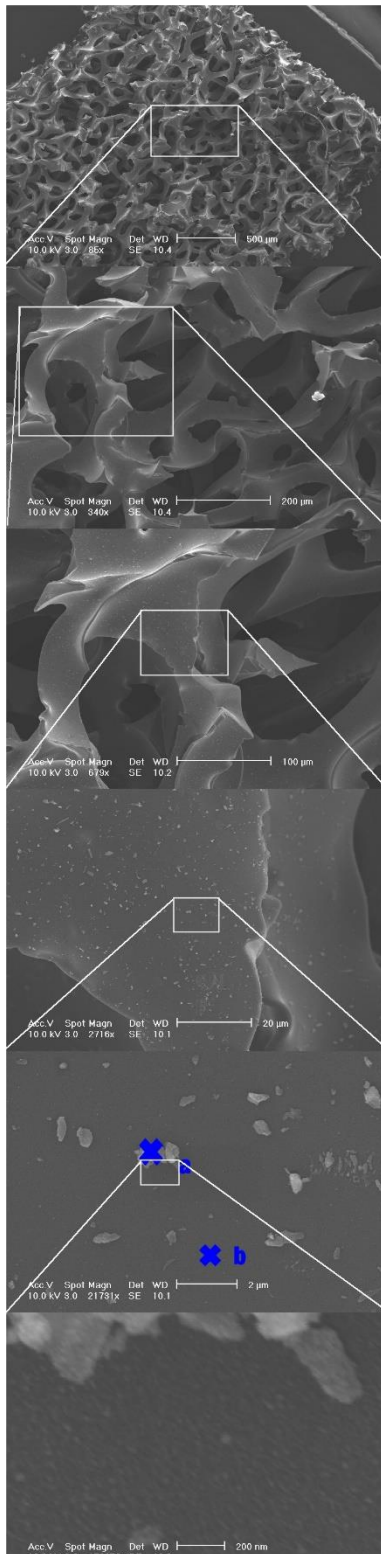
Figure 7.11 - position of areas of interest within the sputter coated RVC sample with the areas where EDx spectra were taken

Without knowing the full details of the methodology used for dip coating, it is difficult to ascertain where the crystal of silicon has arisen. It is apparent that the change in structure and the surface roughness of the pores and void space will affect catholyte material to flow through the sample. This sample was identified for further analysis of the imagery to investigate the penetration of the dip coating modification into the RVC structure.

Sputter coated RVC sample

Sputter coating is an increasing popular technique for depositing a very exact layer of material as the process is becoming cheaper and easier to customize. Companies such as TEER Coating Ltd now offer a range of services and can even approach mass production for certain components, typically for high end motor sport. However, the technique is still relatively expensive compared to other methods and contamination can occur with the sample depending on target choice.

Figure 7.11 shows the route taken to the area of interest on sample 3 and the areas examined with EDX (Figure 7.12). Compared to the dip coated sample there is not a significant reduction in the pore size. It shows a higher resolution image of the area of interest revealing possible 'ash' particles being present. The sample also

254

showed unusual growths on the surface, possible relating to a crystal growth or a positive deformation to the surface. It is also possible these 'growth' patterns are areas of least resistance within the RVC structure which would adhere a disproportionate amount of material due to the method of sputter coating.
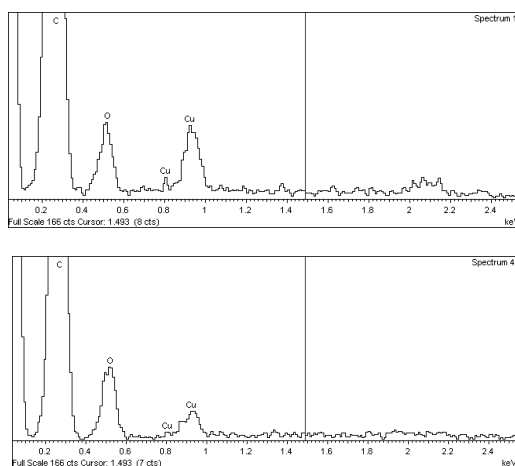
Figure 7.12 - EDX Spectra of sputter coated RVC, position a (top) and position b (bottom)

Figure 7.12 shows the EDX spectra taken in position a and b (Figure 7.11), the spectra indicate that carbon, oxygen and copper are present on the surface of the growth in the same intensity ratios. The presence of copper is unexpected but may be explained if a copper backing to a target was used within the sputter coating procedure.

Figure 7.13 is the highest magnification that could be achieved with these samples and the machine used. The presence of spherical particles on the surface can just be detected. When investigated, these particles were measured at between 37 to 44 nm, however, significant experimental error must be allowed as well as the inability to detect smaller particles that might be present. It must additionally be noted that the larger particles on the surface are also covered in the smaller particles.

Adding to the hypothesis that these are ash particles present after carbonisation. The EDX spectra again shows the presence of carbon, oxygen and copper.
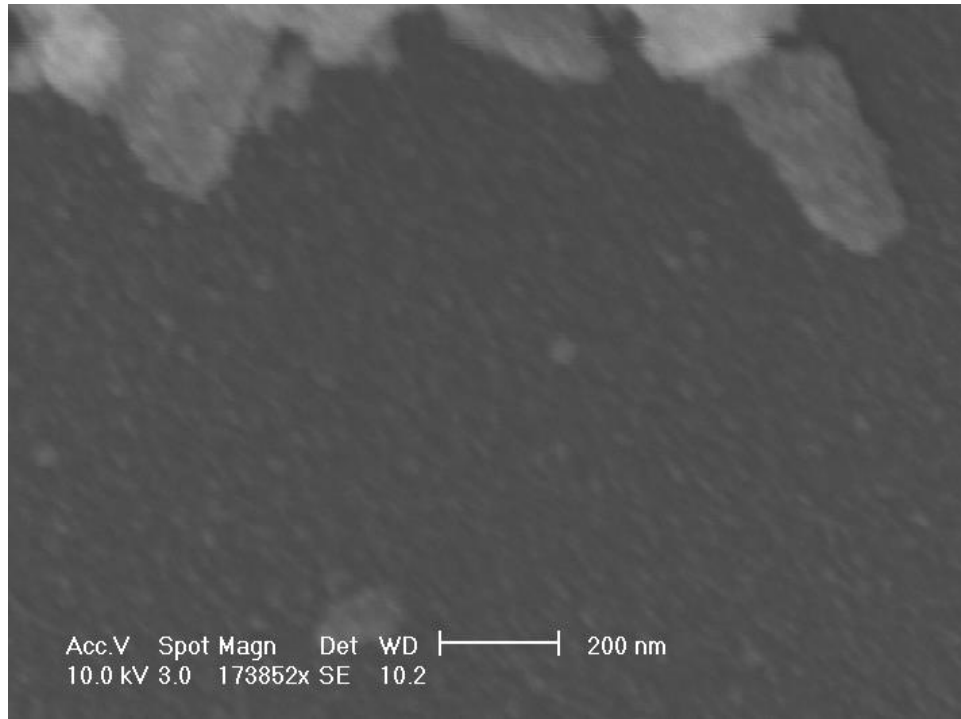
Figure 7.13 - High Resolution SEM image of sputter coated RVC sample.

Depth analysis of dip coated method
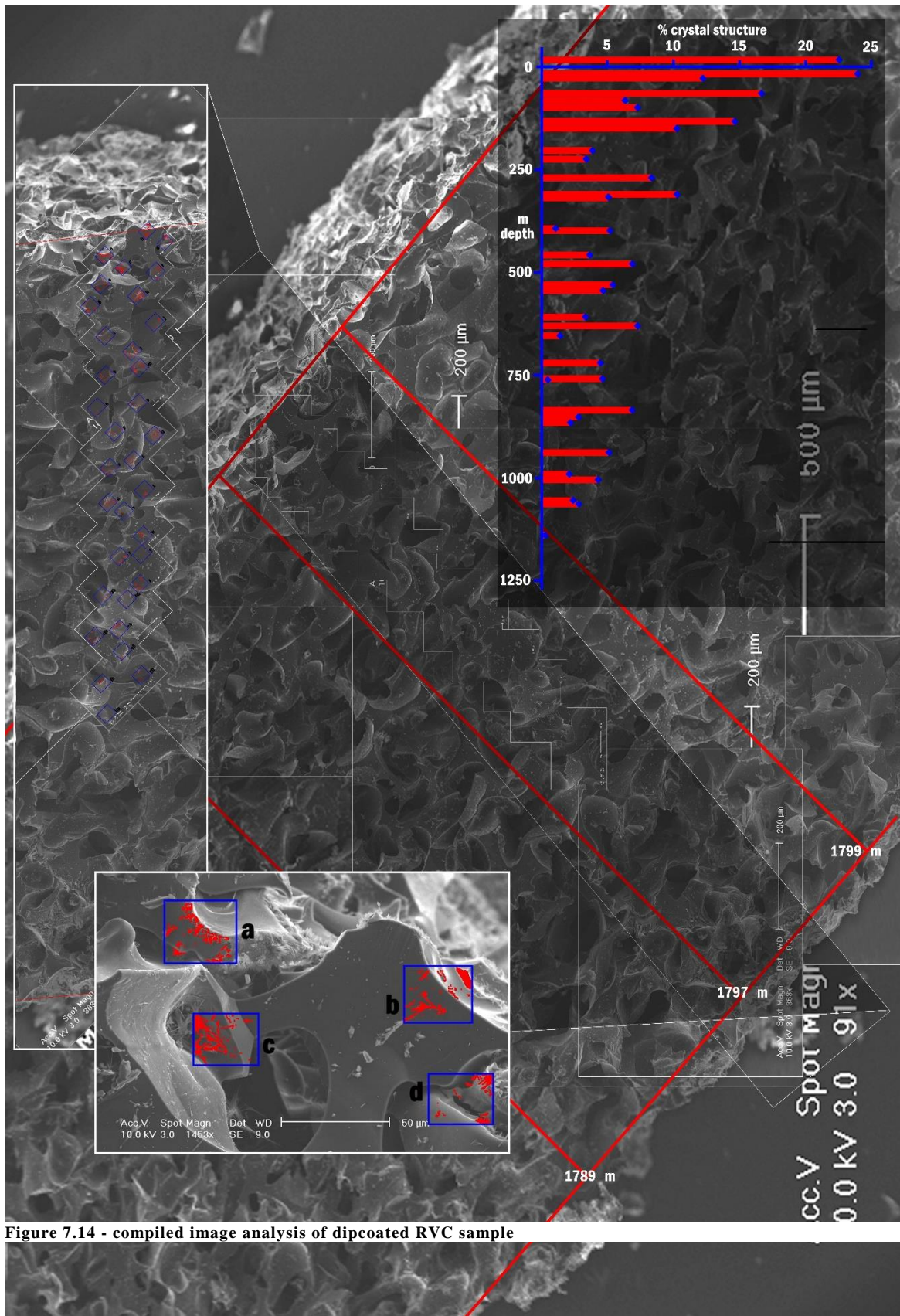
Figure 7.14 - compiled image analysis of dipcoated RVC sample

Figure 7.14 shows a compiled image analysis of the depth of penetration of the dip coating technique. SEM images were taken from a cross section of the cut RVC sample. These were stitched together to form a high resolution image of the cross section. This was then analyzed by taking boxes at random points across the cross section and highlighting areas of crystal growth in red. The percentage coverage of crystal was then computed and plotted against depth, shown on the graph (right). This shows information on the depth of penetration in the dip coated sample. The RVC thickness was approximately 1795 microns. The analysis showed a high percentage of crystal coverage was seen at the surface (22%) and that this dropped exponentially with depth into the sample until reaching a constant coverage of around 5%.

7.1.4 Conclusions

The heat treated sample of RVC showed evidence of damage to the RVC structure. Damage was seen to the peaks of the tetrahedral structure of the RVC. It is possible that these were received in transit but may be because of the heat treatment. Cracks in the struts of the RVC were also seen. Heat treatment may increase the conductivity across the RVC electrode, however the damage caused may result in isolated areas and even a reduction in the surface area of the electrode. No significant change to the overall RVC tetrahedral structure or in the void space was seen between the heat treated sample and the control sample.

The dip coated sample showed coverage of a crystalline structure on the surface. This appeared to reduce the pore size within the sample but only by a small percentage. The crystalline structure was shown to contain sodium, silicone, carbon and oxygen. It was also seen that the extra material would increase the surface area of the electrode, but could lead to a significant pressure drop as a

result of the smaller voids. When the depth of penetration for the treatment was analysed it was seen that the surface exhibited a high coverage of crystals (22%) and that this reduced exponentially when moving into the sample reducing to a constant coverage of around 5 %.

It could be seen that the sputter coating treatment did not reduce the overall pore size of the sample. It could be seen that the surface was covered with small particles measured to be between 37-44nm although significant error resides in this measurement. The composition of the surface was of interest as it contained carbon, oxygen and copper, possibly the result of using a copper target in the sputter coating technique.

7.2. Novel Electrodes within fuel cell science

7.2.1 Introduction

The work covered within this thesis has focused on the three electrode cell. The three electrode cell allows for testing in ex-situ environments and investigation of thermodynamic and kinetic parameters of potential catalysts. The 'two electrode' set-up is often described as an 'in-situ' or a true fuel cell set-up as it is much more akin to the environment of an eventual implementable fuel cell device. In both cases advantages and disadvantages are seen in the choice of set-up.

The choice made for each electrode is extremely important and again has been discussed in great detail in previous sections. In particular, the effect of a drifting reference electrode has been highlighted due to the contamination of phosphomolybdic acid derivatives and subsequently the

'poisoning' of the counter electrode through adsorbed species. Often these effects can be overlooked in designing an appropriate electrochemical set-up.
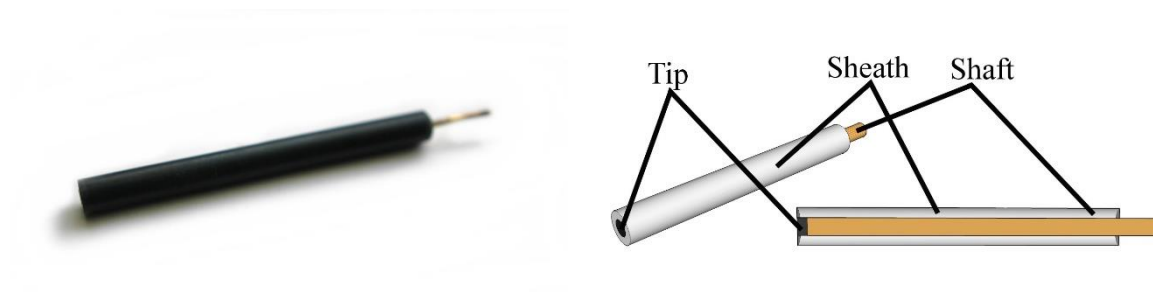
Figure 7.15 - Working electrode design

The working electrode, Figure 7.15, receives the most attention when determining a correct or valid electrochemical set-up and the construction of working electrodes is the focus of the first part of this chapter. The working electrode is the principle electrode that interacts with any redox phenomena and the method by which it does so, drastically changes the design and function of the electrode. The material that this tip is formed of is important and has been discussed in detail in earlier chapters. The concern of this chapter is how to construct electrodes that can be modified in novel processes. The modification of electrodes has been performed for an extremely long time, the dip coating modification explored in chapters 3, 4 and 6 being just one example of a standard modification technique. As was explored, even standard processes need to be investigated for each example to ensure valid and repeatable experimental results.

In fuel cell science, a standard technique to investigate potential electrocatalysts is to modify the electrode surface through 'drop casting' the catalytic material onto the tip: this is the technique used to explore the biological catalysts in chapter 2.1 and to create the control sample in chapter 2.2, Figure 7.15.
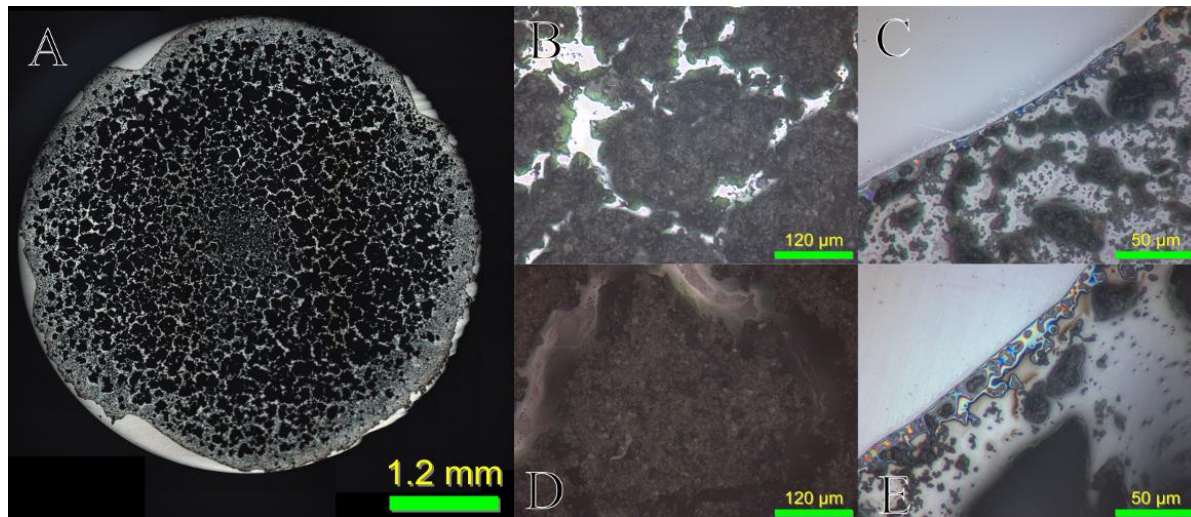
Figure 7.16 - Dropcast electrode surfaces, A - 3mm GC electrode modified with 2mg of biologically produced Pd Catalyst, B - clump on a 2mg Bio-Pd modified electrode, C - edge of 2mg Bio-Pd modified electrode, D - 4 mg Bio-Pd modified electrode, E - edge of 4 mg Bio-Pd modified electrode

In order to develop the understanding of new catalyst production techniques, new forms of electrode construction are needed to allow for novel modification, such as plasma spray deposition, spin coating or lithography (as highlighted in chapter 2). In these techniques, standard electrodes provided by commercial companies cannot be used either because materials cannot withstand the environments, or they are simply too big to fit into the machines. For this reason, new methods for electrode construction were investigated.

'Two electrode' electrochemical set-ups

In the 'two electrode' set-up the electrodes are very different. They are typically much larger; at least several orders of magnitude in terms of effective electrochemical surface area; often they are porous and need to retain a mechanical strength. The methodology to test these electrodes is often very different as well. Instead a polarity is applied between the working and counter electrode (or current demanded). This represents an issue where cross polarization can occur. This is where the polarity of an electrode can inadvertently be inverted causing damage and giving false readings. It is perceived within fuel cell science that if the flow rate of hydrogen at the anode is above the stoichiometric limit that the much faster kinetics of the hydrogen oxidation reaction will lead the anode to function as an 'in situ' reference, with the polarity imposed on the cathode.
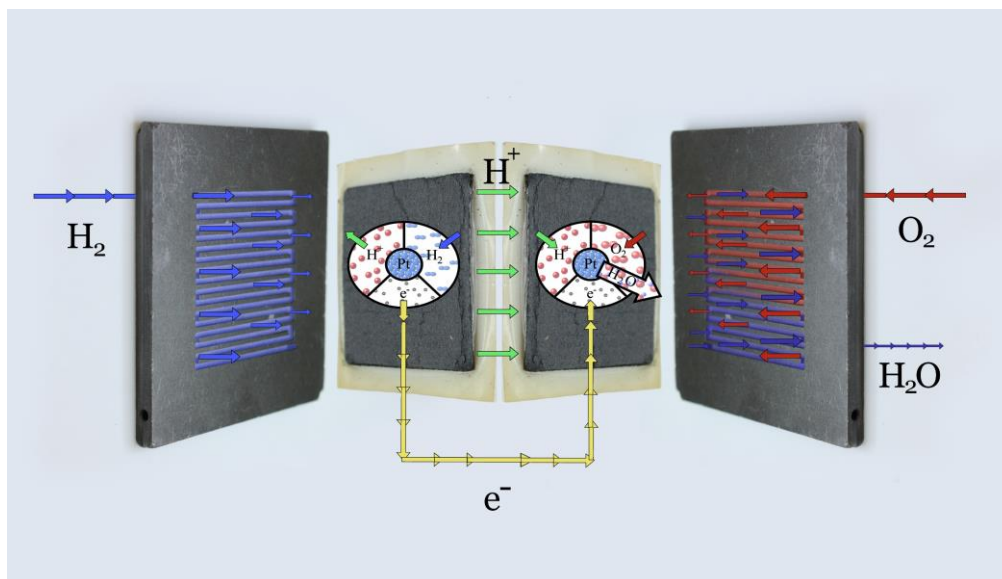
Figure 7.17 - Diagram of a PEMFC showing the MEA and the two associated flow field plates

In addition, the large size of the electrode and the need for a distribution of reactant across the electrode can lead to differential voltage effects across the electrode surface. This can be caused

by a change in partial pressure of reactant as the reactant stream travels the distance across the electrode surface, shown in Figure 7.17. This is of interest in catholyte cells due to the parasitic losses caused by maintaining the reactant stream. There are only limited ways to investigate this phenomenon; modelling has been an important tool in investigating its impact but directly measuring the difference without directly affecting the environment is difficult.

Secondary Electrodes within Fuel Cell Science

One potential method to measure the voltage differential would be to use secondary electrodes. These typically are electrodes that are connected to the system, usually connected to the same counter and reference but that are subject to a different excitation to measure a secondary part of a given electrochemical system. A good example of this kind of set-up is the rotating ring-disc electrode.

In this method, a second ring of Pt is set within the tip of an electrode offset from the main central working electrode tip. In fuel cell science, this is typically to investigate the production of hydrogen peroxide as a parasitic side reaction at many common oxygen reduction catalysts. This ring is typically set at an oxidizing potential and functions as a 'collection' electrode. Any peroxide that is formed by an incomplete reduction, a $2e^-$ process rather than the full $4e^-$ reduction, is reduced at the platinum ring. By measuring the current produced at the rate at which the electrode is rotated, kinetic data can be extrapolated.

Additionally, information can be obtained about the environment that the electrode is placed within. If the open circuit potential of the electrode is monitored any shifts in potential are

263

indicative of a shift in the reaction quotient at the surface. These electrodes are essentially passive to the system they are monitoring. As such an OCP monitor is a good candidate to investigate the differential voltage across a flow field plate.

7.2.2 Experimental

Designing Electrodes

Computer design was used to facilitate the designing and building of the electrodes and the structures to hold the electrodes. The main program used was Google Sketch-Up which allows for easy 3d representation of design ideas, and when combined with other programs such as Cura it can provide access to manufacturing techniques such as 3d printing. It also enables the export of graphical representations like those that have been used in figures throughout this thesis.

Three Electrode cell working electrode development

The main shroud of the electrode that insulates the shaft was constructed out of Teflon or PEEK, directplastics.co.uk. The main tip material was 3mm GC section cut with a diamond blade from longer GC rods (alfa aesar). The plastic rods (various diameters, 6, 8 & 10 mm) were cut to the correct length for each electrochemical cell to be used (4-10 cm) and a central column was lathed from the rod to allow for the copper rod insert to be installed.

The methodology to produce the tips to sit on top of the shrouds forms the first part of the discussion section later in this chapter.

Building the monitoring electrode gaskets (MEG)

Several iterations of the monitoring electrode gasket are discussed. All versions of the monitoring electrode gasket are formed by placing wires within a prefabricated mould and then using a potting compound to add the mechanical strength and gas sealing along the edges. The moulds were made from Teflon sheets (directplastics) and were machine with CNC at the facility at the Heath Technology Centre (Runcorn), from designs generated with the aforementioned computer aided design.

RTV silicone and epoxy resin were used as the main potting compounds. A range of these two part cure compounds were used due to the different characteristics and chemical stability of the compounds. In all cases the compounds chosen had a long working lifetime and were low viscosity. This enables for the mixed compounds to be degassed in a dessicator under vacuum before use. The compound is then poured into the moulds and left to cure for 24hrs before use.

Testing monitoring electrode gasket

To test whether the MEG worked as expected it was mounted into a catholyte fuel cell provided by ACAL Energy ltd, with an electrode cell area of 25 cm^2. The fuel cell was run through an I-V test protocol using an ACAL Energy test rig and potentiostat, whilst the OCP (open circuit potential) of the monitoring electrodes was measured with several Palm sense potentiostats. All devices were time synchronized and measurements recorded to a standard timing allowing for alignment of data afterwards.

After initial IV experiments, EIS scan was completed on the ACAL energy fuel cell with the monitoring gasket still in place.

7.2.3 Results and Discussion

Removable Tip Electrode

The first type of electrode to be made was an electrode suitable to fit in the plasma vapour sputter deposition equipment. This meant the tip had to be of a maximum diameter of 8 mm and a maximum height of 2mm. This was achieved by taking a 4 mm piece of 8mm PEEK rod and inserting a GC section as has previously been described. The whole tip was then machined to 2mm, with a lapping machine.

Cu Core

GC
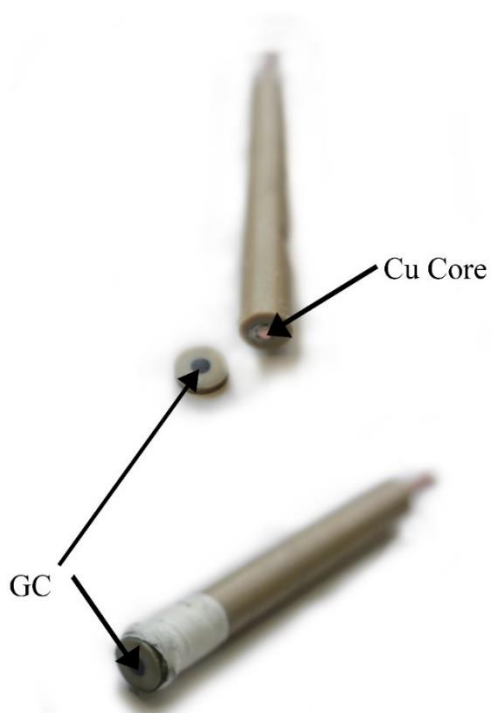
Figure 7.18 - Novel removable tip electrode

This tip could then be modified through sputter coating. To modify it in this way an extra mask of Teflon gasketing was needed to only expose the 3mm GC central column of the tip to be coated. After modification the tip was taken to be mounted on the premade shafts. A small amount of silver epoxy (RS Components) was dabbed onto the exposed copper, and an isolating ring of epoxy resin was used to surround this connection and isolate it from the electrochemical cell. The tip was then placed onto the shaft. This resulted in the electrode shown in Figure 7.18.

These electrodes functioned well initially and an initial study was conducted with them. However, the electrical connection was frequently lost, due to weakening of the epoxy connection. As a result, further electrode designs were investigated.

Screw tip electrode

The main weakness of the removable tip electrode was the epoxy connection between the shaft and the tip. The connection could be lost due to mechanical damage. Additionally, several electrodes were damaged through repeated exposure to acidic conditions eventually weakening the epoxy. Stronger epoxies could be used or specialist chemical resistant epoxies could be trialled. However,
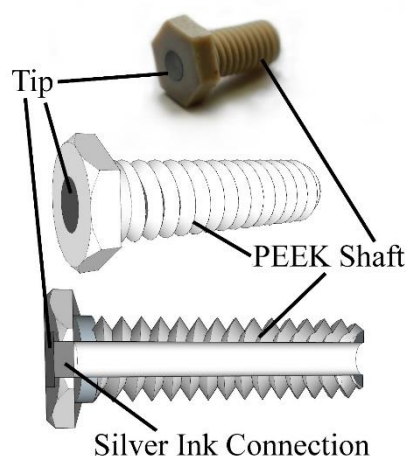
Figure 7.19 - Screw tip electrode

267

even these would not allow the electrodes to be used within organic solvents. RTV silicone compounds like those used for the MEG could be considered for these environments as these can withstand repeated exposure to organic materials, but this would necessitate a mould and would make post-treatments like polishing of the electrode surface difficult.

Instead a mechanical barrier was explored. A PEEK screw was taken and prepared in the same way that the tips were produced. Additionally, the shaft was lathed so that a recess with a screw thread matching that of the screw was present at the head of the shaft. Silver ink was used on the screw, as shown in Figure 7.19, to provide electrical connection to the copper shaft.

These tips were successfully modified and tested. They were not able to fit in the plasma vapour sputter deposition machine, but could be modified with spin coating and lithography. The electrodes tested showed no loss of connection, even after repeated removal of the tip for modification and testing.

Monitoring gasket electrode under power curve testing

The first MGE to be made was produced using epoxy as the encapsulating material and is shown in Figure 7.20. This electrode quickly deteriorated and failed to make a gas seal within the catholyte cell. As with the above removable tip electrode this may have been due to the chemical degradation of the epoxy itself.
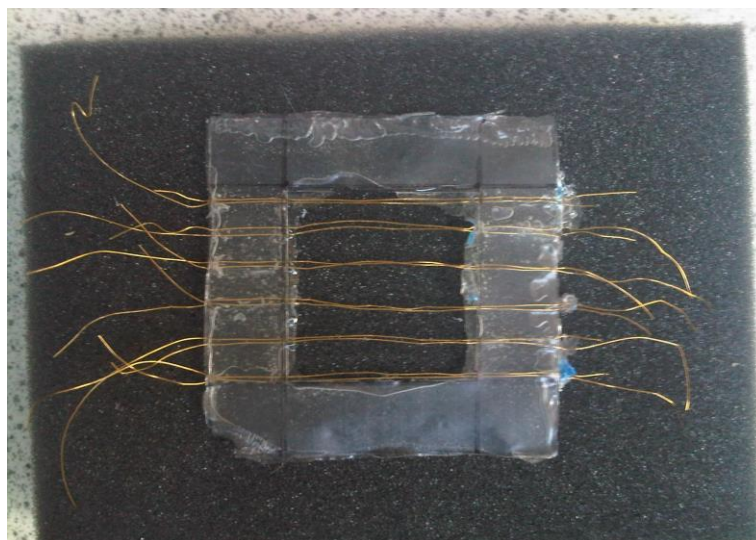
Figure 7.20 - Epoxy MGE

A new MGE was constructed which was designed to use RTV silicone as the encapsulate. The MGE was constructed as described in previous sections and as shown in Figure 7.21. This MGE successfully maintained a gas and liquid seal within the ACAL Ltd. test cell.
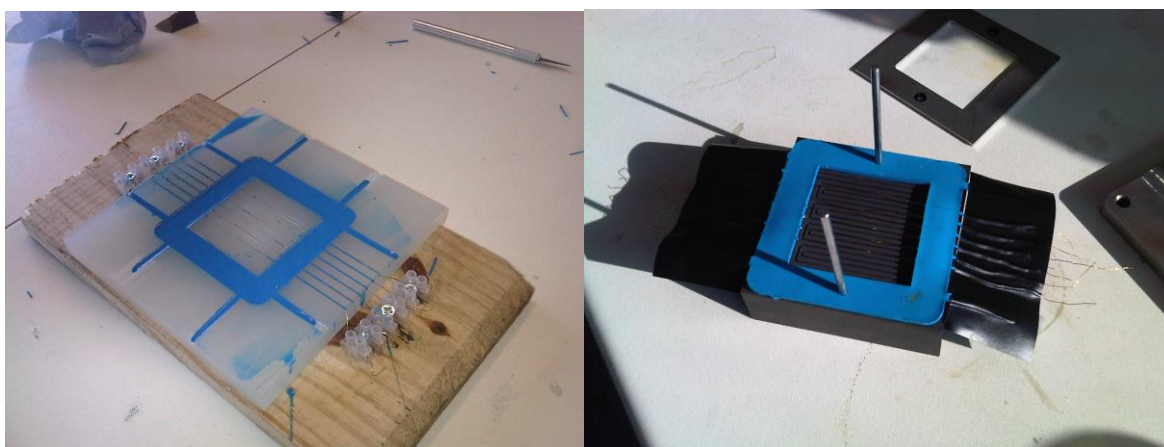
Figure 7.21 RTV siliocone MGE
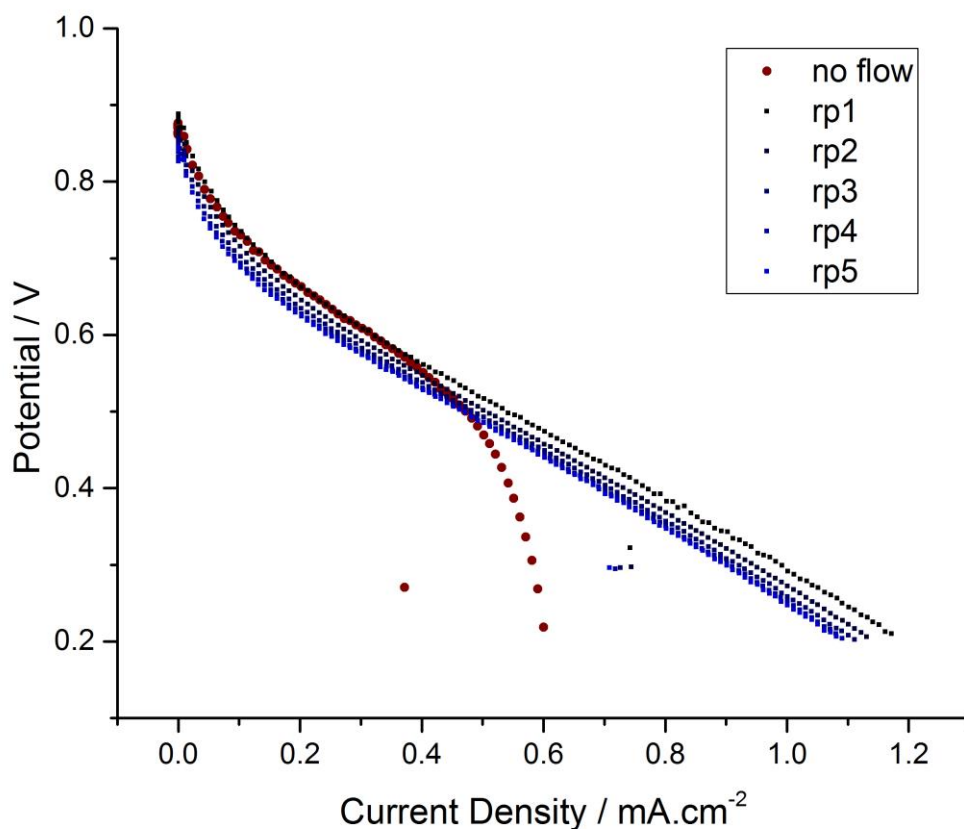
Figure 7.22 - IV curves from MGE test cell, showing the repeated scans (rp1-5) and the difference in flowing and non-flowing conditions

In such form the Fuel cell was operated through an I/V test sequence using a SGL felt cathode, an Ion Power supplied Nafion Membrane and a 34 BC SGL anode. The flow rate of catholyte was 200 mL/min and the IV curve was taken in galvanostatic mode from OCP with a current ramp of 500 mA.s^{-1}. The resultant IV curve of the fuel cell's performance can be seen in Figure 7.22.

Figure 7.22 also highlights the difference that the flow rate of the catholyte made to the fuel cell's performance. With no flow the cell's current quickly became limited by diffusional limitations, but

when flow of catholyte was maintained losses are mainly attributable to resistance and activation losses. After observing the performance of the fuel cell itself the monitoring electrodes across the cell were monitored for their OCP.
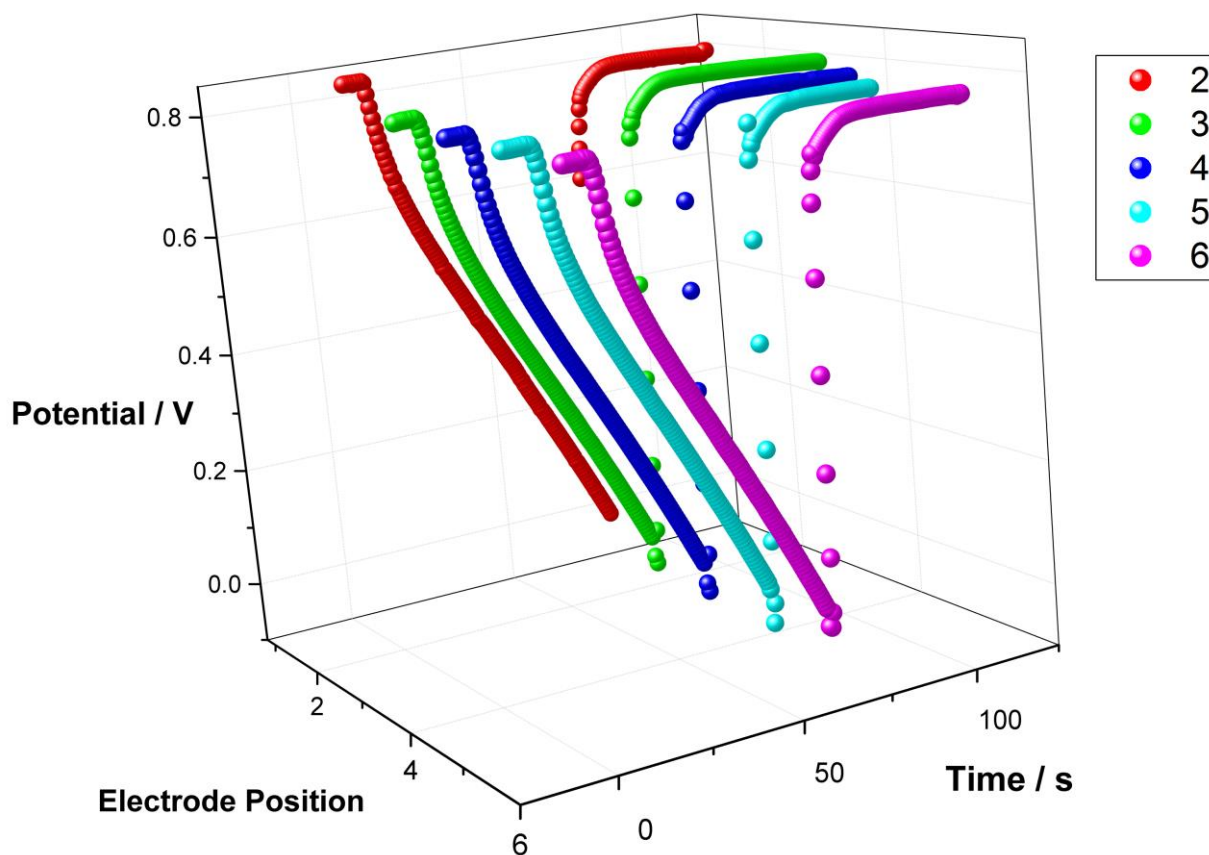
Figure 7.23 - MGE OCP monitoring versus time versus electrode position

In order to obtain results from all the electrodes several IV experiments were conducted on the cell and each electrode's OCP was monitored (shown in Figure 7.22). Unfortunately, the electrode closest to the fuel inlet lost connection due to a mechanical breakage and so results for this electrode could not be recorded. Within the graph the position number increases the further the electrode's position from the fuel inlet. As can be seen in the data generated (Figure 7.23) the OCP and so reaction quotient changed across the cell, as had been hypothesized although this change was slight.

In addition to monitoring during IV curve testing the electrodes were used to monitor the voltage during EIS experiments. During these experiments the response of the cell to an oscillating voltage and increasing frequency is observed. The shift in the applied and recorded signal gives rise to a time constant at each frequency of oscillation leading to information about the resistive, capacitive and diffusional nature of the redox processes occurring at the electrode. It is important during these measurements that the amplitude is high enough to see a response from the cell but not so high as to shift the environment of the electrode chemically. The tests are generally conducted at a steady state and around the OCP of the cell. Within many Fuel cell EIS experiments the amplitude can be significant higher than in usual EIS experiments, as a methodology to overcome the noise in the cell and the large inductance that can be inherent in these devices. Usually an amplitude lower than 10% of the operating voltage is used and in normal electrochemical set-ups this can be commonly 10 mV around an OCP of 0.8-1.0 V.
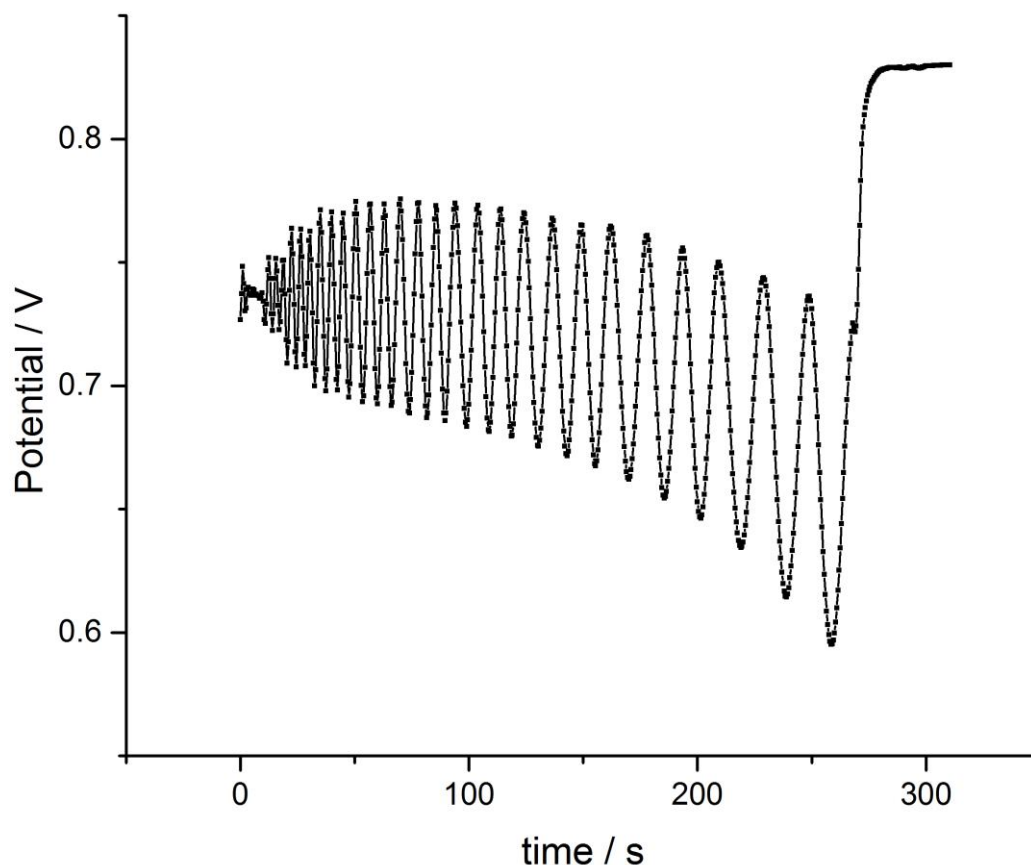
Figure 7.24 - MGE OCP data from EIS experiments

Figure 7.24 shows the data from the OCP monitoring the MGE during an EIS measurement. The OCP measured at the start of the experiment was 734 mV. This is the base line on top of which the oscillating voltage should be applied. What can be seen from the experiment is that this baseline drifts during the experiment with the result that the final midpoint of oscillation is much below the 734 mV OCP. This leads to invalid EIS data that may, in this case, reflect a higher resistance and because the drop occurs at lower frequencies, a more capacitive and diffusion limitation than is true of the system.

The cause of this may be the large amplitude of oscillation being applied. The final change in voltage is 14 mV which represents almost 20 % of the baseline potential. This could be resulting in a change in the chemical environment and the reaction quotient during the EIS experiment.

7.2.4 Conclusion

The development of several different electrode construction types has allowed for novel experimentation to take place. Each type has its advantages and its disadvantages but adds to the library of techniques and electrodes that can be used in experimentation.

The development of the MGE shows the potential to match modelling of fuel cells with experimental data. It differs from current attempts at multi-electrode fuel cell arrays by being a separate electrode that is not part of the usual fuel cell conformation. It has highlighted the need for careful application of EIS parameters and suggests that EIS data in liquid catholyte cells should be taken at constant flows of reactant rather than without flow.

8. Conclusion

This thesis has presented the work conducted by the author into reducing, recycling and removing PGMs from PEMFCs. The following sections conclude the thesis, highlighting its key findings and points to areas for further work.

8.1 Reducing platinum within PEMFCs

Section 2.1 of chapter 2 described the initial electrochemical assessment of a platinum atom containing surface that has been generated through the lithography and ion beam treatment of a fulleropyrrolidine bipyridine platinum chloride complex. The work showed that with the inclusion of platinum in the complex the onset of proton reduction was shifted positive and once the final surface had been generated that this positive shift was maintained and a durable surface was produced generating the same current as the equivalent surface area of bulk platinum.

This finding was significant, given that the material was only 18% platinum by mass. This has led to the inclusion of the work conducted in a research paper which is expected to be submitted for publication shortly.

In addition to the work contributing to this (expected) addition to the literature it has also led to work still being conducted within the research group. The initial assessment needs to be taken forward to full characterisation of the surface's electrochemical behaviour, specifically, the exact ECSA (electrochemical surface area) per gram and the activity towards the ORR. Further, from the

base example of platinum inclusion, the development of bi-metallics and the inclusion of metals such as ruthenium need investigation, especially the possibility of increased tolerance to poisons such as CO.

8.2 Recycling through biohydrometallurgy

Section 2.2 of chapter 2 presented the work conducted into the possibility of recycling PGMs using biohydrometallurgy and producing materials capable of being used as electrocatalysts. It's showed how biomass containing palladium demonstrated electrochemical characteristics, which had previously been unseen under these conditions.

The work highlighted how the bacterial strain, reducing agent and synthetic leachate all had effects on the PGM containing biomass and the particles of PGM formed. This was shown clearly through electron microscope imagery which detailed the large effect on particle formation of changing bacterial strain and reducing agent.

The imagery highlighted how changing from the gram negative to gram positive bacteria caused the largest effect and that the lack of a well-defined cell wall within M.luteous strains caused a significant difference in particle distribution compared with S.oneidensis or E.coli strains. It was hypothesised that changing the reducing agent changed the interaction with the bacteria and caused a large effect on particle size and distribution of particles.

The material was shown to produce electrochemical signals and matched the TEM results showing differences in electrochemical behaviour resulting from the differences in particles formed which were caused by the changes in bio-mineralisation conditions. The finding that this material demonstrated electrochemical behaviour typical of palladium was a significant result. The significance of the work is shown by the a paper on the work published in biotechnology letters.[280]

As has been highlighted in section 2.2.4 a significant amount of additional further work has already been conducted since my contributions. This has led to examples shown producing platinum containing and bimetallic deposits on biomass which are currently awaiting publication. Significantly work to develop these materials as electro catalysts and in application for fuel cell catalysts is ongoing.

8.3 Removing platinum from PEMFCs

The majority of the thesis focused on work directed at removing platinum content from PEMFCs. Working with ACAL Energy Ltd it was determined that studying the electrochemistry of phosphomolybdic acid together with its singularly and doubly substituted derivatives would add valuable information towards this aim that was not available.

These species readily form adsorbed layers and the interaction between these adsorbed layers and the bulk solution is not well understood. As such the project was broken down into stages, developing knowledge on the adsorbed layers before moving onto the system combined.

Chapter 3 presented the initial investigation into the electrochemical response of phosphomolybdic acid and its singularly substituted vanadium derivative. The work showed the change in redox behaviour between the derivatives including vanadium and the original phosphomolybdic acid species. It highlighted that the first reduction wave of the original species had spilt, and a shift positive of 200 mV had occurred. This was indicative that the original two electron reduction seen in phosphomolybdic acid species (documented in previous studies[181,217]) splitting into two one electron processes, which concurs with the general effect observed when substituting vanadium into these species and with experiments published in organic media.[226]

It was also observed how the redox processes deviated from ideal behaviour, with this effect increasing with the substitution of vanadium into the structure, supporting ideas previously held about the deformation and change in behaviour of the species in general with vanadium inclusion.

Chapter 4 presented the continued work into heteropolyacids adsorbed layers, detailing the effect of changing the graphitic electrode surface, the counter ion (cation) to the heteropolyanion and the dramatic effect that pH had on the electrochemistry observed. This extra information allowed for the inclusion of protons within the electron transfer scheme and for the general pathway to be put forward as shown in the following equations.

Equation 8.1
$$NaH_3(PV^V Mo_{11}^{VI} O_{40}) \ + e^- + H^+ \rightarrow NaH_4(PV^{IV} Mo_{11}^{VI} O_{40})$$

Equation 8.2
$$NaH_4(PV^{IV} Mo_{11}^{VI} O_{40}) \ + e^- + H^+ \rightarrow NaH_5(PV^{IV} Mo_1^V Mo_{11}^{VI} O_{40})$$

Equation 8.3

$$NaH_5(PV^{IV}Mo_1^V Mo_{11}^{VI}O_{40}) \ + 2e^- + 2H^+ \rightarrow NaH_7(PV^{IV}Mo_3^V Mo_9^{VI}O_{40})$$

Equation 8.4

$$NaH_7(PV^{IV}Mo_3^V Mo_9^{VI}O_{40}) \ + 2e^- + 2H^+ \rightarrow NaH_8(PV^{IV}Mo_5^V Mo_7^{VI}O_{40})$$
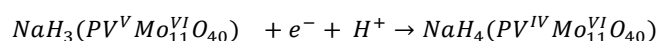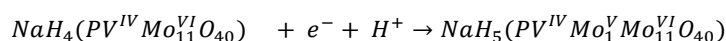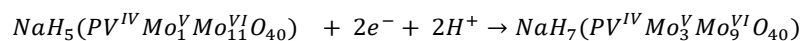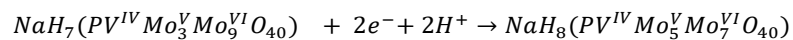
This work added to existing knowledge regarding the adsorbed layer of phosphomolybdic acid and the singularly substituted vanadophosphomolybdic acid. As such it was presented at the 'Electrochem 2014' conference in an oral presentation and has been prepared for submission for publication shortly.

Chapter 5 detailed the work completed into the solution electrochemistry of phosphomolybdic acid and its singularly substituted vanadium derivatives. It highlighted how the interaction between the solution phase and adsorbed layer is extremely complex but that the underlying redox processes still occur. However, that they are dominated by a mediation through the adsorbed layer. This was shown by the transitions in behaviour observed between low and high concentrations and with increasing scan rate. Where the behaviour changed from adsorbed dominated to solution based and the electron transfer rate was out run by fast scan rates. Unfortunately, due to the complexity of the multi-multiple electron transfer evaluation of the rate of the electron transfer have so far been unsuccessful.

Chapter 6 covered the work that substituted a second vanadium centre into the original phosphomolybdic acid. It showed that an adsorbed layer developed in the same manner as with the mother complex and the singularly substituted species.

It was shown that the substitution of a second vanadium centre, again altered the redox processes demonstrated by the adsorbed layer. Through the same experiments that were conducted on the singularly substituted species a general reaction scheme was deduced, that is shown in the following equations.

Equation 8.5

$$Na_2H_3(PV_2^V Mo_{10}^{VI}O_{40}) + 2e^- + 2H^+ \rightarrow Na_2H_5(PV_2^{IV} Mo_{10}^{VI}O_{40})$$

Equation 8.6

$$Na_2H_5(PV_2^{IV} Mo_{10}^{VI}O_{40}) + e^- + H^+ \rightarrow Na_2H_6(PV_2^{IV} Mo^V Mo_9^{VI}O_{40})$$

Equation 8.7

$$Na_2H_6(PV_2^{IV} Mo^V Mo_9^{VI}O_{40}) + e^- + H^+ \rightarrow Na_2H_7(PV_2^{IV} Mo_2^V Mo_8^{VI}O_{40})$$

Equation 8.8

$$Na_2H_7(PV_2^{IV} Mo_2^V Mo_8^{VI}O_{40}) + 2e^- + 2H^+ \rightarrow Na_2H_9(PV_2^{IV} Mo_4^V Mo_6^{VI}O_{40})$$
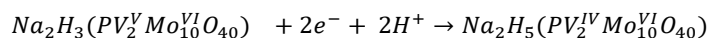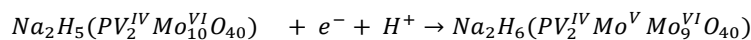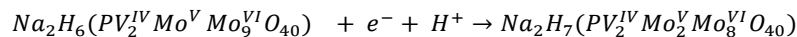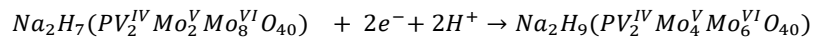
It was also shown that the behaviour of this species was similar to that of the singularly substituted species in respect to changing the electrode surface and cation.

Section 6.3.4 detailed the work into the solution phase doubly substituted phosphomolybdic acid species. This showed a similar mediated process to the solution of the singularly substituted species. However due to the first reduction wave doubling in magnitude, interpreting the resulting electrochemical data was even more of a challenge. Some peak separation allowing for determination of redox events was shown at low pH values which indicated the initial wave was not a single double electron transfer but two processes which behaved independently of each other with respect to pH. This confirmed the mediatory relationship of the adsorbed layer and the solution, as seen in the singularly substituted species.

There is much further work to be conducted on phosphomolybdic acid and its vanadium substituted derivatives. Work is continuing into the modelling of the electron transfer processes to establish possible reaction mechanisms. EPR experiments to determine the method of electron transfer would provide invaluable information. Of significance and worthy of extra experimentation would be any changes in electrochemical behaviour when being exposed to oxygen and how this alters with increased vanadium substitution.

9. References

1.   Korner, Alexander Tam, Cecilia. Bennet, Simon. Gagne, J.-F. *Technology Roadmap - Hydrogen and Fuel Cells*. (2015).

2.   Ringshaw, G. Fear over looming energy crisis in UK. *the sunday times* (2007).

3.   Leake, J. 'Blackout Britain' threatens economy. *the sunday times* (2014).

4.   Energy crisis to hit Britain in 10 years, Chris Huhne warns. *The Evening Standard* (2010).

5.   IMechE. *Engineering the UK electricity gap*. (2016).

6.   Peak Oil Definition - Oxford Learners Dictionary. Available at: http://www.oxfordlearnersdictionaries.com/definition/english/peak-oil?q=peak+oil.

7.   Day, D. T. The petroleum resoucres of the united states''. *U.S.Congress Ed.* **3,** 446–464 (1909).

8.   Adelman, M.A. Lynch, M. C. Fixed view of resource limits creates undue pessimism. *Oil Gas J.* **95,** (1997).

9.   Hubbert, M. K. Energy from Fossil Fuels. *Science (80-.).* **109,** 103–109 (1949).

10.   Bardi, U. Peak oil: The four stages of a new idea. *Energy* **34,** 323–326 (2009).

11.   Hubbert, M. K. Nuclear Energy and the fossil fuel. *Am. Pet. Institutes* (1956).

12.   Krumdieck, S., Page, S. & Dantas, A. Urban form and long-term fuel supply decline: A method to investigate the peak oil risks to essential activities. *Transp. Res. Part A Policy Pract.* **44,** 306–322 (2010).

13.   Shafiee, S. & Topal, E. An econometrics view of worldwide fossil fuel consumption and the role of US. *Energy Policy* **36,** 775–786 (2008).

14.   Stern, N. C. O.-H. treasury. *The economics of climate change*. (Cambridge University Press,

2007).

15. Gauthier, C. & Gilomen, B. Business Models for Sustainability: Energy Efficiency in Urban Districts . *Organ. Environ.* **29,** 124–144 (2016).

16. Jacobsson, S. & Bergek, A. Transforming the energy sector: the evolution of technological systems in renewable energy technology. *Ind. Corp. Chang.* **13,** 815–849 (2004).

17. Dincer, I. Renewable energy and sustainable development: a crucial review. *Renew. Sustain. Energy Rev.* **4,** 157–175 (2000).

18. Jacobsson, S. & Johnson, A. The diffusion of renewable energy technology: an analytical framework and key issues for research. *Energy Policy* **28,** 625–640 (2000).

19. Yu, G., Xie, X., Pan, L., Bao, Z. & Cui, Y. Hybrid nanostructured materials for high-performance electrochemical capacitors. *Nano Energy* **2,** 213–234 (2013).

20. Jones, L. W. Toward a liquid hydrogen fuel economy. (1970).

21. Bockris, J. O. in *Environmental Chemistry* 549–582 (Springer US, 1977). doi:10.1007/978-1-4615-6921-3_17

22. Bockris, J. O. & Appleby, A. J. The hydrogen economy - an ultimate economy. *Environ. This Mon.* **1,** 29–35 (1972).

23. Gregory, D. P., Ng, D. Y. C. & Long, G. M. in *Electrochemistry of Cleaner Environments* 226–280 (Springer US, 1972). doi:10.1007/978-1-4684-1950-4_8

24. The national hydrogen association. the history of hydrogen. Available at: http://schydrogen.org/wp-content/uploads/factSheet_history.pdf. (Accessed: 11th June 2016)

25. Hagenmuller, P. Hydrogen as an energy carrier - A European perspective of the problem. *Solid State Chemistry of Energy Conversion and Storage* 1–14 (1977).

26. fuelcelltoday.com. History. Available at: http://www.fuelcelltoday.com/history. (Accessed: 11th June 2016)

27. Perry, M. L. & Fuller, T. F. An ECS Centennial Series Article A Historical Perspective of Fuel Cell Technology in the 20th Century. (2002). doi:10.1149/1.1488651

28. Lipman, T., Sperling, D., Lipman, T. & Sperling, D. in *Handbook of Fuel Cells* (John Wiley & Sons, Ltd, 2010). doi:10.1002/9780470974001.f313110

29. Smithsonian. Allis-Chalmers Fuel Cell Tractor. *The National Museum of American History* Available at: http://americanhistory.si.edu/collections/search/object/nmah_687671. (Accessed: 1st April 2017)

30. Acres, G. J. K. Recent advances in fuel cell technology and its applications. *J. Power Sources* **100,** 60–66 (2001).

31. SFC Energy. Technology. Available at: http://www.sfc.com/en/the-company/technology/fuel-cells. (Accessed: 11th June 2016)

32. Keränen, T. M. *et al.* Development of integrated fuel cell hybrid power source for electric forklift. *J. Power Sources* **196,** 9058–9068 (2011).

33. Zegers, P. Fuel cell commercialization: The key to a hydrogen economy. *J. Power Sources* **154,** 497–502 (2006).

34. U.S. Department of Energy. Comparison of Fuel Cell Technologies. *Energy Efficiency & Renewable Energy* 3463 (2016). Available at: http://www1.eere.energy.gov/hydrogenandfuelcells/fuelcells/fc_types.html. (Accessed: 1st May 2017)

35. Haigh, G. D. of energy and the environment. Sub-national total final energy consumption statistics LA level statistics (2013 data) Sub-national total final energy consumption

statistics Regional and local authority level statistics (2013 data). *gov.uk*

36. canadian hydrogen fuel cell association. What types of fuel cells are there. Available at: http://www.chfca.ca/education-centre/how-fuel-cells-work/. (Accessed: 11th June 2016)

37. Bar-On, I., Kirchain, R. & Roth, R. Technical cost analysis for PEM fuel cells. *J. Power Sources* **109,** 71–75 (2002).

38. Braga, L. B. *et al.* Comparative analysis between a PEM fuel cell and an internal combustion engine driving an electricity generator: Technical, economical and ecological aspects. *Appl. Therm. Eng.* **63,** 354–361 (2014).

39. Bezmalinović, D., Barbir, F. & Tolj, I. Techno-economic analysis of PEM fuel cells role in photovoltaic-based systems for the remote base stations. *Int. J. Hydrogen Energy* **38,** 417–425 (2013).

40. Wang, J. Barriers of scaling-up fuel cells: Cost, durability and reliability. *Energy* **80,** 509–521 (2015).

41. Ricci, M., Bellaby, P. & Flynn, R. What do we know about public perceptions and acceptance of hydrogen? A critical review and new case study evidence. *Int. J. Hydrogen Energy* **33,** 5868–5880 (2008).

42. Yetano Roche, M., Mourato, S., Fischedick, M., Pietzner, K. & Viebahn, P. Public attitudes towards and demand for hydrogen and fuel cell vehicles: A review of the evidence and methodological implications. *Energy Policy* **38,** 5301–5310 (2010).

43. Hardman, S., Chandan, A., Shiu, E. & Steinberger-Wilckens, R. Consumer attitudes to fuel cell vehicles post trial in the United Kingdom. *Int. J. Hydrogen Energy* **41,** 6171–6179 (2016).

44. Symes, D. *et al. Development of a hydrogen fuelling infrastructure in the Northeast U.S.A.*

International Journal of Hydrogen Energy **39,** 7460–7466 (2014).

45.   Landucci, G., Tugnoli, A. & Cozzani, V. Safety assessment of envisaged systems for automotive hydrogen supply and utilization. *Int. J. Hydrogen Energy* **35,** 1493–1505 (2010).

46.   Schjølberg, I. & Østdahl, A. B. Security and tolerable risk for hydrogen service stations. *Technol. Soc.* **30,** 64–70 (2008).

47.   Gasteiger, H. A., Kocha, S. S., Sompalli, B. & Wagner, F. T. Activity benchmarks and requirements for Pt, Pt-alloy, and non-Pt oxygen reduction catalysts for PEMFCs. *Appl. Catal. B Environ.* **56,** 9–35 (2005).

48.   Offer, G. J., Howey, D., Contestabile, M., Clague, R. & Brandon, N. P. Comparative analysis of battery electric, hydrogen fuel cell and hybrid vehicles in a future sustainable road transport system. *Energy Policy* **38,** 24–29 (2010).

49.   Teagan, W. ., Bentley, J. & Barnett, B. Cost reductions of fuel cells for transport applications: fuel processing options. *J. Power Sources* **71,** 80–85 (1998).

50.   El-Sharkh, M. Y., Tanrioven, M., Rahman, A. & Alam, M. S. Cost related sensitivity analysis for optimal operation of a grid-parallel PEM fuel cell power plant. *J. Power Sources* **161,** 1198–1207 (2006).

51.   Lee, G. *et al.* Development of cost innovative BPs for a PEMFC stack for a 1kW-class residential power generator (RPG) system. *Int. J. Hydrogen Energy* **35,** 13131–13136 (2010).

52.   Guerrero Moreno, N., Cisneros Molina, M., Gervasio, D. & Pérez Robles, J. F. Approaches to polymer electrolyte membrane fuel cells (PEMFCs) and their cost. *Renew. Sustain. Energy Rev.* **52,** 897–906 (2015).

53.   Garland, N. L. Fuel Cells Sub-Program Overview. *2008 DOE Hydrog. Progr. merit Rev.*

peer Eval. Meet. (2008).

54. Satyapal, S. 2014 Progress Report for the D.O.E Hydrogen and Fuel Cells Program. *Doe/Go-102014-4504* 1–5 (2014). doi:10.1007/s13398-014-0173-7.2

55. polinares.eu. *Fact sheet: Platinum Group Metals*. (2012).

56. George, M. W. 2006 Minerals Yearbook PLATINUM-GROUP METALS Platinum-GrouP metals. (2007).

57. Matthey, J. Price Charts - Johnson Matthey. Available at: http://www.platinum.matthey.com/prices/price-charts.

58. Scott, J. H. The Development of Fuel Cell Technology for Electric Power Generation: From NASA's Manned Space Program to the "Hydrogen Economy" *Proc. IEEE* **94,** 1815–1825 (2006).

59. Watkins, D. S., Dircks, K. W. & Epp, D. G. Fuel cell fluid flow field plate. (1992).

60. Banerjee, S. & Curtin, D. E. Nafion® perfluorinated membranes in fuel cells. *J. Fluor. Chem.* **125,** 1211–1216 (2004).

61. Hickner, M. A., Ghassemi, H., Kim, Y. S., Einsla, B. R. & McGrath, J. E. Alternative Polymer Systems for Proton Exchange Membranes (PEMs). *Chem. Rev.* **104,** 4587–4612 (2004).

62. Peighambardoust, S. J., Rowshanzamir, S. & Amjadi, M. Review of the proton exchange membranes for fuel cell applications. *Int. J. Hydrogen Energy* **35,** 9349–9384 (2010).

63. Marken, F. Electrochemistry: Introduction. Lecture Series, University of Bath. (2009).

64. Horsewell, S. Electrochemistry: Introduction, Lecture Series, University of Birmingham. (2011).

65. Fisher, A. C. *Electrode Dynamics*. (Oxford University Press, 1996).

66. Compton, R. G. & Sanders, G. H. W. *Electrode Potentials*. (Oxford University Press, 1996).

67. Brett, C. M. A. & Brett, A. M. O. *Electroanalysis*. (Oxford University Press, 1998).

68. Atkins, P. & Paula, J. *Elements of Physical Chemistry*. (Oxford University Press, 1992).

69. Compton, R. G. & Banks, C. E. *Understanding Voltammetry*. (Imperial College Press, 2011).

70. Rieger, P. H. *Electrochemistry*. (Chaoman & Hall, 1993).

71. Bard, Allen. J. Faulkner, L. R. *Electrochemical methods - Fundamentals and applications*. (John Wiley & Sons, Inc., 1993).

72. Holze, R. & Little, R. D. *Experimental Electrochemistry. Science (New York, N.Y.)* **23,** (WILEY-VCH Verlag, 2009).

73. McCreery, R. L., Cline, K. K., McDermott, C. A. & McDermott, M. T. Control of reactivity at carbon electrode surfaces. *Colloids Surfaces A Physicochem. Eng. Asp.* **93,** 211–219 (1994).

74. Chen, P. & Mccreery, R. L. Control of Electron Transfer Kinetics at Glassy Carbon Electrodes by Specific Surface Modification. *Anal. Chem.* **68,** 3958–3965 (1996).

75. Jenkins, G. M. & Kawamura, K. Structure of Glassy Carbon. *Nat.* **231,** 175–176 (1971).

76. Kuo, T.-C. & Mccreery, R. L. Surface Chemistry and Electron-Transfer Kinetics of Hydrogen-Modified Glassy Carbon Electrodes. *Anal. Chem.* **71,** 1553–1560 (1999).

77. Gillet, A. C. From water to water, hydrogen as a renewable energy vector for the future. (1999).

78. Kazim, A. Exergy analysis of a PEM fuel cell at variable operating conditions. *Energy Convers. Manag.* **45,** 1949–1961 (2004).

79. BARBIR, F. & Gómez, T. Efficiency and economics of proton exchange membrane (PEM)

fuel cells. *Int. J. Hydrogen Energy* **21,** 891–901 (1996).

80. Semelsberger, T. A. & Borup, R. L. Fuel effects on start-up energy and efficiency for automotive PEM fuel cell systems. *Int. J. Hydrogen Energy* **30,** 425–435 (2005).

81. Gu, W., Arisetty, S., Kumaraguru, S. & Mathias, M. (Invited) Elucidating PEMFC Voltage Loss Contributions Via Mathematical Modeling and Differential Cell Testing. *Meet. Abstr.* **MA2016-01,** 1340–1340 (2016).

82. Husar, A., Strahl, S. & Riera, J. Experimental characterization methodology for the identification of voltage losses of PEMFC: Applied to an open cathode stack. *Int. J. Hydrogen Energy* **37,** 7309–7315 (2012).

83. Inaba, M., Yamada, H., Tokunaga, J. & Tasaka, A. Effect of Agglomeration of Pt/C Catalyst on Hydrogen Peroxide Formation. *Electrochem. Solid-State Lett.* **7,** A474 (2004).

84. Curtin, D. E., Lousenberg, R. D., Henry, T. J., Tangeman, P. C. & Tisack, M. E. Advanced materials for improved PEMFC performance and life. *J. Power Sources* **131,** 41–48 (2004).

85. Baschuk, J. J. & Li, X. Carbon monoxide poisoning of proton exchange membrane fuel cells. *Int. J. Energy Res.* **25,** 695–713 (2001).

86. Li, Q., He, R., Gao, J.-A., Jensen, J. O. & Bjerrum, N. J. The CO Poisoning Effect in PEMFCs Operational at Temperatures up to 200°C. *J. Electrochem. Soc.* **150,** A1599 (2003).

87. Cheng, X. *et al.* A review of PEM hydrogen fuel cell contamination: Impacts, mechanisms, and mitigation. *J. Power Sources* **165,** 739–756 (2007).

88. Larminie, J. & Dicks, A. *Fuel Cell Systems Explained*. (John Wiley & Sons, Ltd, 2000).

89. McDougall, A. *Fuel Cells*. (Macmillan Education UK, 1976). doi:10.1007/978-1-349-15693-1

90.   US DRIVE. DOE. *Fuel Cell technical roadmap 2013*. (20130).

91.   Papageorgopoulos, D. V . 0 Fuel Cells Program Overview. 3–8 (2013).

92.   Martin, S., Martinez-Vazquez, B., Garcia-Ybarra, P. L. & Castillo, J. L. Peak utilization of catalyst with ultra-low Pt loaded PEM fuel cell electrodes prepared by the electrospray method. *J. Power Sources* **229,** 179–184 (2013).

93.   Shukla, S., Domican, K., Karan, K., Bhattacharjee, S. & Secanell, M. Analysis of Low Platinum Loading Thin Polymer Electrolyte Fuel Cell Electrodes Prepared by Inkjet Printing. *Electrochim. Acta* **156,** 289–300 (2015).

94.   Kongkanand, A. *et al.* Achieving High-Power PEM Fuel Cell Performance with an Ultralow-Pt-Content Core–Shell Catalyst. *ACS Catal.* **6,** 1578–1583 (2016).

95.   Debe, M. K. Electrocatalyst approaches and challenges for automotive fuel cells. *Nature* **486,** 43–51 (2012).

96.   Rockward, T. *et al.* LA-UR-13-28484 Title: Effect of Surface Adsorbing Contaminants on NanoStructured Thin Film (NSTF) Electrodes. (2013).

97.   Santoro, C., Babanova, S. & Atanassov, P. From Chemical Fuel Cells to Biological Fuel Cells: Challenges and Directions. *Meet. Abstr.* **MA2015-01,** 2295–2295 (2015).

98.   Abbou, S. *et al.* High Potential Excursions during PEM Fuel Cell Operation with Dead-Ended Anode. *J. Electrochem. Soc.* **162,** F1212–F1220 (2015).

99.   Rheinlander, P., Henning, S., Herranz, J. & Gasteiger, H. A. Comparing Hydrogen Oxidation and Evolution Reaction Kinetics on Polycrystalline Platinum in 0.1 M and 1 M KOH. *ECS Trans.* **50,** 2163–2174 (2013).

100.   Pedersen, C. M. *et al.* Benchmarking Pt-based electrocatalysts for low temperature fuel cell reactions with the rotating disk electrode: oxygen reduction and hydrogen oxidation in the

presence of CO (review article). *Electrochim. Acta* **179,** 647–657 (2015).

101. Mello, R. M. Q. & Ticianelli, E. A. Kinetic study of the hydrogen oxidation reaction on platinum and Nafion ® covered platinum electrodes. *Electrochim. Acta* **42,** 1031–1039 (1997).

102. Vogel, W., Lundquist, L., Ross, P. & Stonehart, P. Reaction pathways and poisons—II. *Electrochim. Acta* **20,** 79–93 (1975).

103. Schmidt, T. J. *et al.* Surface Characterization and Electrochemical Behavior of Well-Defined Pt−Pd{111} Single-Crystal Surfaces: A Comparative Study Using Pt{111} and Palladium-Modified Pt{111} Electrodes. *Langmuir* **18,** 6969–6975 (2002).

104. Elliott, J. M., Birkin, P. R., Bartlett, P. N. & Attard, G. S. Platinum Microelectrodes with Unique High Surface Areas. *Langmuir* **15,** 7411–7415 (1999).

105. Zhang, L. & Xia, Z. Mechanisms of Oxygen Reduction Reaction on Nitrogen-Doped Graphene for Fuel Cells. *J. Phys. Chem. C* **115,** 11170–11176 (2011).

106. Tripković, V., Skúlason, E., Siahrostami, S., Nørskov, J. K. & Rossmeisl, J. The oxygen reduction reaction mechanism on Pt(111) from density functional theory calculations. *Electrochim. Acta* **55,** 7975–7981 (2010).

107. Antoine, O. & Durand, R. RRDE study of oxygen reduction on Pt nanoparticles inside Nafion®: H2O2 production in PEMFC cathode conditions. *J. Appl. Electrochem.* **30,** 839–844 (2000).

108. Antoine, O., Bultel, Y. & Durand, R. Oxygen reduction reaction kinetics and mechanism on platinum nanoparticles inside Nafion®. *J. Electroanal. Chem.* **499,** 85–94 (2001).

109. Yu, X. & Ye, S. Recent advances in activity and durability enhancement of Pt/C catalytic cathode in PEMFC: Part I. Physico-chemical and electronic interaction between Pt and

carbon support, and activity enhancement of Pt/C catalyst. *J. Power Sources* **172,** 133–144 (2007).

110. Völkening, S., Bedürftig, K., Jacobi, K., Wintterlin, J. & Ertl, G. Dual-Path Mechanism for Catalytic Oxidation of Hydrogen on Platinum Surfaces. *Phys. Rev. Lett.* **83,** 2672–2675 (1999).

111. Imai, H. *et al.* In Situ and Real-Time Monitoring of Oxide Growth in a Few Monolayers at Surfaces of Platinum Nanoparticles in Aqueous Media. *J. Am. Chem. Soc.* **131,** 6293–6300 (2009).

112. Starz, K. ., Auer, E., Lehmann, T. & Zuber, R. Characteristics of platinum-based electrocatalysts for mobile PEMFC applications. *J. Power Sources* **84,** 167–172 (1999).

113. Sharma, S. & Pollet, B. G. Support materials for PEMFC and DMFC electrocatalysts—A review. *J. Power Sources* **208,** 96–119 (2012).

114. Pollet, B., Newton, J. E., Preece, J. A. & Curnick, O. J. The Use of Ionic and Non-Ionic Surfactants for the Control of Platinum Nanoparticle Aggregation in Proton Exchange Membrane Fuel Cells (PEMFCs). in *ECS Transactions* **41,** 2165–2173 (2011).

115. Newton, J. E., Preece, J. A. & Pollet, B. G. Control of nanoparticle aggregation in PEMFCs using surfactants. *Int. J. Low-Carbon Technol.* **7,** 38–43 (2012).

116. Curnick, O. J. *et al.* Nafion®-stabilised Pt/C electrocatalysts with efficient catalyst layer ionomer distribution for proton exchange membrane fuel cells. *RSC Adv.* **2,** 8368 (2012).

117. Curnick, O. J., Mendes, P. M. & Pollet, B. G. *Enhanced durability of a Pt/C electrocatalyst derived from Nafion-stabilised colloidal platinum nanoparticles*. *Electrochemistry Communications* **12,** (2010).

118. Tseng, A. A., Kuan Chen, K., Chen, C. D. & Ma, K. J. Electron beam lithography in

nanoscale fabrication: recent development. *IEEE Trans. Electron. Packag. Manuf.* **26,** 141–149 (2003).

119. Chen, W. & Ahmed, H. Fabrication of 5–7 nm wide etched lines in silicon using 100 keV electron-beam lithography and polymethylmethacrylate resist. *Appl. Phys. Lett.* **62,** 1499 (1993).

120. Vieu, C. *et al.* Electron beam lithography: resolution limits and applications. *Appl. Surf. Sci.* **164,** 111–117 (2000).

121. Pease, R. F. W. Electron beam lithography. *Contemp. Phys.* **22,** 265–290 (1981).

122. Lau, C., Martin, G., Minteer, S. D. & Cooney, M. J. Development of a Chitosan Scaffold Electrode for Fuel Cell Applications. *Electroanalysis* **22,** 793–798 (2010).

123. Zhi, M. *et al.* Nanofiber scaffold for cathode of solid oxidefuel cell. *Energy Environ. Sci.* **4,** 417–420 (2011).

124. Metz, K. M., Tse, K.-Y., Baker, S. E., Landis, E. C. & Hamers, R. J. Ultrahigh-Surface-Area Metallic Electrodes by Templated Electroless Deposition on Functionalized Carbon Nanofiber Scaffolds. *Chem. Mater.* **18,** 5398–5400 (2006).

125. Metz, K. M., Goel, D. & Hamers, R. J. Molecular Monolayers Enhance the Formation of Electrocatalytic Platinum Nanoparticles on Vertically Aligned Carbon Nanofiber Scaffolds. *J. Phys. Chem. C* **111,** 7260–7265 (2007).

126. Ng, Y. H., Lightcap, I. V., Goodwin, K., Matsumura, M. & Kamat, P. V. To What Extent Do Graphene Scaffolds Improve the Photovoltaic and Photocatalytic Response of TiO_2 Nanostructured Films? *J. Phys. Chem. Lett.* **1,** 2222–2227 (2010).

127. Kongkanand, A., Martínez Domínguez, R. & Kamat, P. V. Single Wall Carbon Nanotube Scaffolds for Photoelectrochemical Solar Cells. Capture and Transport of Photogenerated

Electrons. *Nano Lett.* **7,** 676–680 (2007).

128. Jha, M. K. *et al.* Hydrometallurgical recovery/recycling of platinum by the leaching of spent catalysts: A review. *Hydrometallurgy* **133,** 23–32 (2013).

129. Binnemans, K. *et al.* Recycling of rare earths: a critical review. *J. Clean. Prod.* **51,** 1–22 (2013).

130. REMOVAL OF PLATINUM GROUP METALS FROM THE USED AUTO CATALYTIC CONVERTER. (2008).

131. Jinglei Yu, J., Williams, E. & Meiting Ju, M. Review and prospects of recycling methods for waste printed circuit boards. in *2009 IEEE International Symposium on Sustainable Systems and Technology* 1–5 (IEEE, 2009). doi:10.1109/ISSST.2009.5156727

132. Xu, J. *et al.* A review of processes and technologies for the recycling of lithium-ion secondary batteries. *J. Power Sources* **177,** 512–527 (2008).

133. Binnemans, K., Pontikes, Y., Jones, P. T., Van Gerven, T. & Blanpain, B. *Recovery of rare earths from industrial waste residues: a concise review*. (2013).

134. Ravilious, K. Digging downtown: the hunt for urban gold. *New Sci.* **218,** 40–43 (2013).

135. Syed, S. Recovery of gold from secondary sources—A review. *Hydrometallurgy* **115,** 30–51 (2012).

136. Jadhav, U. U. & Hocheng, H. A review of recovery of metals from industrial waste Industrial management and organisation. *J. Achiev. Mater. Manuf. Eng.* **54,** (2012).

137. Mishra, D., Kim, D.-J., Ahn, J.-G. & Rhee, Y.-H. Bioleaching: A microbial process of metal recovery; A review. *Met. Mater. Int.* **11,** 249–256 (2005).

138. Akcil, A., Vegliò, F., Ferella, F., Okudan, M. D. & Tuncuk, A. A review of metal recovery from spent petroleum catalysts and ash. *Waste Manag.* **45,** 420–433 (2015).

139.	Deplanche, K. & Macaskie, L. E. Biorecovery of gold byEscherichia coli andDesulfovibrio desulfuricans. *Biotechnol. Bioeng.* **99,** 1055–1064 (2008).

140.	Deplanche, K., Murray, A., Mennan, C., Taylor, S. & Macaskie, L. Biorecycling of Precious Metals and Rare Earth Elements.

141.	Schröfel, A. & Kratošová, G. in 373–409 (Springer Netherlands, 2011). doi:10.1007/978-94-007-1248-5_14

142.	Creamer, N. J. *et al.* Novel supported Pd hydrogenation bionanocatalyst for hybrid homogeneous/heterogeneous catalysis. *Catal. Today* **128,** 80–87 (2007).

143.	Attard, G., Casadesús, M., Macaskie, L. E. & Deplanche, K. Biosynthesis of Platinum Nanoparticles by *Escherichia coli* MC4100: Can Such Nanoparticles Exhibit Intrinsic Surface Enantioselectivity? *Langmuir* **28,** 5267–5274 (2012).

144.	Bennett, J. A. *et al.* Improving Selectivity in 2-Butyne-1,4-diol Hydrogenation using Biogenic Pt Catalysts. *ACS Catal.* **2,** 504–511 (2012).

145.	Deplanche, K. *et al.* Catalytic activity of biomass-supported Pd nanoparticles: Influence of the biological component in catalytic efficacy and potential application in 'green' synthesis of fine chemicals and pharmaceuticals. *Appl. Catal. B Environ.* **147,** 651–665 (2014).

146.	Macaskie, L. E. *et al.* Today's wastes, tomorrow's materials for environmental protection. *Hydrometallurgy* **104,** 483–487 (2010).

147.	Deplanche, K., Caldelari, I., Mikheenko, I. P., Sargent, F. & Macaskie, L. E. Involvement of hydrogenases in the formation of highly catalytic Pd(0) nanoparticles by bioreduction of Pd(II) using Escherichia coli mutant strains. *Microbiology* **156,** 2630–2640 (2010).

148.	Deplanche, K. *et al.* Microbial synthesis of core/shell gold/palladium nanoparticles for applications in green chemistry. *J. R. Soc. Interface* **9,** 1705–12 (2012).

149. Deplanche, K., Woods, R. D., Mikheenko, I. P., Sockett, R. E. & Macaskie, L. E. Manufacture of stable palladium and gold nanoparticles on native and genetically engineered flagella scaffolds. *Biotechnol. Bioeng.* **101,** 873–880 (2008).

150. Foulkes, J. M., Deplanche, K., Sargent, F., Macaskie, L. E. & Lloyd, J. R. A Novel Aerobic Mechanism for Reductive Palladium Biomineralization and Recovery by *Escherichia coli*. *Geomicrobiol. J.* **33,** 230–236 (2016).

151. Yong, P., Mikheenko, I. P., Deplanche, K., Redwood, M. D. & Macaskie, L. E. Biorefining of precious metals from wastes: an answer to manufacturing of cheap nanocatalysts for fuel cells and power generation via an integrated biorefinery? *Biotechnol. Lett.* **32,** 1821–1828 (2010).

152. Orozco, R. L. *et al.* Towards an integrated system for bio-energy: hydrogen production by Escherichia coli and use of palladium-coated waste cells for electricity generation in a fuel cell. *Biotechnol. Lett.* **32,** 1837–1845 (2010).

153. Yong, P., Mikheenko, I. P. & Macaskie, L. E. A Novel Fuel Cell Catalyst for Clean Energy Production Based on a Bionanocatalyst. *Adv. Mater. Res.* **20–21,** 655–658 (2007).

154. Yong, P., Mikheenko, I. P., Deplanche, K., Sargent, F. & Macaskie, L. E. Biorecovery of Precious Metals from Wastes and Conversion into Fuel Cell Catalyst for Electricity Production. *Adv. Mater. Res.* **71–73,** 729–732 (2009).

155. Ogi, T., Honda, R., Tamaoki, K., Saitoh, N. & Konishi, Y. Direct room-temperature synthesis of a highly dispersed Pd nanoparticle catalyst and its electrical properties in a fuel cell. *Powder Technol.* **205,** 143–148 (2011).

156. Holton, O. T. & Stevenson, J. W. The Role of Platinum in Proton Exchange Membrane Fuel Cells. *Platin. Met. Rev.* **57,** 259–271 (2013).

157. Nørskov, J. K. *et al.* Origin of the Overpotential for Oxygen Reduction at a Fuel-Cell Cathode. *J. Phys. Chem. B* **108,** 17886–17892 (2004).

158. Bonakdarpour, A. *et al.* Corrosion of Transition Metals in Pt 1-x M x (M = Fe, Ni, Mn) Proton Exchange Membrane Fuel Cell (PEMFC) Electrocatalysts.

159. Toda, T., Igarashi, H., Uchida, H. & Watanabe, M. Enhancement of the Electroreduction of Oxygen on Pt Alloys with Fe, Ni, and Co. *J. Electrochem. Soc.* **146,** 3750 (1999).

160. Renjith, A. *et al.* One step preparation of 'ready to use' Au@Pd nanoparticle modified surface using deep eutectic solvents and a study of its electrocatalytic properties in methanol oxidation reaction. *J. Mater. Chem. A* **3,** 3019–3028 (2015).

161. Zhang, J., Vukmirovic, M. B., Xu, Y., Mavrikakis, M. & Adzic, R. R. Controlling the Catalytic Activity of Platinum-Monolayer Electrocatalysts for Oxygen Reduction with Different Substrates. *Angew. Chemie Int. Ed.* **44,** 2132–2135 (2005).

162. Greeley, J. *et al.* Alloys of platinum and early transition metals as oxygen reduction electrocatalysts. *Nat. Chem.* **1,** 552–556 (2009).

163. Koh, S. & Strasser, P. Electrocatalysis on Bimetallic Surfaces: Modifying Catalytic Reactivity for Oxygen Reduction by Voltammetric Surface Dealloying. *J. Am. Chem. Soc.* **129,** 12624–12625 (2007).

164. Suo, Y., Zhuang, L. & Lu, J. First-Principles Considerations in the Design of Pd-Alloy Catalysts for Oxygen Reduction. *Angew. Chemie Int. Ed.* **46,** 2862–2864 (2007).

165. Mazumder, V., Chi, M., More, K. L. & Sun, S. Core/Shell Pd/FePt Nanoparticles as an Active and Durable Catalyst for the Oxygen Reduction Reaction. *J. Am. Chem. Soc.* **132,** 7848–7849 (2010).

166. Antolini, E., Salgado, J. R. C. & Gonzalez, E. R. The stability of Pt–M (M=first row

transition metal) alloy catalysts and its effect on the activity in low temperature fuel cells: A literature review and tests on a Pt–Co catalyst. *J. Power Sources* **160,** 957–968 (2006).

167. Shao, M.-H., Sasaki, K. & Adzic, R. R. Pd−Fe Nanoparticles as Electrocatalysts for Oxygen Reduction. *J. Am. Chem. Soc.* **128,** 3526–3527 (2006).

168. Wei, P.-J., Yu, G.-Q., Naruta, Y. & Liu, J.-G. Covalent Grafting of Carbon Nanotubes with a Biomimetic Heme Model Compound To Enhance Oxygen Reduction Reactions. *Angew. Chemie Int. Ed.* **53,** 6659–6663 (2014).

169. Lee, D. H., Lee, W. J., Lee, W. J., Kim, S. O. & Kim, Y.-H. Theory, Synthesis, and Oxygen Reduction Catalysis of Fe-Porphyrin-Like Carbon Nanotube. *Phys. Rev. Lett.* **106,** 175502 (2011).

170. Weng, Y. C., Fan, F.-R. F. & Bard, A. J. Combinatorial Biomimetics. Optimization of a Composition of Copper(II) Poly- l -Histidine Complex as an Electrocatalyst for O $_2$ Reduction by Scanning Electrochemical Microscopy. *J. Am. Chem. Soc.* **127,** 17576–17577 (2005).

171. Dai, L., Xue, Y., Qu, L., Choi, H.-J. & Baek, J.-B. Metal-Free Catalysts for Oxygen Reduction Reaction. *Chem. Rev.* **115,** 4823–4892 (2015).

172. Kong, C. S., Kim, D.-Y., Lee, H.-K., Shul, Y.-G. & Lee, T.-H. Influence of pore-size distribution of diffusion layer on mass-transport problems of proton exchange membrane fuel cells. *J. Power Sources* **108,** 185–191 (2002).

173. Singh, D., Lu, D. M. & Djilali, N. A two-dimensional analysis of mass transport in proton exchange membrane fuel cells. *Int. J. Eng. Sci.* **37,** 431–452 (1999).

174. Kandlikar, S. G. & Lu, Z. Thermal management issues in a PEMFC stack – A brief review of current status. *Appl. Therm. Eng.* **29,** 1276–1280 (2009).

175. Shao, Y., Yin, G., Wang, Z. & Gao, Y. Proton exchange membrane fuel cell from low temperature to high temperature: Material challenges. *J. Power Sources* **167,** 235–242 (2007).

176. Chandan, A. *et al.* High temperature (HT) polymer electrolyte membrane fuel cells (PEMFC) – A review. *J. Power Sources* **231,** 264–278 (2013).

177. Cindrella, L. *et al.* Gas diffusion layer for proton exchange membrane fuel cells—A review. *J. Power Sources* **194,** 146–160 (2009).

178. Ji, M. & Wei, Z. A Review of Water Management in Polymer Electrolyte Membrane Fuel Cells. *Energies* **2,** 1057–1106 (2009).

179. Berzelius, J. J. Beitrag zur näheren Kenntniss des Molybdäns. *Ann. Phys.* **82,** 369–392 (1826).

180. HIll, C. L. Introduction: PolyoxometalatessMulticomponent Molecular Vehicles To Probe Fundamental Issues and Practical Problems. *Chemcial Rev.* **98,** (1998).

181. Li, F. *et al.* Coordination assemblies of polyoxomolybdate cluster framework: From labile building blocks to stable functional materials. *Dalt. Trans.* **40,** 4024 (2011).

182. Griffith, W. P. Transition metal oxo complexes. *Coord. Chem. Rev.* **5,** 459–517 (1970).

183. Papaconstantinou, E. Photochemistry of polyoxometallates of molybdenum and tungsten and/or vanadium. *Chem. Soc. Rev.* **18,** 1 (1989).

184. Chen, Q. & Zubieta, J. Coordination chemistry of soluble metal oxides of molybdenum and vanadium. *Coord. Chem. Rev.* **114,** 107–167 (1992).

185. Müller, A., Peters, F., Pope, M. T. & Gatteschi, D. Polyoxometalates: Very Large ClustersNanoscale Magnets. *Chem. Rev.* **98,** 239–272 (1998).

186. Pope, M. T. *Heteropoly and isopoly oxometalates*. (Springer-Verlag, 1983).

187. Hill, C. L. & Prosser-McCartha, C. M. Homogeneous catalysis by transition metal oxygen anion clusters. *Coord. Chem. Rev.* **143,** 407–455 (1995).

188. Gouzerh, P. & Proust, A. Main-Group Element, Organic, and Organometallic Derivatives of Polyoxometalates. *Chem. Rev.* **98,** 77–112 (1998).

189. Katsoulis, D. E. A Survey of Applications of Polyoxometalates. *Chem. Rev.* **98,** 359–388 (1998).

190. Sadakane, M. & Steckhan, E. Electrochemical Properties of Polyoxometalates as Electrocatalysts. *Chem. Rev.* **98,** 219–238 (1998).

191. Weinstock, I. A. Homogeneous-Phase Electron-Transfer Reactions of Polyoxometalates [†]. *Chem. Rev.* **98,** 113–170 (1998).

192. Dolbecq, A., Dumas, E., Mayer, C. R. & Mialane, P. Hybrid Organic−Inorganic Polyoxometalate Compounds: From Structural Diversity to Applications. *Chem. Rev.* **110,** 6009–6048 (2010).

193. Wang, S.-S. & Yang, G.-Y. Recent Advances in Polyoxometalate-Catalyzed Reactions. *Chem. Rev.* **115,** 4893–4962 (2015).

194. Long, D.-L., Tsunashima, R. & Cronin, L. Polyoxometalates: Building Blocks for Functional Nanoscale Systems. *Angew. Chemie Int. Ed.* **49,** 1736–1758 (2010).

195. Kortz, U. *et al.* Polyoxometalates: Fascinating structures, unique magnetic properties. *Coord. Chem. Rev.* **253,** 2315–2327 (2009).

196. Carraro, M. & Gross, S. Hybrid Materials Based on the Embedding of Organically Modified Transition Metal Oxoclusters or Polyoxometalates into Polymers for Functional Applications: A Review. *Materials (Basel).* **7,** 3956–3989 (2014).

197. Jiang, M., Zhu, D., Cai, J., Zhang, H. & Zhao, X. Electrocatalytic Hydrogen Evolution and

Oxygen Reduction on Polyoxotungstates/Graphene Nanocomposite Multilayers. *J. Phys. Chem. C* **118,** 14371–14378 (2014).

198. Ma, H., Peng, J., Chen, Y., Feng, Y. & Wang, E. Photoluminescent multilayer film based on polyoxometalate and tris(2,2-bipyridine)ruthenium. *J. Solid State Chem.* **177,** 3333–3338 (2004).

199. Kourasi, M., Wills, R. G. A., Shah, A. A. & Walsh, F. C. Heteropolyacids for fuel cell applications. *Electrochim. Acta* **127,** 454–466 (2014).

200. Grate, J. H. Keggin phosphomolybdovanadates for catalytic oxidations. *J. Mol. Catal. A Chem.* **114,** 93–101 (1996).

201. Park, D. R. *et al.* Redox Properties and Catalytic Oxidation Activities of Polyatom-Substituted H n PW11M1O40 (M = V, Nb, Ta, and W) Keggin Heteropolyacid Catalysts. *Catal. Letters* **132,** 363–369 (2009).

202. Meister, G. E. & Butler, A. Molybdenum(VI)- and Tungsten(VI)-Mediated Biomimetic Chemistry of Vanadium Bromoperoxidase. *Inorg. Chem.* **33,** 3269–3275 (1994).

203. Mimoun, H. *et al.* Vanadium(V) peroxy complexes. New versatile biomimetic reagents for epoxidation of olefins and hydroxylation of alkanes and aromatic hydrocarbons. *J. Am. Chem. Soc.* **105,** 3101–3110 (1983).

204. McKenna, C. E., Benemann, J. R. & Traylor, T. G. A vanadium containing nitrogenase preparation: Implications for the role of molybdenum in nitrogen fixation. *Biochem. Biophys. Res. Commun.* **41,** 1501–1508 (1970).

205. Thompson, K. H., McNeill, J. H. & Orvig, C. Vanadium Compounds as Insulin Mimics. *Chem. Rev.* **99,** 2561–2572 (1999).

206. Otto Folin, B. ON PHOSPHOTUNGSTIC-PHOSPHOMOLYBDIC COMPOUNDS AS

COLOR REAGENTS. (1912).

207. Watson, M. L. Staining of Tissue Sections for Electron Microscopy with Heavy Metals. *J. Cell Biol.* **4,** 475–478 (1958).

208. LOWRY, O. H. & LOPEZ, J. A. The determination of inorganic phosphate in the presence of labile phosphate esters. *J. Biol. Chem.* **162,** 421–428 (1946).

209. Martin, J. B. & Doty, D. M. Determination of Inorganic Phosphate. *Anal. Chem.* **21,** 965–967 (1949).

210. KOZHEVNIKOV, I. V. Heteropoly Acids and Related Compounds as Catalysts for Fine Chemical Synthesis. *Catal. Rev.* **37,** 311–352 (1995).

211. Kozhevnikov, I. V. Heterogeneous acid catalysis by heteropoly acids: Approaches to catalyst deactivation. *J. Mol. Catal. A Chem.* **305,** 104–111 (2009).

212. Kozhevnikov, I. V. Sustainable heterogeneous acid catalysis by heteropoly acids. *J. Mol. Catal. A Chem.* **262,** 86–92 (2007).

213. Wang, X.-L., Wang, E.-B., Lan, Y. & Hu, C.-W. Renewable PMo 12 -Based Inorganic-Organic Hybrid Material Bulk- Modified Carbon Paste Electrode: Preparation, Electrochemistry and Electrocatalysis.

214. Savadogo, O. & Carrier, F. The hydrogen evolution reaction in basic medium on iron electrodeposited with heteropolyacids. *J. Appl. Electrochem.* **22,** 437–442 (1992).

215. Stanis, R. J., Kuo, M.-C., Rickett, A. J., Turner, J. A. & Herring, A. M. Investigation into the activity of heteropolyacids towards the oxygen reduction reaction on PEMFC cathodes. *Electrochim. Acta* **53,** 8277–8286 (2008).

216. Ferrell, J. R., Kuo, M.-C., Turner, J. A. & Herring, A. M. The use of the heteropoly acids, H3PMo12O40 and H3PW12O40, for the enhanced electrochemical oxidation of methanol

for direct methanol fuel cells. *Electrochim. Acta* **53,** 4927–4933 (2008).

217. Oh, S.-Y. Y. *et al.* Self-assembled monolayers of diamine molecules and phosphomolybdic acid on an ITO surface. *New J. Chem.* **28,** 495 (2004).

218. Lapham, D. & Moffat, J. B. Preparative effects on the surface area and pore structure of microporous heteropoly oxometalates. *Langmuir* **7,** 2273–2278 (1991).

219. Keïta, B. & Nadjo, L. Activation of electrode surfaces. *J. Electroanal. Chem. Interfacial Electrochem.* **191,** 441–448 (1985).

220. Wang, Y. Q. *et al.* Methanol Electrochemical Oxidation on Au/Pt Electrode Enhanced by Phosphomolybdic Acid. *J. Phys. Chem. C* **112,** 18672–18676 (2008).

221. Wang, P. & Li, Y. Electrochemical and electrocatalytic properties of polypyrrole film doped with heteropolyanions. *J. Electroanal. Chem.* **408,** 77–81 (1996).

222. Gunn, N. L. O., Ward, D. B., Menelaou, C., Herbert, M. A. & Davies, T. J. Investigation of a chemically regenerative redox cathode polymer electrolyte fuel cell using a phosphomolybdovanadate polyoxoanion catholyte. *J. Power Sources* **348,** 107–117 (2017).

223. Odyakov, V. F., Zhizhina, E. G. & Matveev, K. I. Redox potentials of molybdovanadophosphoric heteropoly acids in aqueous solutions. *J. Mol. Catal. A Chem.* **158,** 453–456 (2000).

224. Li, Q. *et al.* Spontaneous Redox Synthesis and Characterization of the Tetrathiafulvalene–Vanadium-Substituted Polyoxometalate Charge-Transfer Material TTF $_4$ [SVW $_{11}$ O $_{40}$]: Comparison with the Mo Analogue. *Inorg. Chem.* **53,** 10996–11006 (2014).

225. Li, Q. *et al.* Spontaneous Redox Synthesis of the Charge Transfer Material TTF $_4$ [SVMo $_{11}$ O $_{40}$]. *Inorg. Chem.* **51,** 12929–12937 (2012).

226. Nambu, J. *et al.* Detailed voltammetric and EPR study of protonation reactions

accompanying the one-electron reduction of Keggin-type polyoxometalates, [XVVM11O40]4− (X = P, As; M = Mo, W) in acetonitrile. *Dalt. Trans.* **39,** 7364 (2010).

227. Ueda, T. *et al.* Structurally characterised vanadium(v)-substituted Keggin-type heteropolysulfates [SVM11O40]3− (M = Mo, W): voltammetric and spectroscopic studies related to the V(v)/V(iv) redox couple. *Dalt. Trans.* **43,** 5462 (2014).

228. Keita, B. & Nadjo, L. New aspects of the electrochemistry of heteropolyacids. *J. Electroanal. Chem. Interfacial Electrochem.* **227,** 77–98 (1987).

229. Wroblowa, H. S., Yen-Chi-Pan & Razumney, G. Electroreduction of oxygen. *J. Electroanal. Chem. Interfacial Electrochem.* **69,** 195–201 (1976).

230. Marković, N. M., Adžić, R. R., Cahan, B. D. & Yeager, E. B. Structural effects in electrocatalysis: oxygen reduction on platinum low index single-crystal surfaces in perchloric acid solutions. *J. Electroanal. Chem.* **377,** 249–259 (1994).

231. Perez, J., Villullas, H. M. & Gonzalez, E. R. Structure sensitivity of oxygen reduction on platinum single crystal electrodes in acid solutions. *J. Electroanal. Chem.* **435,** 179–187 (1997).

232. Maciá, M. D., Campiña, J. M., Herrero, E. & Feliu, J. M. On the kinetics of oxygen reduction on platinum stepped surfaces in acidic media. *J. Electroanal. Chem.* **564,** 141–150 (2004).

233. Grgur, B. N., Marković, N. M. & Ross, P. N. Underpotential Deposition of Lead on Pt(111) in Perchloric Acid Solution: RRD Pt(111) E Measurements. *Langmuir* **13,** 6370–6374 (1997).

234. Markovic, N. M., Gasteiger, H. A. & Ross, P. N. Oxygen Reduction on Platinum Low-Index Single-Crystal Surfaces in Sulfuric Acid Solution: Rotating Ring-Pt(hkl) Disk Studies. *J. Phys. Chem.* **99,** 3411–3415 (1995).

235. Clavilier, J., Faure, R., Guinet, G. & Durand, R. Preparation of monocrystalline Pt

microelectrodes and electrochemical study of the plane surfaces cut in the direction of the {111} and {110} planes. *J. Electroanal. Chem. Interfacial Electrochem.* **107,** 205–209 (1979).

236. Hayden, B. E. Particle Size and Support Effects in Electrocatalysis. *Acc. Chem. Res.* **46,** 1858–1866 (2013).

237. Porter, N. S., Wu, H., Quan, Z. & Fang, J. Shape-Control and Electrocatalytic Activity-Enhancement of Pt-Based Bimetallic Nanocrystals. *Acc. Chem. Res.* **46,** 1867–1877 (2013).

238. Chen, X., Palmer, R. E. & Robinson, A. P. G. A high resolution water soluble fullerene molecular resist for electron beam lithography. *IOP Publ. Nanotechnol. Nanotechnol.* **19,** 275308–5 (2008).

239. Robinson, A. P. . *et al.* Exposure mechanism of fullerene derivative electron beam resists. *Chem. Phys. Lett.* **312,** 469–474 (1999).

240. Shibano, T., Nakamura, K., Takenaga, T. & Ono, K. Platinum etching in Ar/Cl2 plasmas with a photoresist mask. *J. Vac. Sci. Technol. A* **17,** (1999).

241. Contreras, A. M., Grunes, J., Yan, X.-M., Liddle, A. & Somorjai, G. A. Fabrication of platinum nanoparticles and nanowires by electron beam lithography (EBL) and nanoimprint lithography (NIL): comparison of ethylene hydrogenation kinetics. *Catal. Letters* **100,** 115–124 (2005).

242. Robinson, A. P. G., Palmer, R. E., Tada, T., Kanayama, T. & Preece, J. A. A Fullerene derivative as an electron beam resist for nanolithography. *Appl. Phys. Lett.* **72,** (1998).

243. Robinson, A. P. G. *et al.* Electron beam induced fragmentation of fullerene derivatives. *Chem. Phys. Lett.* **289,** 586–590 (1998).

244. Kissinger, P. T. & Heineman, W. R. *Laboratory Techniques in Electroanalytical Chemistry,*

Second Edition. (Marcel Dekker, 1996).

245. Ekkels, P., Rottenberg, X., Puers, R. & Tilmans, H. A. C. Evaluation of platinum as a structural thin film material for RF-MEMS devices. *J. Micromech. Microeng. J. Micromech. Microeng* **19,** (2009).

246. Köllensperger, P. A. *et al.* Patterning of platinum (Pt) thin films by chemical wet etching in Aqua Regia. *J. Micromechanics Microengineering* **22,** 67001 (2012).

247. Jacobs, P. W., Ribeiro, F. H., Somorjai, G. A. & Wind, S. J. New model catalysts: uniform platinum cluster arrays produced by electron beam lithography. *Catal. Letters* **37,** 131–136 (1996).

248. Figueira-Duarte, T. M. *et al.* Synthesis and electronic properties of fullerene derivatives substituted with oligophenylenevinylen–ferrocene conjugates. *New J. Chem.* **32,** 54–64 (2008).

249. Allemand, P. M. *et al.* Two different fullerenes have the same cyclic voltammetry. *J. Am. Chem. Soc.* **113,** 1050–1051 (1991).

250. Lebedeva, M. A. *et al.* Tuning the interactions between electron spins in fullerene-based triad systems. *Beilstein J. Org. Chem.* **10,** 332–343 (2014).

251. Park, J.-W. *et al.* Dual ion beam irradiation of polymeric materials for the modification of optical properties with improved adhesion. *Nucl. Instruments Methods Phys. Res. Sect. B Beam Interact. with Mater. Atoms* **281,** 51–55 (2012).

252. Barbagini, F. *et al.* Critical aspects of substrate nanopatterning for the ordered growth of GaN nanocolumns. *Nanoscale Res. Lett.* **6,** 632 (2011).

253. Smythe, E. J., Dickey, M. D., Whitesides, G. M. & Capasso, F. A Technique to Transfer Metallic Nanoscale Patterns to Small and Non-Planar Surfaces. *ACS Nano* **3,** 59–65 (2009).

254. Cussler, E. L. *Diffusion Mass transfer in fluid systems*. (Cambridge University Press, 1997).

255. Brierley, J. A. A perspective on developments in biohydrometallurgy. *Hydrometallurgy* **94,** 2–7 (2008).

256. Brierley, J. A. & Brierley, C. L. Present and future commercial applications of biohydrometallurgy. *Process Metall.* **9,** 81–89 (1999).

257. Bosecker, K. Bioleaching: metal solubilization by microorganisms. *FEMS Microbiol. Rev.* **20,** 591–604 (1997).

258. Krebs, W. Brombacher, C. Bosshard, P.P. Bachofen, Reinhard. Brandl, H. Microbial recovery of metals from solids. *FEMS Microbiol. Rev.* **20,** 605–617 (1997).

259. Rossi, G. The design of bioreactors. *Hydrometallurgy* **59,** 217–231 (2001).

260. Johnson, D. B. Biohydrometallurgy and the environment: Intimate and important interplay. *Hydrometallurgy* **83,** 153–166 (2006).

261. Das, N. Recovery of precious metals through biosorption — A review. *Hydrometallurgy* **103,** 180–189 (2010).

262. Dobson, R. S. & Burgess, J. E. Biological treatment of precious metal refinery wastewater: A review. *Miner. Eng.* **20,** 519–532 (2007).

263. De Corte, S., Hennebel, T., De Gusseme, B., Verstraete, W. & Boon, N. Bio-palladium: from metal recovery to catalytic applications. *Microb. Biotechnol.* **5,** 5–17 (2012).

264. Iravani, S. Bacteria in Nanoparticle Synthesis: Current Status and Future Prospects. *Int. Sch. Res. Not.* **2014,** 359316 (2014).

265. de Vargas, I., Macaskie, L. E. & Guibal, E. Biosorption of palladium and platinum by sulfate-reducing bacteria. *J. Chem. Technol. Biotechnol.* **79,** 49–56 (2004).

266. Lloyd, J. R., Yong, P. & Macaskie, L. E. Enzymatic recovery of elemental palladium by

using sulfate-reducing bacteria. *Appl. Environ. Microbiol.* **64,** 4607–9 (1998).

267. Yong, P., Rowson, N. A., Farr, J. P. G., Harris, L. R. & Macaskie, L. E. A novel electrobiotechnology for the recovery of precious metals from spent automotive catalysts. *Environ. Technol.* **24,** 289–297 (2003).

268. Creamer, N. J., Baxter-Plant, V. S., Henderson, J., Potter, M. & Macaskie, L. E. Palladium and gold removal and recovery from precious metal solutions and electronic scrap leachates by Desulfovibrio desulfuricans. *Biotechnol. Lett.* **28,** 1475–1484 (2006).

269. Lengke, M. F., Fleet, M. E. & Southam, G. Synthesis of Platinum Nanoparticles by Reaction of Filamentous Cyanobacteria with Platinum(IV)-Chloride Complex. *Langmuir* **22,** 7318–7323 (2006).

270. Riddin, T. L., Govender, Y., Gericke, M. & Whiteley, C. G. Two different hydrogenase enzymes from sulphate-reducing bacteria are responsible for the bioreductive mechanism of platinum into nanoparticles. *Enzyme Microb. Technol.* **45,** 267–273 (2009).

271. Bennett, J. A. *et al.* Palladium supported on bacterial biomass as a novel heterogeneous catalyst: A comparison of Pd/Al2O3 and bio-Pd in the hydrogenation of 2-pentyne. *Chem. Eng. Sci.* **65,** 282–290 (2010).

272. Mikheenko, I. P., Bennett, J. A., Shannon, I. J., Wood, J. & Macaskie, L. E. Biomineralised Palladium is an Effective Hydrogenation Catalyst. *Adv. Mater. Res.* **71–73,** 725–728 (2009).

273. Wood, J., Bodenes, L., Bennett, J., Deplanche, K. & Macaskie, L. E. Hydrogenation of 2-Butyne-1,4-diol Using Novel Bio-Palladium Catalysts. (2009).

274. Courtney, J. M. Bio-Engineered Gas Diffusion Electrodes (GDEs) for Proton Exchange Membrane Fuel Cells (PEMFCs). (University of Birmingham , 2011).

275. Yong, P., Paterson-Beedle, M., Mikheenko, I. P. & Macaskie, L. E. From bio-mineralisation

to fuel cells: biomanufacture of Pt and Pd nanocrystals for fuel cell electrode catalyst. *Biotechnol. Lett.* **29,** 539–544 (2007).

276. Wu, X. *et al.* A Role for Microbial Palladium Nanoparticles in Extracellular Electron Transfer. *Angew. Chemie Int. Ed.* **50,** 427–430 (2011).

277. Charlot, G. Chimie analytique quantitative. *Masson* **1,** (1974).

278. De Windt, W. *et al.* Biological control of the size and reactivity of catalytic Pd(0) produced by Shewanella oneidensis. *Antonie Van Leeuwenhoek* **90,** 377–389 (2006).

279. Windt, W. De, Aelterman, P. & Verstraete, W. Bioreductive deposition of palladium (0) nanoparticles on Shewanella oneidensis with catalytic activity towards reductive dechlorination of polychlorinated biphenyls. *Environ. Microbiol.* **7,** 314–325 (2005).

280. Courtney, J., Deplanche, K., Rees, N. V & Macaskie, L. E. Biomanufacture of nano-Pd(0) by Escherichia coli and electrochemical activity of bio-Pd(0) made at the expense of H2 and formate as electron donors. *Biotechnol. Lett.* **38,** 1903–1910 (2016).

281. Søbjerg, L. S., Lindhardt, A. T., Skrydstrup, T., Finster, K. & Meyer, R. L. Size control and catalytic activity of bio-supported palladium nanoparticles. *Colloids Surfaces B Biointerfaces* **85,** 373–378 (2011).

282. Ogi, T., Honda, R., Tamaoki, K., Saito, N. & Konishi, Y. Biopreparation of Highly Dispersed Pd Nanoparticles on Bacterial Cell and Their Catalytic Activity for Polymer Electrolyte Fuel Cell. *MRS Proc.* **1272,** 1272-NaN-3 (2010).

283. Shao, M., Chang, Q., Dodelet, J.-P. & Chenitz, R. Recent Advances in Electrocatalysts for Oxygen Reduction Reaction. *Chem. Rev.* **116,** 3594–3657 (2016).

284. Martel, David. Sojic, Neso. Kuhn, A. A simple student experiment for teaching surface electrochemistry: adsorption of polyoxometalate on graphite electrodes. *J. Chem. Educ.* **79,**

(2002).

285. Sun, C. *et al.* Fabrication of multilayer films containing 1:12 phosphomolybdic anions on the surface of a gold electrode based on electrostatic interaction and its application as an electrochemical detector in flow-injection amperometric detection of hydrogen peroxide. *J. Electroanal. Chem.* **435,** 63–68 (1997).

286. Mizuno, N. & Misono, M. Heterogeneous Catalysis. *chem rev* **98,** 199–217 (1998).

287. Serwicka, E. M., Broclawik, E., Bruckman, K. & Haber, J. TPD/TPR and quantum chemical study of methanol interaction with H3+n PV n Mo12-n O40 heteropolyacids. *Catal. Letters* **2,** 351–360 (1989).

288. Arichi, J., Eternot, M. & Louis, B. Synthesis of V-containing Keggin polyoxometalates: Versatile catalysts for the synthesis of fine chemicals? *Catal. Today* **138,** 117–122 (2008).

289. Heravi, M. M. & Sadjadi, S. Recent developments in use of heteropolyacids, their salts and polyoxometalates in organic synthesis. *J. Iran. Chem. Soc.* **6,** 1–54 (2009).

290. Zhou, Y. *et al.* Recent advances in polyoxometalate-based heterogeneous catalytic materials for liquid-phase organic transformations. *RSC Adv.* **4,** 42092–42113 (2014).

291. Maksimov, G. M. Advances in the synthesis of polyoxometalates and in the study of heteropolyacids. *Russ. Chem. Rev.* **64,** 445–461 (1995).

292. Kostantinos Kourtakis. Cation and vanadium substituted heteropolyacid catalyts for vapor phase oxidation. (1994).

293. Ji, Y. *et al.* Polyoxometalate-functionalized nanocarbon materials for energy conversion, energy storage and sensor systems. *Energy Environ. Sci.* **8,** 776–789 (2015).

294. Kim, Y. *et al.* A polyoxometalate coupled graphene oxide–Nafion composite membrane for fuel cells operating at low relative humidity. *J. Mater. Chem. A* **3,** 8148–8155 (2015).

295. Xu, D. *et al.* The assembly of vanadium(iv)-substituted Keggin-type polyoxometalate/graphene nanocomposite and its application in photovoltaic system. *J. Mater. Chem. A* **3,** 10174–10178 (2015).

296. Suárez-Guevara, J. *et al.* Stable graphene–polyoxometalate nanomaterials for application in hybrid supercapacitors. *Phys. Chem. Chem. Phys.* **16,** 20411–20414 (2014).

297. Casarini, D., Centi, G., Jiru, P., Lena, V. & Tvaruzkova, Z. Reactivity of Molybdovanadophosphoric Acids: Influence of the Presence of Vanadium in the Primary and Secondary Structure. *J. Catal.* **143,** 325–344 (1993).

298. Palermo, V. *et al.* New Vanadium Keggin Heteropolyacids Encapsulated in a Silica Framework: Recyclable Catalysts for the Synthesis of Highly Substituted Hexahydropyrimidines Under Suitable Conditions. *Catal. Letters* **145,** 1022–1032 (2015).

299. Song, I. K. & Barteau, M. A. Correlation of Negative Differential Resistance (NDR) Peak Voltages of Nanostructured Heteropolyacid (HPA) Monolayers with One Electron Reduction Potentials of HPA Catalysts. *Langmuir* **20,** 1850–1855 (2004).

300. Zhou, M., Guo, L., Lin, F. & Liu, H. Electrochemistry and electrocatalysis of polyoxometalate-ordered mesoporous carbon modified electrode. *Anal. Chim. Acta* **587,** 124–131 (2007).

301. Keita, B. & Nadjo, L. New oxometalate-based materials for catalysis and electrocatalysis. *Mater. Chem. Phys.* **22,** 77–103 (1989).

302. Haghighi, B. & Hamidi, H. Electrochemical Characterization and Application of Carbon Ionic Liquid Electrodes Containing 1 : 12 Phosphomolybdic Acid. *Electroanalysis* **21,** 1057–1065 (2009).

303. Keita, B., Nadjo, L. & Haeussler, J. P. Distribution of oxometalates on polymer-covered

electrodes. *J. Electroanal. Chem. Interfacial Electrochem.* **243,** 481–491 (1988).

304. Song, I. K., Kaba, M. S., Coulston, G., Kourtakis, K. & Barteau, M. A. Scanning Tunneling Microscopy of Ordered Arrays of Heteropolyacids Deposited on a Graphite Surface. *Chem. Mater.* **8,** 2352–2358 (1996).

305. Ingersoll, D., Kulesza, P. J. & Faulkner, L. R. Polyoxometallate-Based Layered Composite Films on Electrodes. *J. Electrochem. Soc.* **141,** 140 (1994).

306. Laviron, E. & Gabriel, S. The use of linear potential sweep voltammetry and of A.C. voltammetry for the study of the surface electrochemical reaction of stronly adsorbed systems and of redox modified electrodes. *J. Electroanal. Chem.* **100,** 263–270 (1979).

307. Laviron, E. G e n e r a l expression of the l i n e a r potential sweep v o l t a m m o g r a m in the case o f d i f f u s i o n l e s s electrochemical systems. *J. Electroanal. Chem.* **101,** 19–28 (1979).

308. Laviron, E. G e n e r a l expression of the l i n e a r potential sweep voltammogram for a surface redox reaction with interactions between the adsorbed molecules applications to modified electrodes. *J. Electroanal. Chem.* **115,** 65–74 (1980).

309. Laviron, E. A.C. Polarography and faradaic impedance of strongly adsorbed electroactive species Part 1. *J. Electroanal. Chem.* **97,** 135–149 (1979).

310. Eckermann, Amanda. L. Feld, Daniel, J. Shaw, Justine. A. Meade, T. J. Electrochemistry of redox-active self-assembled monolayers. *Coord. Chem. Rev.* **254,** (2012).

311. Cheng, L. & Dong, S. Comparative studies on electrochemical behavior and electrocatalytic properties of heteropolyanion-containing multilayer films prepared by two methods. *J. Electroanal. Chem.* **481,** 168–176 (2000).

312. Genovese, M., Foong, Yee, W. & Lian, K. Designing polyoxometalate based layer-by-layer

thin films on carbon nanomaterials for pseudocapacitive electrodes. *J. Electrochem. Soc.* **165,** a5041–a5046 (2015).

313. Wang, B. & Dong, S. Electrochemical study of isopoly- and heteropoly-oxometallates film modified microelectrodes—part 3. Further study of electrode process of isopolymolybdic anion doped in polyaniline film. *Electrochim. Acta* **38,** 1029–1035 (1993).

314. Cheng, L., Niu, L., Gong, J. & Dong, S. Electrochemical growth and characterisation of polyoxometalate-containing monolayers and multilayers on alkanethiol monolayers self-assembled on gold electrodes. *Chem. Mater.* **11,** 1465–1475 (1999).

315. Zuoping, Wang. Qunxiang, R. Lin, Xu. Enhong, Shen. Enbo, W. Isolation and studies on properres of the heteropoly blues conating vanadium keggin structure. *J. Inorg. Chem.* **1,** (1995).

316. Liu, W., Qi, W., Guo, X. & Su, D. Heteropoly Acid/Nitrogen Functionalized Onion-like Carbon Hybrid Catalyst for Ester Hydrolysis Reactions. *Chem. - An Asian J.* **11,** 491–497 (2016).

317. Ye, J.-J. *et al.* Immobilization of polyoxometalates in crystalline solids for highly efficient heterogeneous catalysis. *Dalt. Trans.* **98,** 1 (2016).

318. Wang, S.-M. *et al.* Vanadium substituted Keggin-type POM-based electrochromic films showing high performance in a Li $^+$ -based neutral non-aqueous electrolyte. *RSC Adv.* **6,** 38782–38789 (2016).

319. Rohlfing, D. F. & Kuhn, A. Preparation and characterization of polyoxometalate-modified carbon nanosheets. *Carbon N. Y.* **44,** 1942–1948 (2006).

320. Teague, C. M. *et al.* Vibrational Spectroscopy of a Keggin Polyoxometalate on Metal Electrode Surfaces. *J. Phys. Chem. B* **108,** 1974–1985 (2004).

321. Tang, Z., Liu, S., Wang, E. & Dong, S. Self-Assembled Monolayer of Polyoxometalate on Gold Surfaces: Quartz Crystal Microbalance, Electrochemistry, and in-Situ Scanning Tunneling Microscopy Study. *Langmuir* **16,** 4946–4952 (2000).

322. Sun, H. *et al.* Two New Armtype Polyoxometalates Grafted on Titanium Dioxide Films: Towards Enhanced Photoelectrochemical Performance. *ChemSusChem* **9,** 1125–1133 (2016).

323. Tessonnier, J.-P., Goubert-Renaudin, S., Alia, S., Yan, Y. & Barteau, M. A. Structure, Stability, and Electronic Interactions of Polyoxometalates on Functionalized Graphene Sheets. *Langmuir* **29,** 393–402 (2013).

324. Muñiz, J., Cuentas-Gallegos, A. K., Robles, M. & Valdéz, M. Bond formation, electronic structure, and energy storage properties on polyoxometalate–carbon nanocomposites. *Theor. Chem. Acc.* **135,** 92 (2016).

325. Yin, P., Li, D. & Liu, T. Counterion Interaction and Association in Metal-Oxide Cluster Macroanionic Solutions and the Consequent Self-Assembly. *Isr. J. Chem.* **51,** 191–204 (2011).

326. Song, I. K., Kim, H. S. & Chun, M.-S. On the reduction potential of cation-exchanged heteropolyacids (HPAs). *Korean J. Chem. Eng.* **20,** 844–849 (2003).

327. Pamin, K., Jachimska, B., Onik, K., Połtowicz, J. & Grabowski, R. Electrostatic Self-assembly of Polyoxometalates on Chitosan as Catalysts of Oxidation of Cyclic Hydrocarbons. *Catal. Letters* **127,** 167–174 (2009).

328. Ruiz Montoya, M., Marín Galvín, R. & Rodríguez Mellado, J. M. Electrooxidation of 2-Mercaptopyridine-N-oxide (Pyrithione) at Carbon Electrodes versus Mercury Electrodes. *Electroanalysis* **10,** 1030–1033 (1998).

329. Kinoshita, H., Suda, Y., Kawakubo, T., Takayama, K. & Ikeda, T. Electroanalysis of NADH Using a New Electrode Prepared from Plastic Formed Carbon. *Microchem. J.* **49,** 226–234 (1994).

330. Keita, B., Lu, Y. W., Nadjo, L. & Contant, R. *Salient electrochemical and electrocatalytic behaviour of the crown heteropolyanion K28Li5H7P8W48O184·92H2O*. *Electrochemistry Communications* **2,** (2000).

331. Kozhevnikov, I. V. Catalysis by Heteropoly Acids and Multicomponent Polyoxometalates in Liquid-Phase Reactions. *Chem. Rev.* **98,** 171–198 (1998).

332. Volker, E., Calvo, E. J. & Williams, F. J. Formation, characterization and electrocatalytic activity of layer-by-layer self-assembled films containig polyoxomolybdate over Au surfaces. *J. Electroanal. Chem.* **673,** 1–7 (2012).

333. Ammam, M. *et al.* Polyoxometalates: formation, structures, principal properties, main deposition methods and application in sensing. *J. Mater. Chem. A* **1,** 6291 (2013).

334. Liu, M. & Dong, S. Electrochemical behavior of molibdosilicic heteropoly complex with dysprosium and its doped polypyrrole film modified electrode. *Electrochim. Acta* **40,** 197–200 (1995).

335. Cheng, L., Liu, J. & Dong, S. Layer-by-layer assembly of multilayer films consisting of silicotungstate and a cationic redox polymer on 4-aminobenzoic acid modified glassy carbon electrode and their electrocatalytic effects. *Anal. Chim. Acta* **417,** 133–142 (2000).

336. Chen, J.-J. J. & Barteau, M. A. Electrochemical Properties of Keggin-Structure Polyoxometalates in Acetonitrile: Effects of Countercation, Heteroatom, and Framework Metal Exchange. *Ind. Eng. Chem. Res.* **55,** 9857–9864 (2016).

337. Zhizhina, E. G., Odyakov, V. F. & Simonova, M. V. Catalytic oxidation of organic

compounds with oxygen in the presence of Mo-V-phosphoric heteropoly acid solutions. *Kinet. Catal.* **49,** 773–781 (2008).

338. Bajuk-Bogdanovic, D., Holclaftner-Antunovic, I., Todorovic, M., Mioc, U. & Zakrewska, J. A study of 12-tungstosilicic and 12-molybdophosphoric acids in solution. *J. Serbian Chem. Soc.* **73,** 197–209 (2008).

339. Maeda, K., Himeno, S., Osakai, T., Saito, A. & Hori, T. A voltammetric study of Keggin-type heteropolymolybdate anions. *J. Electroanal. Chem.* **364,** 149–154 (1994).

340. Tangestaninejad, S., Moghadam, M., Mirkhani, V., Mohammadpoor-Baltork, I. & Salavati, H. Sonochemical and visible light induced photochemical and sonophotochemical degradation of dyes catalyzed by recoverable vanadium-containing polyphosphomolybdate immobilized on TiO2 nanoparticles. *Ultrason. Sonochem.* **15,** 815–822 (2008).

341. Fernandes, D. M., Teixeira, A. & Freire, C. Multielectrocatalysis by Layer-by-Layer Films Based on Pararosaniline and Vanadium-Substituted Phosphomolybdate. *Langmuir* **31,** 1855–1865 (2015).

342. Raj, N. K. K., Ramaswamy, A. V. & Manikandan, P. Oxidation of norbornene over vanadium-substituted phosphomolybdic acid catalysts and spectroscopic investigations. *J. Mol. Catal. A Chem.* **227,** 37–45 (2005).

343. Gall, R. D., Hill, C. L. & Walker, J. E. Selective Oxidation of Thioether Mustard (HD) Analogs by tert-Butylhydroperoxide Catalyzed by H 5 PV 2 Mo 10 O 40 Supported on Porous Carbon Materials. *J. Catal.* **17,** 473–478 (1996).

344. Turek, W., Lapkowski, M., Debiec, J. & Krowiak, A. Studies of the activity of catalysts based on heteropolyacids. *Appl. Surf. Sci.* **252,** 847–852 (2005).

345. White, A. . & Slade, R. C. . Investigation of vapour-grown conductive

polymer/heteropolyacid electrodes. *Electrochim. Acta* **48,** 2583–2588 (2003).

346. Zhong, L.-F., Zhang, Y.-M., Tang, Y. & Bai, Y. Synthesis and characterization of Keggin P–Mo–V heteropolyanion and its Langmuir–Blodgett film. *Polyhedron* **22,** 2647–2653 (2003).

347. Lyne, A. ACAL energy company background - technolgy strategy board/ decc funded demonstration project. (2011).

348. ACAL Energy Ltd. ACAL Energy leads field demonstration of platinum-free cathode fuel cell system. *www.acalenergy.co.uk* (2010).

349. renewable energy focus. ACAL Energy preparing for first installation of low-cost fuel cell system. *www.renewableenergyfocus.com* (2011).

350. ACAL Energy Ltd. ACAL Energy and Gordan Murray design to develop affordable fuel cell vehicle concpet. *www.acalenergy.co.uk* (2011).

351. Lyne, A. The route to afforable fuel cells for transport applications. *www.nwautoalliance.com* (2011).

352. Friedrich, J. M., Ponce-de-León, C., Reade, G. W. & Walsh, F. C. Reticulated vitreous carbon as an electrode material. *J. Electroanal. Chem.* **561,** 203–217 (2004).

353. Gonçalves, E. S., Rezende, M. C., Takahashi, M. F. K. & Ferreira, N. G. Electrochemical reversibility of reticulated vitreous carbon electrodes heat treated at different carbonization temperatures. *Mater. Res.* **9,** 147–152 (2006).

354. Locke, B. R., Ichihashi, A., Hyun Ha Kim, H. H. & Mizuno, A. Diesel engine exhaust treatment with a pulsed streamer corona reactor equipped with reticulated vitreous carbon electrodes. *IEEE Trans. Ind. Appl.* **37,** 715–723 (2001).

355. Walsh, F. C. Electrochemical technology for environmental treatment and clean energy

conversion. *Pure Appl. Chem.* **73,** (2001).

356.   Muehleisen, R. T., Beamer, C. W. & Tinianov, B. D. Measurements and empirical model of the acoustic properties of reticulated vitreous carbon. *J. Acoust. Soc. Am.* **117,** 536 (2005).

357.   Harris, P. J. F. Fullerene-related structure of commercial glassy carbons. *Philos. Mag.* **84,** (2006).

358.   Otani, S., Oya, A., Otani, S. & Oya, A. in *Materials Science and Technology* (Wiley-VCH Verlag GmbH & Co. KGaA, 2006). doi:10.1002/9783527603978.mst0099

359.   Cummings, C. Y. *et al. Direct reversible voltammetry and electrocatalysis with surface-stabilised Fe2O3 redox states*. *Electrochemistry Communications* **10,** (2008).

360.   Spotnitz, M. E. *et al.* Dip coating for the alignment of carbon nanotubes on curved surfaces. *J. Mater. Chem.* **14,** 1299 (2004).